8-2018

Slip-Stick Contact Conditions for the Thermo-Mechanically Coupled Flow Drill Screw Process

Jamie Daniel Skovron
Clemson University, jskovro@gmail.com

Follow this and additional works at: https://tigerprints.clemson.edu/all_dissertations

SLIP-STICK CONTACT CONDITIONS FOR THE THERMO-MECHANICALLY
COUPLED FLOW DRILL SCREW PROCESS

A Dissertation
Presented to
the Graduate School of
Clemson University

In Partial Fulfillment
of the Requirements for the Degree
Doctor of Philosophy
Automotive Engineering

---

by
Jamie Daniel Skovron
August 2018

Accepted by:
Dr. Laine Mears, Committee Chair
Dr. Gregory Mocko
Dr. Srikanth Pilla
Dr. David Schmueser

ABSTRACT

Automakers have adopted a heavy focus towards lightweighting their fleets due to the stringent emission standards placed upon them. Lightweighting can be done using several methods but material substitution is proven to be most effective considering the traditional powertrains are on the border of theoretical limits. Designing multi-material body structures is a recognized strategy, replacing steels with lightweight metals such as aluminum, magnesium, and fiber-reinforced composites. The issue now arises on how to join these materials that possess such varied thermo-mechanical properties, with resistance spot welding (RSW) currently not an option. One of the newly-adopted joining technologies is Flow Drill Screwing (FDS) which is currently the only structurally viable joining technology that does not require access to the back side of the joint.

FDS is a coupled thermo-mechanical process due to the frictional behavior between the rotating screw and stationary workpiece. An understanding of the process is limited to empirical methods mainly based on experimental findings with little known about the frictional behavior at the screw-workpiece interface. This lack of understanding not only inhibits the potential of the process, but more importantly, whether its application borders on the edge of reliability; and without an understanding to the transient contact conditions, accurate torque and temperature modeling is not feasible. Current models have limited accuracy as their methodology couples a friction coefficient and material strength term. A modeling approach that incorporates both a slipping and sticking condition is theorized to be more appropriate for frictional processes of this nature, but no coupled models currently exist. The following research aims at integrating these two conditions under a single model to enable more accurate modeling and prediction of the FDS process performance.

A secondary objective presented in this research is to determine whether FDS processing time could benefit from the assistance of supplementary energy sources. Replacing RSW with these alternate joining technologies, such as FDS, comes at the expense of an increased process time.

ii

This research aims at augmenting FDS with heat to lower the impact of this decreased process efficiency while also testing the potential to open the design space to thicker/stronger materials.

DEDICATION

To the power of persistence

ACKNOWLEDGMENTS

TABLE OF CONTENTS

LIST OF FIGURES

LIST OF TABLES

1. INTRODUCTION

1.1. Research Objective

The objective of this research is to provide a fundamental understanding of the Flow Drill Screw process to better understand why process limits exist, along with establishing safeguards to ensure high manufacturing efficiency and low process defect rate. The goal of this research is to develop temperature-dependent models of the process to understand the interfacial behavior between the screw and workpiece, and to use those models for prediction and subsequent process planning. To achieve this, process models, both analytical and numerical, are developed that couple both a slipping and sticking contact condition, with models verified through accurate torque and temperature predictions.

1.2. Motivation

The Corporate Average Fuel Economy (CAFE) standards have been steadily increasing since 2010 and are slated to reach 55.3 miles per gallon by 2025, Figure 1–1. Lightweighting has become a key strategy in the automotive industry to meet these imposed standards, with Original Equipment Manufacturers (OEMs) pushing heavy resources towards lightweighting their fleets. The most significant example being the Ford F-150, which went from an all-steel to all-aluminum body.
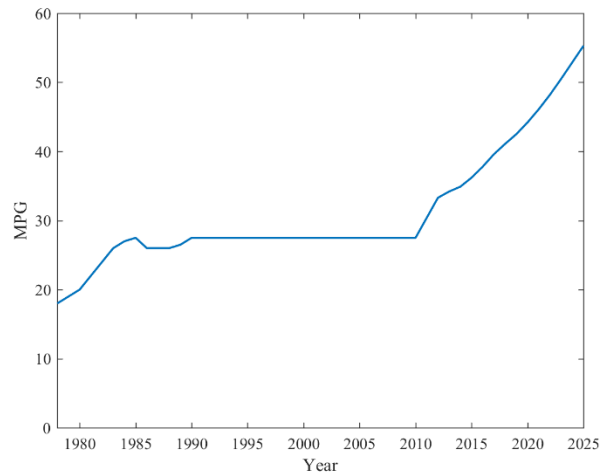
Figure 1–1: CAFE standards [1]

A significant way to reduce vehicle weight is by material substitution, which in today's world means transitioning from predominantly steel-based bodies to ones composed of aluminum alloys, ultra-high-strength steels (UHSS), and plastics. The challenge when trying to integrate all these materials into a single structure is joining them together. As these materials possess such varied thermo-mechanical properties, OEMs can no longer rely solely on resistance spot welding (RSW), and must seek other technologies such as Flow Drill Screws (FDS). FDS is the leading technology for single-sided multi-material joining although literature on the topic is limited due to its only recent mass-production adoption. One million FDS fasteners are installed every day yet reference to the process in literature is limited to broad discussions on multi-material joining. OEMs are known to have had issues with their FDS due to lack of fundamental understanding of the process. One case even had an assembly line halted due to stripped joints caused by over-tightening of the screws; a costly error for every minute of downtime. Screw manufacturers state the technology has a workpiece restriction of 5 mm for aluminum; however, we do not yet have sciences-based models to understand why this limit is necessary. These knowledge gaps must be filled for such a widely-used process. Therefore, a model of heat generation, temperature evolution, and torque during installation will lead to a full understanding of process limits in the form of stackup thickness

feasibility and tightening limitation. Such an understanding would drastically reduce errors that occur on active production lines, and lead to better process planning approaches.

1.3. Research Questions

The research objective can be fulfilled by answering the following research questions:

Research Question 1: Can determining the interfacial contact condition lead to an understanding of torque, and therefore heat generation, contributions during FDS?

Research Question 2: Can augmenting FDS with a supplementary energy source reduce process limitations of time and installation torque without reducing joint quality?

2. BACKGROUND

2.1. Multi-Material Joining

A significant transition to using aluminum as a structural material began with Audi and their Audi Space Frame, *Figure 2–1,* debuting in the early 1990s. It was composed entirely of aluminum; allowing it to shed a vast amount of weight without compromising structural rigidity. Audi could do so due to the high price point of the A8, which could not be said for lower classed vehicles during that time.

Figure 2–1: 2011 Audi A8 spaceframe [2]

Consider such strategies in the context of today's CAFE standards (mean fleet average 40 miles per gallon) and the push for incorporating aluminum into affordable vehicles is at its highest. A recent noteworthy announcement towards incorporating aluminum came when Ford announced the new generation F-150 would be constructed from the lightweight material, *Figure 2–2*.
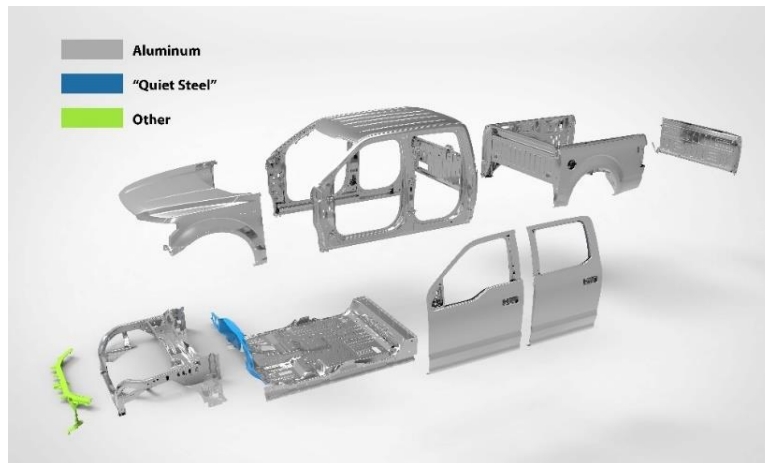
Figure 2–2: Ford F-150 aluminum body [3]

As the industry transitions from steel-based bodies to those constructed of multi-materials, the structural joining technologies must also follow suit. The challenge that occurs with multi-material bodies is the technology available to join these materials possesses highly-varied thermo-mechanical properties. Resistance Spot Welding (RSW), Self-Piercing Rivets (SPR), and Flow Drill Screws all have their place in an automotive structure yet all possess a unique advantage over each other.

Resistance Spot Welding (RSW), *Figure 2–3*, is the leading technology for steel-to-steel double-sided joining. The process entails passing electricity between two or more sheets that are sandwiched between two copper alloy electrodes. The resistance created from the material melts the workpiece and forms a solid nugget once cooled.
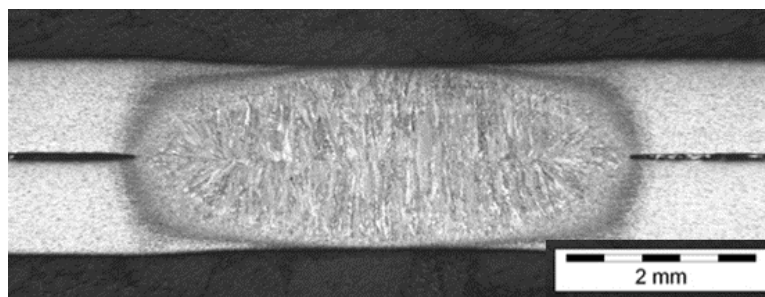
Figure 2–3: RSW cross-section [4]

It has a short process time and does not require a fastening element which leads to reduced cost and weight. It is possible to use RSW to join aluminum sheets together, however issues with workpiece material adhering requires resurfacing of the electrodes on a higher frequency than OEMs would like. General Motors has patented copper electrodes with concentric circles that reduce this adhesion and therefore are one of the few OEMs to use this technology on aluminum-to-aluminum joining. The technology for aluminum-to-steel spot welding has been demonstrated in lab environments but is not fully developed for mass production; therefore, self-piercing rivets are typically implemented.

SPR, *Figure 2–4*, are the leading alternative to RSW when joining dissimilar materials. The process comprises a semi-tubular rivet being driven down which pierces the top sheet. The rivet tail is then flared out as the bottom sheet material flows into the die to complete the joint. SPR also carry the advantage of a short process time and low cost but require access to both sides of the joint.
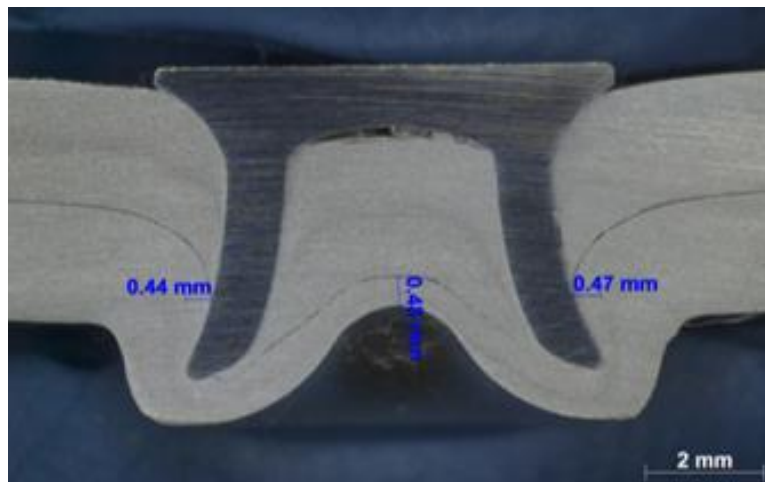
Figure 2–4: SPR cross-section [5]

A recently developed technology for the joining of aluminum and advanced high strength steel (AHSS) is Friction Element Welding (FEW), *Figure 2–5*. It is a double-sided process whereby a fastener is rotated at high rotational speeds and forces, up to 8000RPM and 8kN, to penetrate the

6

top aluminum sheet and then friction weld itself to the base steel sheet. It is currently the only structurally sound joining technology for joining direction aluminum to AHSS.

Figure 2–5: FEW cross-section [6]

When joining sheet metal to extruded profiles or when the joint is located on a flange, the above technologies are not viable due to requiring access to the back side of the joint. Blind rivets are an option but require both sheets to have clearance/pilot holes which adds cost to create the holes along with the issue of hole-finding during manufacturing. Therefore, when only one side is accessible, FDS are used and rely on the rigidity of the part to support itself during the process.
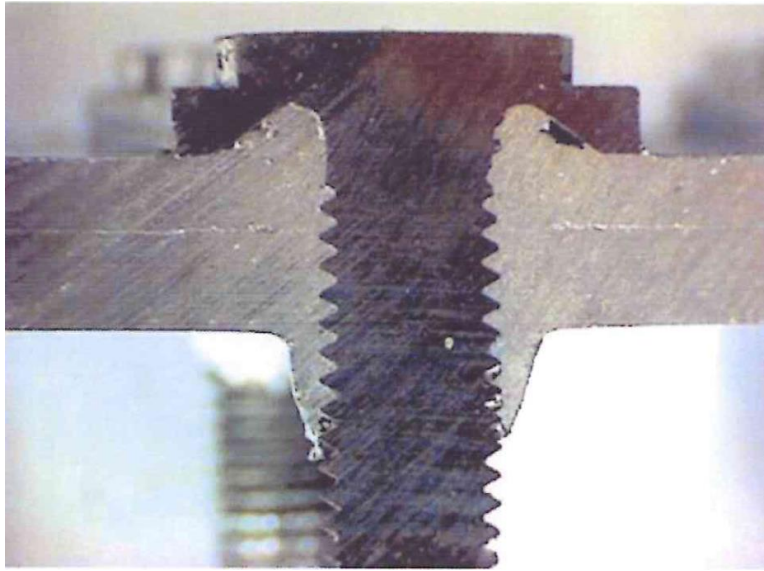
Figure 2–6: FDS cross-section [7]

Spaceframe-derived designs are increasing in usage with this drive to incorporate more aluminum into the structure. Extruded aluminum profiles offer no access to the backside of the joint, therefore OEMs have no other but to apply this FDS technology. Broader usage of this technology is the driving force behind this research especially with the lack of fundamental process understanding as presented in the form of a literature review in the next section.

2.2. Flow Drill Screwing

Process

Flow Drill Screwing (FDS) is a one-sided thermo-mechanical joining process heavily used in the automotive sector since the recent transition to multi-material bodies. FDS is based upon the concept of generating frictional heat between a rotating conical tool and a workpiece to soften the material and allow the tool to penetrate and form an extrusion. This formed extrusion increases the surface area for thread-forming that would normally be limited for thin sheet metal. Once the screw has penetrated the two sheets, female threads are formed in the stackup using the pre-formed threads on the screw. As the screw heads approaches the top sheet, the speed is lowered and a pre-

8

determined tightening torque is achieved. The increase of threadable area allows for a higher tightening torque, therefore more clamp load, and overall, a more reliable joint.

FDS is classified by 6 steps, *Figure 2–7*: heating, penetration, extrusion forming, thread forming, screwdriving, and final torquing. The screw is subjected to high rotational speeds (6000RPM for aluminum and 2000RPM for steel) on the surface of the top material (step 1: heating). The frictional forces generated lead to localized softening of the material which allows the screw to penetrate the material stackup (step 2: penetration). Material then flows axially along the screw and forms an extrusion on the back side of the stackup (step 3: extrusion forming). Once the extrusion is formed, the screw forms female threads on the interior of the stackup (step 4: thread forming). The screw continues to be installed and the male screw threads are engaged (step 5: screwdriving). The rotational speed is then lowered and the screw head is seated on the top material, and the screw is torqued to a desired value (step 6: tightening).
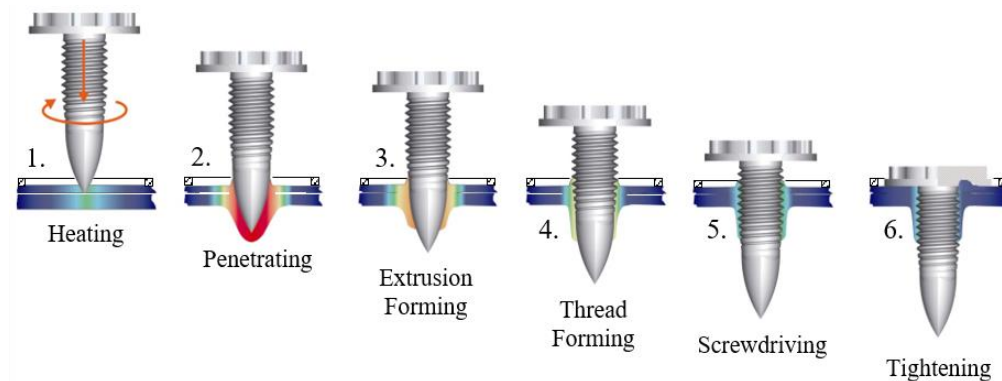
Figure 2–7: Six steps of the FDS process [8]

One of the advantages of the FDS process is that the tool used to create the hole and form the threads is also the steel screw element used to fasten the joint together. The screw differs from that of a traditional self-tapping screw due to its conical tip that forms the hole through friction drilling

rather than cutting the hole as in a conventional drilling operation. The two types of FDS used in

this research are the standard tip M5x20, Figure 2–8, and the pointed tip M5x25, Figure 2–9.
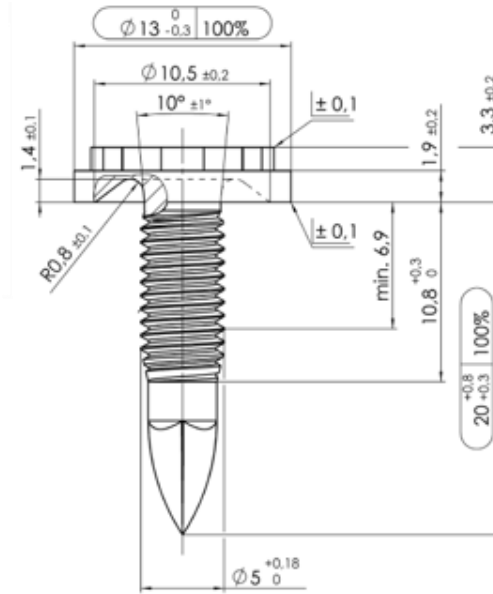
Figure 2–8: Standard tip M5x20
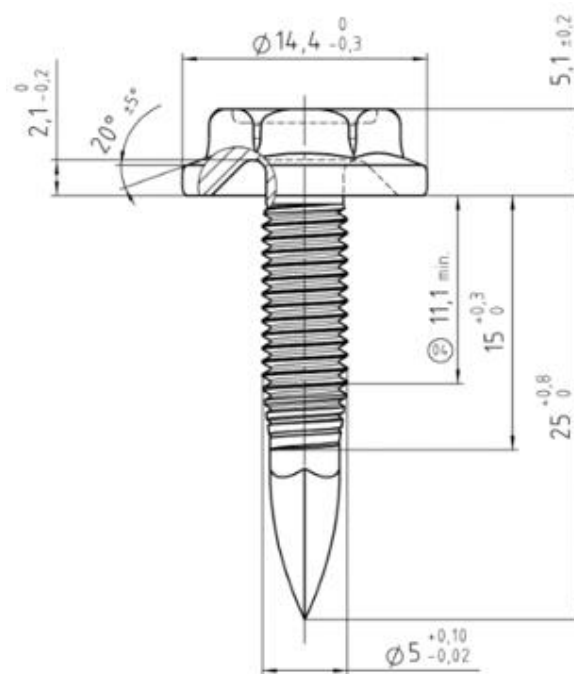
Figure 2–9: Pointed tip M5x25

Friction Drilling (FD) is based on the same concept of a rotating tool plasticizing a workpiece, in fact, FDS is a derivation of FD. The friction drilling and FDS processes differ greatly after the extrusion forming phase due to the geometrical differences of the tools. As the tool used during friction drilling is smooth in the cylindrical region, it does not form threads, and thus a tap is required in addition to separate installation of a screw. An FDS fastener combines these three-steps into one; it can form an extrusion, thread-form the workpiece, and be tightened to provide a clamp load between the sheets, all in a single operation.

Friction Drilling is a hole forming process that utilizes the friction between a rotating tool, *Figure 2–10*, and a workpiece. This friction generates heat which thermally softens the material and allows the tool to penetrate to form the hole. Unlike a traditional hole drilling operation, whereby chips are created, friction drilling displaces the material above (classified as the boss) and below (classified as the extrusion) the workpiece, therefore utilizing all material. The extrusion forms to be approximately two to three times the original sheet thickness which increases thread-able area for the subsequent thread-tapping operation, *Figure 2–11*. The last step, as part of the three-step joining operation, would be the manual/automated installation of the screw. As friction drilling requires elevated temperatures to displace the material, coolant is not implemented and thus is a cleaner hole-creation process than conventional drilling.
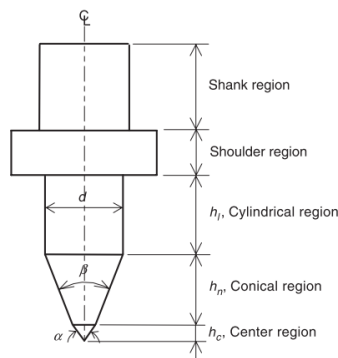
Figure 2–10: Friction drilling tool [9]
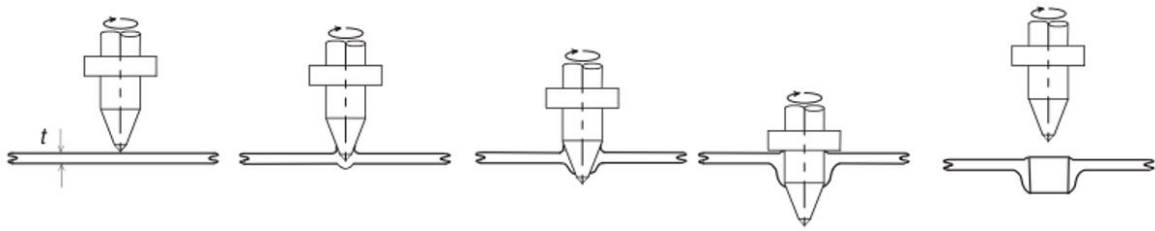
Figure 2–11: Friction drilling steps [9]

Due to the recent adoption of FDS in the transportation industry few papers exist in literature, which confirms the need for research contributions towards the process. As FDS and FD exhibit similar process physics, the literature review of these two processes is coupled together in the following sections.

Flow Drill Screws evolved from friction drilling whereby the three-step operation (hole formation, thread-tapping, screw installation) has been combined into one continuous process. FDS carries over the same advantages from friction drilling but significantly reduces the process time due to lack of tool change; and as the FDS fastener is used as the tool and securing agent, tool wear is not an issue. Due to the similarities between the process mechanics in addition to the lack of FDS publications, a literature search on the state of the art of Friction Drilling along with thread-forming fasteners is presented.

Experimental Studies

One of the initial papers [7] to introduce the technology to the literary field was written by the company that developed the process, EJOT GmbH. The authors described the steps of the process, why this technology was developed, and how it fared better in peel tests over spot welding. The paper is largely considered an overview and lacks any detailed experiments

Joining of a fiber reinforced polymer (FRP) and an aluminum alloy using FDS was studied by Szlosarek *et al.* [10] however all of the emphasis was on how the FRP material failed. The joint was mechanically tested at various loading angles with maximum loads and damage mechanisms

the focus of the study's outputs, *Figure 2–12*; yet again, no discussion or contribution to the mechanics of the FDS process was studied in the paper.
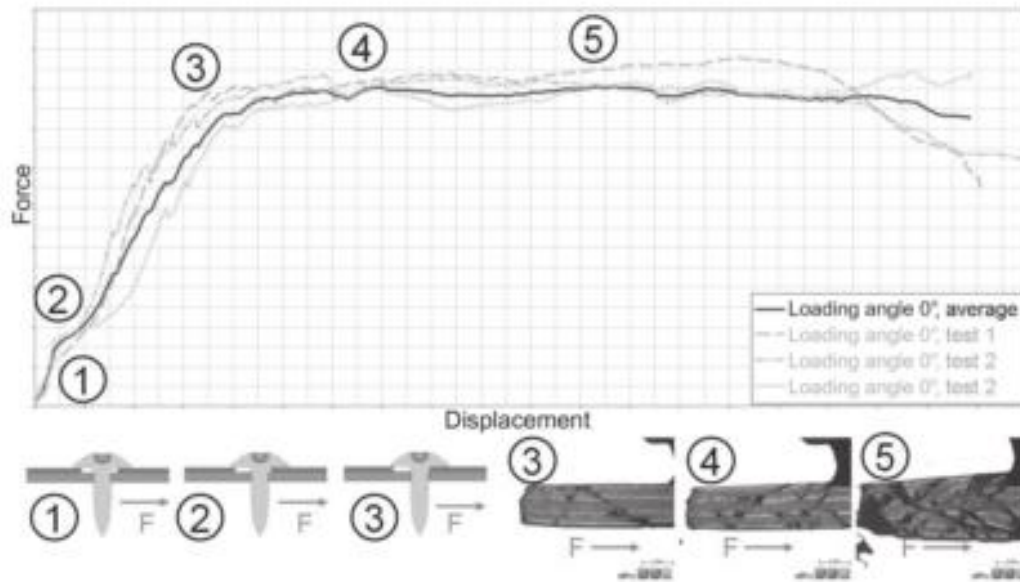
Figure 2–12: Fracture behavior of FRP joined with FDS [10]

Due to the high temperatures and plastic deformation that occur during the friction drilling process, Miller *et al.* investigated how the process affected the microstructure of steel, aluminum, and titanium workpiece materials [11]. Regardless of workpiece material, the material closest to the hole exhibited the highest hardness values due to being the location of the highest temperature and pressure. Due to aluminum's high thermal conductivity, the hardness gradually decreases from 0.8GPa to the as-received value of 0.6GPa 200μm away, *Figure 2–13*.
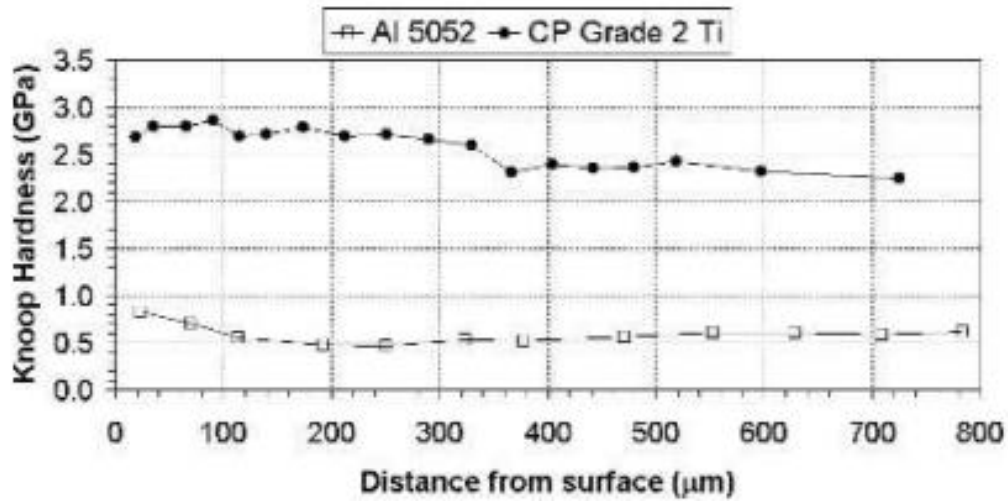
Figure 2–13: Subsurface microhardness profile measurements [11]

Similar trends, *Figure 2–14* and *Figure 2–15*, were observed from Lee *et al.* [12] and Chow *et al.* [13] although the authors explanation to why high hardness values were observed closest to the hole went beyond Miller's. Lee and Chow both stated that rapid cooling of the material occurs when the tool retracts and therefore hardens the interior surface of the hole.
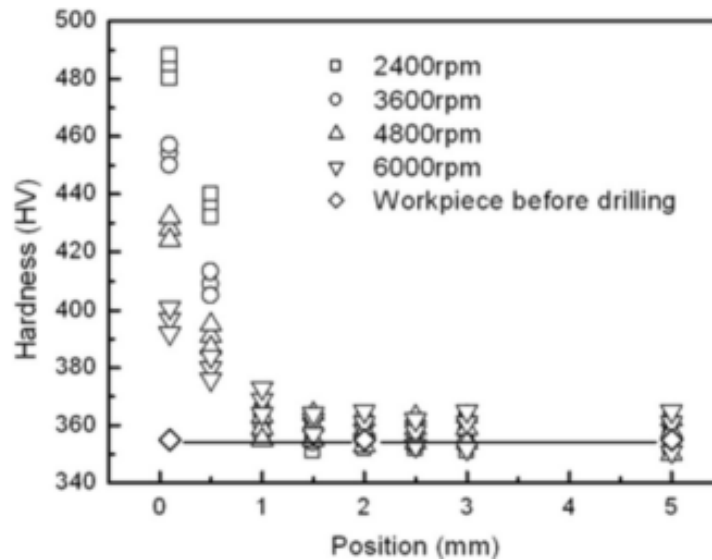
Figure 2–14: Microhardness of N-713LC superalloy [12]

14
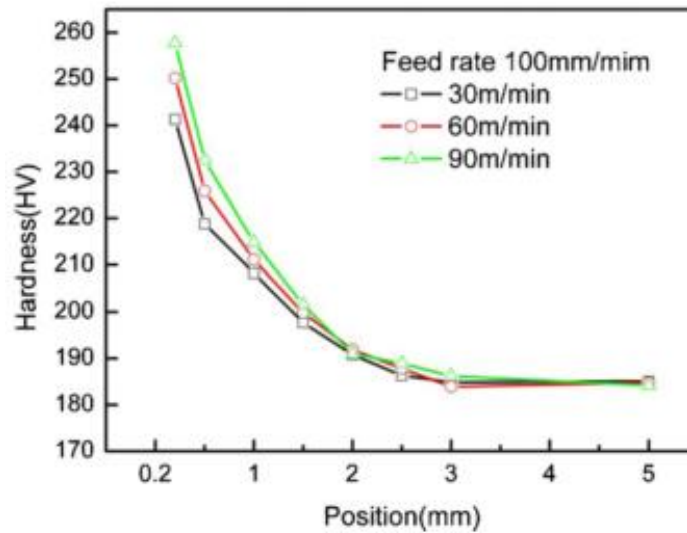
Figure 2–15: Microhardness of AISI 304 stainless steel [13]

The fast removal of the tool during friction drilling causes rapid cooling of the interior surface of the hole. This recrystallization is the reason why the surface closest to the hole exhibits the highest hardness. As the tool/fastening element of FDS is one and the same, it acts as a heat source in the workpiece and thus the post-process heat dissipation differs from that of friction drilling. An investigation into how FDS affect the microhardness of a workpiece is presented in this study with observations expected to show softer material near the hole due to this post-process annealing.

The benefit of solid-state joining technologies is the lack of porosity issues that may occur during those technologies that inhibit material melting. Despite the high temperatures that occur during friction drilling, no evidence of material melting has been observed [11,14].

A majority of friction drilling literature has focused on experimental work showing how the hole geometry is influenced by: process parameters [13–17], tool geometry[13,18–20], and workpiece material [21–23]. These types of studies are certainly good for parameter optimizations, but they do not generate any fundamental understanding of the technology which could be extrapolated to different combinations of tools, materials, and parameters.

Statistical and Optimization Modeling

Statistical-based optimization approaches have been conducted to find the 'optimal' parameters based on the input parameter influence on temperature, time, torque, force, microhardness, extrusion length, and tool angle [24,25]. Regression models are developed based on extensive testing across input parameter ranges, namely a Design of Experiment analysis. Depending on the number of factors and corresponding levels, the testing can be exhaustive, and although a regression model is the resultant, it is heavily dependent upon that parameter window including workpiece geometry.

A finding from Krishna [26] was that tool angle was a significant parameter to changes in force and torque having a contribution percentage of 20 and 88%, respectively. Ku [27] used the Taguchi method to find parameter and geometry influence on surface roughness and extrusion length. An interesting finding was that a reduction in the friction contact area ratio (FCAR), defined as the ratio between friction contact area and circumferential area, caused an elongation in the extrusion length owed to the intermittent stirring effect on the hole wall.
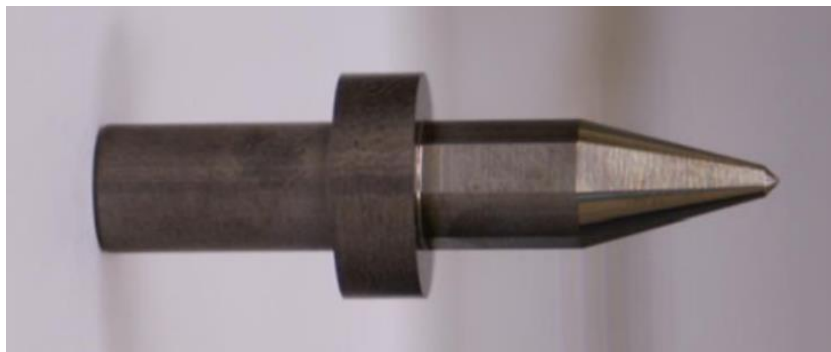
Figure 2–16: FCAR of 50%

Joint Strength Modeling

A FEM of the FDS process was developed by Grujicic [28] to establish joint connectors for virtual joint testing under varying loading conditions. The workpieces were modeled as Eulerian while the screw was Lagrangian which due to the nature of these modeling approaches a penalty

method was implemented for the contact condition but no discussion was presented to the nature of this contact condition. The paper did not present any experimental validation of the simulation as the focus was on modeling the mechanical strength of the joint.

Failure modes during fatigue of FDS was studied by Pan *et al.* [29] with the analysis being of a two material stackup (2T) joint of aluminum with and without a clearance hole in the top sheet. Absence of the top sheet clearance hole was found to develop a small sheet separation due to the material extruding between the sheets. Those samples with and without top sheet clearance holes had similar failure mechanisms in cyclic loading with the low cycle, *Figure 2–17*, and high cycle, *Figure 2–18*, tests varying in failure mechanisms. The authors then applied a closed-form structural stress solution to predict the high-cycle fatigue life of the joints with the model having a general agreement to the experimental results.
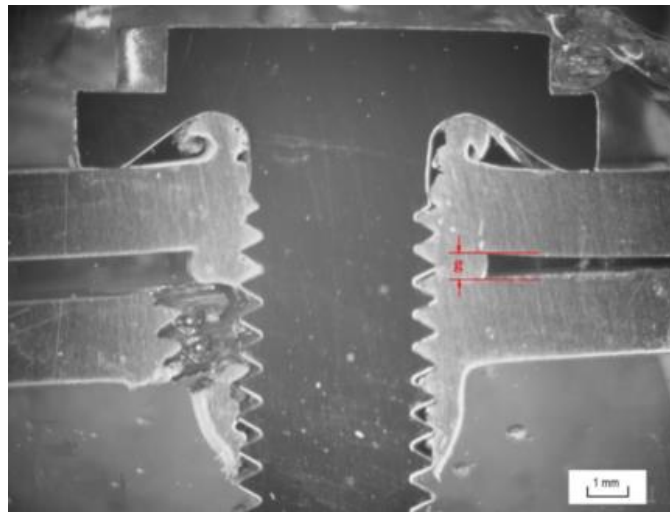
Figure 2–17: Low-cycle failure mode of sample without clearance hole [29]
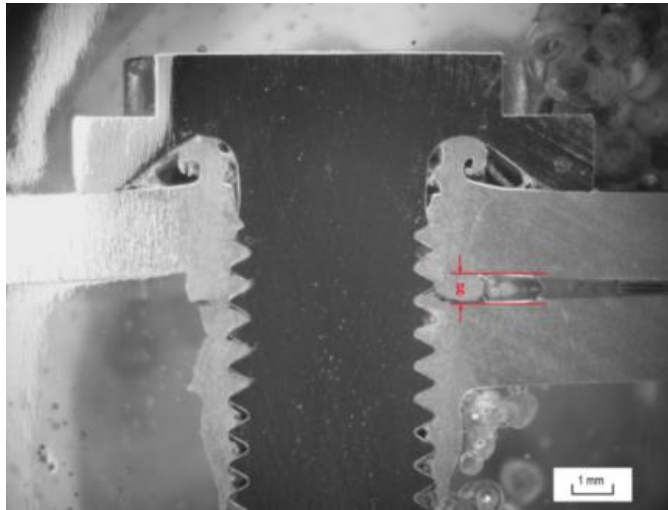
Figure 2–18: High-cycle failure mode of sample without clearance hole [29]

Models of the FDS process currently existing in literature are limited and those that exist are solely focused on how the joint performs in a crash-simulated environment; none exist of the installation process which is known to be most critical for joint feasibility. Researchers at the Norwegian University of Science and Technology have focused their FDS studies on the behavior of the joint, after screw installation, and how the failure properties of the joint can be characterized. The first study conducted by Sønstabø *et al.* [30] looked at failure mechanisms for joints tested in tensile, shear, and a mixed tensile-shear mode, *Figure 2–19*; while their second study developed macroscopic connection models, *Figure 2–20*, of these already observed failure mechanisms [31]. While modeling of joint failure is critical due to OEMs performing large full-scale crash models, the studies fail to address the installation of the screw.
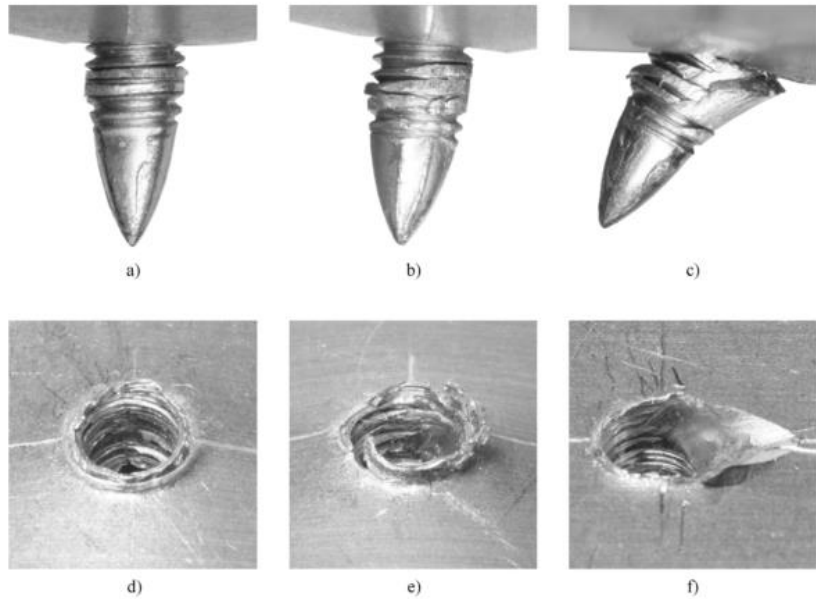
Figure 2–19: Post tensile, mixed, and shear loading cases [30]
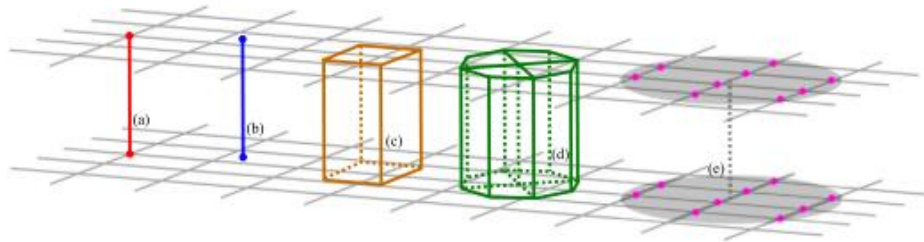
Figure 2–20: Different connection modeling techniques (a) rigid link, (b) beam element, (c) hexahedral element, (d) cluster of hexahedral elements, (e) constraint [31]

An additional computational study on the modeling of the FDS process [28] aimed at determining the mechanical properties of the joints, post installation, along with using these properties to simulate virtual mechanical testing. The simulated and experimental static tests seem to correlate well but no validation exists for the modeling of the process and that is what the research in this study aims at providing.

Additional studies on the impact of joint strength in regards to exposure to corrosive environments [32], embedded steel wire reinforcements [33] have been conducted but do not support the main focus of this research which is process modeling.

Torque and Temperature Modeling

Temperature and torque modeling is extremely limited due to recent adoption of this process into industry along with the complicated coupled thermo-mechanics of the process. Miller *et al.* were the first to attempt modeling of the process [34]. A basic heat flux equation based on the experimentally measured torque, rotational speed, and contact area was used to determine heat input into a FEM to predict temperature rise during the initial portion of the process as described in Equation 1;

$$q = \frac{2\pi T n}{60 A_i} a \tag{1}$$

where power into the system is taken as the instantaneous torque, T, multiplied by the spindle speed, n. The contact area between the tool and workpiece, A_i, is determined parametrically with the geometry of the tool broken down into six stages whether the tool is contacting the workpiece conically, cylindrically, or both. The last term in the equation, a, is the fraction of frictional energy converted to heat which was listed as 0.9 for this study. Miller used this analytical equation to determine the rise in temperature from the beginning of the process until the 250°C threshold of the thermal camera was reached. The onset of divergence between experimental and FEM temperature values, *Figure 2–21*, towards the end is most likely why the authors did not model the entire process.
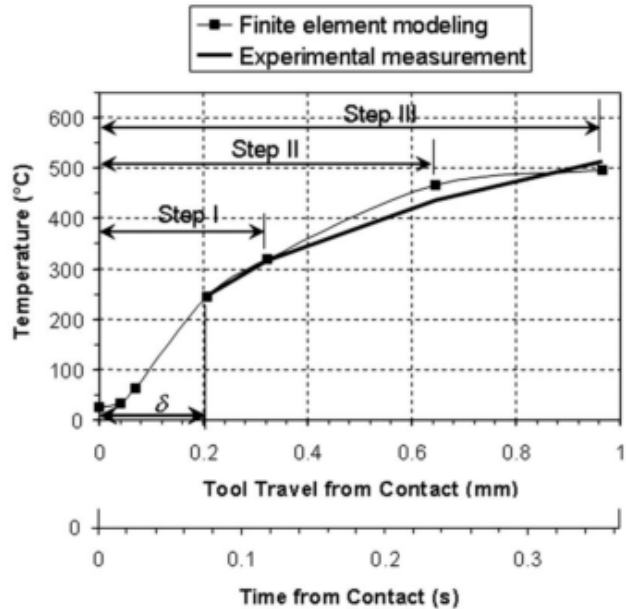
Figure 2–21: Temperature modeling of FD process [34]

Oversimplified modeling assumptions such as ignoring workpiece deformation, absence of tool geometry, exclusion of temperature-dependent properties, and arbitrary selection of energy partitioning without justification are not sufficient to accurately model this process.

The same authors also tried to analytically model the force (Equations 3, 4) and torque (Equations 5, 6) based on pressure and contact area between the tool and workpiece. Due to the non-uniform geometry of the tool, the contact area equations were split into one representing the conical/tapered shape of the tool and the other of the cylindrical shape, *Figure 2–22*. The pressure acting against the tool, p, was defined as the temperature-dependent yield stress of the workpiece as the nature of the process is to plastically deform the material. The model incorporated a simplified friction model that had independent coefficients of friction for the axial and tangential directions, 0.4 and 2.0, respectively. Friction coefficients should not be dependent upon relative motion direction which leads to the assumption of a curve-fitting approach.

21

$$F_{conical} = \int_{h_1}^{h_2} p \sin\frac{\theta}{2} dA + \int_{h_1}^{h_2} \mu_a p \cos\frac{\theta}{2} dA \qquad (2)$$

$$F_{cylind} = 2\pi\mu_a p R h_3 \qquad (3)$$

$$T_{conical} = \int_{h_1}^{h_2} \mu p r dA \qquad (4)$$

$$T_{cylind} = 2\pi\mu p R^2 h_3 \qquad (5)$$
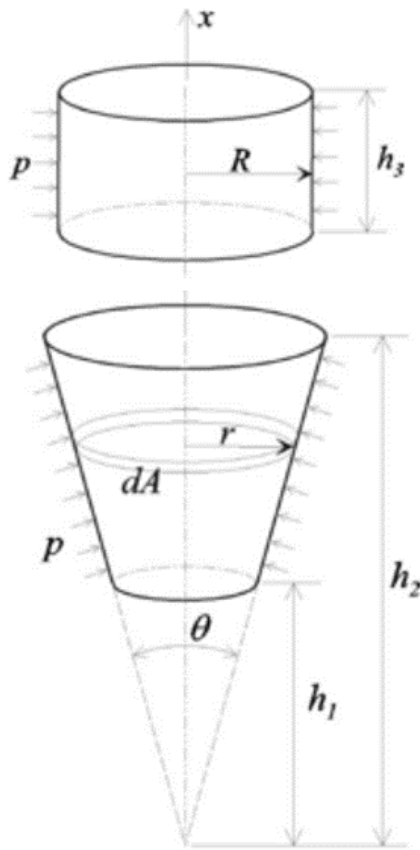
Figure 2–22: Friction drilling tool nomenclature [34]

Miller used temperature dependent yield stress for this pressure value however the temperature

was not based on the through-thickness temperature gradient but on what the maximum temperature

22

at each time step the thermal camera was reading. As the thermal camera was only able to read surface temperatures of the workpiece, this assumption may be the reason behind the difference between the experimental and model values, *Figure 2–23*. Other assumptions made by Miller were; the tool is perfectly sharp at the tip and all corners, deformation of the workpiece is negligible, the coefficients of friction are constant throughout process, and that no workpiece material from the recently-formed extrusion contributes to the force or torque modeling in regard to contact area with the tool.
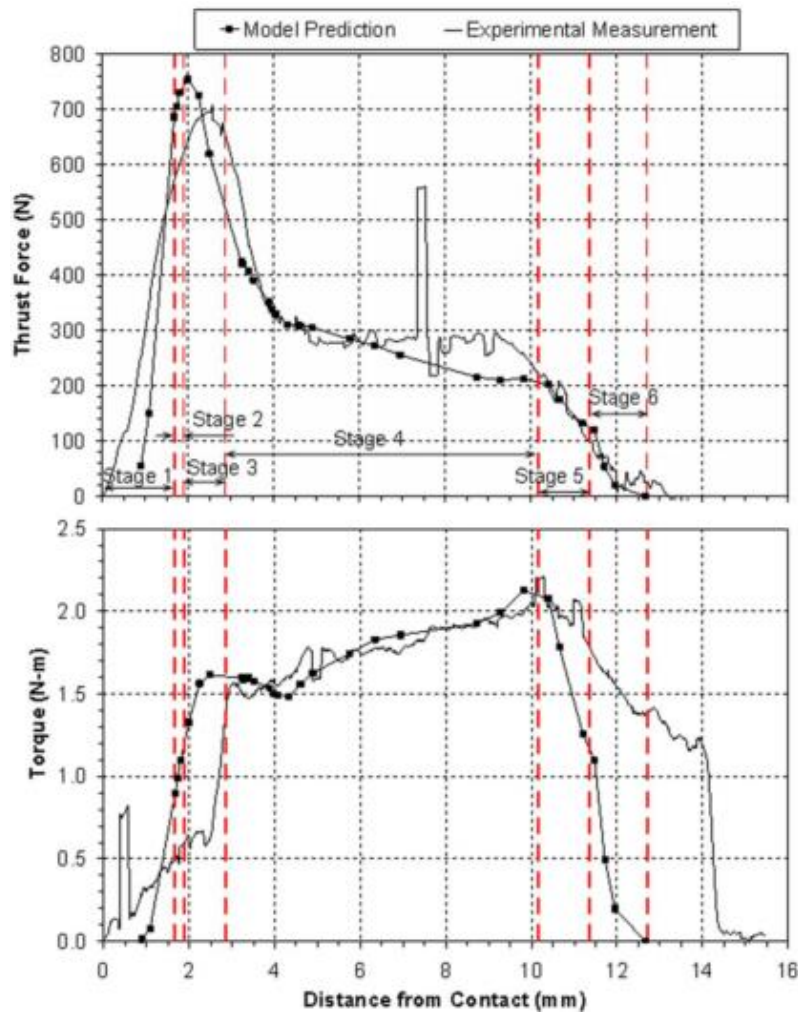
Figure 2–23: Predicted vs. experimental force and torque models [34]

The author explained that the discrepancy between the experimental measurements and model prediction were likely caused by the variation of friction values due to the temperature and speed.

In a future study, a three-dimensional FEM was created by the same authors [35] in an attempt to analyze the material deformation. A constant coefficient of friction 0.7, determined through the inverse approach *Figure 2–24*, along with the simplified Coulomb's law was selected as the friction approach to the model.
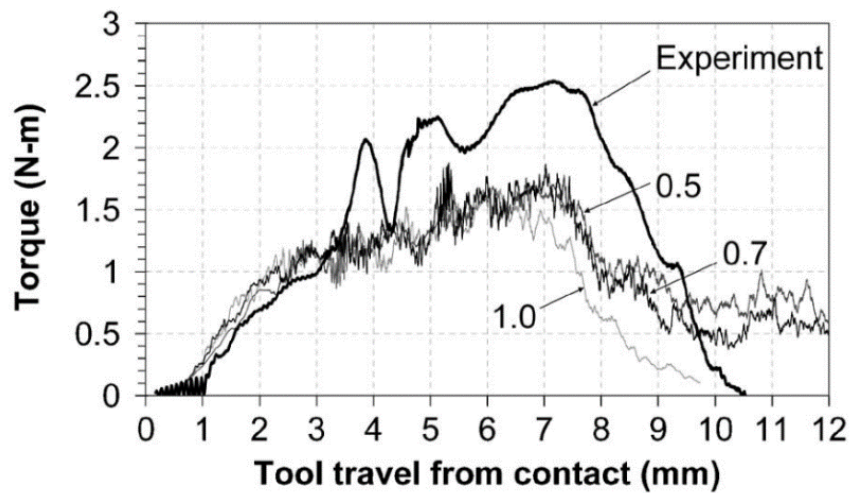
Figure 2–24: Torque comparison based on friction coefficient

The authors state that this simple model is not adequate to accurately model the friction conditions but no other model is available to implement. Temperature predictions compared to experimental measurements were shown to be fairly accurate at large distances away from the center with the error increasing towards the location of the heat source *Figure 2–25*.
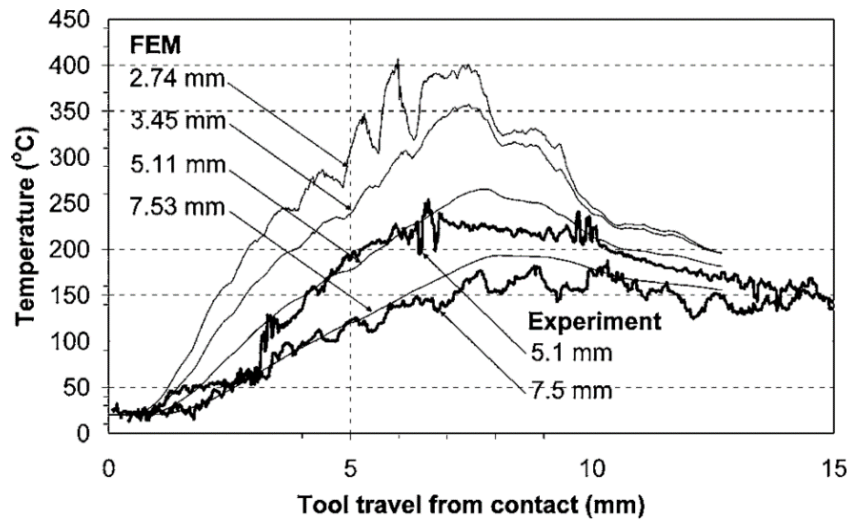
Figure 2–25: Experimental vs Predicted Temperature

An extension of Miller's analytical torque model was performed by Qu [36] to determine the shear stresses and friction coefficients during FD. It used the same approach of contact pressure between the tool and workpiece but used yield in shear rather than yield in compression. The shear stresses, *Figure 2–26*, and friction coefficients, *Figure 2–27*, were determined by back-solving from the experimental values of force and torque.
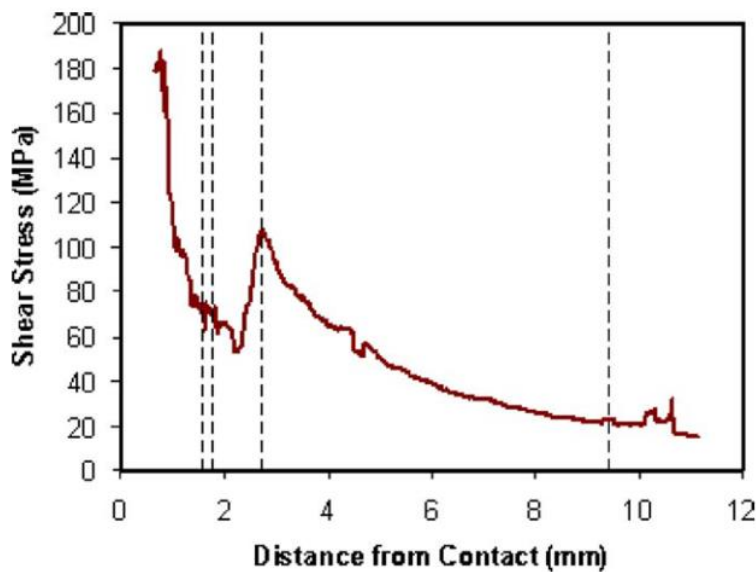
Figure 2–26: Shear stress profile

25
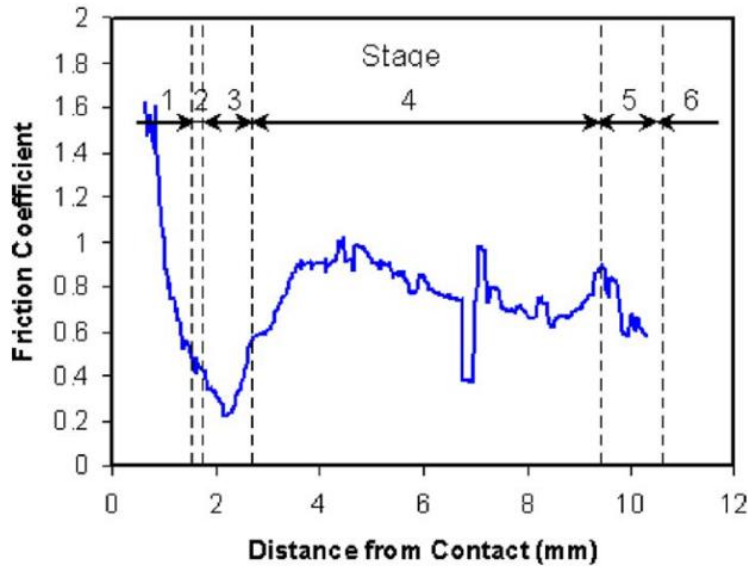
Figure 2–27: Friction coefficient profile

The authors believed the friction value started high due to material shearing occurring at the beginning of the process. Methods such as these are unable to be validated as the two unknowns are interconnected and depend on the analytical setup of the geometry and mechanics.

The literature review presented in this section demonstrates the heavy focus towards experimental studies and the insufficiencies of those papers that attempt a modeling approach. The simplified friction assumptions presented by those authors demonstrate the need for a more comprehensive understanding of the screw-to-workpiece interfacial contact behavior.

2.3. Slip-Stick Interfacial Contact Conditions

Heat generation during friction-based processes depends on the contact condition occurring at the interface between the two objects, in this case the tool and workpiece. These conditions are classified as stick, slip, or a coupling of both; with the condition determined based upon the relation between the material shear strength and the product of the normal pressure and friction coefficient (i.e. Coulomb's law). Temperature rise cannot be modeled accurately without an understanding to what contact condition is present as each generates heat using a different mechanism.

26

A slip condition occurs when the workpiece shear yield strength exceeds the product of the friction coefficient and normal pressure, as detailed in Equation 6. Under this condition, heat is generated due to the frictional force and relative velocities between the tool and workpiece. The heat generation rate due to this frictional sliding is represented by Equation 7.

$$\tau_y > \mu P_N \tag{6}$$

$$\frac{dQ_{friction}}{dt} = \eta P_N \mu \omega r dA \tag{7}$$

A stick condition occurs when the workpiece shear yield strength is exceeded by the product of the friction coefficient and normal pressure, as detailed in Equation 8. This condition leads to plastic deformation of the workpiece and thus heat generation is from shear deformation, as represented by Equation 9.

$$\tau_y < \mu P_N \tag{8}$$

$$\frac{dQ_{deform}}{dt} = \beta \tau_y \omega r dA \tag{9}$$

A term describing the extent of slipping that occurs at the interface is the slip rate (δ). When $\delta = 1$, a full slip condition is occurring whereby no workpiece material sticks to the tool and all heat is generated through frictional sliding. The other extreme is when $\delta = 0$, whereby no slipping between the tool and workpiece occurs and all heat is generated through plastic deformation.

The nature of these equations reinforces the necessity of comprehending why and to what extent this slip rate value changes for an understanding of torque, and therefore heat generation, during FDS. Due to the shortage of in-depth studies on interfacial contact conditions during FDS,

background work has been expanded to another solid-state stirring operation, namely Friction Stir Welding.

2.4. Tribological Influences on Friction Coefficient

Friction is an empirically-fit value that cannot be derived from first principle mechanics. It is considered a 'system property' and thus is specific to the process itself. Studies have been performed in which these individual variables have tried to be isolated to determine their influence but this is never truly the case. The dominant factors believed to influence friction coefficients during friction stir processes are the temperature and relative velocity between the parts.

Influence of Temperature on Friction Coefficient
The general belief is that temperature and friction coefficient have an indirect relation to one another, yet most studies do not and cannot isolate their experimental setup to purely a temperature change. A study conducted in the 1950's concluded that the friction coefficient between steel and Inconel has a significant decrease after 300°C, Figure 2–28 [37]. A more recent study of friction stir processing have determined the friction coefficient between aluminum and steel to be 0.3 at room temperature and declining to 0 at the melting temperature as shown by Figure 2–29 [38].
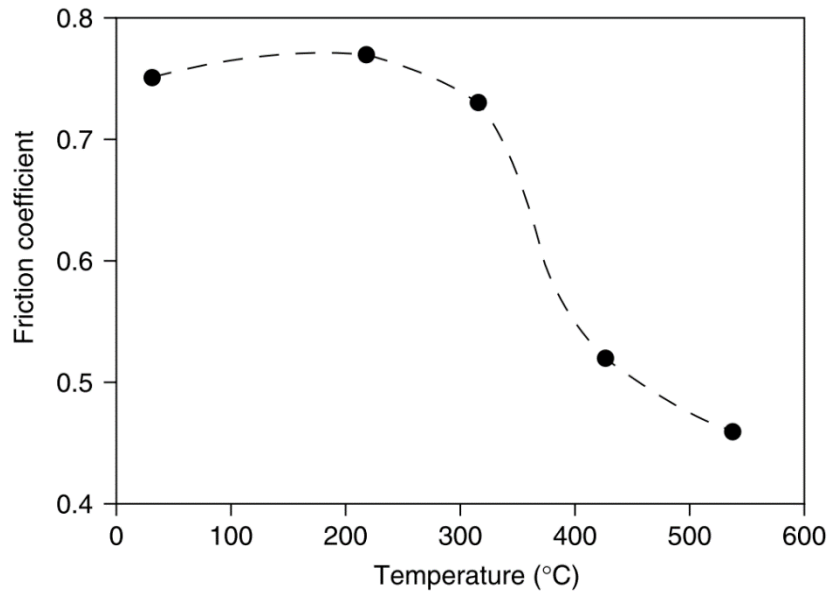
Figure 2–28: Temperature-dependent friction coefficient for Inconel sliding on an tool steel disk [37]
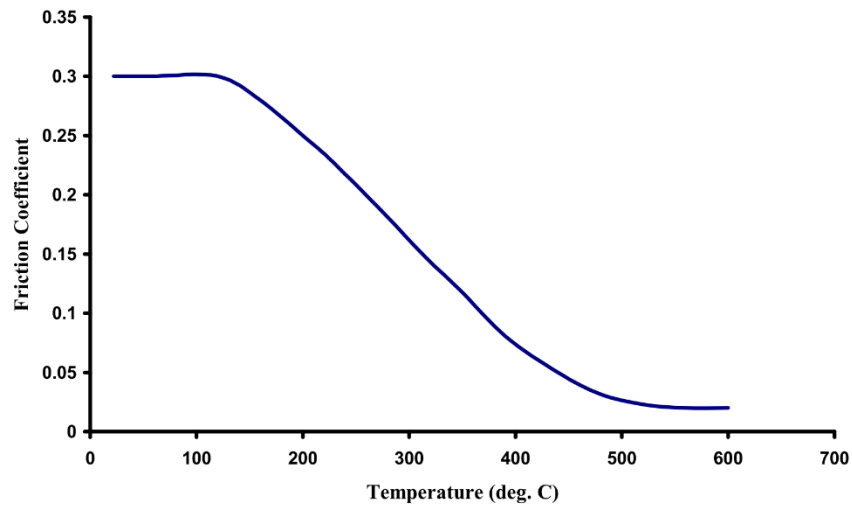
Figure 2–29: Temperature-dependent friction coefficient in FSP [38]

Influence of velocity on Friction Coefficient

The same relationship is believed to exist between the friction coefficient and relative velocity of the two parts. Based upon the proven relationship between power and velocity, a higher velocity is therefore believed to increase temperature at the interface, causing the workpiece to become weaker and therefore less able to resist the movement. Values determined from FSP show a linear tradeoff between the the friction and velocity Figure 2–30 [38].

29
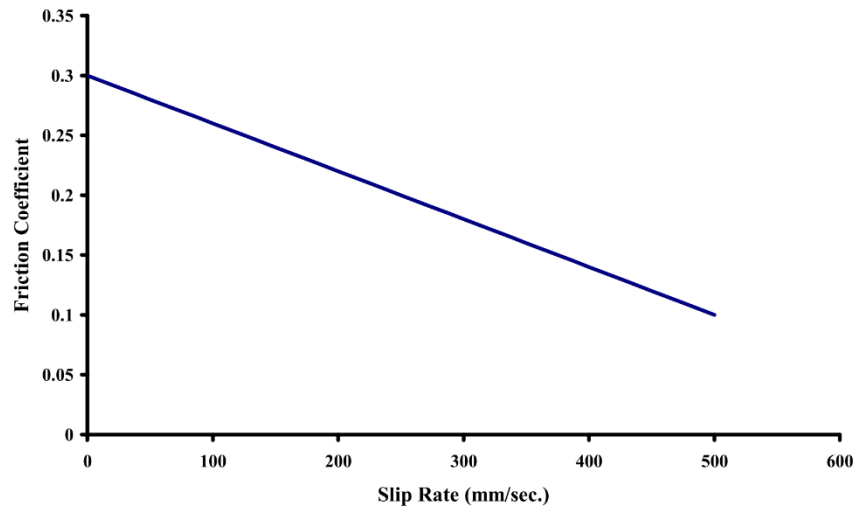
Numerous friction coefficients have been reported with most relying on fitting the value to obtain good agreement between their model and experimentally measured torque, temperature, or both [35,39–44].

2.5. Friction Stir Welding

Friction Stir Welding (FSW), *Figure 2–31*, is characterized by a non-consumable tool, equipped with shoulder and pin features, rotating and traversing across the seam line between two plates. The interfacial friction and plastic deformation heat softens the workpiece and coupled with the tool movement causes the material to flow and be forged into a solid-state joint. FSW and FDS share the existence of multiple interfacial contact conditions but differ with the following: FSW's tool includes both a cylindrical shoulder and a pin, FDS's tool is a screw and therefore features no shoulder; FSW's tool is non-consumable and thus leaves the system once complete, FDS's tool (screw) is vital to the joint integrity and becomes part of the system; FSW has a volumetrically larger stir zone as material flows back into the channel created by tool, material does not need to fill void during FDS as this volume is replaced by the screw; joining step of FSW treated as pseudo

30

steady-state as tool is traversing and surrounding workpiece material is already plasticized, FDS

joining is fully transient due to time-dependence on contact area, surface speed, and temperature.
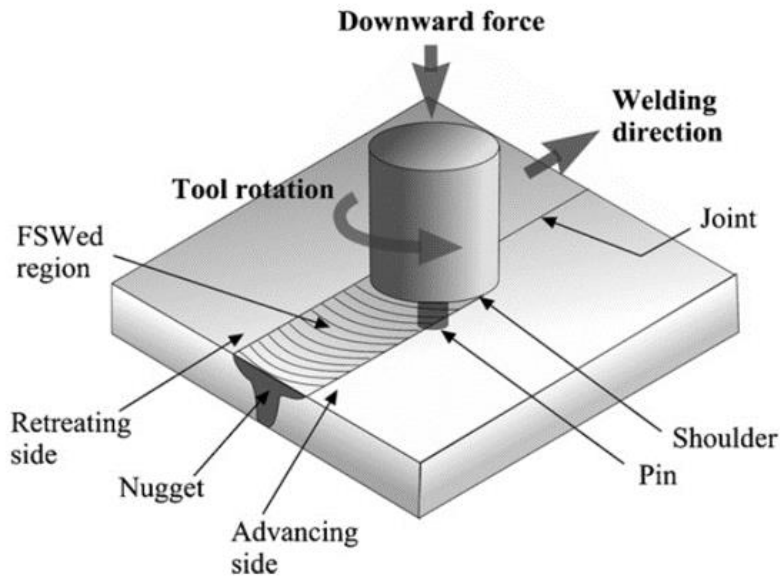
Figure 2–31: FSW process [45]

Despite FSW and FDS both exhibiting frictional contact between a rotating tool and workpiece

with the intent of thermal softening and plastic deformation, the process physics differ and therefore

a cautious approach was implemented when adopting assumptions and values without justification.

FSW researchers have attempted to determine this slip rate value using experimental, analytical,

numerical, and "fitting" methods; yet each approach relies on questionable assumptions.

Experimental Approaches

Material flow patterns and velocities were investigated by Schmidt *et al.* [46] by embedding a

thin copper foil across the weld zone. Tracing the movements of this 'marker-material' using X-

Ray, CT, and metallurgical analysis, Schmidt presented two procedures for determining the

material velocity. The first measured the distance between the unmoved and deposited markers and

used the calculated tool travel distance and time for a velocity approximation. The second approach

determined the average velocity across the shear layer by measuring the area covered by the

markers but had issues distinguishing the transition-rotation zone boundary. Average transition zone velocities were determined to be approximately 10 to 30% of the tool rotation speed, i.e. an average slip factor between 0.7 and 0.9.
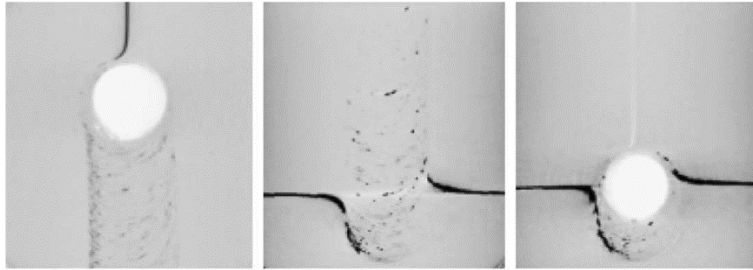
Figure 2–32: CT images of marker movement [46]

Schmidt's finding established the existence of a sheared layer around the tool pin and prompted researchers to investigate the material flow of this zone. Chen [47] implemented a "freeze" method in which tools that were heat treated to exhibit more brittle behavior would fail during the process. This would cause the pin movement to suddenly stop and be embedded in the workpiece. The velocity of this sheared layer could be approximated by observing and measuring the flow of the deformed material behind the pin along with the known geometry and welding speed of the tool. The velocity of this sheared layer was calculated to be 10% of that of the tool velocity leading to a slip factor of 0.9.

Analytical Approaches

An energy-based approach for determining the slip factor was proposed by Hamilton [48] which determined a ratio of the maximum observed welding temperature to the solidus temperature and experimentally measured welding energy. Hamilton decided to ignore the heat from plastic deformation for simplification purposes and accounted the underprediction at low energy levels to this missing heat generation term. Other analytical models have been developed to predict torque and temperature, but they rely on numerous fitting variables that must be found through experimental measures; resulting in regression-based models [49]. The other common approach

requires a model input of experimentally measured torque, temperature, or both [50–52]; something that this research aims at being independent on.

Numerical Approaches

Liechty and Webb [53] looked at predicting the slip rate through two modeling approaches; a sticking condition under constant velocity and a slipping condition with varying shear stress. The constant velocity approach assumed the velocity of the material adjacent to the tool was a constant fraction of the tool velocity. It was allegedly accurate in predicting temperature yet only when this fraction was 1% owing to a slip factor of 0.99. The varying shear approach was believed to be a more accurate method to allow for variation in this slip factor yet a maximum weld material velocity of 9% was calculated owing to a slip factor of 0.91.
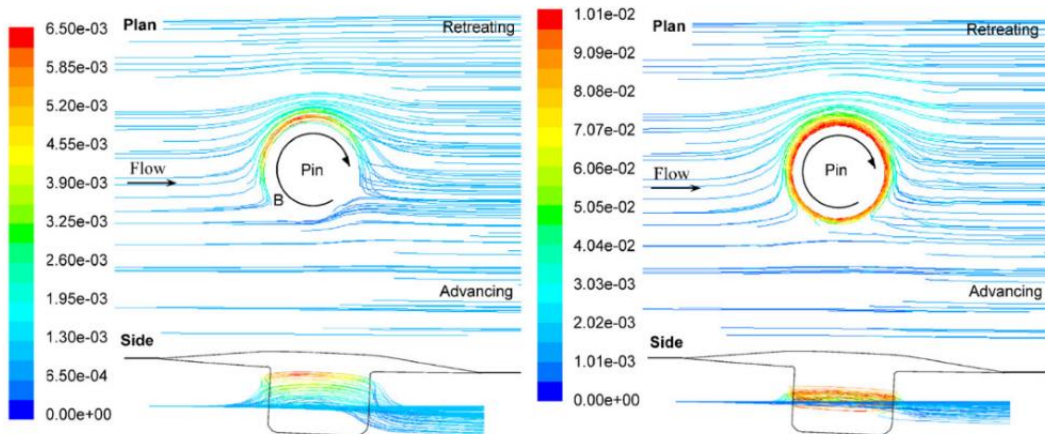
Figure 2–33: Flow paths during (a) variable shear and (b) constant velocity [53]

Fitting Approaches

Unfortunately, the most widespread approach in determining the extent of slip is through fitting an equation originally developed for cross wedge rolling; Equation 10 [54]

$$\delta = 1 - e^{\left(-\frac{1}{\delta_0}\frac{\omega}{\omega_0}\frac{r}{R_s}\right)} \tag{10}$$

Initially used by Nandan [55], reverting to this method has now become the standard for FSW. Coefficients are altered until model outputs match that of experimental; however, this approach is contingent upon all other previous assumptions and values being correct otherwise error summations are merely compiled into this value. Numerous variations of this model are listed in Table 2–1.

Table 2–1: Published slip-rate equations

$\delta = 0.2 + 0.8(1 - e^{\left(-\delta_0 \frac{\omega\ r}{\omega_0 R_s}\right)})$	Nandan, 2008	[56]
$\delta = 0.2 + 0.6\left(1 - e^{\left(-\delta_0 \frac{\omega\ r}{\omega_0 R_s}\right)}\right)$	Arora, 2009	[57]
$0.31e^{\left(\frac{\omega r}{1.87}\right)} - 0.026$	Mehta, 2011	[58]
$0.31e^{\left(\frac{\omega r}{1.87}\right)} - 0.026$	Arora, 2011	[59]

The main issue with this fitting approach for determining slip-rate is that the friction coefficient is calculated from this too; with the generalized equation shown in Equation 11. Several researchers have relied on this method to achieve good agreement between experiment and model values [57,60]

$$\mu_f = \mu_0 e^{\left(-\delta \frac{\omega\ r}{\omega_0 R_s}\right)} \tag{11}$$

The pseudo steady-state behavior of FSW has allowed many researchers to model it under steady-state conditions [61–66]. This has led most of them to select a single value for the friction coefficient, which may not be representative of a process with a large velocity gradient owed to the high souled to pin diameter ratio.

Although generalized claims about the slip-stick contact condition occurring at the tool-workpiece interface during FSW have been established, they are valid only for the pseudo steady-state phase of the process. During this step, the surrounding workpiece material is already at an

elevated temperature that significantly lowers the material flow stress. The consensus during pseudo steady-state FSW is that large amounts of slippage will occur at the shoulder-workpiece interface as this is the location of the largest surface velocities. FDS exhibits no steady-state phase and features no shoulder to its tool.

The accepted exponential behavior of this slip rate as a function of radius and surface velocity is contingent upon the existence of the shoulder region and warrants belief that this relationship would not be representative of contact conditions during FDS. Although FDS does not exhibit a steady-state phase, the tool movement only occurs in the direction normal to the workpiece surface and thus is believed to exhibit a radially symmetric deformation. Material flow during FSW is three-dimensional and thus why FEM has been the focus of understanding this process further. The assumed radially symmetric deformation of FDS due to the radially symmetric nature of the process simplifies material flow dependence despite being a transient process.

2.6. Candidate Materials

The use of aluminum in the automotive sector has increased drastically due to its attractive properties which accompany its low density. Automakers are under pressure to conform to the highly-set CAFE standards and typically address this through lightweighting. The engineers at Ford for example have lead the way in the pickup-truck class by constructing the body of the 2016 F-150 using aluminum alloys and even implementing FDS as a joining process to do so.

Various types of aluminums are used throughout the body of vehicle; both panels and structural members. FDS is used as a structural joining technology in the automotive sector and thus a widely-used material for this application is sought after. Al5052-O, Al6063-T5, and Al6061-T6 have been chosen as candidate materials for this research due to their widespread use as a Body-in-White (BiW) structural components.

3. EXPERIMENTAL CHARACTERIZATION OF FLOW DRILL SCREWING

Due to its recent adoption into the mass automotive market, no studies have been conducted towards an understanding of process mechanics. Therefore, the first step in this research was to gain an empirical understanding of the technology through a series of Design of Experiments studies.

The most significant data output from the process is the torque-time graph, Figure 3–1; from which the installation/driving torque, M_i, stripping torque, M_s, and process time can be determined. The beginning of the process is marked by a slow increase in torque during steps 1-3 of the process with the initial peak occurring during step 4 when the thread-forming screws contact the workpiece. Once the threads are engaged there is a reduction in workpiece resistance and thus a decrease in torque is observed during step 5. The second torque peak occurs during step 6 when the screw head contacts the top of the workpiece and adds resistance to the rotational movement. The torque increases drastically until the applied shear stress exceeds that of the workpiece material and the threads strip. The tightening torque, M_t, therefore, is selected to be less than the stripping torque to prevent failure during the joining process; typically taken as 75%.

Several Design of Experiments studies (DoEs) were conducted to understand how process parameters effect the joint in terms of: torque values, process time, max temperature, cross-sectional geometry, and joint performance. The initial DoE focused on how the driving factors for heating and penetrating of the workpiece, drilling speed [RPM] and drilling force [N], along with the tightening torque [N-m] affect joint geometry. The DoE consisted of these three factors with each having two levels. Three replications were created for each of the parameter sets with experimental outputs including the total process time [s], the sheet gap area [mm^2] which occurs

36

because of material flow, and the extrusion length [mm] that extends the threadable area of the stackup. The detailed test matrix is shown in Table 3–1. An additional DoE was performed on a different material stackup, but this stackup had a pilot hole in the top sheet to isolate any effect one sheet may be having on the other. As the top sheet had a pilot hole, 7.2mm in diameter, the heat generation and torque were solely due to the frictional contact between the screw and bottom sheet workpiece. The varied DoE factors were the drilling speed [RPM], drilling force [N], and screwdriving speed [RPM]. The drilling speed consisted of two levels while the drilling force and screwdriving speed each had three levels; with each parameter set having three replications. The outputs for this DoE focused on the process metrics of installation torque [N-m], stripping torque [N-m], and process time [s]; with the detailed test matrix shown in Table 3–2.
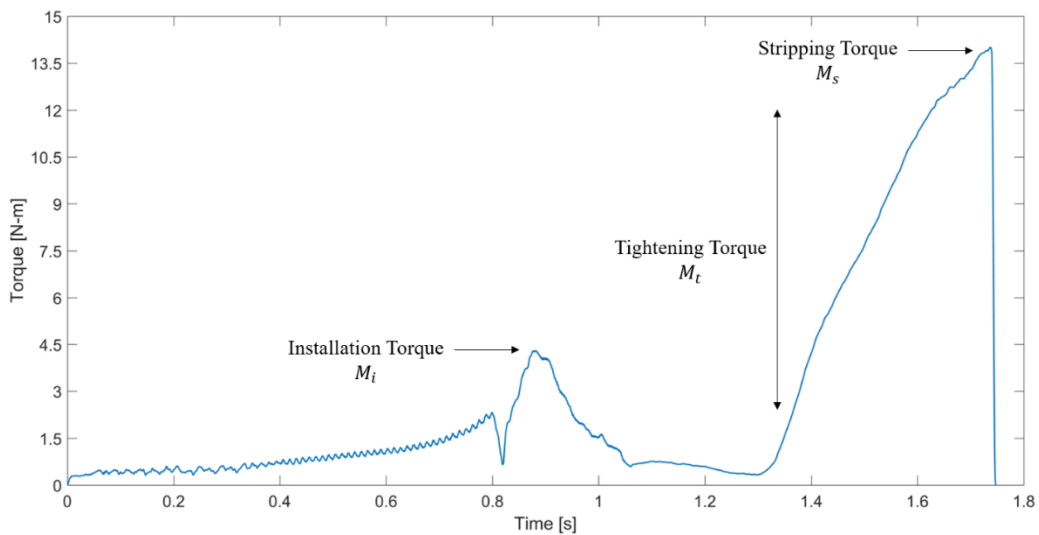
Figure 3–1: FDS Torque Plot

Table 3–1: DoE Test Matrix 1

	Alloy	**Thickness [mm]**
Top Sheet Material	5052-O	1.5
Bottom Sheet Material	5052-O	1.5
Factor	**Level 1**	**Level 2**
Drilling Speed [RPM]	2000	6000
Drilling Force [N]	745	1858
Tightening Torque [N-m]	9	14

Outputs
Process Time [s]
Sheet Gap Area [mm^2]
Extrusion Length [mm]

Table 3–2: DoE Test Matrix 2

	Alloy		Thickness [mm]
Top Sheet Material	6061-T6 (w/ pilot hole)		1.6
Bottom Sheet Material	6061-T6		1.6
Factor	**Level 1**	**Level 2**	**Level 3**
Drilling Speed [RPM]	3000	4000	-
Drilling Force [N]	600	750	900
Screwdriving Speed [RPM]	1000	2000	3000
Outputs			
Installation Torque [N-m]			
Stripping Torque [N-m]			
Process Time [s]			

3.1. Influence on Process Metrics

Installation Torque

Installation torque is the most critical value in determining joint feasibility; with the limiting factor coming from the maximum shear stress of the M5 screw. ISO-898 requires require a minimum breaking torque of 8.3N-m [67], which imposes workpiece strength and thickness limitations on the process. This torque value has a direct relationship to the workpiece thickness and strength, with thicker/stronger materials requiring a higher torque for thread forming. The workpiece thickness is not something that changes during the process, however the strength does due to the rise in temperature from frictional heat generation.

If stackup installation torque approaches this 8.3N-m critical value, it may be desirable to lower it to ensure a larger margin of safety during a full production scale application. A DoE study was conducted on a 2T (two sheet) stackup to understand which parameters have the greatest influence on the installation torque.

The DoE analysis showed that the screwdriving speed was the most influential factor in the resultant installation torque, Figure 3–2. It can be noted though, that the trend is non-linear amongst the 1000, 2000, and 3000RPM screwdriving speeds; with installation torque increasing from 1000 to 2000RPM and decreasing from 2000 to 3000RPM. As previously mentioned, installation torque is highly dependent upon the strength of the material (which is temperature dependent). Higher rotational speeds will provide increased heat generation and thus a momentary decrease in material strength. The slight increase in installation torque from 1000 to 2000RPM is believed to be from the increase in the velocity-dependent friction coefficient. The increase in temperature for the 3000RPM samples outweighs the increase in friction coefficient and brings the overall installation torque down.

The influence of temperature on the installation torque is apparent from the slopes of the drilling speed and drilling force parameters. The following sections will show that a decrease in force will increase the process temperature, thus decreasing the installation torque. The drilling speed relation agrees with knowledge of traditional machining operations in which drilling speed and temperature and directly related, thus a higher drilling speed will decrease the installation torque. The same findings were reported in a recent study [68], in which an indirect relationship exists between drilling speed and installation torque while a direct relationship exists between drilling force and installation torque.
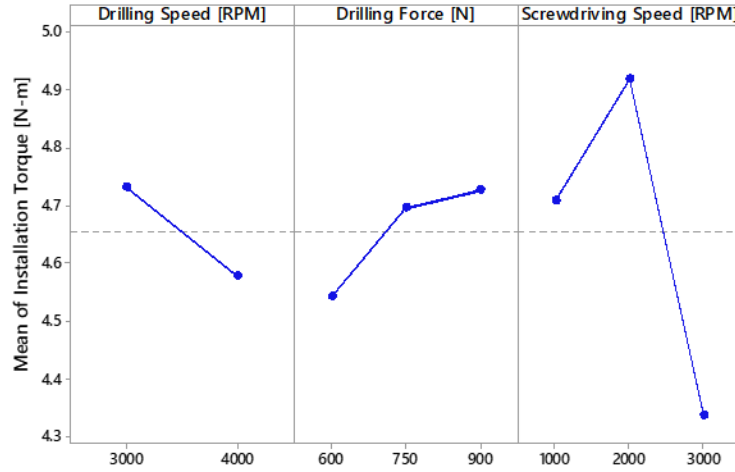
Figure 3–2: Main effects plot for installation torque

Stripping Torque

An important metric of a bolted connection is the clamp force (F). It has been shown that this value significantly affects the joints stiffness along with its ability to resist loosening during service. The tightening torque (M_t) applied to the joint creates this clamp force, with a direct relationship existing between them as shown in Equation 12 [69]; whereby P is the thread pitch, μ_t is thread friction coefficient, μ_b is the under-head friction coefficient, α is the thread half-angle, r_t is the effective thread radius, and r_b is the effective bolt head radius.

$$F = \frac{M_t}{\left(\dfrac{P}{2\pi} + \dfrac{\mu_t r_t}{\cos \alpha} + \mu_b r_b\right)} \tag{12}$$

It is desirable, therefore, to tighten the joint to the highest value possible without overcoming the shear strength of the threads on the screw, nut, or in the case of FDS, the newly-created workpiece threads. This torque value, that causes failure of the workpiece threads, is denoted as the stripping torque as shown in Equation 13 [69]; whereby K is the nut factor, D is the bolt major diameter, σ_u is the ultimate strength of the workpiece, A_t is the tensile stress area, d_t is the effective thread diameter, and d_{min} is the thread minor diameter.

$$M_s = \frac{KD\sigma_u}{\frac{1}{2A_t} + \sqrt{(\frac{1}{2A_t})^2 + [\frac{16(0.16P + 0.58d_t\mu_t)}{\pi d_{min}^3}]^2}} \qquad (13)$$

An analysis on the stripping torque of the joint must be performed before determining the in-service tightening torque. The DoE analysis showed that the screwdriving speed was the most influential factor in the joint's stripping torque, Figure 3–3. The results indicate that a lower screwdriving speed will increase the stripping torque of the joint, which is believed to be on the account of two reasons. Firstly, although a lower screwdriving speed will increase process time, it allows a longer time for the material to cool down and regain some of its strength. Equation 13 shows that the stripping torque is dependent upon the strength of the material, which aluminum has sensitivity to at elevated temperatures; therefore, an increased cooling time before final tightening will lead to a less thermally-diminished material strength. Secondly, a lower screwdriving speed will give the threads more time to form and increase the percent of threads filled by the workpiece. An increased drilling speed was shown to increase stripping torque, which is believed to be from this parameters influence on heat generation. A higher rotational speed will increase heat generation, thus increasing the formability of the workpiece. If the workpiece flow stress is lowered, it can more efficiently fill the area between the threads, ultimately increasing the contact area term in the Equation 13. The drilling force parameter shows a non-linear relation to the stripping torque with an increase from 600 to 750N and a decrease from 750 to 900N. This is due to the influence the drilling force has on the formation of the extrusion. The threadable area for the lower force parameters will show to be larger but these are also susceptible to larger degrees of thermal softening. The midpoint of 750N is therefore the optimal drilling force for a combination of threadable area and thermally-softened material. Further discussions on the extrusion quality and length will be carried out in the next section.
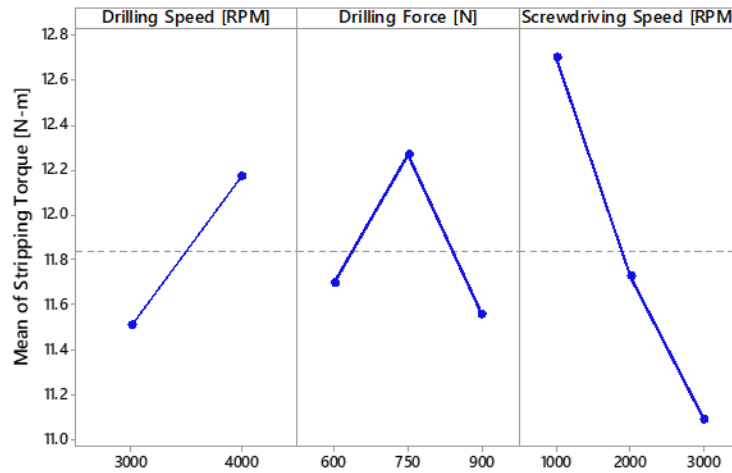
Figure 3–3: Main effects plot for stripping torque

Process Time

A significant output for any joining technology is the process time. A process that takes too long is not viable for mass production, regardless of what benefits it may provide. Considering that these newly adopted multi-material joining technologies are replacing traditional spot welding, whose process time can be less than 0.6 seconds, time is certainly an important factor to consider and improve upon wherever possible.

The DoE analysis showed that the drilling force was, by far, the most influential factor in the process time, Figure 3–4. As expected, a higher drilling force will force the screw through the stackup quicker and thus reduce the overall time; with the main effects for this parameter having a large range from 2.3 to 3.4 seconds. The influence of the drilling speed and tightening torque are minimal yet their relationships to the process time are reasonable. An increased drilling speed will lead to higher heat generation, softening the material faster, and thus allowing the screw to penetrate the workpiece sooner. The same findings were reported in a recent study [68], in which an increase of drilling force and drilling speed provided a significant reduction to process time.

The direct relationship between tightening torque and time is owed to the fact that the screw must be torqued beyond 9N-m to reach the increased value of 14N-m. Assuming a constant

frictional contact between the top of the workpiece and underside of the screw head, this relation should be linear amongst all feasible tightening torques.
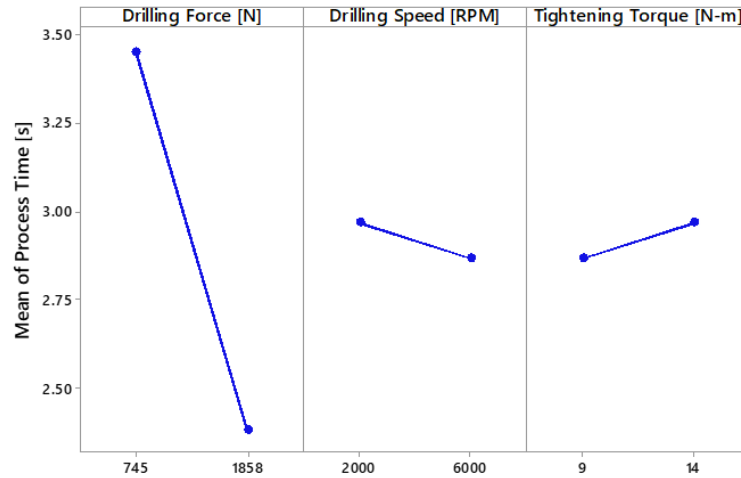
Figure 3–4: Main effects plot for process time

Breakloose Torque

Taking into consideration that FDS joints will be exposed to high vibrational environments, the self-loosening performance of the joints must be measured and studied [70]. The measure of a screws susceptibility to loosening is called its breakloose torque, with the following studies aimed at understanding how to maximize it.

The breakloose torques of the test matrix samples were experimentally measured to determine if the varied process parameters had an influence on the joint's breakloose torque. The samples were placed in a fixture, which was in turn placed in a table-top vice for stability. A digital torque wrench, model DTW-265i, equipped with an EP12 socket, was used to loosen the screws and measure their peak torque. Tightening torque values for the 1st and 2nd breakloose studies were 7.5N-m and 6.5N-m, respectively.

The first study showed that the drilling force had a greater influence on the breakloose torque than the drilling speed. In fact, the drilling speed had almost no impact, which leads to believe that

a varied heat generation rate does not alter the joints breakloose torque. Although the drilling force is known to influence process time, and therefore max process temperature, it will also be shown in the next section that it greatly influences the joint geometry. A higher force increases the radial deflection of the bottom sheet and thus reduces the potential threadable area within the extrusion. This observation is likely the reason the study showed an indirect relationship between drilling force and breakloose torque.

The second study introduced the process parameter of torque holding time; a programmable step in which the machine holds the screw at the tightening torque for a designated time. Drilling force was kept as a DoE factor as a result of the previous breakloose torque study findings with torque holding times selected to be 0, 0.5, 1, 3, and 6 seconds. The influence of drilling force on breakloose torque exhibited the same trend as the 1st study, but it was shown that the torque holding time had a far greater influence. An increased torque holding time led to an increased breakloose torque across all samples, but the benefit was shown to diminish after 1 second. Cooling and contraction of the aluminum workpiece around the steel screw is believed to be the reason this direct relationship exists between the torque holding time and breakloose torque. Although adding a torque holding time would increase the total process time, the breakloose torque would benefit from a 15% rise for only an additional 0.5 seconds.
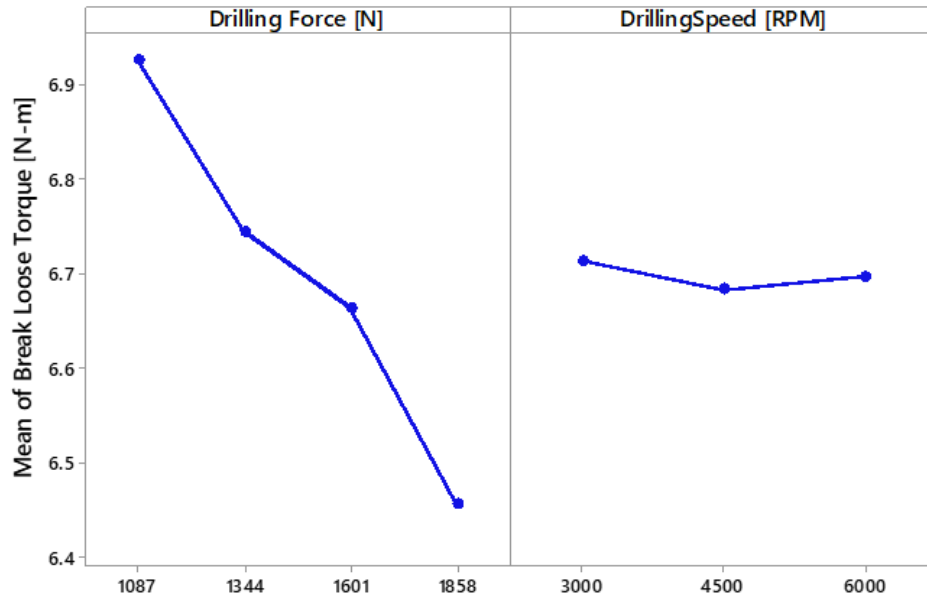
Figure 3–5: Main effects plot for breakloose torque (1st study)
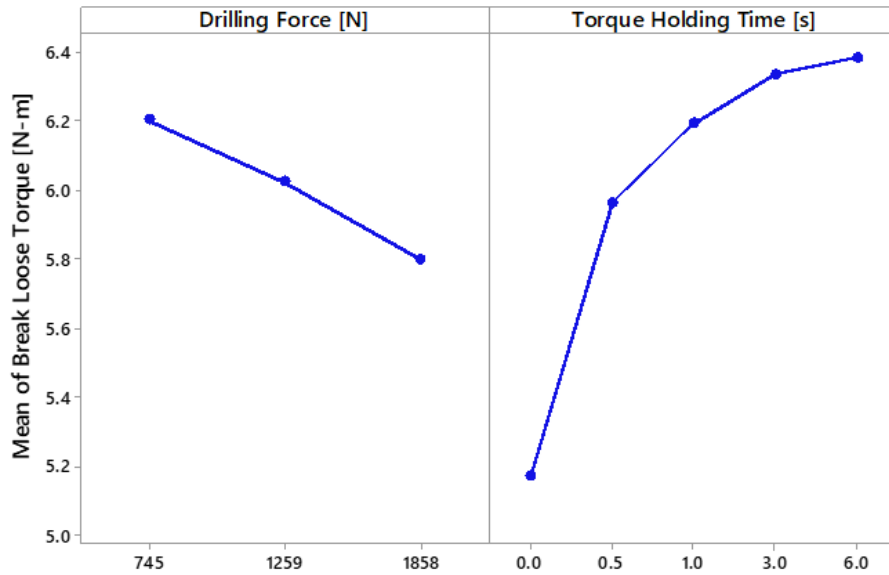
Figure 3–6: Main effects plot for breakloose torque (2nd study)

Maximum Temperature

FDS is a coupled thermos-mechanical process, and therefore an understanding towards how process parameters influence temperature was vital. The direct relationship between rotational speed and temperature in conventional drilling operations has far beyond been established and

therefore variation in the drilling speed was not studied. A constant drilling speed of 6000RPM was used across all temperature tests, with drilling force being the only variable of the study. Temperature measurements were captured by a FLIR Systems A40 thermal camera sampled at 12.5Hz with a 0.1°C resolution. All the top material samples were spray painted black to increase the emissivity and thus obtain more accurate temperature measurements. The workpiece stackup was the same as that listed in Table 3–1.

An indirect relationship between the drilling force and maximum surface temperature was observed under a constant drilling speed, Figure 3–7. The plot shows that as drilling force increases, the maximum surface temperature endured by the material decreases. This relationship is observed because as the drilling force increases, the contact time for drilling decreases and thus gives the screw less time to generate heat. The data confirms a direct relationship between the maximum surface temperature generated and the contact time, as it was previously shown that drilling force and process time are inversely related.
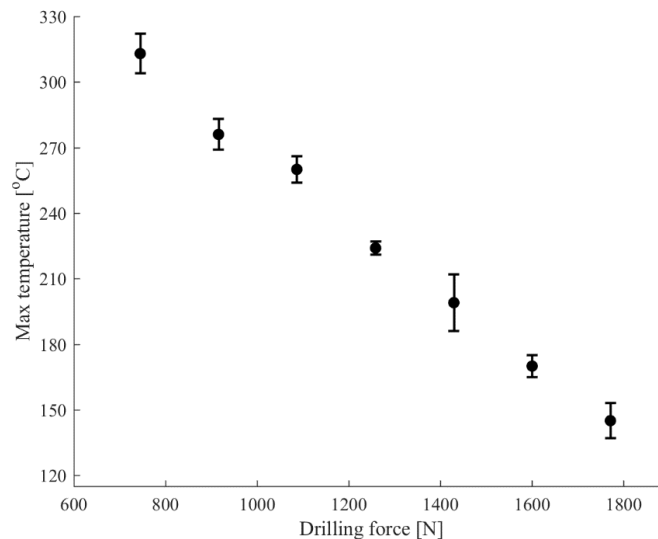
Figure 3–7: Influence of drilling force on max temperature

3.2. Influence on Joint Geometry

46

Sheet Gap and Deflection

Certain joint characteristics were consistently observed throughout the samples that possessed the same process parameters. During a high drilling speed, 6000RPM, and a low drilling force of 745N, the top sheet was observed to deflect upwards while the lower sheet remained disposed as it was prior to the process Figure 3–8(a). The vertical red lines in the figure correspond to the limit in which the sheet gap should not extend beyond without the possibility of affecting the joint's water-tightness. In this sample, the gap is not contained within the screw head, although not by a significant amount; thus, it violates the recommended gap width. Regardless of drilling speed, at a high drilling force of 1858N, the top sheet remained disposed as it was prior to the process while the bottom sheet deflected downward (opposite deflection characteristic) Figure 3–8(c). The gap under the head was also measured to be smaller and within the diameter of the head, thus being classified as an acceptable joint. A deflection in both the top and bottom sheets occurred at the midpoint drilling force of 1601N, Figure 3–8(b), and it was also observed that this deflection characteristic coincided with a minimum gap between the materials.

The DoE analysis showed that all three factors are inversely related to the gap area between the sheets, Figure 3–9, and that they all exhibit approximately the same slope. As slope is a measure of the parameter influence, all three are highly influential towards the gap area. A high drilling force resists the upward material flow from the top sheet which would normally separate the sheets and increase the gap between them. A high drilling speed increases heat generation, temperature, and therefore material flow which better fills the void between the sheets. A high tightening torque would increase clamp load and would therefore force the sheets closer together and reducing the gap.
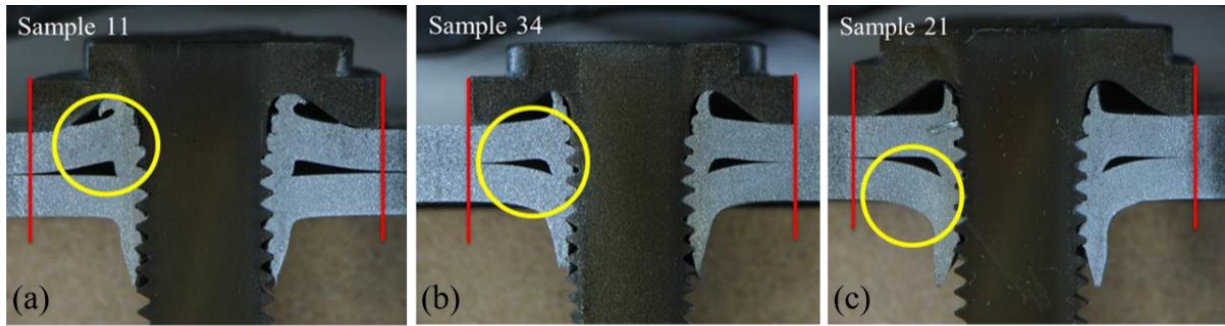
Figure 3–8: Cross-sections of the (a) low, (b) mid, and (c) high parameter drilling forces
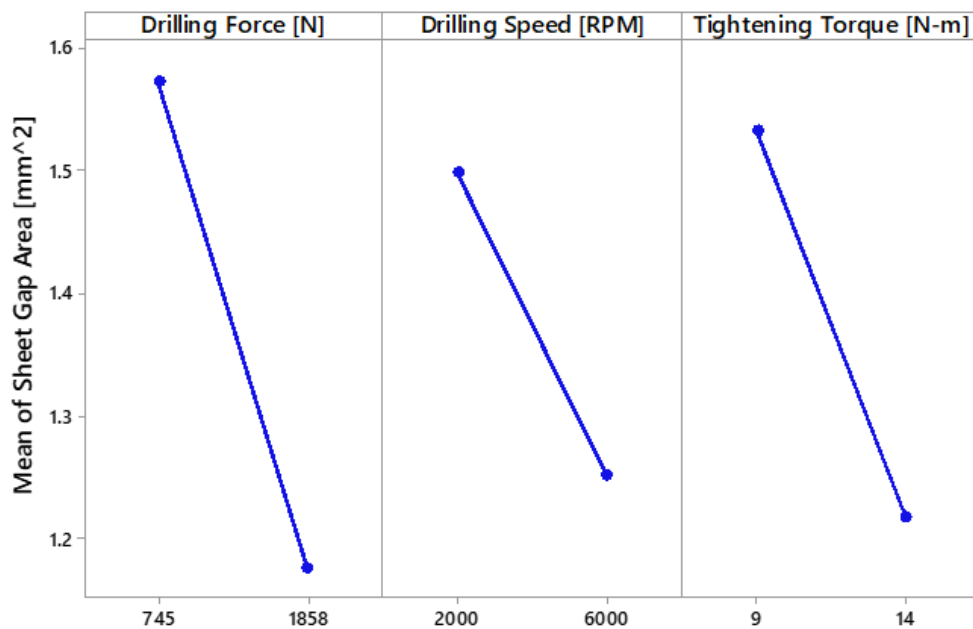
Figure 3–9: Main effects plot for sheet gap area

Extrusion Appearance and Length

An additional observation was observed between the drilling force and joint geometry, in the form of the extrusion quality and length. When the drilling force was at 745N, Figure 3–10(a), the extrusion exhibited consistent petalling around the opening with heights of 0.5mm. At an increased drilling force of 1601N, Figure 3–10(b), there are fewer petals but the magnitude of these petals is greater than the 745N ones. The largest drilling force of 1858N, Figure 3–10(c), has even greater sized petals measured around 1mm in height. The variation in extrusion height can be related to overall contact thread area with the lower drilling force exhibiting the most contact area. When the

drilling force is set too high, the material does not have enough time to form around the tip of the screw and thus creates these higher magnitude petals.

The DoE analysis showed that drilling force is the dominant parameter in influencing the length of the extrusion, Figure 3–11. A higher drilling force puts more stress on the material and therefore increases the total elongation. As the temperature of the high drilling force samples is less than that of the low drilling forces ones, the material deforms in a more brittle manner as evident by the brittle fracture of the extrusion. Similar findings were established from the friction drilling process in which a higher axial feed was determined to be the driving factor in extending the length of the extrusion [25]. Drilling speed also has a positive relation to the extrusion length which can be explained by the increased ductility of the material with increasing temperature. The tightening torque does not influence the extrusion length as by the time the screw head is seated on the top surface, the extrusion and threads have already been formed.
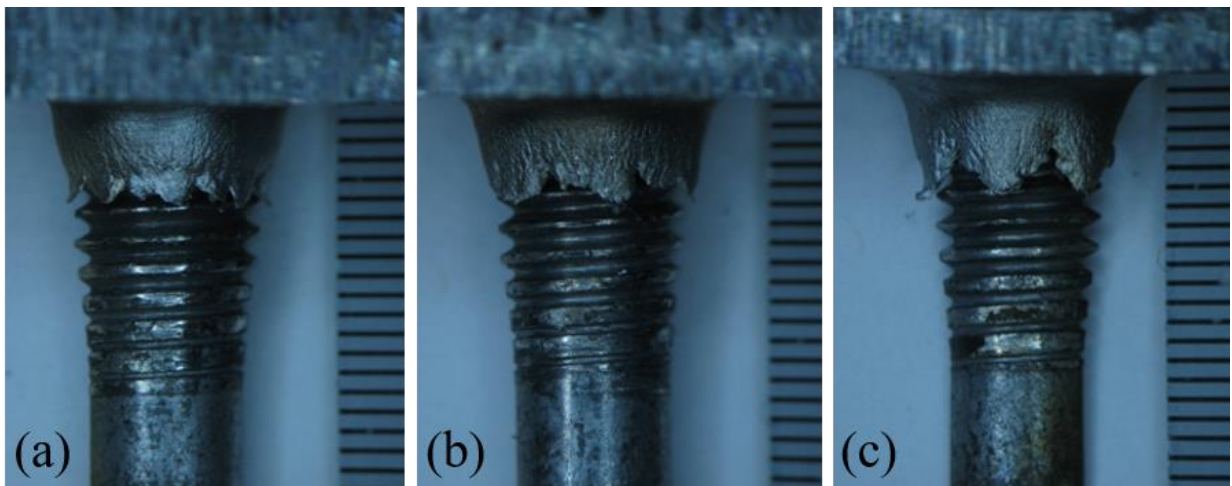
Figure 3–10: Extrusions of the (a) low, (b) mid, and (c) high parameter drilling forces
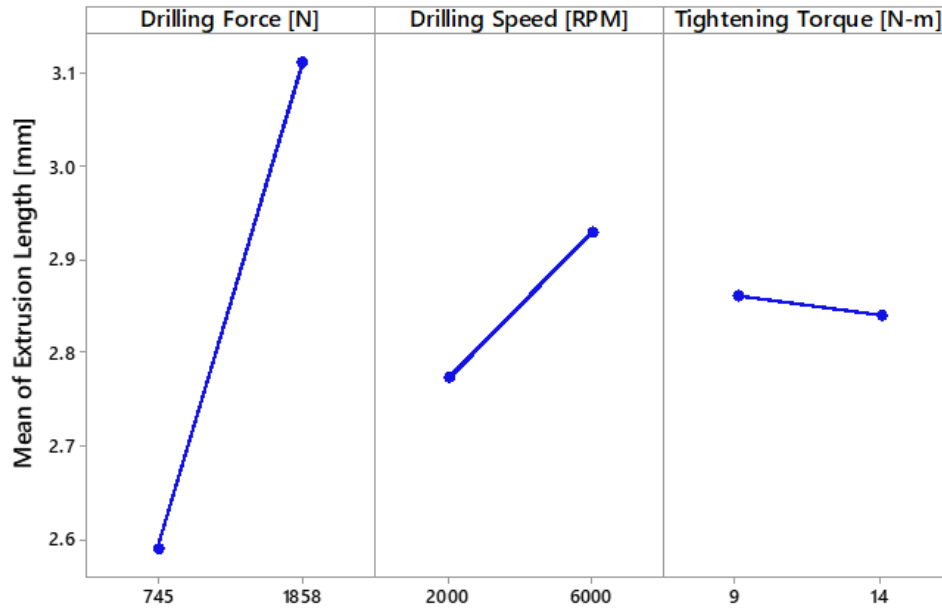
Figure 3–11: Main effects plot for extrusion length

3.3. Influence on Static and Dynamic Joint Strength

The two most significant metric outputs of any joining process are the process time and strength of the joint. Discussions regarding process time were covered previously with the following section aimed at evaluating the joint strength under the different configurations of static coach-peel, static lap shear, and dynamic lap shear.

Static Coach-Peel and Lap Shear

Coach-peel samples, Figure 3–12, are designed to evaluate the strength of the joint under a combined tensile-shear loading. At first the loading is tensile dominated, then becomes a mixed mode inclusive of shear once the workpieces begin to deform. This combined loading condition is the ultimate failure mode for the coach-peel configuration, Figure 3–13, with previous FDS studies confirming these observations [30,31,71].

Lap shear samples are ideally designed to evaluate the strength of the joint under a pure shear loading condition, but the loading condition is one of a mixed tensile-shear mode, Figure 3–14. This occurs due to the off-axis loading caused primarily by the workpiece's low stiffness.

The coach-peel and lap shear joint configurations consisted of a 1.5mm sheet of Al5052-O for both the top and bottom sheets. Coach-peel samples had a workpiece width and overlap of 25mm while the lap shear samples were increased to a 50mm width and 40mm overlap; each had the screw installed at the centerpoint of the overlap. The tests were displacement controlled at a rate of 50mm/min. Data collected from the experiments included load and displacement.

The DoE study on influence of process parameters on joint strength did not provide any conclusive findings to whether an association exists. Under both the coach-peel and lap shear sample configurations, the stackups all failed due to the stress concentration of the screw head on the top sheet ultimately causing the bottom side of the head to pierce the sheet and thus cause the joint to fail. The joint strength, under both configurations, exceeded that of the workpiece with coach-peel samples averaging a maximum force of 2.2kN, while the lap shear averaged 5.2kN; both had standard deviations of only 100N.

Figure 3–12: Coach-peel sample configuration

Figure 3–13: Fractured static coach-peel sample

Figure 3–14: Fractured static lap shear sample

Static Lap Shear Failure Mechanisms

A wide variety of material stackup combinations including sheet, cast, and extruded aluminum alloys with thicknesses from 1 to 5mm were created and tested during this research study. Three distinct failure mechanisms were observed for joints configured under a lap shear loading condition: sheet tear-out, screw pull-out, and screw fracture.

Sheet tear-out: This failure mechanism will occur if the strength of the top sheet (taking consideration of the thickness) is less than that of both the bottom sheet and the shear strength of the steel screw. The screw acts as a stress concentration on the workpiece, and under shear loading will be the first to fail by tearing-out around the screw; as shown in Figure 3–15. Under this failure mechanism, the joint strength would be independent of the base material thickness with a 1+2mm, 1+3mm, and 1+4mm stackup all failing at the same value due to the 1mm sheet thickness weak-point.

52
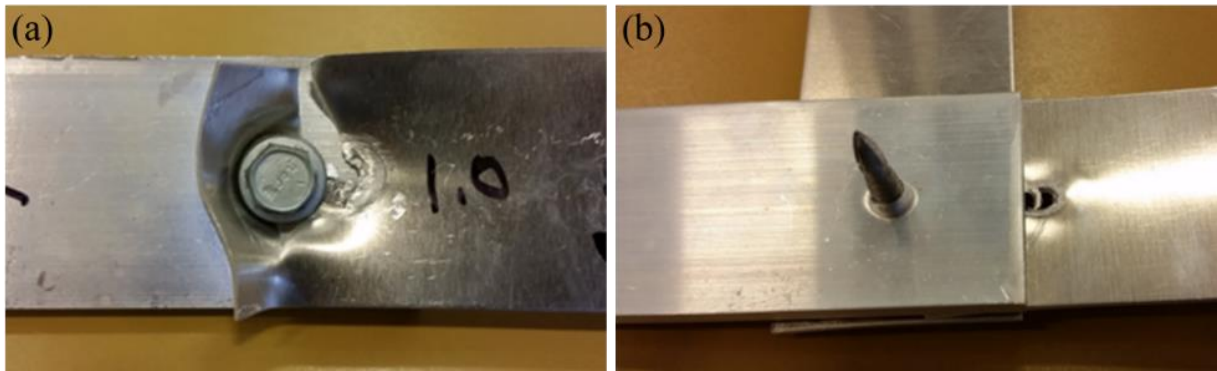
Figure 3–15: Sheet tear-out failure mechanism (a) top sheet of 2T, (b) middle sheet of 3T

Screw pull-out: Failure of this kind occurs if the top and bottom workpieces possess approximately the same strength values, and that these values do not exceed the shear strength of the screw. As the two workpieces deform to the same degree, the screw will pivot from the off-axis loading and cause the extruded hole to expand enough where the screw will pull-out of the base sheet, Figure 3–16.
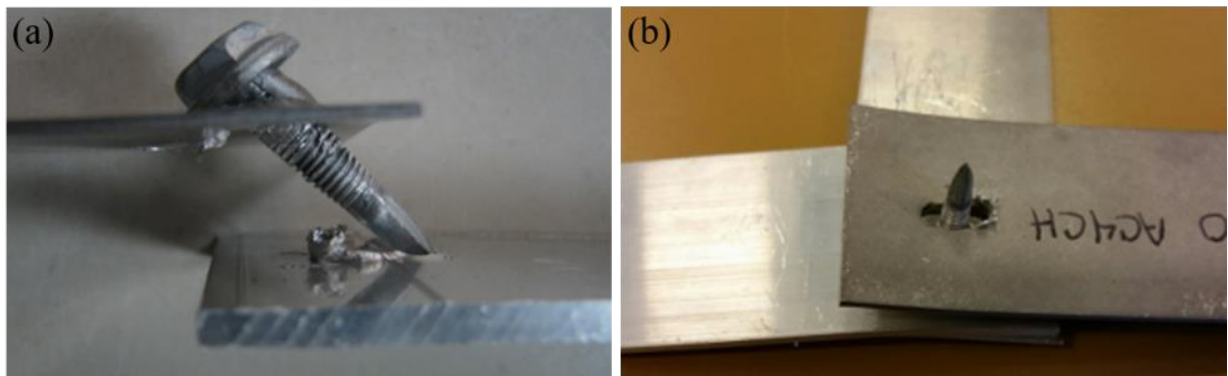
Figure 3–16: Screw pull-out failure mechanism (a) 2T stackup, (b) 3T stackup

Screw fracture: The last and highest force-magnitude failure mechanism occurs when the top and bottom workpieces are both stronger than the shear strength of the screw. The screw will undergo severe plastic deformation before the extruded hole can enlarge enough for the pull-out mode to occur and thus the screw fractures at the shaft-head interface, Figure 3–17. The same failure mechanism was observed by Pan *et al.* during their FDS joint testing study [29], with their post static test sample shown in Figure 3–18.
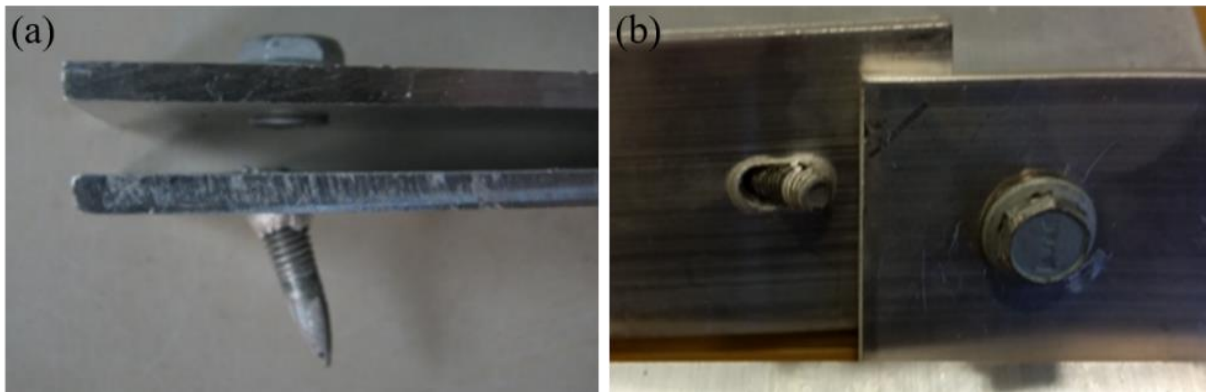
Figure 3–17: Screw fracture failure mechanism (a) side view, (b) top view
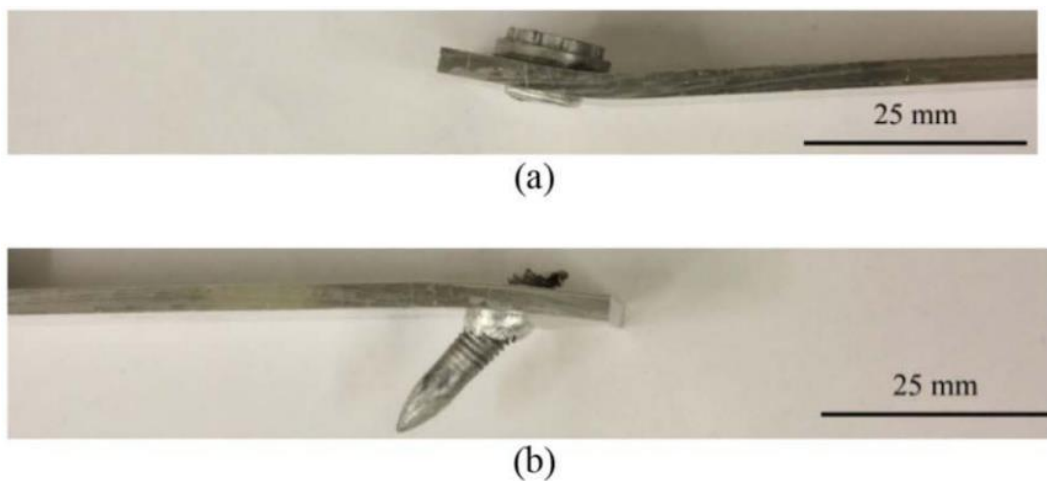
Figure 3–18: Similar screw failure mechanism observed by Pan et al. [29]

Dynamic Lap Shear

The final joint strength study was on the fatigue life of joints in a lap shear configuration. Longevity is certainly an important aspect for automotive designers to consider when selecting joining technologies for their multi-material structures. Static lap shear joints did not provide a definitive relation between process parameters and joint strength as all workpieces failed due to the screw stress concentration. The study varied the drilling force to which these screws were installed with high, mid, and low values of 1858N, 1515N, and 745N. Samples were tested at a load frequency of 20Hz with tests ceasing after sample fracture.

The study revealed that samples created under high drilling forces exhibited higher cycles to failure than those installed at lower drilling forces, Figure 3–19. The previous chapter section revealed that the drilling force can have a drastic effect on the maximum process temperature, with the 745N samples averaging 310°C while the 1858N samples averaged only 140°C. Due to the low temperature associated with the high drilling force samples, these samples may have been cold worked; ultimately increasing their strength from their previous as-received annealed state. Despite noticeable cycles-to-failure values, all fatigue samples exhibited the same failure mechanism, Figure 3–20. Once again, the same failure mechanism was observed by Pan *et al.* during their FDS joint testing study [29], as can be seen in Figure 3–21. This mechanism was unique to the dynamic loading condition as it was not previously observed as one of the static failure mechanisms.
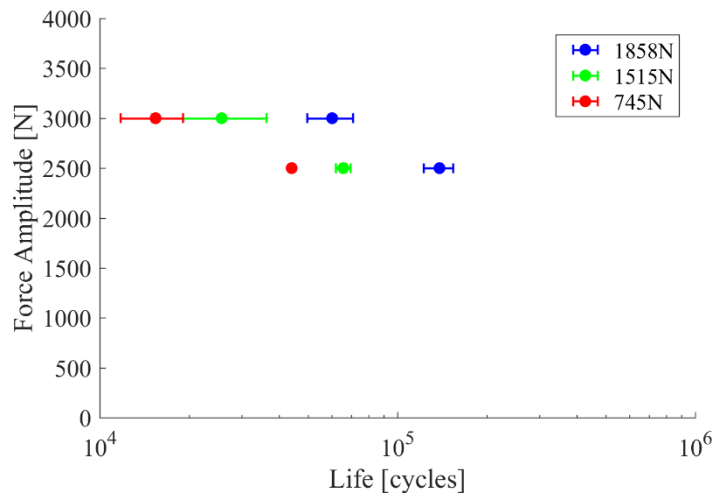
Figure 3–19: Fatigue force-life plot
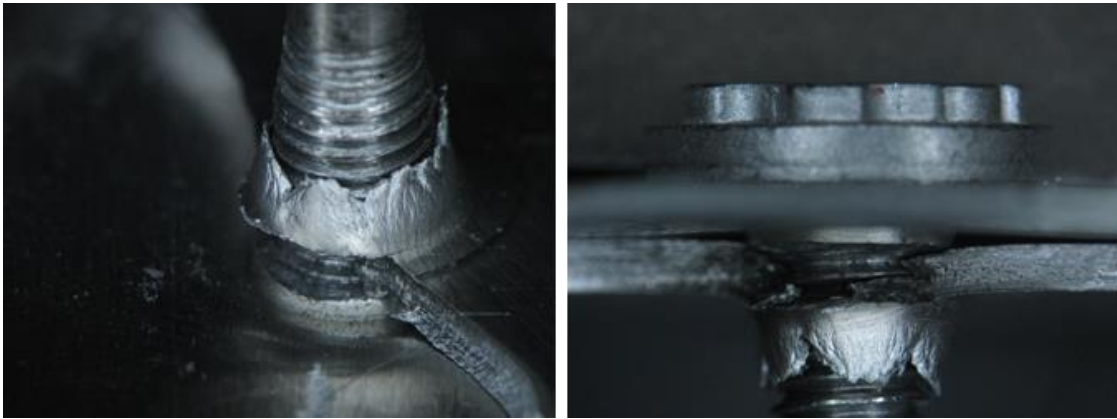
Figure 3–20: Fractured dynamic lap shear sample
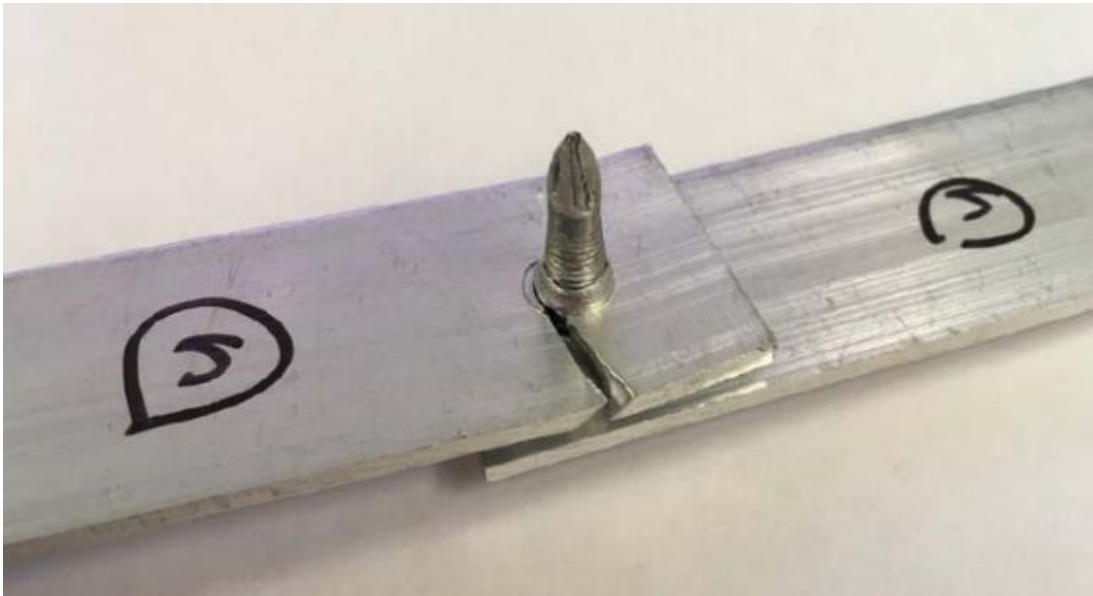
Figure 3–21: Similar post dynamic lap shear sample observed by Pan et al. [29]

3.4. Conclusions

The experimental studies aimed at characterizing the FDS process, showed that:

- Installation torque is dependent upon workpiece temperature, with increased screwdriving speeds being the dominant factor in reducing the torque

- Screwdriving speed is also the main driving factor for stripping torque, but is more beneficial towards increasing this torque at a reduced speed

- Process time can be significantly reduced by increasing the drilling force

- The joint can retain a higher percentage of its originally tightened torque through addition of a torque holding time, but benefits showed to diminish after holding for longer than 1 second

- The max process temperature can vary within a 150°C window, with the dominant factor of drilling force shown to have an indirect relationship to the temperature

- The joint geometry is sensitive to process parameters, having both an effect on the sheet deflection along with the length and quality of the formed extrusion

- Parameters were not observed to influence the static joint strength, but higher drilling forces were shown to increase the joint fatigue life

- Three failure mechanisms exist under a static lap shear loading configuration: sheet tear-out, screw pull-out, and screw fracture

These conclusions demonstrate the tradeoffs that exist when adjusting process parameters. The joint metric that should be minimized or maximized is dependent upon the stackup being joined. As an example, the installation torque for a thin stackup will be far below the 8.3N-m limit to be of concern, it will however, have a low stripping torque and thus parameters should be selected to maximize this torque value. The opposite can be said for a thick stackup to which reducing the installation torque will be its main parameter selection driving factor. The tradeoffs between parameter inputs to process outputs are summarized in Table 3–3, with dominant parameters signified by larger arrows.

This chapter demonstrated how a wide range of temperature and torque vales can occur during the FDS process. The conducted experimental studies helped link together the process parameters

to the process metrics, but only on a macro-scale. Now that these relations have been established, the next chapter refines this understanding on the micro-scale by analyzing the material deformation that is a result of these varying temperature and torque values.

Table 3–3: Process parameter tradeoffs

Process Parameter	Process Time	Installation Torque	Stripping Torque	Breakloose Torque	Sheet Gap
↑ Drilling Speed	↓ (green)	↓ (green)	↑ (green)		↓ (green)
↑ Drilling Force	↓ (green)	↑ (red)		↓ (red)	↓ (green)
↑ Screwdriving Speed	↓ (green)		↓ (red)		
↑ Torque Holding Time	↑ (red)			↑ (green)	
↑ Tightening Torque	↑ (red)			↑ (green)	↓ (green)

4. EVALUATION OF TRANSIENT MATERIAL DEFORMATION USING THE STOP-ACTION TECHNIQUE

FDS is a transient process, with temperature, surface velocity, and material properties varying throughout the process. To gain a better understanding of how material near the screw-workpiece interface is altered during the process, the stop-action technique was implemented. This technique has been used in FSW in which the tool is forcibly stopped to preserve the material flow for observation [47,72,73]. As FSW is a pseudo steady-state process, stopping the tool during any part of the welding step will lead to the same observable findings. FDS, on the other hand, is fully transient and therefore this technique was modified to create several 'stepped' samples which had been controlled to stop at designated material penetration depths.

These 'stepped' samples were all created under the same conditions with the difference being in how far the screw penetrated the workpiece before ceasing the test. Using the same process parameters, batch of workpiece material, batch of screws, and machine justifies the assumption of each sample being exposed to the same deformation as the one before it.

4.1. Experimental Setup

All tests were conducted at WEBER Screwdriving Systems in Mooresville, NC using their RSF21 unit. The RSF21 FDS unit is capable of rotational speeds up to 5000RPM, endload up to 2500N, and torque up to 15N-m. RPM, endload, torque, displacement, and time data were all acquired by the RSF unit which sampled at 1000Hz. Surface temperature data was acquired using a FLIR A8201sc thermal camera sampling at 100Hz. The screw used for these experiments is the standard tip EJOT FDS M5x20 screw, Figure 2–8, with a zinc-flake corrosion-mitigating coating. The workpiece material used during this study was 6061-T6 with thicknesses of 1.6, 2.0, and

2.5mm. As one of the assumptions during this research is the radial symmetry of the process, the workpieces were water-jetted into circular parts, Figure 4–1. They were painted black to emulate a black body and assigned an emissivity value of 0.95. The purpose of the extended tab was to prevent the workpiece from rotating with the screw while in the fixture. The fixture was fabricated from Delrin, a plastic with low thermal conductivity, which allowed the model-based boundary condition to be that of an insulative condition on the bottom & sides of the sheet.

60mm
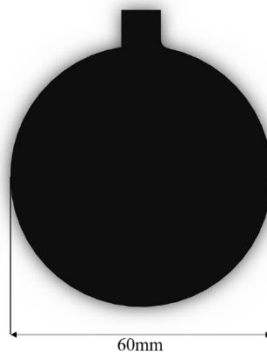
Figure 4–1: Black-painted circular workpiece

The experimental procedure was conducted in a repeatable manner which consisted of using a new workpiece and screw for each test, initiating the thermal camera data acquisition, and inserting the screw at the same process parameters, Table 4–1, albeit altering the final displacement for the screw to attain these 'stepped' samples. The full experimental setup including workpiece, fixture, thermal camera, and RSF unit is shown in Figure 4–2.

Table 4–1: Process parameters

Drilling Speed [RPM]	Drilling Force [N]	Thread-Forming & Screwdriving Speed [RPM]	Thread-Forming & Screwdriving Force [N]	Screw Displacement
5000	600	2500	400	Varying

Figure 4–2: Experimental setup

Once all tests were completed, six samples were selected to be cut, mounted, polished, etched, and microstructurally analyzed. The six samples were chosen to give a good representation of how the workpiece material changes from the start of heating step (step 1) until the beginning of thread-forming (step 4); the location of each sample relative to a full process is shown in Figure 4–3. Duplicate samples, those with equal screw displacements, were created during experimentation to allow for microstructural analysis in both the tangential and radial directions at a given point in the process. The tangential microstructure analysis was done by orientating the samples in a 'top-view' manner, while the radial samples were mounted in a 'cross-section' manner, Figure 4–4.
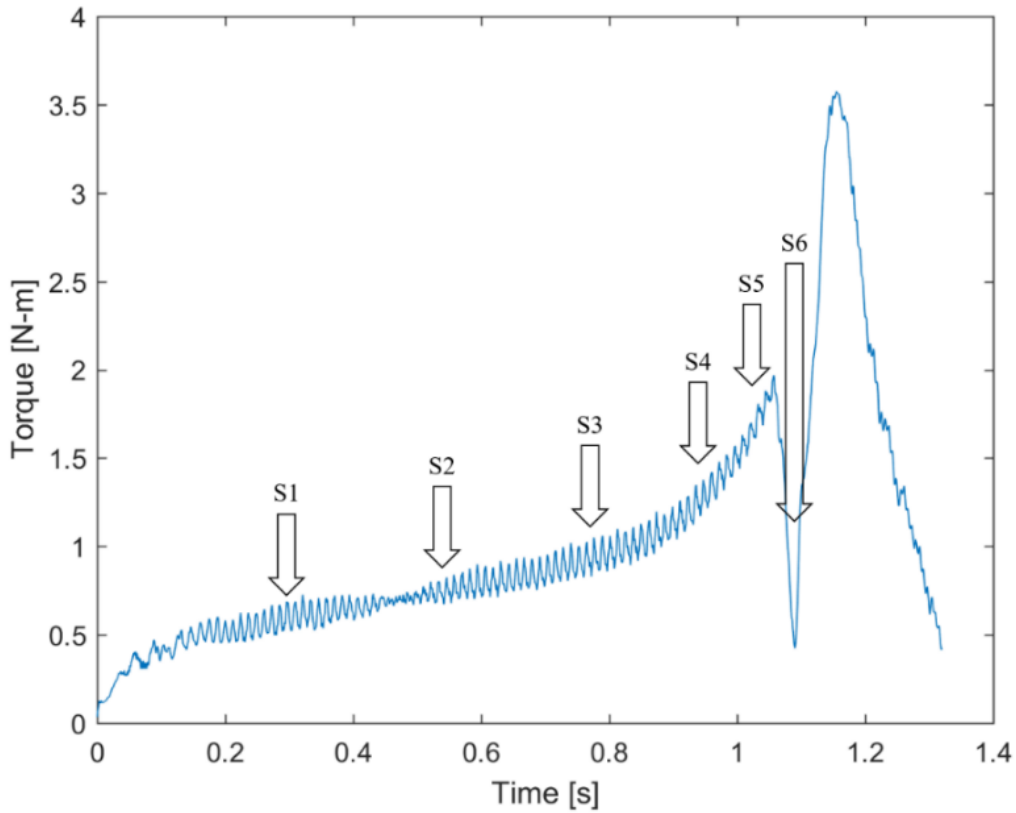
Figure 4–3: Locations of selected samples illustrated on the torque-time curve
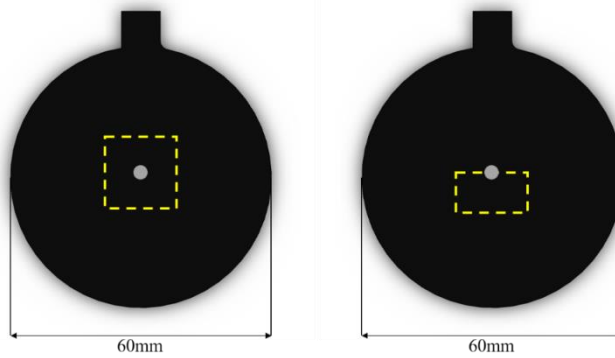
Figure 4–4: Top-view (left) and cross-section (right) sample orientations

After being sectioned the samples were mounted in a glass-filled epoxy with the grinding and polishing procedure done in accordance with ASTM E3-11: 320grit, 9µm, 3µm, 1µm diamond suspensions, followed by a 0.05µm colloidal silica final polishing. The samples were submerged

in a Weck's reagent for ~11 seconds then rinsed to stop the etching process. Microscopy images of the grains were then taken for both the 'top-view' and 'cross-section' orientations. As the tip of the screw is of a conical nature, all locations across the workpiece thickness will be exposed to different surface velocities from the rotating screw; leading to non-uniform interfacial contact conditions. To study this at multiple points in the process, the grinding procedure was repeated to remove ~0.6mm of material from the 'top-view' samples, followed once again by etching and imagery to observe the microstructure at this location; an additional ~0.6mm was removed for the last slice, Figure 4–5. Analysis was completed at three locations (top, middle, and bottom) for each of the six top-view samples, Figure 4–6; as well as the single cross-section views for each of the six duplicate samples, Figure 4–7.
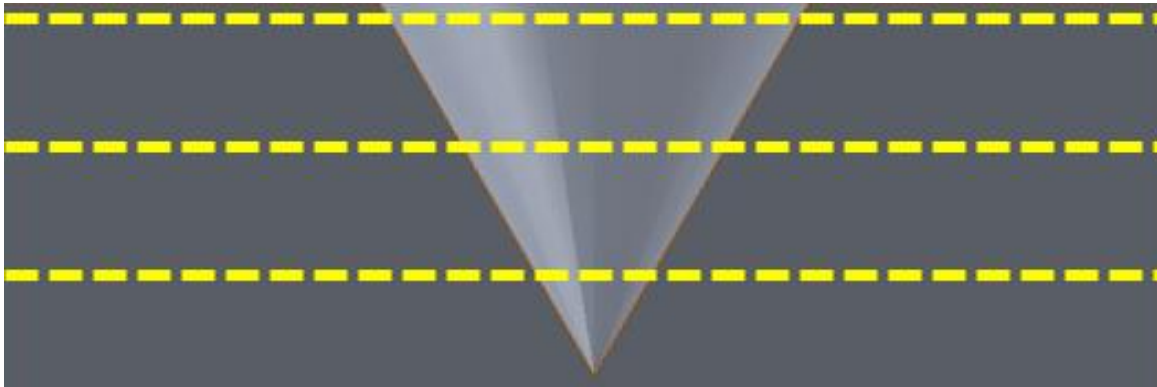
Figure 4–5: Locations for top, middle, and bottom 'top-view' slicing
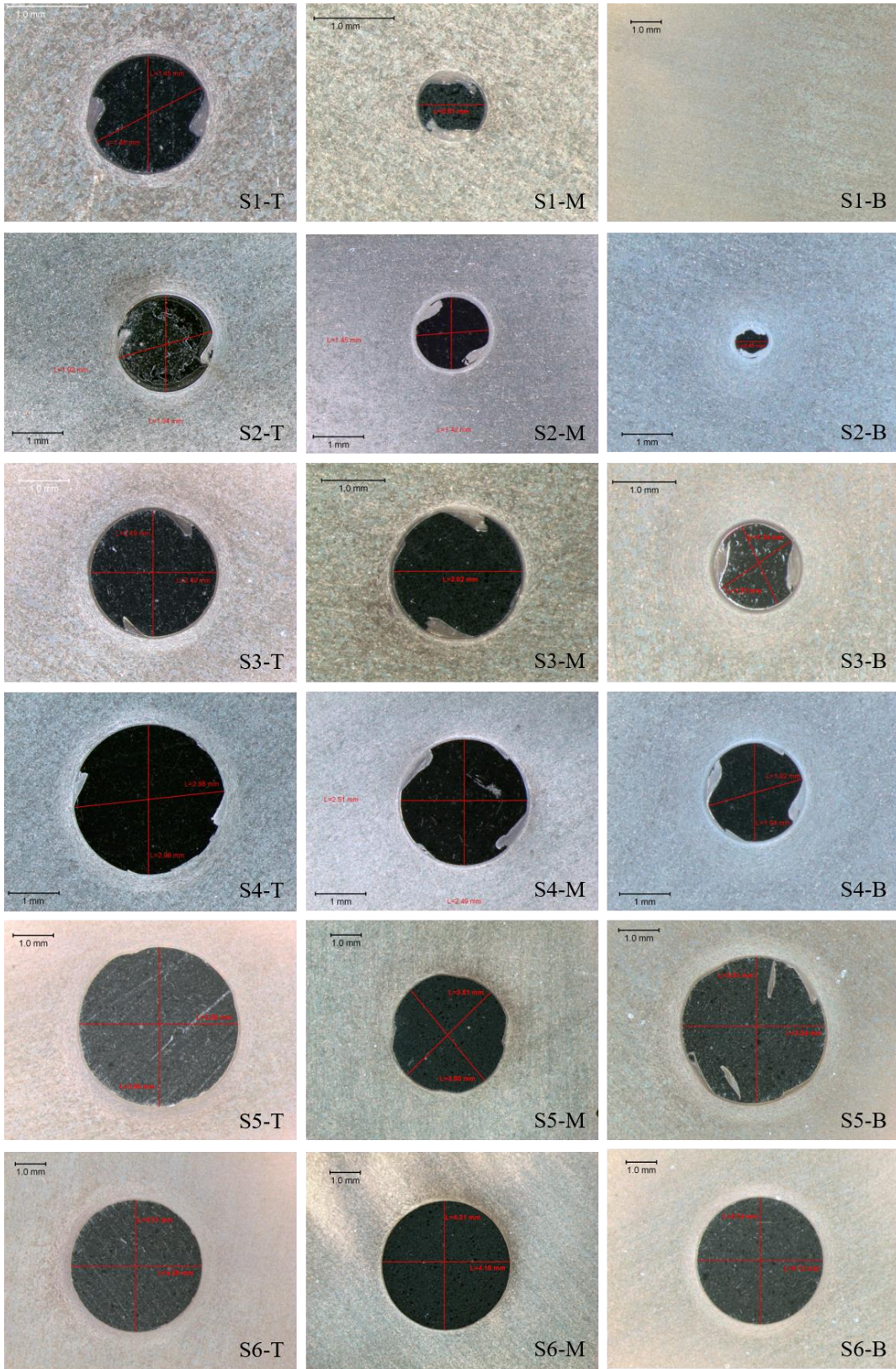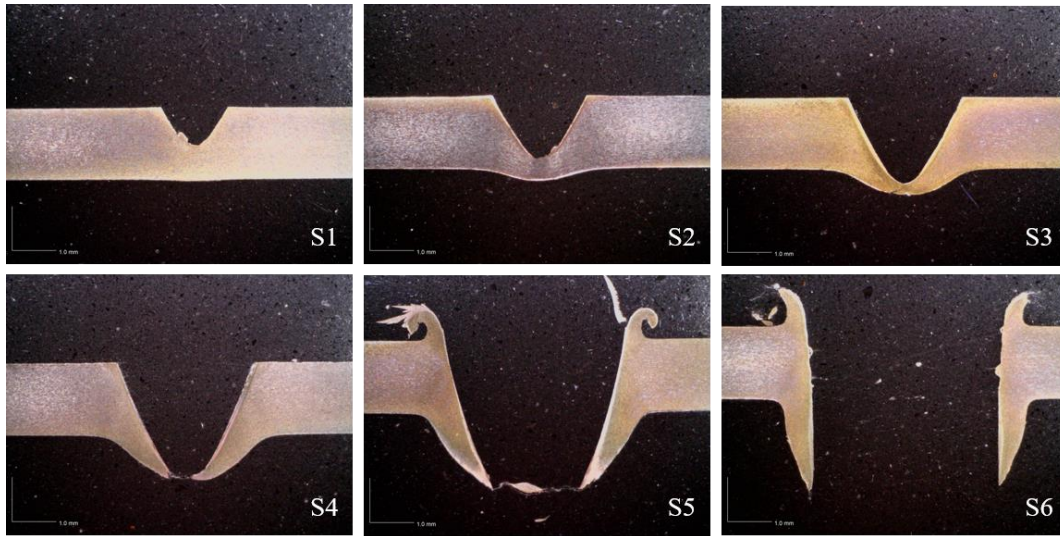
Figure 4–7: Cross-section views of 'stepped' samples

4.2. Microstructural Analysis

Four microstructural zones exist in friction stir processing: the stir zone (SZ), the thermo-mechanical affected zone (TMAZ), the heat affected zone (HAZ), and the base material (BM), as displayed in Figure 4–8. The grain size and level of distortion determines into which category the area of grains is associated with. The SZ is located at the tool-workpiece interface and is characterized by small and highly refined grains. The high temperatures and levels of distortion near this interface cause dynamic recrystallization to occur leading to these small grains. The TMAZ is located outside of the SZ (away from the interface) and is characterized by elongated/distorted grains due to plastic deformation of the material. Grains in the TMAZ do not go through recrystallization, as those in the SZ do, and thus exhibit a larger grain size. Further away from the interface is the HAZ, whose grains have an altered microstructure due to exposure to a thermal cycle; HAZ grains are not plastically deformed. The remaining material outside of the HAZ is the BM, whose grains are the same as those of the material prior to the process.
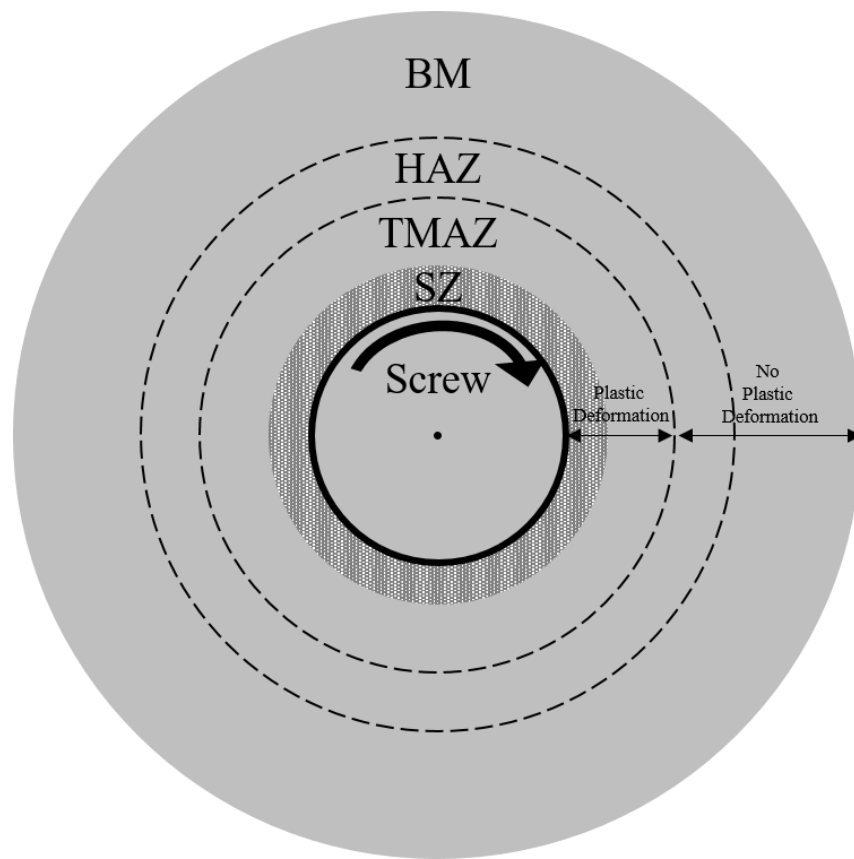
Figure 4–8: Schematic of the microstructural zones

Stir Zone Analysis

Grains in the SZ have been measured to be around 1-2µm for a similar friction stir process [74]. Grain boundaries are the first to be revealed during etching and thus appear darker than the actual grain itself. A grain boundary's thickness is independent of the grain size, it's finite, thus a higher concentration of grains would appear as a darkened region than that of an area with larger grains. Observations of the etched samples show a darkened region near the screw-workpiece interface, Figure 4–9; for the reason previously mentioned, it has been identified as a SZ.
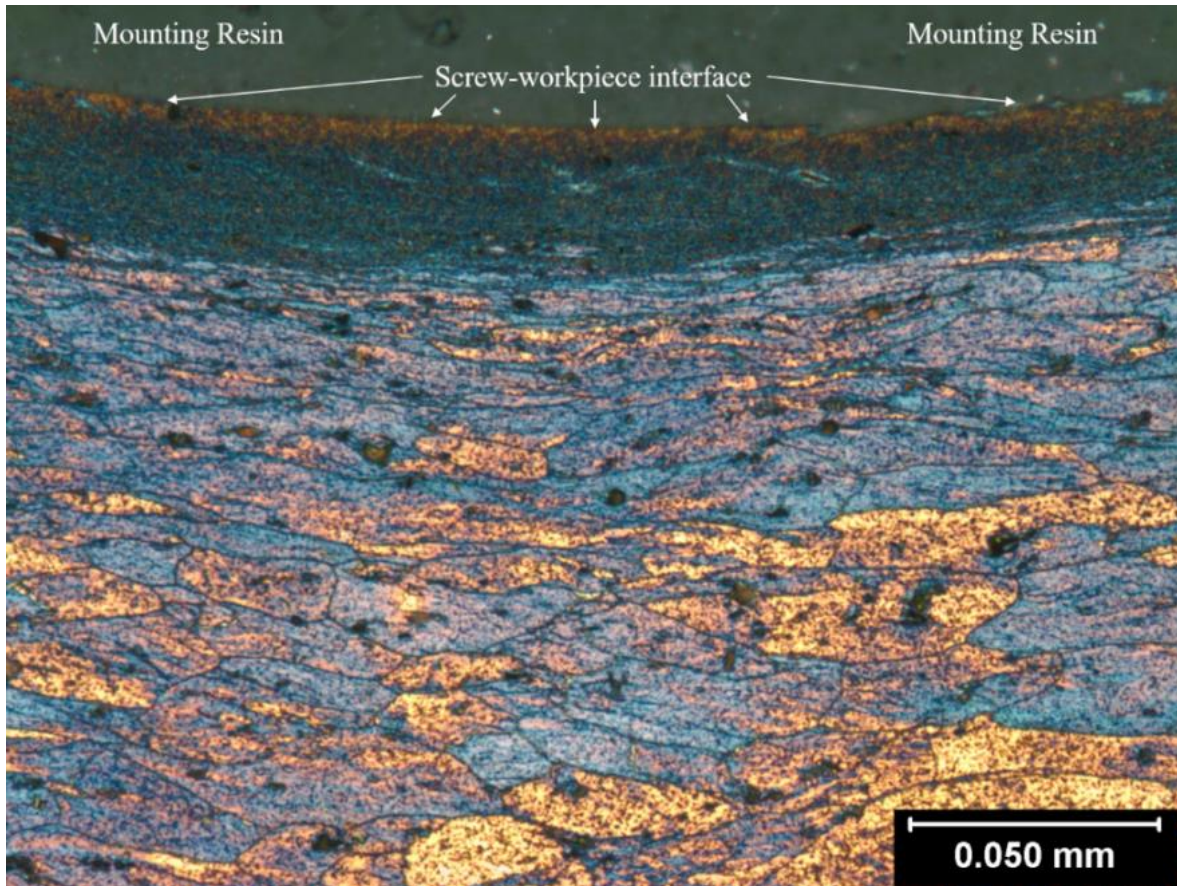
Figure 4–9: Etched material near the screw-workpiece interface – sample 1 top

The transition from SZ to TMAZ is not a distinguishable point, rather it's a region; therefore, image processing was used to quantitatively determine the thickness of each samples SZ. Each image was imported into ImageJ [75] whereby it was converted to an 8-bit grayscale image and the area of interest, starting at the interface and extending radially-outward, was selected, Figure 4–10. The image's intensity values were measured on a scale of 0 to 255; the former being pure black and the latter being pure white. These measured values were plotted against their distance from the interface as shown in Figure 4–11.
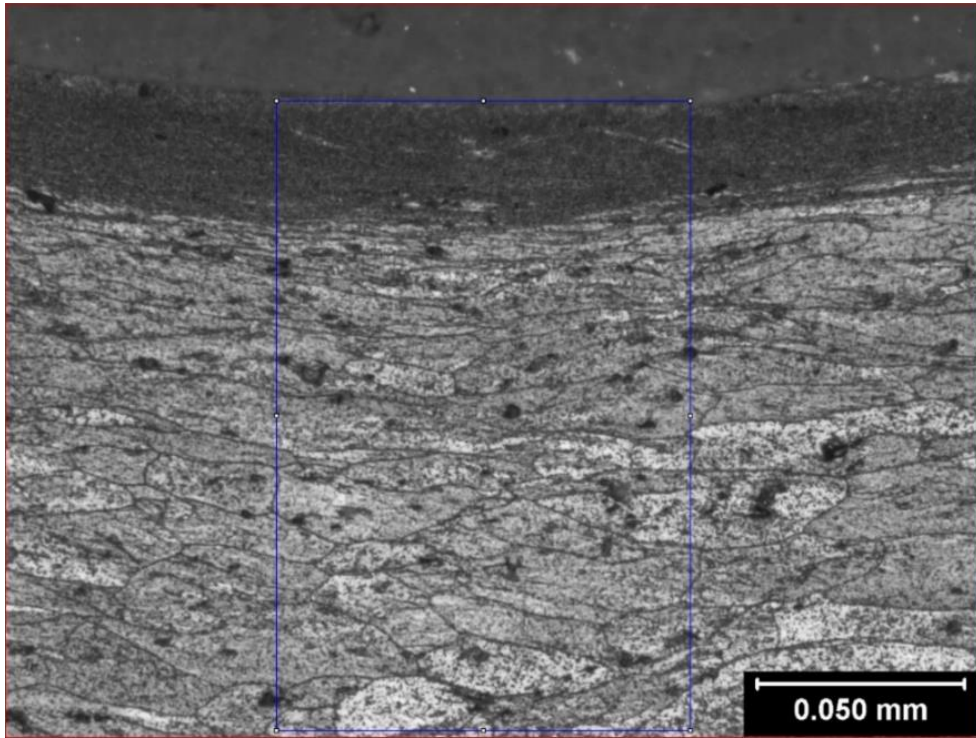
Figure 4–10: Image intensity region of interest - sample 1 top
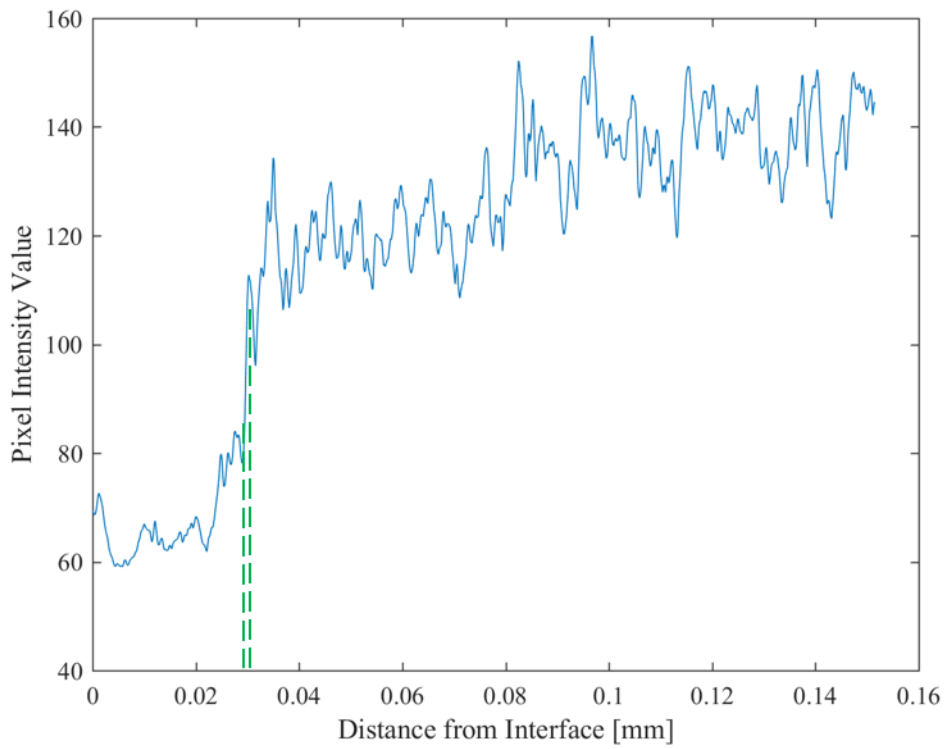
Figure 4–11: SZ image intensity plot - sample 1 top

Due to the larger grain boundary to grain body volumetric ratio in the SZ, lower intensity values were measured near the interface. Pixel intensity values increase further away from the interface as grain sizes approach their pre-process base material form. A transition from low to high intensity values is apparent at a distance between 0.29 and 0.31mm from the interface, signifying the location of the SZ-to-TMAZ transition zone for this sample. A pixel intensity analysis was performed on the remaining samples, with the SZ thicknesses shown in Table 4–2.

Table 4–2: SZ sample thicknesses

Sample	Top [µm]	Middle [µm]	Bottom [µm]
1	30	30	N/A
2	40	90	60
3	50	60	60
4	60	70	50
5	50	30	40
6	30	30	30

Thermo-Mechanical Affected Zone Analysis

Determining the TMAZ thickness is vital to knowing the extent of plastic deformation that occurs during the process. Without being able to quantify the volumetric zone that undergoes this plastic deformation, the contribution towards the sticking aspect of the torque cannot be accurately verified. If observations showed no grain distortion (i.e., no plastic deformation), the process would solely be of the slipping-kind. The grain orientation (with respect to the screw-workpiece interface) combined with the level of distortion (quantified through aspect ratio) were used as criteria to determine if an area of material outside of the SZ had been plastically deformed.

Four samples were etched from the as-received material to be used as a reference of the un-deformed base material outside of the TMAZ. Observable grain boundaries were traced leading to identification of 67 individual grains from the as-received material, Figure 4–12. The grain outlines were then isolated from the image in which they were traced from by copying them onto a blank

canvas, Figure 4–13. The code [76] identified the grain boundary and fitted an ellipse around the grain's centroid, Figure 4–14.
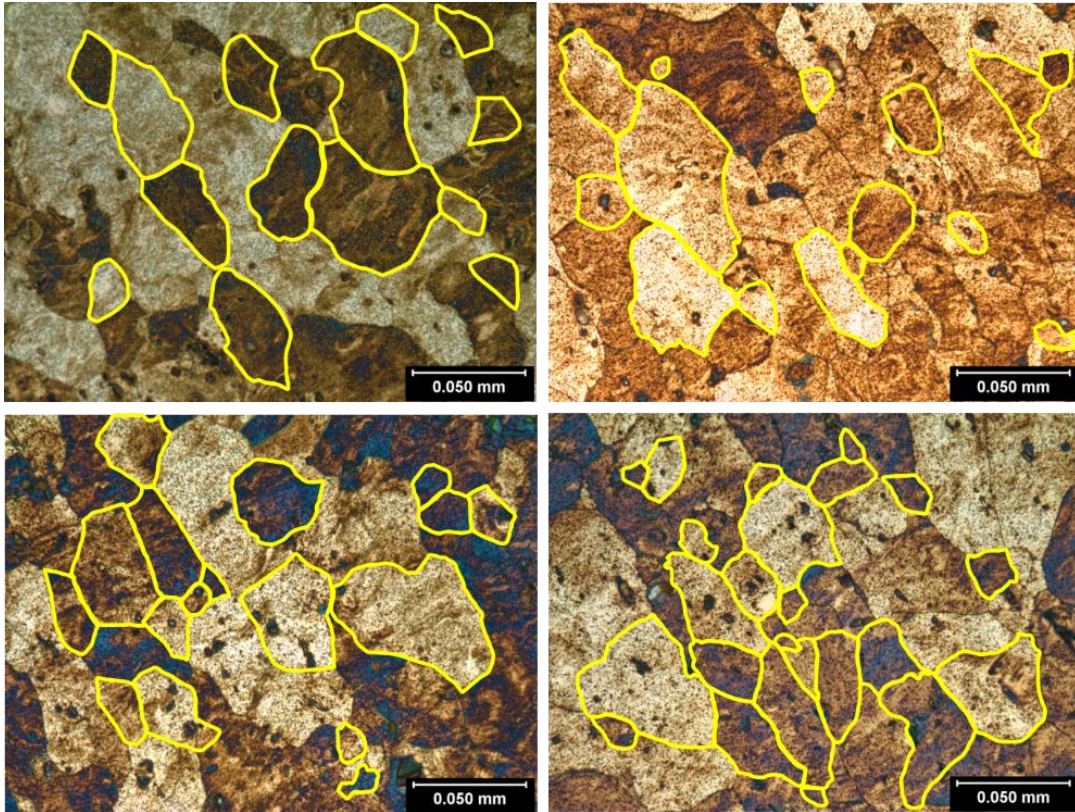
Figure 4–12: Traced grains – as-received material
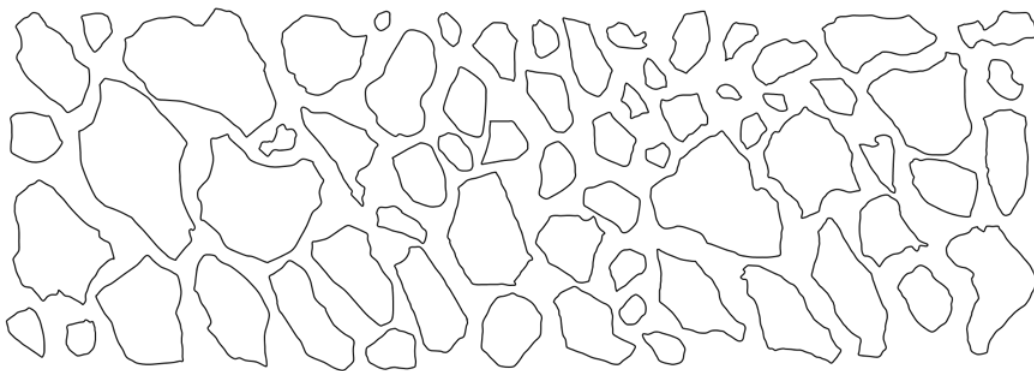
Figure 4–13: Isolated grain outlines – as-received material

70
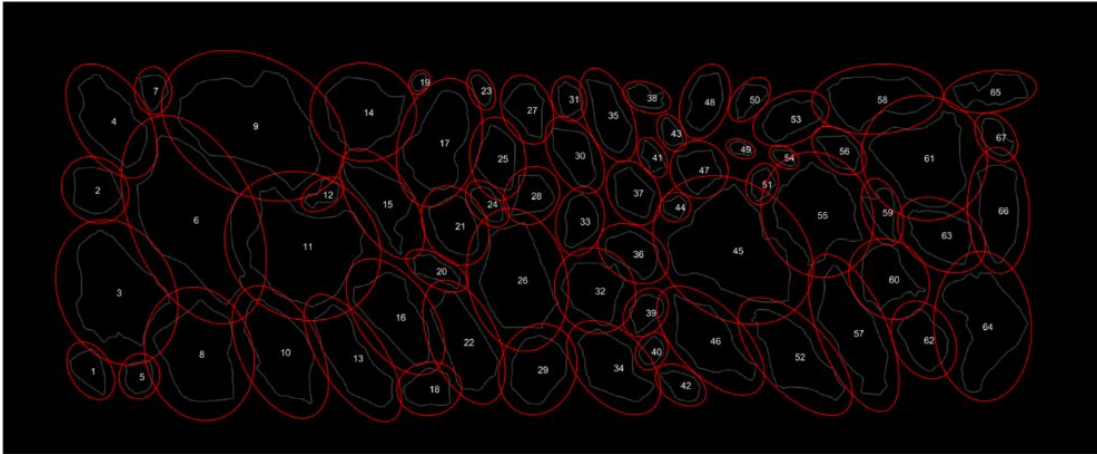
Figure 4–14: Superimposed ellipses on grains – as-received material

Each ellipse's aspect ratio (AR) and orientation were measured; whereby AR is the ratio between the minor and major axis lengths and orientation is measured relative to the vertical edges of the image. The magnitude of grain distortion (GD) was taken to be '1-AR' so that a direct relationship between measurable grain distortion and degree of plastic deformation would exist; otherwise a low AR would signify a high level of grain elongation/distortion. Orientation was taken on a scale of 0 to 90° whereby the former would signify a grain orientated perfectly parallel to the interface and the latter would signify one that lies perfectly perpendicular.

An average grain distortion value for the 67 as-received material grains was calculated to be 0.32. Once quantitative measures were developed for how non-deformed grains would appear, the transition from TMAZ to HAZ was determined. Each sample underwent an identical microstructural analysis to that of the as-received material grains including: tracing of the grains Figure 4–15, isolating the grain outlines Figure 4–16, and fitting ellipses Figure 4–17; with grain orientation and distortion values being the outputted values.
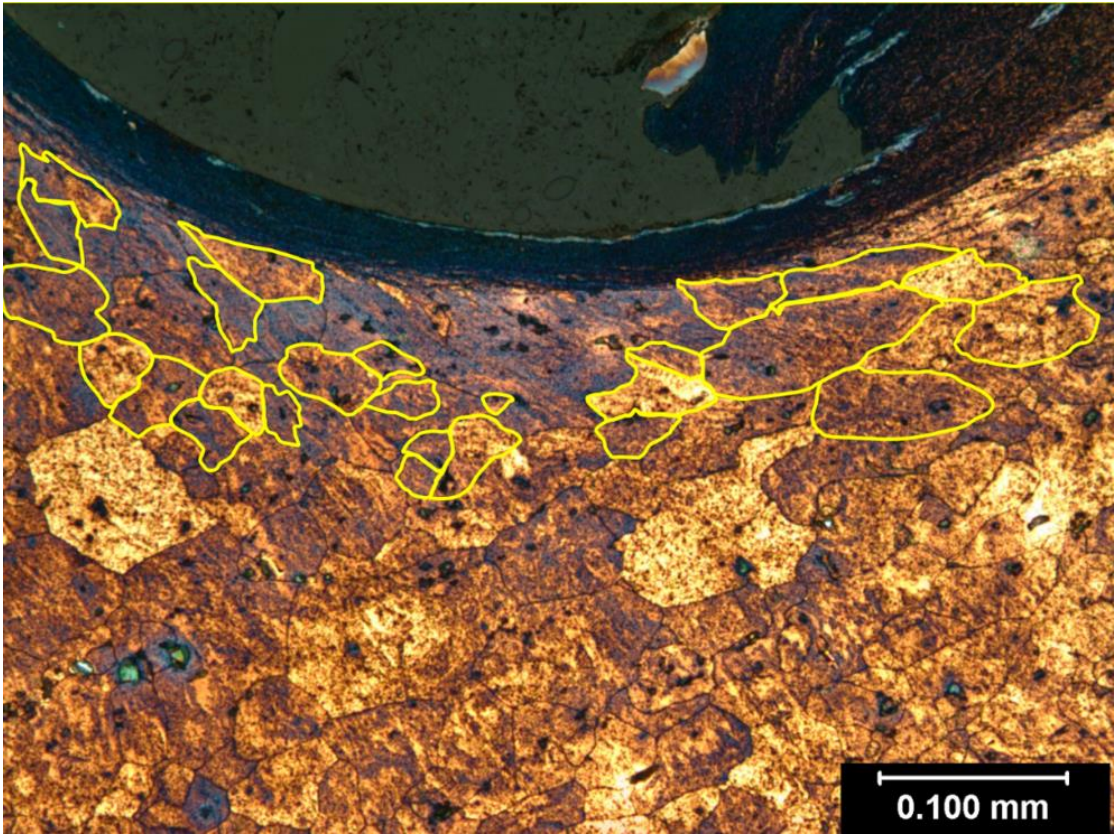
Figure 4–15: Traced grains – sample 1 middle

Figure 4–16: Isolated grain outlines – sample 1 middle
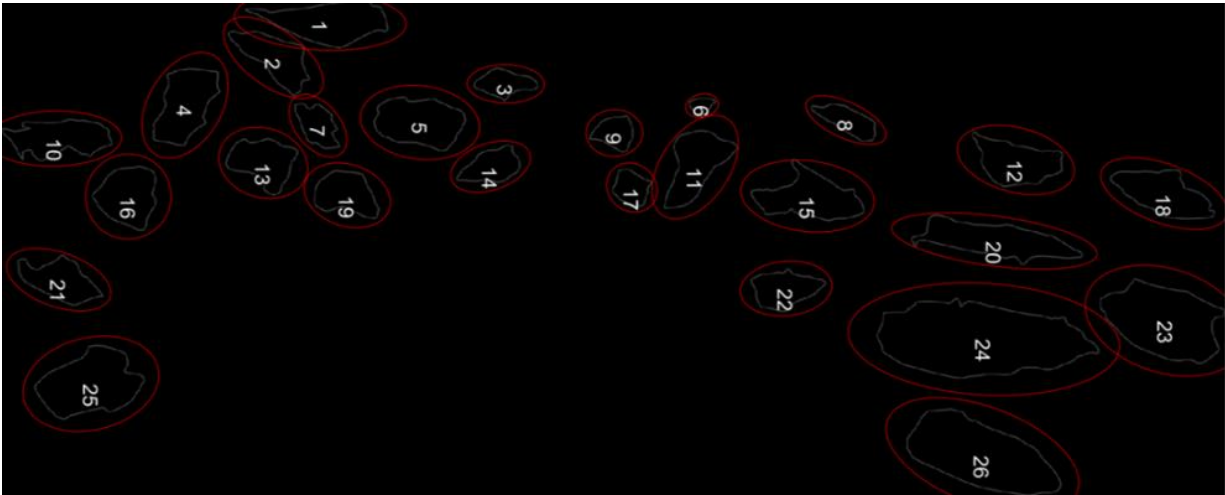
Figure 4–17: Superimposed ellipses on grains – sample 1 middle

Given the wide range of grain distortion values (0.04 to 0.6) found in the as-received material, this criterion alone would not be sufficient to whether a grain was in the TMAZ. The same could be said for a grain's orientation, as its inclusion would be dependent on its position relative to the hole and rolling direction of the as-received sheet metal; for this reason, inclusion into the TMAZ would be both orientation and grain distortion dependent.

Low orientation values were observed just outside of the SZ, Figure 4–18, providing evidence that these grains exhibited the highest degree of plastic deformation being oriented primarily parallel to the interface. Identical observations were made during FSP in which more elongated grains were oriented parallel with the interface [77–79] .A large variation in grain orientation was observed at approximately 0.11mm from the interface; with the first grain having an orientation of 18° while the one only 2µm further has an orientation of 56°. After this point was identified as a potential location for the transition back to BM, the secondary criteria of grain distortion values were considered. The grain distortion plot, Figure 4–19, presented a clear association between the grain's level of plastic deformation and its distance from the interface. The two grains previously examined had distortion values of 0.30 and 0.41; which, given an average BM value of 0.32, are reasonable values for them to be considered part of the TMAZ. In this case, the decisive criterion

was the orientation value; which lead to the combined SZ and TMAZ thickness to be 0.112mm as indicated by the dashed line. The criteria for a grain to have been plastically deformed, and therefore part of the TMAZ, was to exhibit an orientation value >45° or a distortion value <0.3. All remaining samples showed good agreement with these criteria, with the results tabulated in Table 4–3. A similar trend is observed between the top and bottom measurements in which the TMAZ increases up through sample 4, then decreases to a stable value for samples 5 and 6. This trend demonstrates a growth in the workpiece area undergoing plastic deformation, then a decrease signaling the transition from sticking to slipping. Referring to Figure 4–7, sample 5 shows that the screw is on the verge of fully forming the hole, while the hole is completely formed in sample 6. At these steps in the process, the level of plastic deformation needed to complete the hole-forming operation is at a minimum and indicates the location of a transition from stick to slip contact condition. The values, although transient, provide good agreement to the 250µm value reported in FSW [80–83].
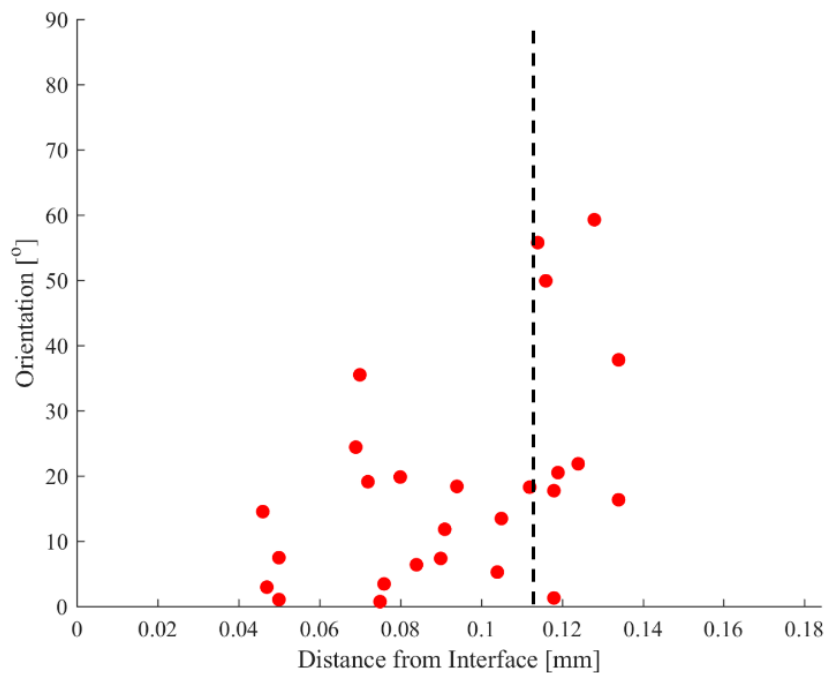
Figure 4–18: Grain orientations – sample 1 middle
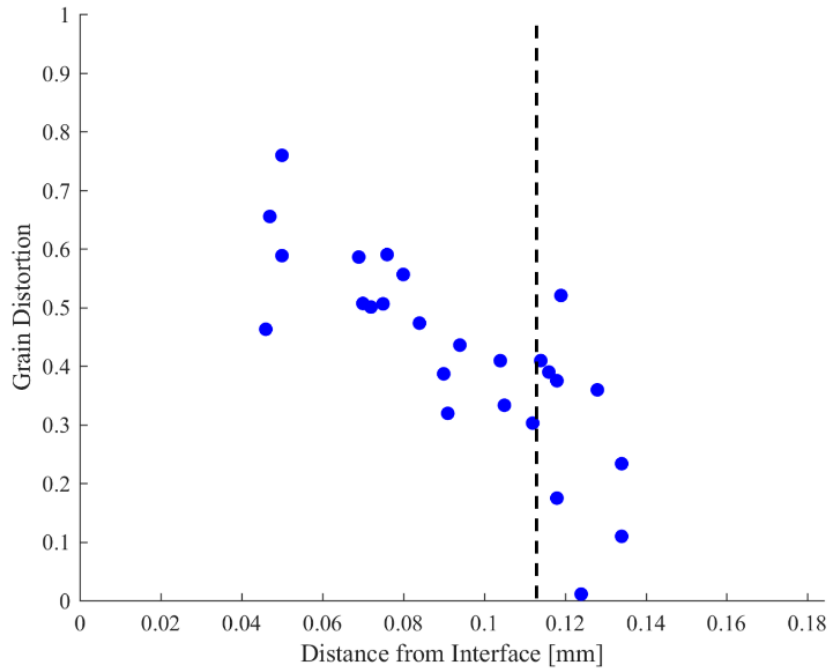
Figure 4–19: Grain distortions – sample 1 middle

Table 4–3: TMAZ thicknesses

Sample	Top [μm]	Middle [μm]	Bottom [μm]
1	190	80	N/A
2	230	190	260
3	400	140	240
4	410	160	360
5	340	170	270
6	330	210	270

TMAZ to Plastic Strain

Evidence of a TMAZ is owed to the plastic deformation that the material undergoes. However, knowing that plastic deformation is present is not sufficient alone; knowledge towards the degree of plastic deformation is important for better process understanding and therefore modeling. After having determined the thickness of the TMAZ, this corresponding radial distance was imposed as a boundary condition to the point where the plastic strain is zero, as shown by Equation 14. Plastic strain will be a maximum at the screw-workpiece interface; this additional boundary condition is

75

shown by Equation 15. The maximum plastic strain was selected to be 3.5, which was calculated from material flow observations during FSW [72]. The relation between these material zones, depicted in Figure 4–20, and the degree of plastic strain is described by Equation 16. The computed plastic strain values were integrated into the Johnson-Cook plasticity model, discussed in the subsequent modeling chapter.

$$\varepsilon_{pl}(r_{TMAZ}) = 0 \qquad (14)$$

$$\varepsilon_{pl}(r_{int}) = \varepsilon_{pl,max} \qquad (15)$$

$$\varepsilon_{pl}(r) = [1 - \frac{(r - r_{int})^2}{(r_{TMAZ} - r_{int})^2}]\varepsilon_{pl,max} \qquad (16)$$
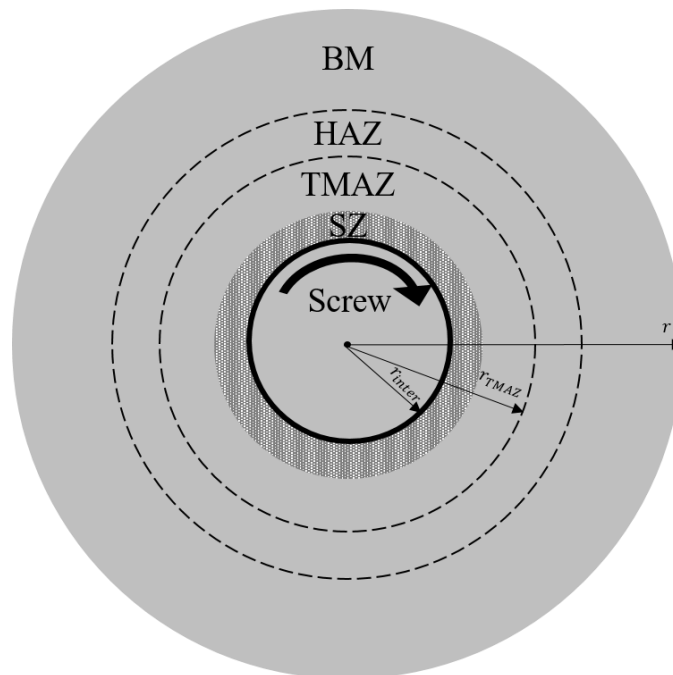
Figure 4–20: Schematic of material zone geometry

Microhardness

Microhardness tests were conducted on the cross-section samples to determine whether a relationship exists between post-process material hardness and the level of plastic deformation it underwent. A Vickers microhardness tester was utilized for all tests under the same conditions: an applied load of 100gf, dwell time of 15 seconds, and measurement spacing of 0.1mm. Indentations started at the SZ and extended radially outward for the top, Figure 4–21; middle, Figure 4–22; and bottom, Figure 4–23 of the sheets. Measurements of the as-received material reported an average value of 104HV, which was used as a reference indicating unaffected material.
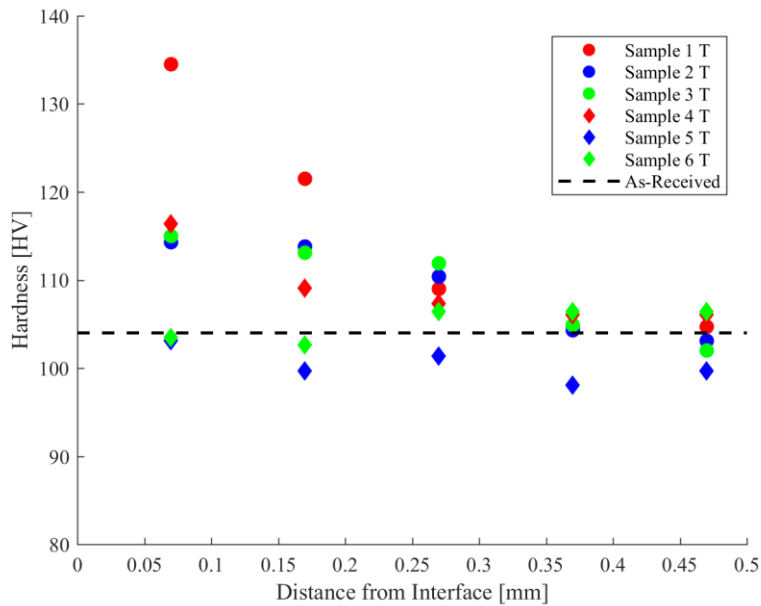
Figure 4–21: Cross-section microhardness - top of sheet
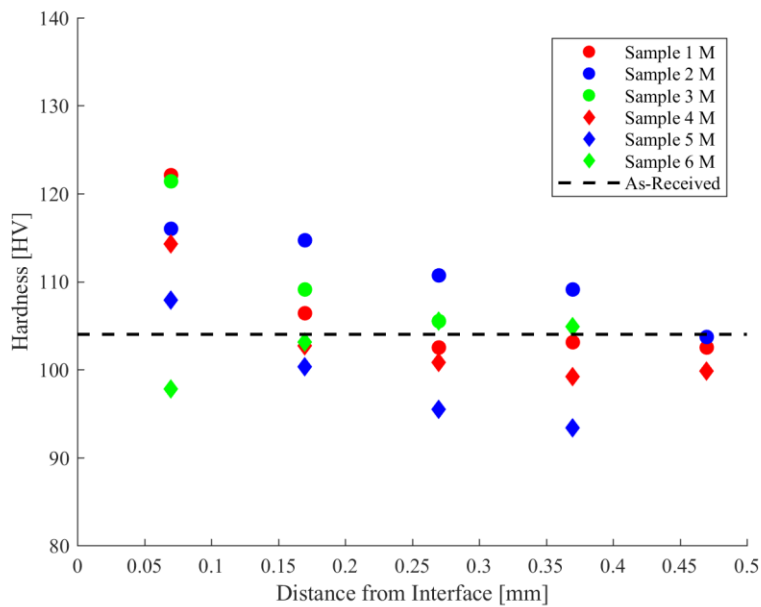
Figure 4–22: Cross-section microhardness - middle of sheet
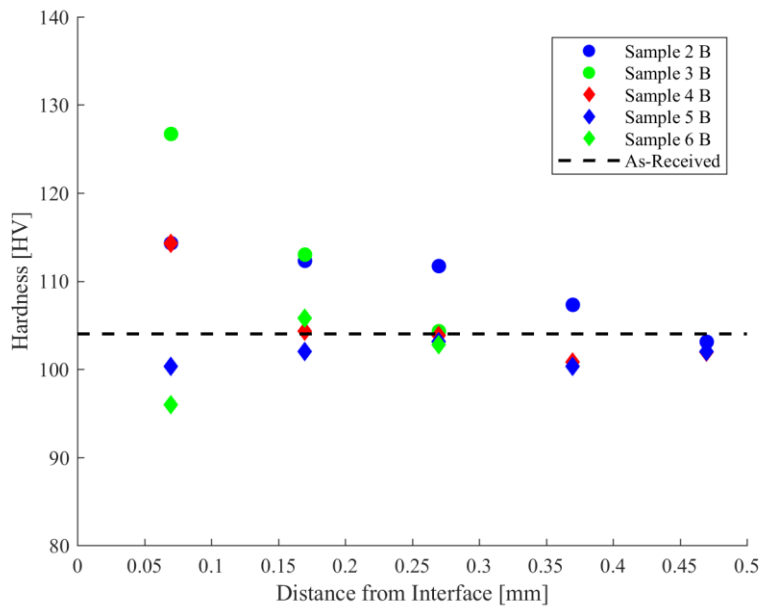
Figure 4–23: Cross-section microhardness - bottom of sheet

Samples 1-4 had increased hardness values near the screw-workpiece interface which gives evidence towards material strain hardening. Samples 5 and 6 had lower values near the interface, which indicates thermal softening. The reason these two samples had reduced hardness values,

while the others had increased hardness, was due to the way in which they were created. During creation of the stepped samples, if the screw had displaced more than 4mm into the workpiece, it would become fixed to the sample. The screws became un-wedged from the samples during the cross-sectional cutting procedure; however, the heat retained in the steel screw from the FDS process had acted like an extended heat source to the aluminum workpiece while it cooled back down, annealing the workpiece to a softened state. Despite the initial increased hardness from strain hardening followed by the reduced hardness from thermal softening, the process-affected zone extended less than 0.5mm outward. The microhardness measurements taken by Sønstabø *et al.* [84] were of a sample that underwent a full FDS process. Those results also showed material hardness values were lowered near the screw-workpiece interface with a final process-affected zone of less than 0.5mm. If stepped samples were not created, the initial evidence of material strain hardening would have been concealed by the screw-imposed thermal softening.
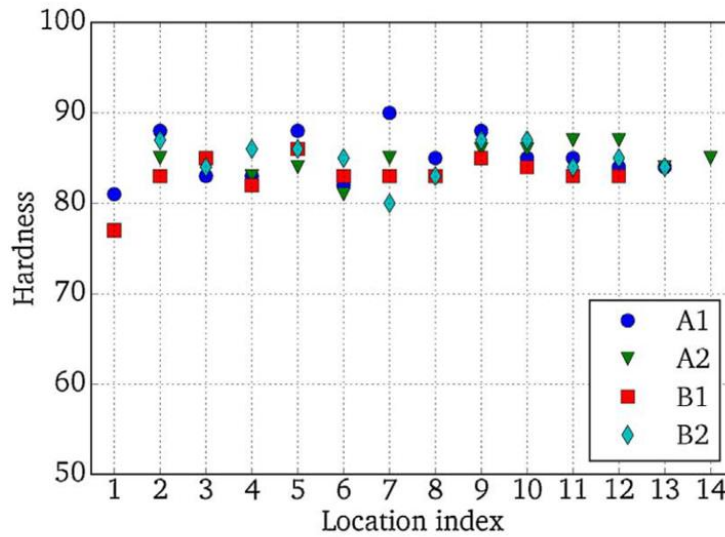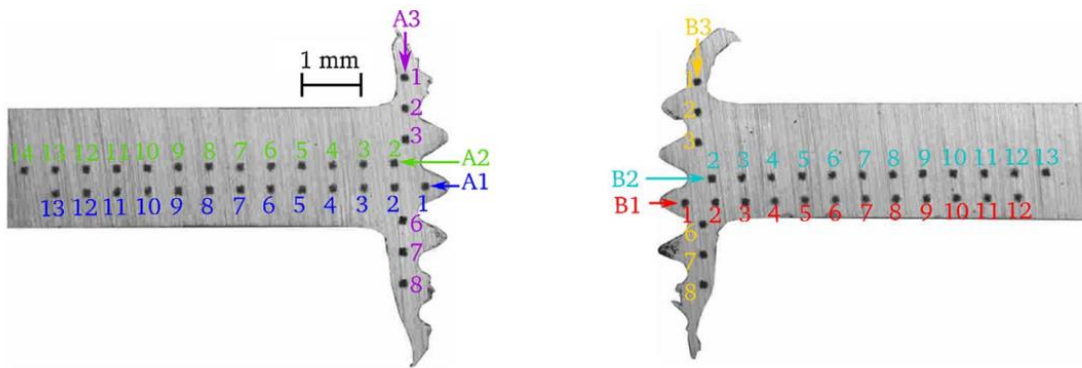
Figure 4–24: Microhardness by Sønstabø et al. [84]

Measurements and observations presented in this chapter supply evidence that material deformation during FDS occurs in a transient fashion. The microstructural observations have shown that the contact condition is non-uniform across the entire screw-workpiece interface; with fluctuating values owed to the varying temperatures and surface velocities. The next chapter introduces the numerical approach used to predict temperature and torque based upon findings from this chapter.

5. FINITE VOLUME TEMPERATURE & TORQUE MODELING

5.1. Temperature Modeling Approach

The heat transfer model is numerically solved using an explicit finite volume method (FVM) approach. The system is assumed to be axisymmetric about the z-axis and thus the heat equation, formulated in cylindrical coordinates, is reduced to Equation 17. The workpiece is discretized into individual control volumes (CVs) and indexed according to Figure 5–1.

$$\rho C_p \frac{\partial T}{\partial t} = \frac{1}{r}\frac{\partial}{\partial r}\left(kr\frac{\partial T}{\partial r}\right) + \frac{\partial}{\partial z}\left(k\frac{\partial T}{\partial z}\right) + d\dot{Q}_{friction} + d\dot{Q}_{deform} \tag{17}$$
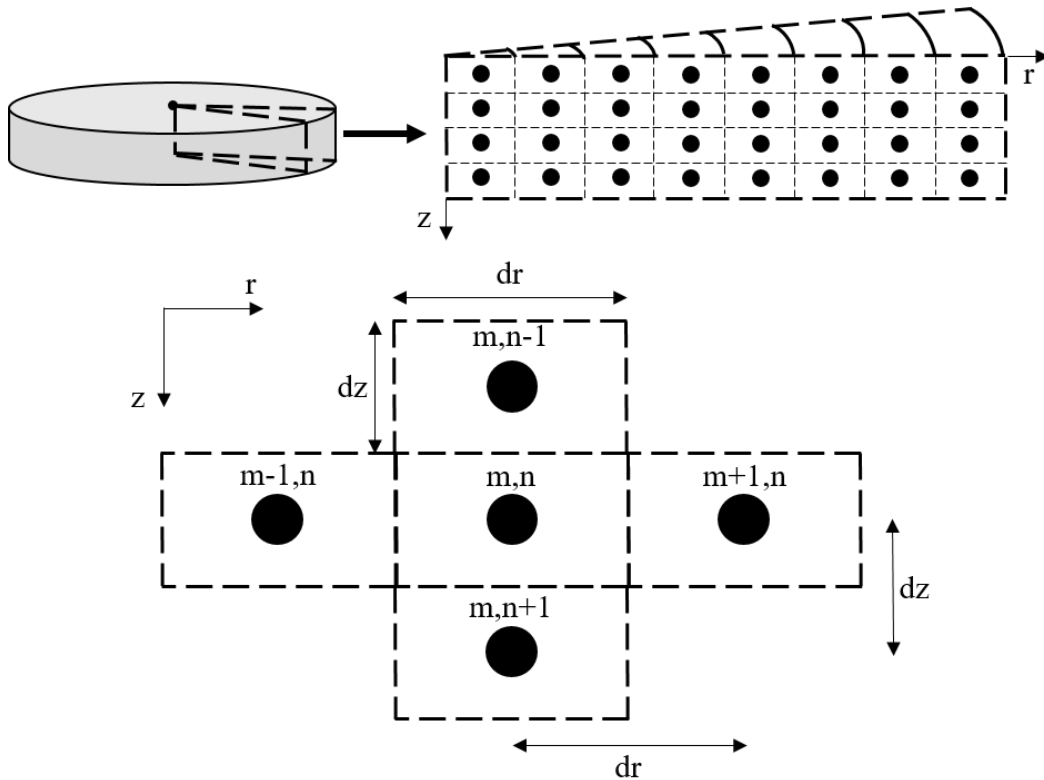
Figure 5–1: Nodal indexing in cylindrical coordinates

The mesh consists of 4 nodes through the sheet thickness and 30 across the part radius. As the workpiece thickness is 1.6mm and the radius is 30mm, the nodal spacings were 0.4mm and 1mm, respectively. Each CV is indexed by assigning an *m* and *n* value, whereby the first term is the mth node in the *r*-direction and the second term is the nth node in the *z*-direction. A timestep of 0.58ms was less than the required 0.64ms timestep needed to satisfy the stability criteria based upon the Fourier number.

Although the 2D assumption reduces the system to a planar representation in which the dr and dz terms are constant, the CVs increase in size further away from the z-axis due to the $rd\theta$ and $(r + dr)d\theta$ terms used to describe the CV geometry, Figure 5–2. The model accounts for this by establishing surface area equations for the 4 different surfaces along with the radial dependence for each individual CV; as can be seen in Equations 18–21.
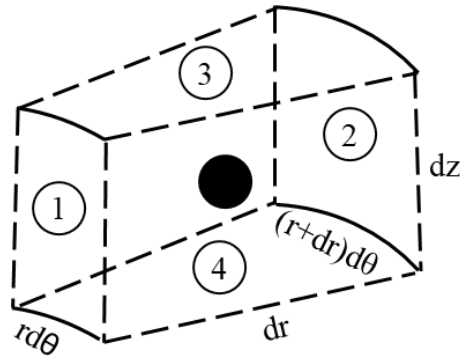
Figure 5–2: Individual CV with indexed surfaces

$$SA1(m) = (m - 1)drd\theta dz \tag{18}$$

$$SA2(m) = mdrd\theta dz \tag{19}$$

$$SA3(m) = SA4(m) = \left(mdr - \frac{dr}{2} \right) drd\theta \tag{20}$$

$$Vol(m) = \left(mdr - \frac{dr}{2}\right) dr d\theta dz \qquad (21)$$

Insulated boundary conditions were placed on the bottom surface and edges of the workpiece as experiments were conducted in a low-conductive thermoplastic fixture. The top surface had a convective boundary condition with a convection coefficient of 22W/m²K. The temperature of each CV was calculated through an energy balance influenced by the heat flow across surfaces 1 through 4.

The process mechanics influence how the temperature is modeled as while the screw is axially traversing, the diameter is also increasing until the screw's major diameter of 5mm is reached; leading to both a moving heat source and deletion of nodes that began as aluminum. Those nodes within 2.5mm of the workpiece centerline will have varying boundary conditions at surface areas 1 and 3, before eventually being deleted by the penetrating screw.

The distribution of heat generated at the interface, either by frictional sliding or shear deformation, was calculated based upon the effusivity of the two materials; with the fraction of heat transferred to the workpiece determined through Equation 22. Implementation of the material properties listed in Table 5–1, lead to 88% being transferred to the workpiece and 12% to the screw.

$$Q_{wp} = \left(\frac{\sqrt{\rho c k_{wp}}}{\sqrt{\rho c k_{screw}} + \sqrt{\rho c k_{wp}}}\right) Q_{Inter} \qquad (22)$$

Table 5–1: Screw and workpiece material properties

Part	Material	Density [kg/m³]	Specific Heat [J/kgK]	Thermal Conductivity [W/mK]
Screw	Steel	7800	475	36
Workpiece	Aluminum	2700	896	167

The interfacial heat source term acting on each CV is determined from the contact condition between the rotating screw and stationary workpiece; with heat generation occurring due to frictional sliding (slipping condition) or shear deformation (sticking condition). Without an understanding to which condition is present, accurate temperature modeling is unattainable as each mechanism generates heat in a different manner and to a different degree. A slipping condition is characterized by asperity collision of the two surfaces, with the heat generation rate being a result of frictional sliding, given by Equation 23. A sticking condition is characterized by yielding of the workpiece, with the heat generation rate being a result of shear deformation, given by Equation 24. Terms in these equations include: efficiency of mechanical work to heat (η), given as 0.95; normal pressure between the screw and workpiece (P_N); friction coefficient (μ); inelastic heat fraction (β), given as 0.9; flow/yield stress of the workpiece (τ_y); surface velocity (ω); instantaneous screw radius (r); and the differential contact area between the screw and workpiece (dA).

$$\frac{dQ_{friction}}{dt} = \eta P_N \mu \omega r dA \tag{23}$$

$$\frac{dQ_{deform}}{dt} = \beta \tau_y \omega r dA \tag{24}$$

The next section outlines how observations and calculations lead to determination of the interfacial contact condition for implementation in a combined thermos-mechanical model used to predict torque and temperature.

5.2. Torque Modeling Approach

Slip-Stick Contact Relations

Defining which contact condition is present between the rotating tool and stationary workpiece is vital towards accurate torque and temperature predictions. As FDS is a coupled thermo-

mechanical process, selection towards contact condition will influence the heat generation mechanism, which in turn will influence the mechanics of the subsequent contact condition. Two possible contact conditions can occur at this screw-workpiece interface: slipping or sticking. Determining which contact condition is present is dependent upon the relation between the normal pressure, friction coefficient, and shear yield strength of the material. The relations defining these two conditions are presented in Table 5–2.

Table 5–2: Contact condition relations

Contact Condition	Interaction Criteria	Contact Shear Stress	Heat Generation Mechanism	Plastic Deformation
slipping	$P_N \mu < \tau_y$	$\tau_{contact} = P_N \mu$	frictional sliding	no
sticking	$P_N \mu > \tau_y$	$\tau_{contact} = \tau_y$	shear deformation	yes

The difficulty in determining whether the contact condition is one of slipping or sticking is owed to the accepted inability to calculate friction coefficient. If the interfacial friction coefficient could be calculated, then knowing whether the normal pressure multiplied by the friction coefficient exceeded the shear stress of the material would be a simpler task. As there still exists a lack of knowledge towards accurate determination of friction coefficients, observations and measurements from the 'stepped' samples were used to justify the presence of instantaneous contact conditions.

Torque Oscillations

Periodic oscillations in the experimental torque data were observed during the heating, penetration, and extrusion forming steps, Figure 5–3. A frequency analysis was performed to determine whether these torque spikes were due to the presence of noise or due to the actual process mechanics. The process rotational speed was set at 5000RPM which converts to a component frequency of 83.3Hz; given that the data sampling rate was 1000Hz, which satisfies the Nyquist criterion, the 83.3Hz oscillations were confirmed to be from the process itself.
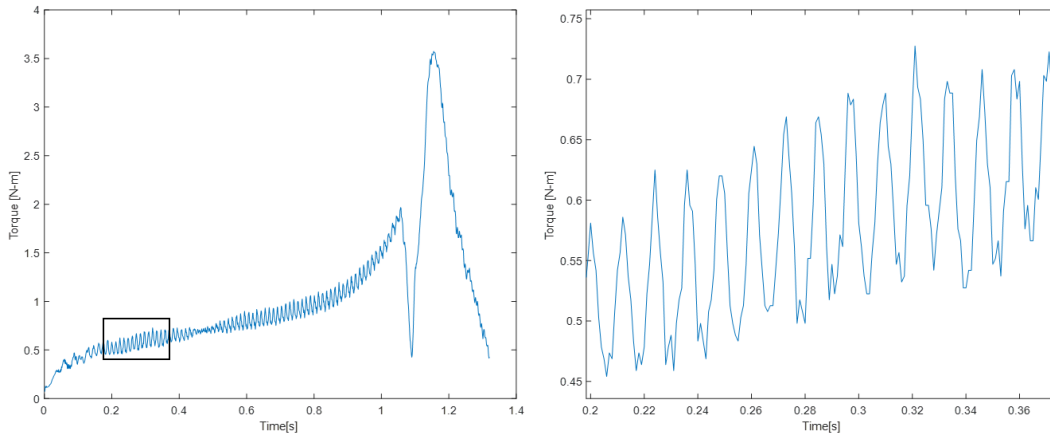
Figure 5–3: Periodic torque oscillations

Similar torque oscillations have been observed in oil and gas drilling [85,86], along with FSW [87] which were later determined to be from the relative slip-stick motion between the drill and bore hole Figure 5–4. These torque oscillations along with the those previously discussed microstructural observations give evidence towards a process that exhibits both a slipping and sticking contact condition.
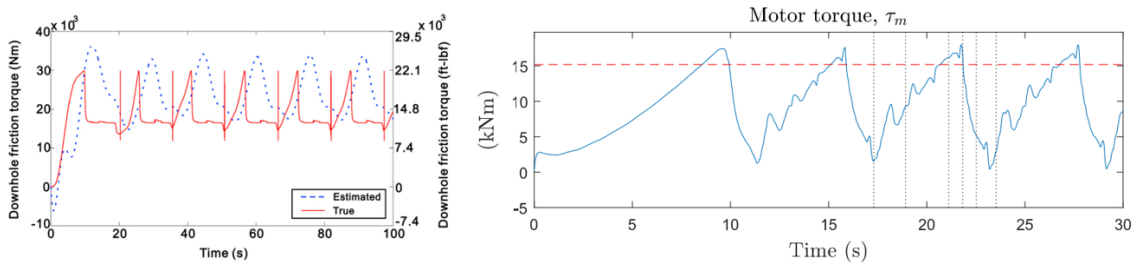
Figure 5–4: Observed slip-stick oscillations from Hong [85] and Aarsnes [86]

The torque spikes in Figure 5–3 have a frequency of 83.3Hz, which is equivalent to a single revolution during a 5000RPM process rotational speed. The rise from min to max torque during this single revolution took 0.04s, i.e. 1/3 of a revolution. Observations of the screw tip will show an angular dependence on the type of tool-face geometry, with 2 "flat" faces and 4 "cutting" faces apparent, Figure 5–5. Measurements of these individual faces showed that the surface area of two cutting faces equated to 1/3 of the total surface area; explaining the rise in torque during these

oscillations. The geometry of the flat faces was translated to be the surface areas under a slipping condition while the cutting faces were translated to that of the sticking condition.
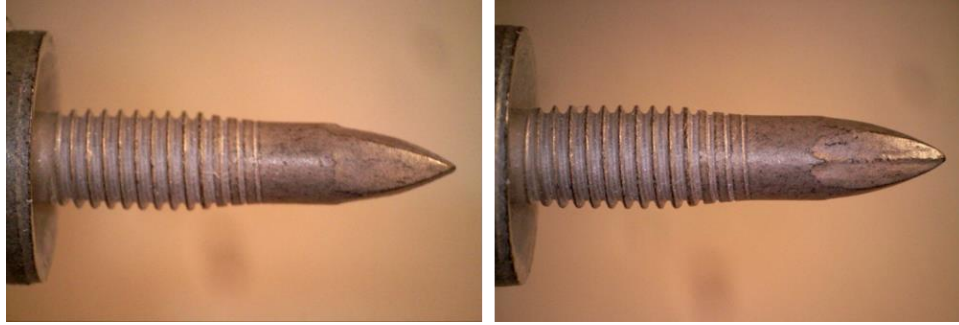
Figure 5–5: Screw tip flat face (left) and cutting face (right)

Once the thread-forming step begins, the contact area between the screw and workpiece is described using the thread with and length geometry; given by Equations 25-28 [88]. Terms in these equations include: the major (r_{major}) and minor (r_{minor}) radii of the screw; the screw thread angle (β), 60deg for an M5 screw; the average thread radius (r_{mean}); the screw pitch (p), 0.8mm for an M5 screw; the CV thickness (dz); and the screw lead ($lead$), 0.8mm for an M5 screw.

$$w_{thread} = (r_{major} - r_{minor})\sqrt{1 + \tan^2\frac{\beta}{2}} \tag{25}$$

$$\delta l_{thread} = \sqrt{r_{mean}^2 + \left(\frac{p}{2\pi}\right)^2} \, 2\pi \frac{dz}{lead} \tag{26}$$

$$r_{mean} = \frac{r_{major} + r_{minor}}{2} \tag{27}$$

$$CA_{thread} = w_{thread}\,\delta l_{thread} \tag{28}$$

87

Normal Pressure

The controllable process parameter of force (F), along with the screw geometry, were used together to determine the normal pressure term in the contact condition criteria equations listed in Table 5–2. Calculation of the normal pressure term was made under the assumption of a uniform pressure distribution. The initial normal pressure term was calculated from Equation 29, where (r_{max}) is the maximum instantaneous radius (i.e. the radius of the screw at the top surface of the workpiece), and (r_{min}) is the minimum instantaneous radius (i.e. the radius of the screw at the bottom surface of the workpiece). Once the screw threads contacted the top of the workpiece, the normal pressure term was then calculated using Equations 30 and 31, where (n) denotes the instantaneous number of threads engaged with the workpiece.

$$P_N = \frac{F}{\pi(r_{max}^2 - r_{min}^2)} \tag{29}$$

$$P_{N,threads} = \frac{F/\cos\frac{\beta}{2}}{A_{proj}n} \tag{30}$$

$$A_{proj} = \pi(r_{major}^2 - r_{minor}^2) \tag{31}$$

Flow Stress Material Model

The Johnson Cook plasticity model was used to describe the workpiece flow/yield stress behavior. It is an empirical-based relation consisting of a strain-hardening term, a strain-rate term, and a thermal-softening term; Equation 32. As the interaction between the screw and workpiece is primarily shear dominated, the JC model is translated into the shear yield stress through Equation 33.

$$\sigma_y = \left[A + B\varepsilon_{pl}^n\right]\left[1 + Cln\left(\frac{\dot{\varepsilon}}{\dot{\varepsilon}_0}\right)\right][1 - T^{*m}] \tag{32}$$

$$T^{*m} = \frac{(T - T_{room})}{(T_{melt} - T_{room})}$$

$$\tau_y = \frac{\sigma_y}{\sqrt{3}} \tag{33}$$

Elevated temperature tests were conducted to validate the A, B, n, and m parameters for the as-received material; due to the strain-rate insensitivity of aluminum the C parameter was disregarded from the equation. Samples were created from the same batch of 1.6mm 6061-T6 material used previously, with the specimen geometry shown in Figure 5–6. Samples were tested at 23°C, 100°C, and 200°C at a constant strain rate of 0.005/s; 3 replications were performed for each temperature. The parameters selected for use in the model are shown in Table 5–3, with the model showing good agreement with the experimental curves, Figure 5–7.
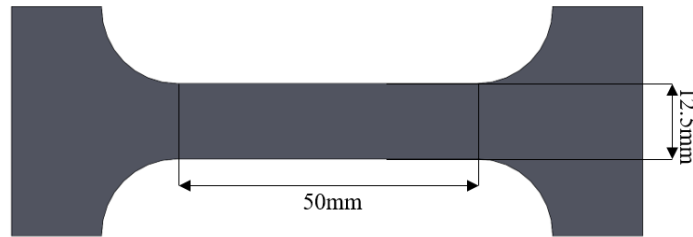
Figure 5–6: JC specimen geometry
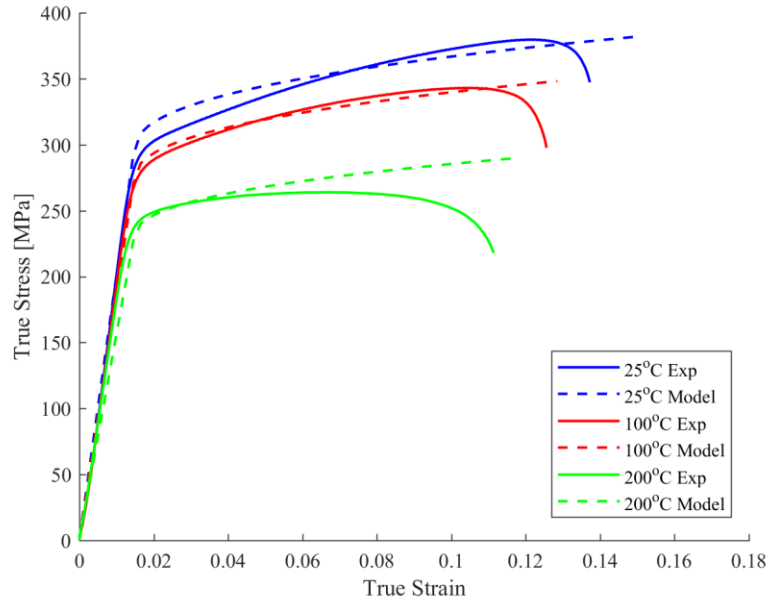
Figure 5–7: Plasticity model vs experimental at elevated temperatures

Table 5–3: JC parameters

A [MPa]	B [MPa]	n	m	T_{melt} [K]	T_{room} [K]
292	200	0.4	1.3	855	298

The plastic strain at each radial distance is there tracked to how its plastic strain values vary throughout the process with a contour/checkered color plot of strain values showing how they change during the process. These values, which dictate the degree of plastic deformation (i.e. accumulated strain value for JC model) are inputted into the JC model for the shear deformation sticking condition.

5.3. Model Evaluation

The coupled torque-temperature model was run under the three possible contact conditions: fully sticking, fully slipping, and a combined slip-stick scenario. The workpiece used for experimental data comparison was a 1.6mm sheet of 6061-T6 with the process parameters listed in Table 4–1.

Fully Sticking Condition

A fully sticking condition assumes that the entire mechanics of the process entail plastic deformation; meaning that the contact shear stress between the screw and workpiece is that of the shear strength of the material. The model under a fully sticking condition was shown to greatly overestimate the torque, due to using the high shear strength values of the workpiece material as the contact shear stress term, as can be seen in Figure 5–8. The one exception to the model inaccuracy is during the thread-forming step of the process. A fully sticking condition can accurately model this step's rise in torque because thread-forming is known to be a plastic deformation process. Predicting temperature under a fully sticking condition also overestimates the temperature rise due to an increased heat source term owed by the overestimated torque, Figure 5–9.

The overestimate of the predicted values confirms why past researchers have incorporated a friction coefficient into their model to increase the accuracy, despite the wrongfulness of this methodology. Material shear strength and friction coefficient should not be coupled terms, but a lack of understanding during these types of frictional processes are lacking and researchers can cover up their "false statements" with a variable friction coefficient that coincides with developing accurate models; especially knowing that others cannot disprove their choice of unverifiable friction coefficients. In this scenario, adding a friction coefficient of around 0.3 would lower the total torque closer to the actual experimental values; with the past methodology seemingly deeming the model to be accurate.
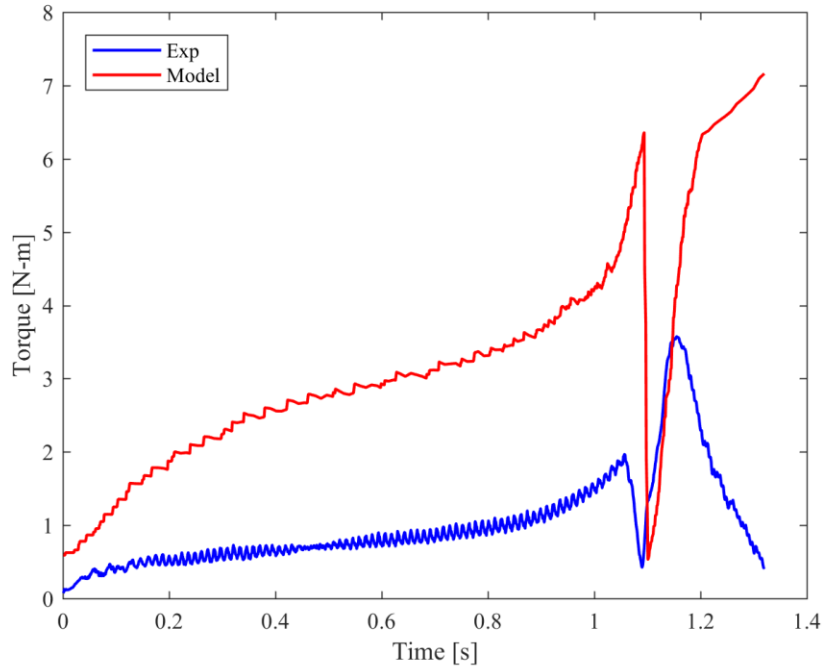
Figure 5–8: Torque prediction under fully sticking condition
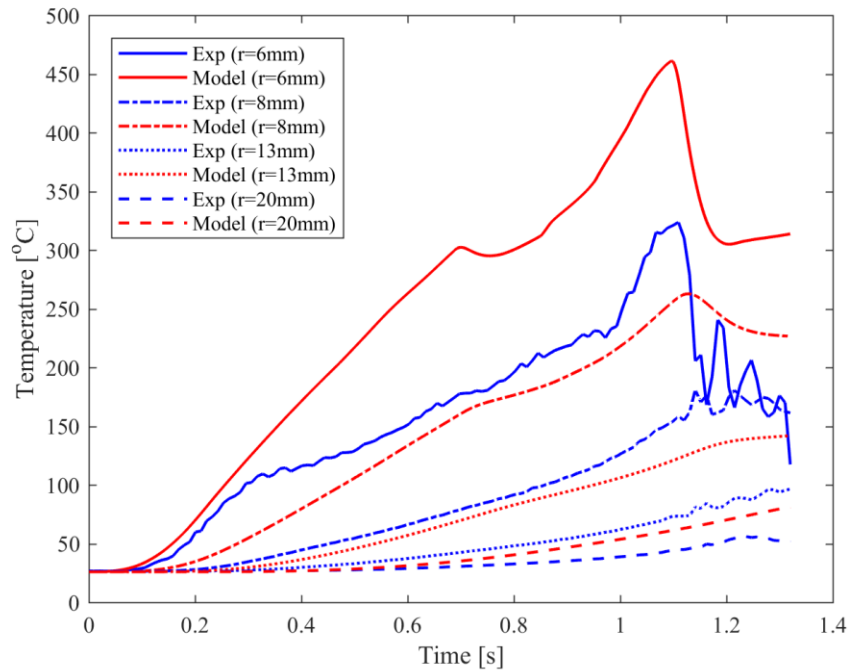
Figure 5–9: Temperature prediction under fully sticking condition

92

Fully Slipping Condition

   A contact condition of fully slipping is merely just not suitable for the FDS process. A full slipping condition signifies that absolutely no plastic deformation has occurred; which, from previous observations, has shown not to be true. If the process were to be modeled under this sole condition, the friction coefficient needed for accurate torque prediction was shown to be higher than what could be expected, Figure 5–10; with values starting at 0.7 and increasing close to 1.2. The values at the beginning and end of the process, do however, seem reasonable. At the beginning of the process, the force is low as the air pressure must be built up in the screwdriving machine cylinder, which is responsible for the force on the screw. Towards the end of the process, the plastic deformation ends once all the threads are formed and a solely slipping condition takes over. The friction coefficient values lower to 0.15, which is reasonably close to an expected 0.2 value for a zinc-flake coating. Once threads are formed and the screw is being driven down until head contact, a fully slipping condition is appropriate and accurate.
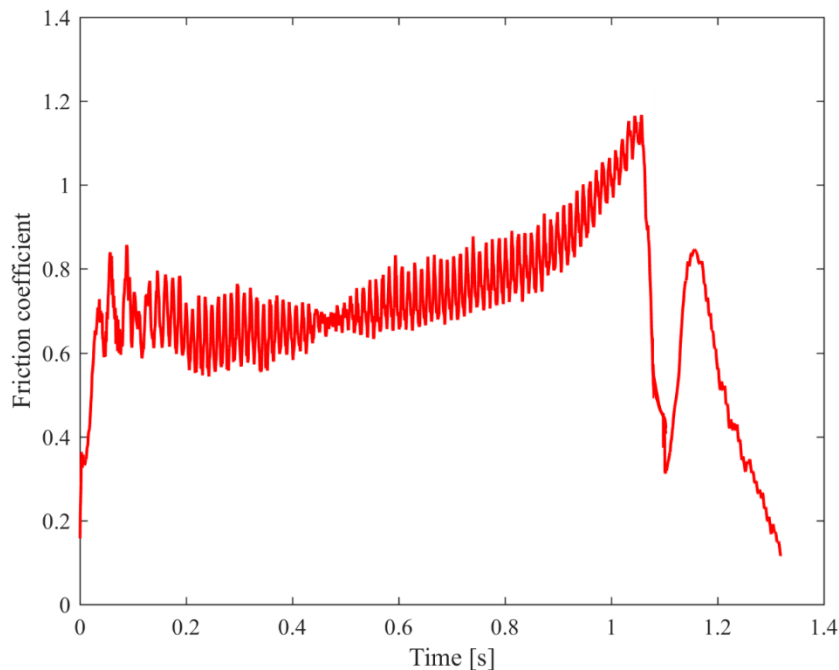
Figure 5–10: Friction coefficient needed to satisfy fully slipping condition

93

Combined Slip-Stick Condition (research contribution)

The combined slipping-sticking model uses the observations made throughout this research to incorporate both conditions for an understanding of torque and temperature contributions. It was shown that a fully sticking condition overpredicts the torque and provides evidence to why previous researchers have incorporated a friction coefficient into their model to lower the torque values. This approach is incorrect as friction coefficient and the material shear strength should be mutually exclusive. The fully slipping condition, on the other hand, was shown to under predict the torque and requires an exceedingly high friction coefficient to predict the correct torque values.

Due to the reasons above, the slipping and sticking contact conditions were incorporated within the same model to predict torque and temperature. Based on observations from the torque oscillations, the cutting faces were found to contribute to the sticking condition, while the flat faces contributed to the slipping. A fitting approach was used to determine the friction coefficient, at every step in the process. The instantaneous friction values were plotted against their corresponding process temperature, which created the curve shown in Figure 5–11. A similar trend can be observed with tool flank wear Figure 5–12, despite no observed damage to the screw. Tool wear occurs in three stages during traditional machining operations: initial, uniform, and accelerated [89]; with the tool-workpiece temperature noted to have a significant impact on the stage transitions.
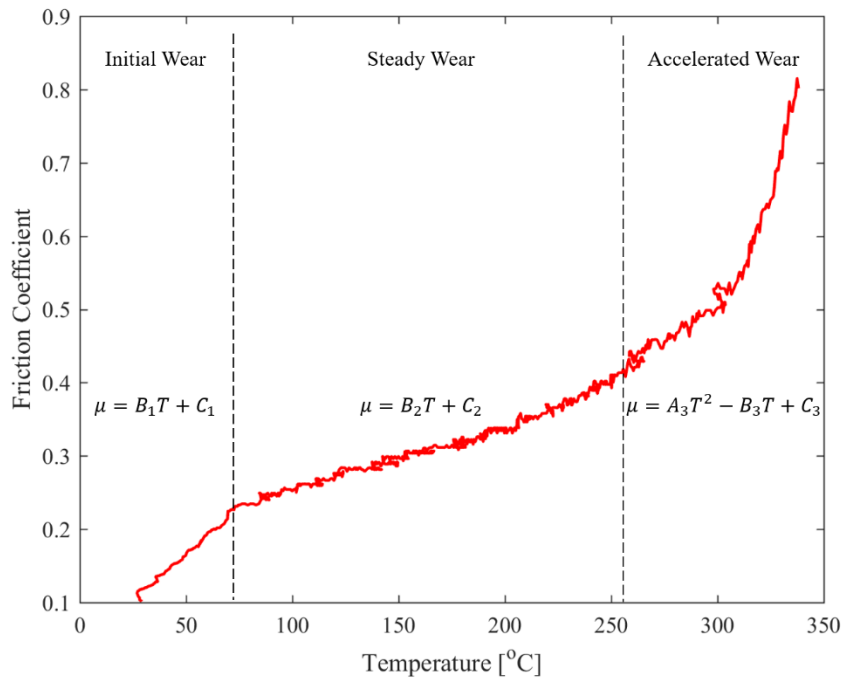
Figure 5–11: Piecewise temperature-dependent friction coefficient curve

The friction coefficient curve is divided into three regions: Initial Wear, Steady Wear, and Accelerated Wear, with equations $\mu = B_1 T + C_1$, $\mu = B_2 T + C_2$, and $\mu = A_3 T^2 - B_3 T + C_3$ respectively.
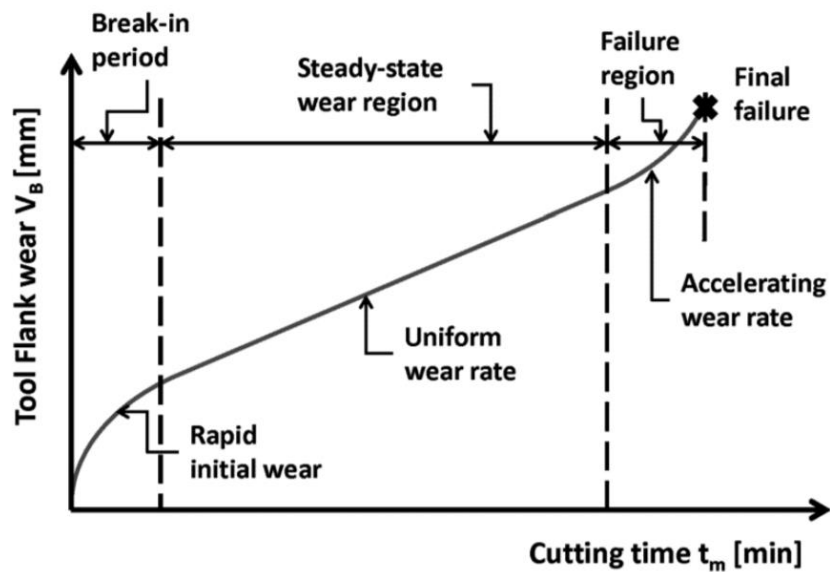
Figure 5–12: Time-dependent stages of tool flank wear [89]

One alternate reason behind the similar trends was the influence that the zinc-flake coating could have on the friction. The coating's primary function is to mitigate the possibility of corrosion between the dissimilar steel screw and aluminum workpiece materials. It does possess a secondary

benefit of increasing lubricity between these parts, which lowers friction and thus torque required by the screw for installation. Typical reported friction coefficients for steel on aluminum are around 0.65, but keep in mind that this value is for bare steel on bare aluminum; the presence of the zinc will alter that value. The friction coefficient between zinc-coated steel and aluminum is approximately 0.15, however this value was measured from installation into parts at room temperature.

Temperatures during FDS have measured over 300°C, with reports indicating that zinc coating will disband itself from steel when exposed to temperatures above 250°C. Coupled with these temperature effects is the added relative motion between the steel and aluminum that causes some of the zinc coating to be removed as the screw passes through the workpiece, as evident by Figure 5–13. The coating thickness has shown to influence the apparent friction coefficient with a 27% decrease in coating thickness increasing the friction coefficient by 19% [90]. As the tribology of transient coating removal is not well understood, relationships were established based upon the common trend in time-dependent tool wear in traditional machining operations were taken.
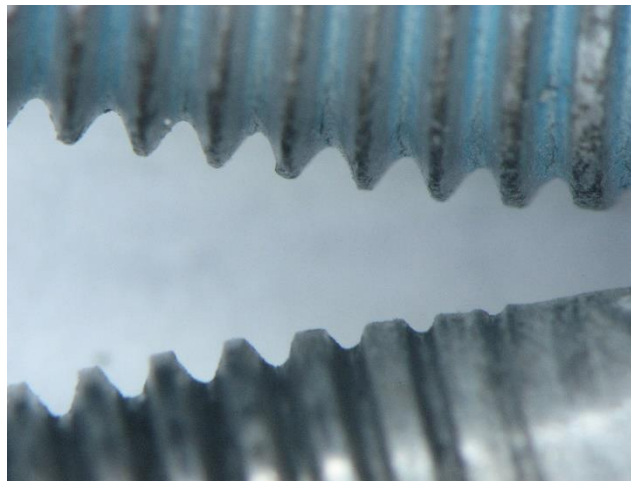
Figure 5–13: Reduction in coating between before (top) and after (bottom) installation

A rapid rise in the friction coefficient is observed during the initial phase as during this part of the process, the fastener is barely displacing and thus the same screw area is being rotated against the workpiece causing a rapid decrease in that area's coating thickness. Once the temperature starts to rise, the screw can axially progress through the workpiece and a steady coating removal is observed. Although temperature is increasing linearly, the rate at which coating is being removed near the screw tip is the same at which the screw surface area with full-spec coating thickness is entering the workpiece. The third region exhibits an exponential trend due to process temperatures exceeding 250°C; the temperature at which zinc will begin to detach itself from the steel and therefore coating wear is accelerated. The agreement between trends of tool wear and friction coefficients confirm that temperature-dependent coating removal is the primary cause of transient friction coefficients during FDS, and thus equations were developed to describe the process friction coefficient for the three coating wear phases with their constants listed in Table 5–4.

Table 5–4: Friction equation constants

Wear Phase	Constants						
	B_1	C_1	B_2	C_2	A_3	B_3	C_3
Initial	2.6×10^{-3}	3.8×10^{-2}					
Steady			9.0×10^{-4}	1.6×10^{-1}			
Accelerated					7.0×10^{-5}	3.7×10^{-2}	5.4×10^{0}
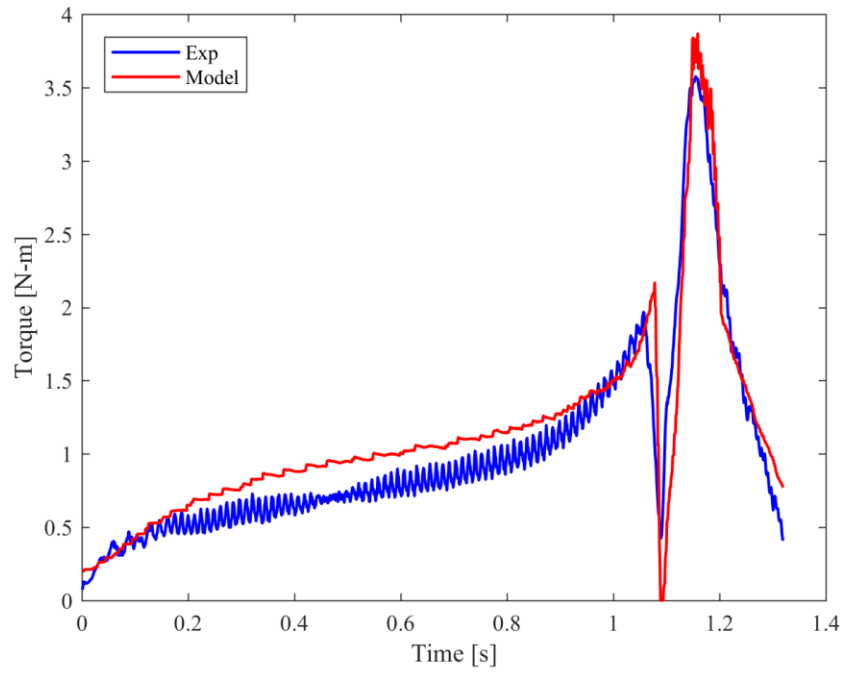
Figure 5–14: Torque prediction under combined slip-stick condition
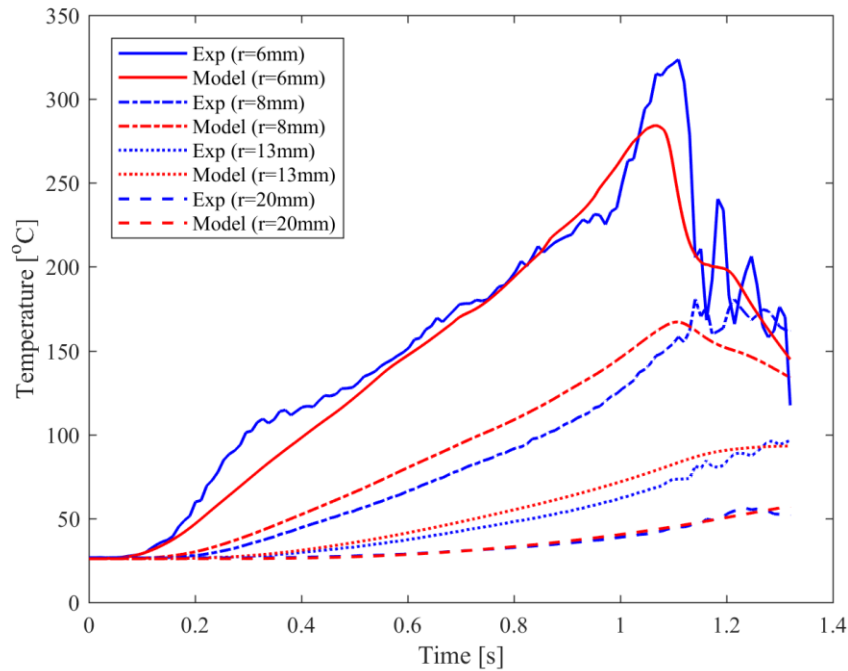
Figure 5–15: Temperature prediction under combined slip-stick condition

Testing Model Robustness

The model was run against two alternative data sets in which the parameters and/or the sheet thickness were varied from the original data set 1. All data sets are listed in Table 5–5 for comparison.

Table 5–5: Process parameters used for model validation

Data Set	Sheet Thickness [mm]	Drilling Speed [RPM]	Drilling Force [N]	Thread-Forming & Screwdriving Speed [RPM]	Thread-Forming & Screwdriving Force [N]
1	1.6	5000	600	2500	400
2	1.6	5000	750	2500	500
3	2.5	5000	1300	2500	700

The drilling and screwdriving forces were increased for data set 2, with a 25% increase in drilling force reducing the process time by almost 50%. The model was run under the exact same conditions as those in data set 1, with the only difference being updating the screw rotational and axial displacement for this data set. Conducting the model under the same conditions as data set 1 shows good agreement to the measured experimental values, Figure 5–16. The underprediction of the installation torque is likely due to the 3.5 maximum strain value imparted on the model. Increased strain values are expected to be because of the larger process forces and why a slight underprediction exists. Temperature predictions also showed good agreement to the experimentally measured ones, Figure 5–17. An underprediction is evident at 0.55 seconds, which coincides with the underprediction of torque at the same part of the process.
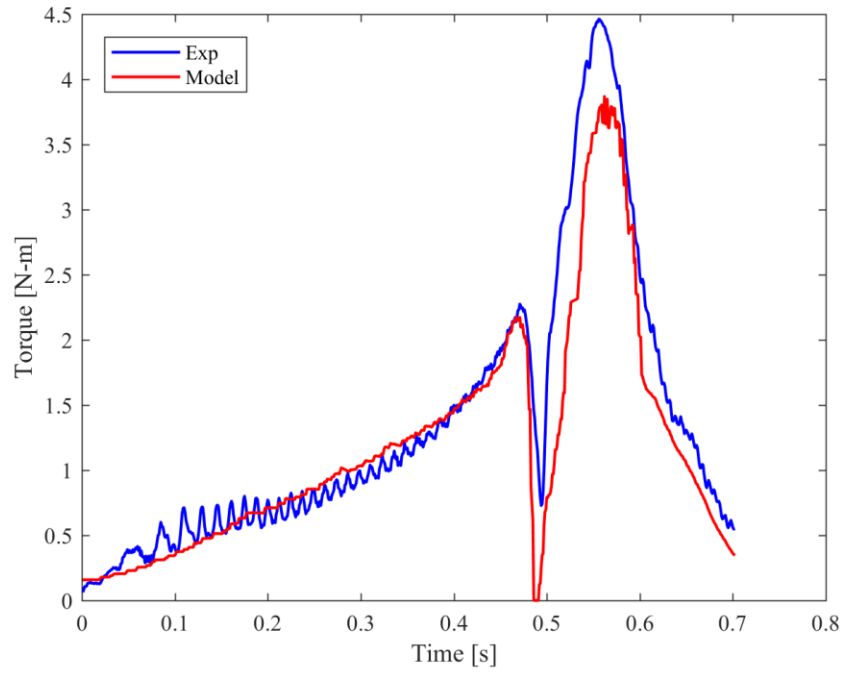
Figure 5–16: Data set 2 torque prediction
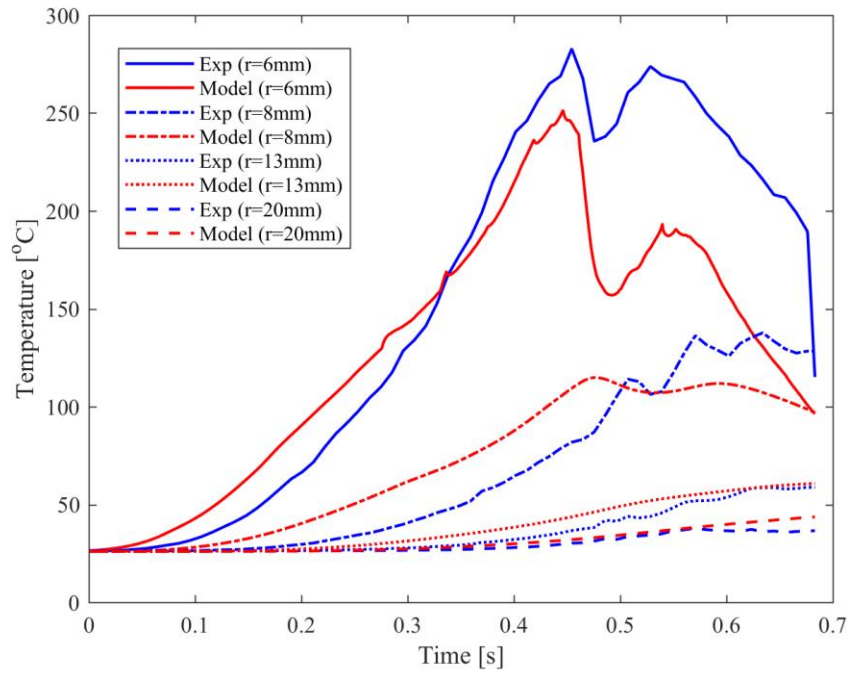
Figure 5–17: Data set 2 temperature prediction

100

The last data set used to measure the model robustness was from FDS of a 2.5mm sheet of 6061-T6. The drilling force parameter was increased to 1300N to penetrate the far thicker sheet. Once again, the model and experimental values showed good agreement for both torque, Figure 5–18, and temperature, Figure 5–19, predictions. A temperature prediction inaccuracy is observed after 0.7 seconds for the measurement taken at 5mm from the center. This was due to a sudden shift in the relative position between the workpiece and thermal camera caused by the dynamic effect of the process spindle.
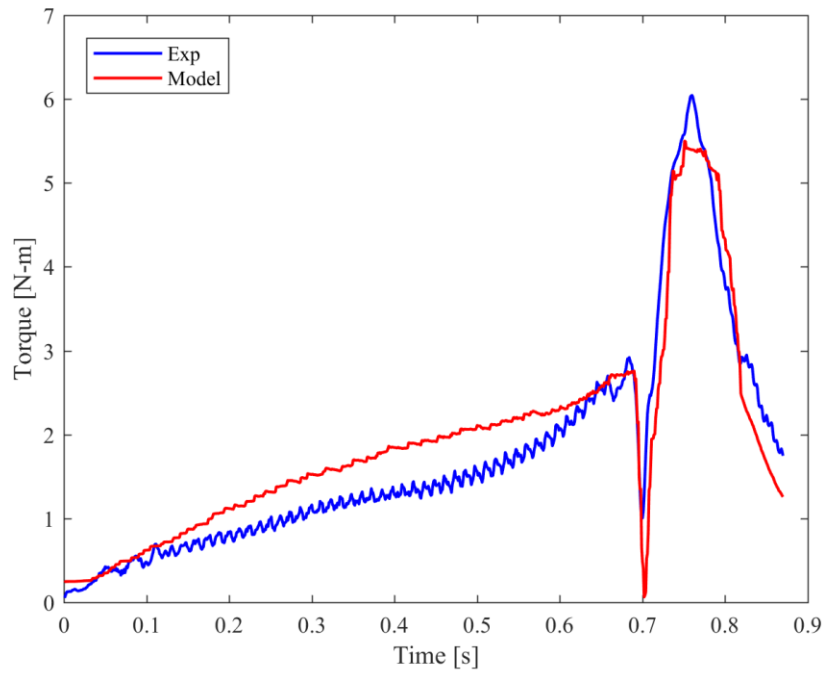
Figure 5–18: Data set 3 torque prediction
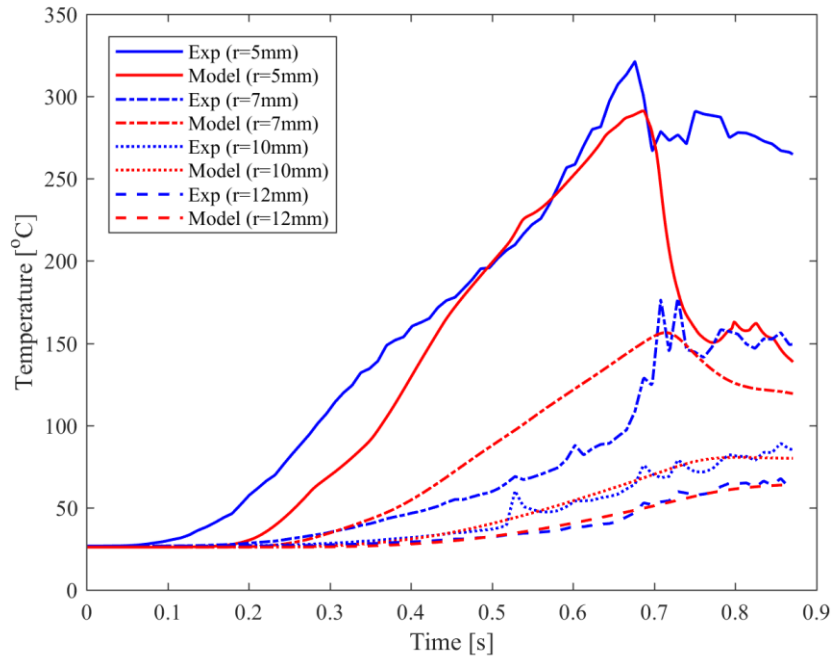
Figure 5–19: Data set 3 temperature prediction

6. THERMALLY-ASSISTED FLOW DRILL SCREWING

6.1. Background in Thermally-Assisted Processes

The current limitation with FDS occurs with the imposed 8.3N-m maximum installation torque standardized for M5 self-tapping screws. Warm forming of aluminum has been shown to increase ductility and formability of the material and thus a reduction in installation torque is sought after along with an expected decrease in process time. In this section, workpieces were heated to different temperatures to study how this pre-heat temperature would influence process time, installation torque, cross-sectional geometry, microhardness, and joint strength.

A study on the friction drilling of cast metals by Miller [9] showed a reduction in thrust force and torque for workpiece pre-heating temperatures ranging from 25 °C to 300 °C of Al380. The benefits presented by this cast metal study prompted investigation into the pre-heating of material to affect a reduction in installation torque to open the design space for the joining of thicker, stronger materials.

Research in warm (200-350°C) forming of aluminum alloys has shown a benefit toward increasing the material formability [91,92]. In processes that involve both thermal and mechanical aspects, researchers are motivated to introduce external heating to the process to increase material ductility. This increased ductility brought on by an increased material temperature influences material flow between the sheets. In a feasibility study in this area, an increase in the maximum draw height with increasing die temperature was discovered during warm aluminum drawing [93]. The study conducted by Bolt can be related to FDS through the extrusion forming step whereby the bottom material is drawn out to increase thread engagement area. When heated to 250°C, the height of a conical stretched-drawn product increased by 65% compared to that of a similar product at 20°C. It is essential to understand and utilize the effect of these elevated temperatures on the

mechanical properties of the material after the forming process. This validation will be carried out through post-forming microhardness measurements and mechanical joint strength tests.

Research in the post warm-forming mechanical properties of AA7075 [94] showed that when forming temperature is between 220°C and 260°C, the yield strength decreases by 10-14% and hardness decreases by 8-9% as compared with the as-received material. When temperatures reached 300°C, the yield strength and hardness dropped 44% and 27%, respectively.

Similar warm forming research topics were carried out by Li and Ghosh with their uniaxial [95] and biaxial [96] warm forming research on aluminum alloys. In their uniaxial tensile deformation study, they showed an increase in elongation with an increase in temperature and a decrease in elongation with an increase in strain rate. Strain rate during Li and Ghosh's study is related to the axial force through the screw during the FDS process, whereby the engineer can control how quickly the screw is installed into the material stackup. A lower axial force would allow greater elongation and thus a larger extrusion (drawn material from bottom sheet) for thread forming. However, this would not only increase process time but also increase forming temperature, which can lower the post-forming mechanical properties of the joint. In Li and Ghosh's biaxial tensile deformation study, they implemented a punch-die experimental setup where they discovered similar results in terms of a reduced yield strength but higher elongation percentage for high forming temperatures.

Steps 1-3 of the FDS process amount to approximately 73% of the total process time and therefore has the largest potential for time reduction, Figure 6–1. Through the literature review of friction drilling and warm forming, it was expected that as the workpiece material pre-heat temperature increased, both the process time and installation torque would decrease.
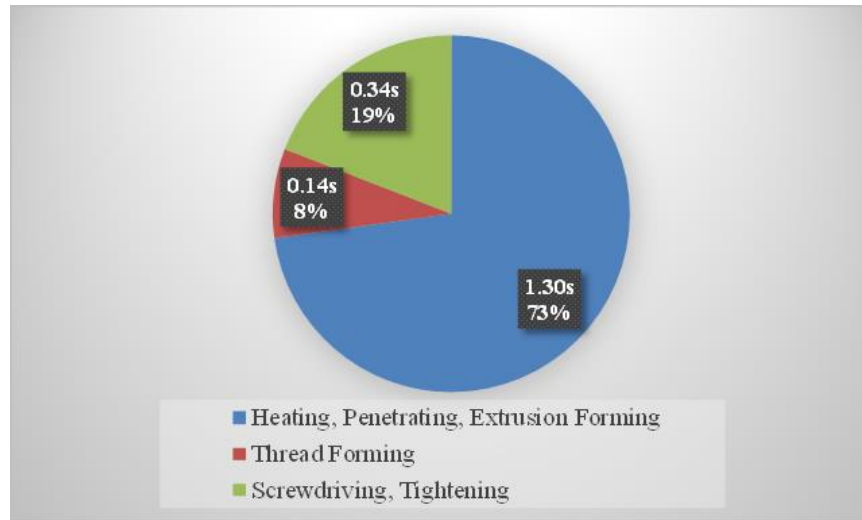
Figure 6–1: Process step times

6.2. Experimental Design and Setup

Experiments were conducted on 2T stackups of 3.4mm Al6063-T5 specimens; pre-heated to two temperatures with a room temperature sample utilized as a baseline, Table 6–1. A 200W capacity conduction ring heater was built into a fiberglass-reinforced thermoset support frame. The conduction ring was positioned to ensure the screw would be installed within the inner diameter opening while the frame insulated the heat. A 130V variable transformer was included into the experimental setup to power the conduction ring.

Table 6–1: Thermally assisted test matrix

Pre-Heat Temp [°C]	Drilling Speed [RPM]	Drilling Force [N]	Tightening Torque [N-m]
23			
143	6000	1650	10
247			

Due to the joining of the two sheets during the process, a thermocouple was not able to be placed between the sheets to avoid any conflict with material flow. A thermocouple, therefore, was placed on the top surface approximately 12mm from where the outside diameter of the screw head

would be, to eliminate any conflict between the thermocouple and the downholder. Although the reading from the thermocouple would be a slight misrepresentation of the temperature at the installation point (due to high thermal conductivity), the location was consistent throughout all experiments and thus can be used as a distinguishable measurement value for the three temperature data sets. The downholder displaces downwards towards the top surface of the top sheet and registers that as the 'zero-point' for the distance-controlled process. During the process, the downholder applies a force of 280N to reduce sheet separation. An additional thermocouple was placed between the bottom material and the ring heater to monitor heat source temperature *Figure 6–2*. The average material temperature was calculated through an average of the two thermocouple readings.
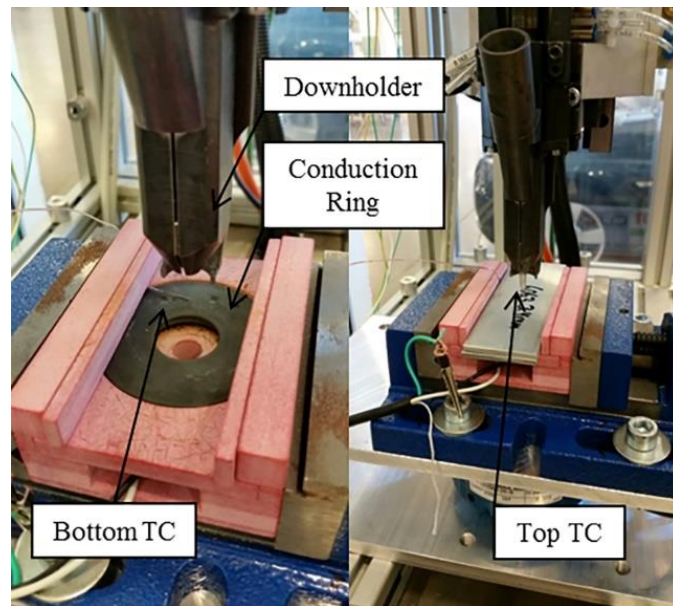
Figure 6–2: TA experimental setup

The two-material stackup was placed in a fiberglass-reinforced thermoset support frame and heated to an average temperature of 23°C, 143°C, and 247°C. The three temperatures were chosen based on the 250°C limiting operating temperature of the fiberglass polymer, a room temperature baseline sample, and a mid-point between the two, 143°C. The variable transformer was then

switched on at a low voltage of ~40V (67W) with increasing increments until desired top surface temperature was reached. As the authors desired the top sheet and bottom sheet to rise in temperature simultaneously, the samples took approximately 30 minutes to reach the desired values. Once desired temperature was obtained, the conduction ring was switched off to stop material temperature rise, data sensors were initiated, and the test was run. For this study, the screw was installed at 6000RPM and an axial force of 1650N, the spindle speed was then lowered to 200RPM for the final tightening operation which was held at 10N-m for 1 second.

Implementation of conduction heating for mass production would be more viable if the conduction ring were attached to the equipment downholder (thus retaining the one-sided access). As the downholder contacts the workpiece material to determine the 'zero-point', the pre-heated conduction ring would be heating the material prior to screw installation. The authors decided to implement the conduction-ring in the support frame to eliminate any modifications to the equipment along with careful monitoring of workpiece temperature.

6.3. Joint Evaluation

Process Time
It is shown, Figure 6–3, that as the material pre-heat temperature increases, the process time decreases. As the material is thermally softened prior to installation, the screw can penetrate and form an extrusion more quickly due to a reduction in mechanical resistance of the material. When the average material temperature is 247°C, the screw installs 52% faster than an identical stackup at a room temperature of 23°C. Analyzing the change in process time for each step shows that a reduction in the heating, penetrating, and extrusion forming steps is the largest contributor to the overall decrease in process time, Figure 6–4; thus confirming and satisfying the goal of this study.

107
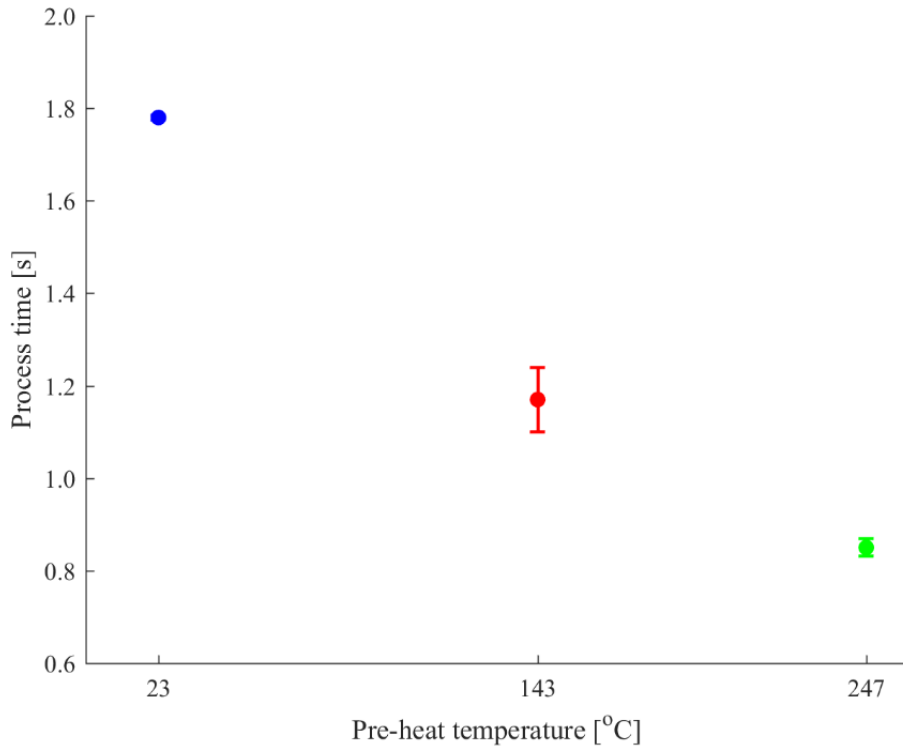
Figure 6–3: Effect of TA on process time
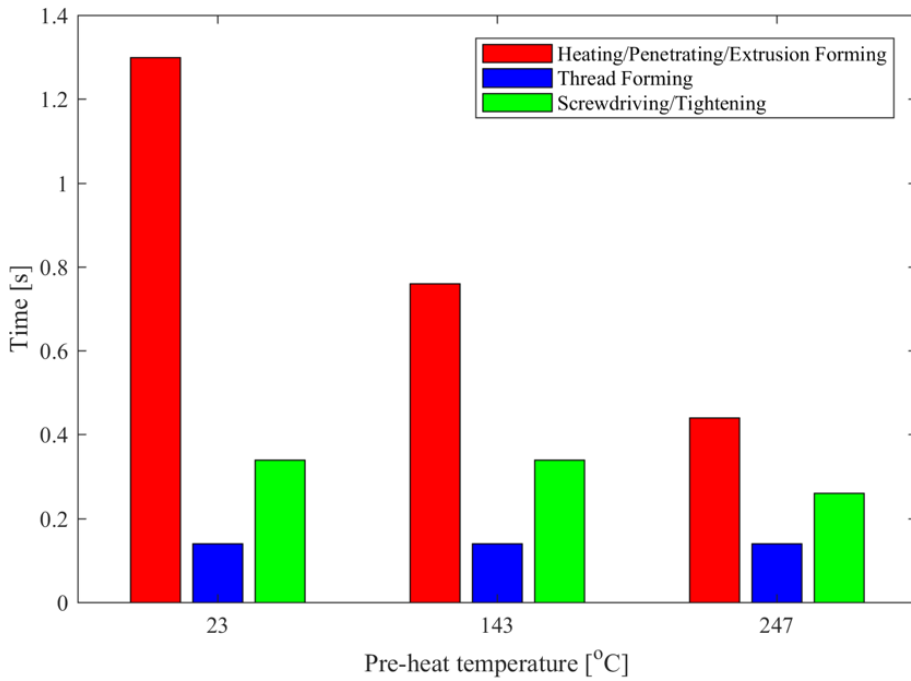
Figure 6–4: Effect of TA on individual process step times

Installation Torque

The torque-time curves were studied to determine any effect from pre-heating the material. It was observed that as the material pre-heat temperature increased, the required installation torque decreased, Figure 6–5. Compared to material that was not pre-heated, the maximum installation torque was reduced by 20% when the samples were heated to 247°C, Figure 6–6. Decreasing the installation torque is advantageous as it deviates further from the minimum breaking torque of the screw. Whereby the minimum breaking torque is the torque required to shear the screw head from the shaft. Although the minimum breaking torque of an M5 self-tapping screw is 8.3N-m, the screw can be tightened beyond this value due to the under-head friction occurring between the screw head and the top workpiece material. For this study, however, the tightening torque was kept constant at 10N-m based on sponsor specification.
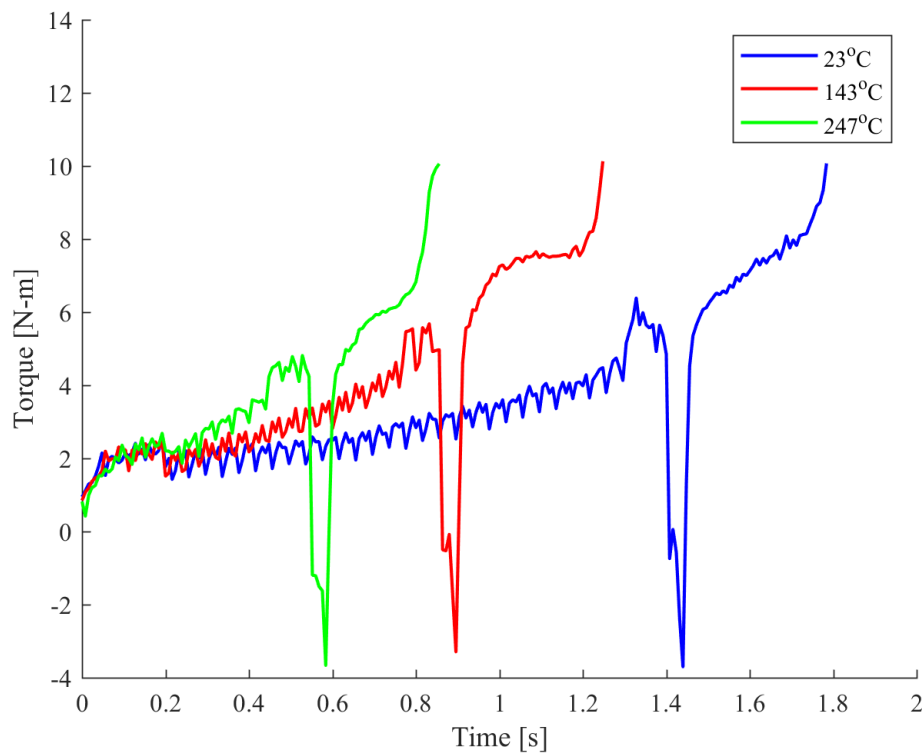
Figure 6–5: TA-FDS torque curves
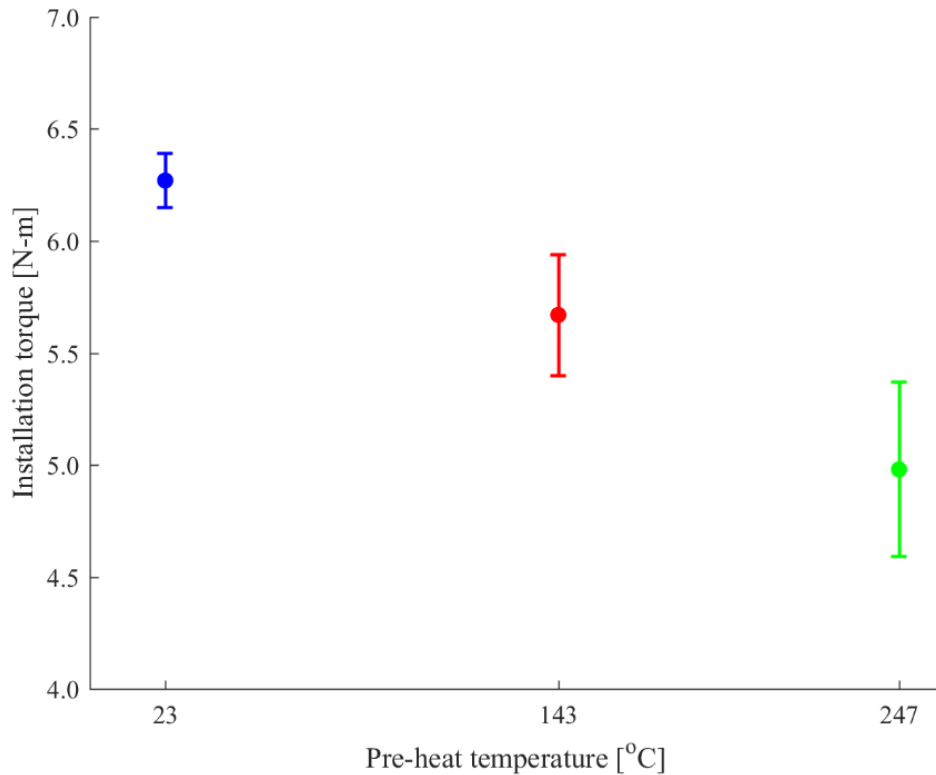
Figure 6–6: Effect of TA on installation torque

Despite the room temperature samples having only an installation torque of 6.2N-m (far below the 8.3N-m limit). The implementation of pre-heating a workpiece demonstrates its advantage of decreasing the installation torque. Not only does this reduce the risk of screw failure during installation but the maximum stackup thickness can be overcome with workpiece preheating.

Sheet Separation

Cross-sectional images were taken to measure the material sheet separation that occurs when joining thick stackups, Figure 6–7. As FDS is a forming operation and not a drilling operation, no material is removed from the stackup. The screw installation causes the top sheet material to flow downward and the bottom sheet material to flow upwards, this material flow forces the sheets apart. Equipment and screw manufacturers suggest implementing a pilot (or through) hole in the top sheet to allow the bottom sheet material a place to flow. However, this eliminates an advantage of FDS

where no hole alignment is necessary. The effect of thermal assistance on the sheet separation is studied to determine if this can aid in material flow and reduce or even eliminate this gap. To understand the effect of material temperature on sheet separation, the distance between the material sheets is measured at each material temperature, Figure 6–7. A distance measurement was taken on either side of the screw head and for each half sample cross-section, totaling four measurements per sample. As there were three replications, 12 data points were obtained for each temperature set. The average sheet separation for the 23°C, 143°C, and 247°C samples were 1.41mm, 1.45mm, and 1.25mm, respectively, Figure 6–8. There is an insignificant increase of separation distance from 23°C to 143°C shown on the boxplot, where the average values fall within the spread. Aside from measurement errors, variations in original sheet thickness also contribute to this slight increase, which indicates that from 23 to 143°C, there is no thermal contribution to reducing sheet separation. The 247°C samples had a slight sheet separation reduction of 11% due to the elevated temperature. As the temperature in the installation zone increases the viscosity of the material in this area decreases. This increase in formability allows the material to flow better which is shown through the larger horizontal displacement of those samples pre-heated to a higher temperature. It is possible to reduce the sheet separation through thermal assistance to the process but temperatures above 247°C may be required to reduce further.
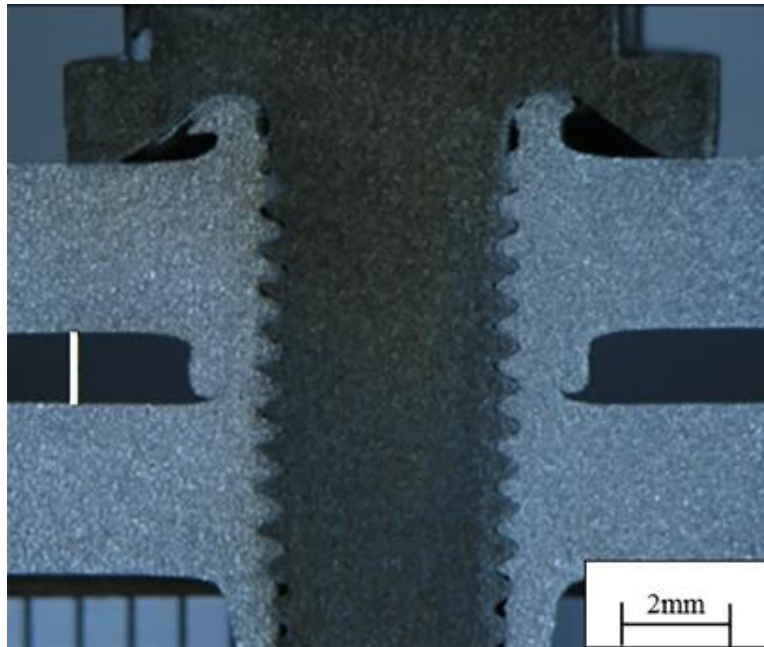
Figure 6–7: Measurement location for sheet separation
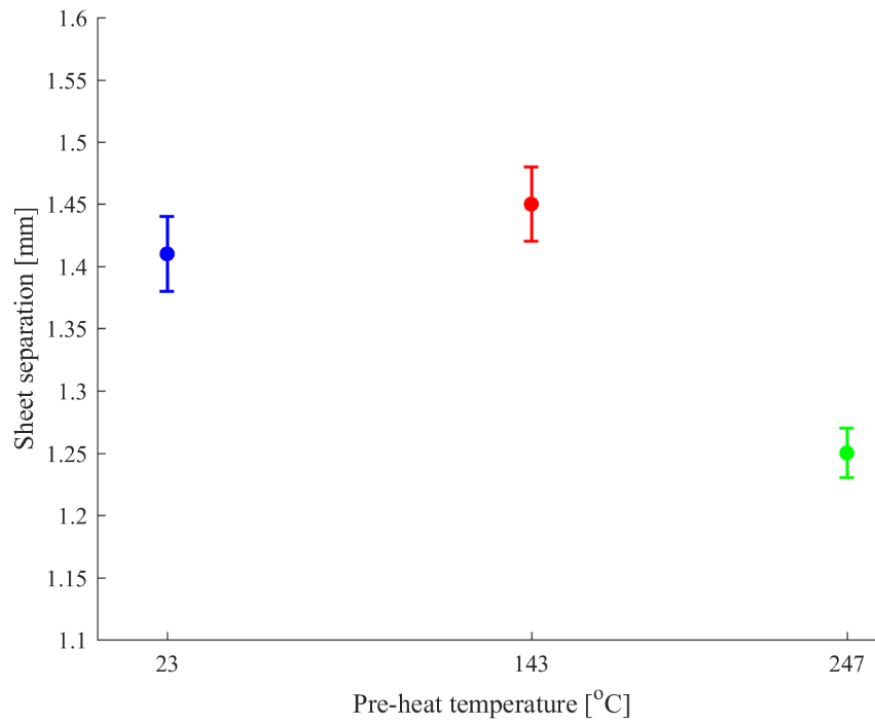
Figure 6–8: Effect of TA on sheet separation

Microhardness

Vickers material hardness tests were conducted on the 23°C, 143°C, and 247°C samples with measurements taken on the top, *Figure 6–9*, and bottom, *Figure 6–10*, sheets, spaced 1mm apart. The load applied during the Vickers tests was 100 grams with a dwell time of 15 seconds. 10 measurements were taken on each of the sides of the top and bottom sheets totaling 40 measurements per sample. The measurements were taken at the midpoint of each sheet, starting 0.76mm from the tip of the thread, with 1 mm between the indentations.

As the material had a T5 temper, the hardness tests confirmed that despite a high material pre-heat temperature of 247°C, this did not affect the hardness of the material away from the <2 mm heat-affected zone. Two notable observations were made from the microhardness tests: First, as the pre-heat temperature increases, the hardness values of the material located in the heat-affected zone decrease. These values decrease with increasing pre-heat temperature due to the additional thermal softening caused by the heat generation of the rotating screw. However, outside of the 2mm heat-affected zone, the three sets of materials at different temperatures produce the same hardness values because of the T5 heat treatment. Secondly, within the 2mm heat-affected zone, the hardness values of the top sheet are less than those of the bottom with exception for the 247°C samples. This observation confirms that the top sheet is exposed to higher temperatures than the bottom sheet as the "heating" step occurs primarily when the screw is in contact with the top sheet. The observed reduction in hardness values for the elevated temperature samples justified reason to evaluate the effect on the joint strength.
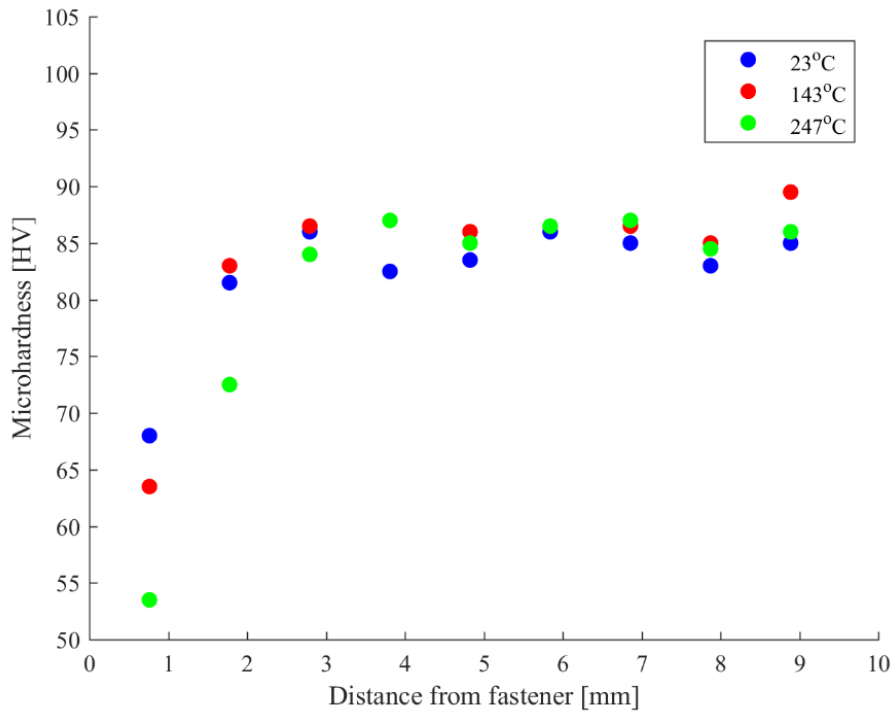
Figure 6–9: Top sheet microhardness
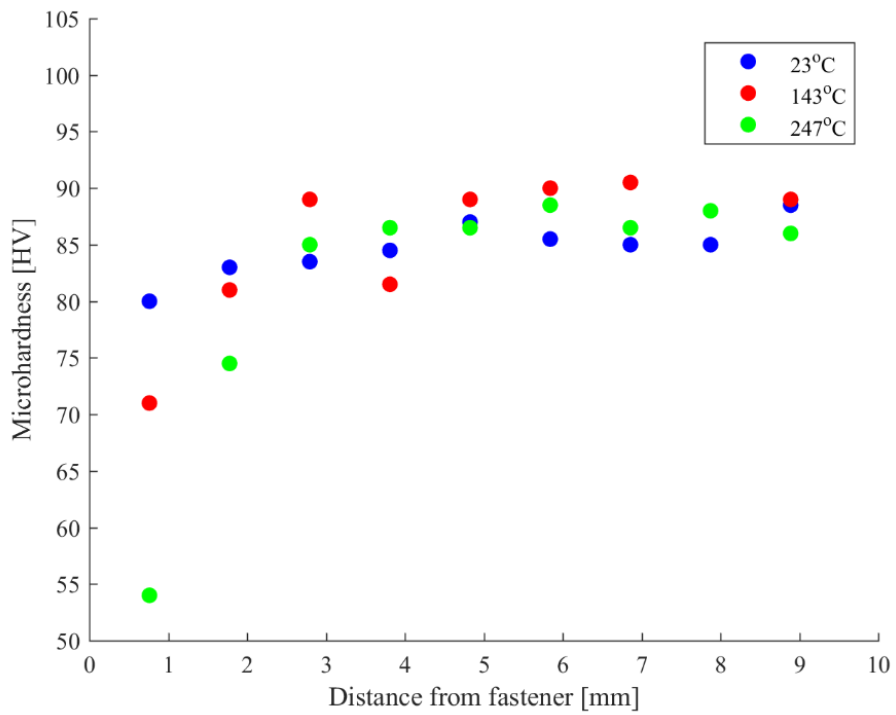
Figure 6–10: Bottom sheet microhardness

114

Breakloose Torque

Despite its uniqueness as a multi-material joining technology, FDS is still a screw and is therefore susceptible to loosening after installation; a metric to measure its post-joining secureness is the joints breakloose torque. A positive correlation is observed between a workpiece's pre-heat temperature and the torque required to loosen its screw; with no benefit limitation observed through 250°C.
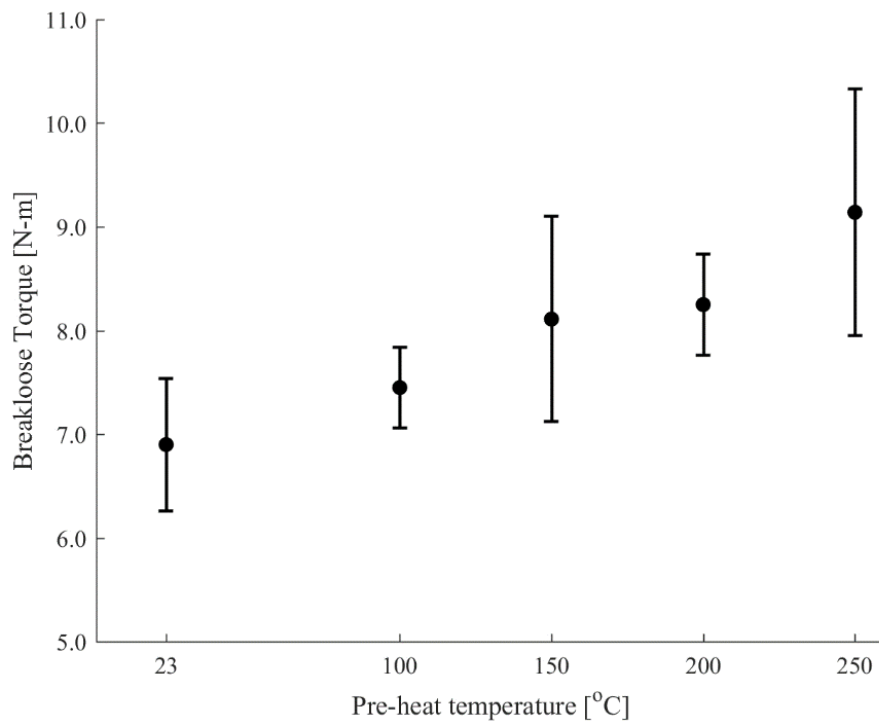
Figure 6–11: Effect of TA on breakloose torque

Joint Strength

Static tests were conducted on the three sets of pre-heat temperatures to determine what influence pre-heating the workpieces would have on the joint strength. The samples were tested at a displacement rate of 50 mm/min, in accordance with JIS-Z-3136. Similar trends were observed for both the joints tested in a lap shear configuration, Figure 6–12, and those in a cross-tension configuration, Figure 6–13. Pre-heating the workpieces to 143°C had to effect on the joint strength

of either configuration, although a pre-heat temperature of 247°C decreased both the lap shear and cross tension strengths by 12 and 21%, respectively. The elevated temperature of 247°C had caused a larger and more significant heat-affected zone in the workpiece, thus decreasing the strength of the material below that of those samples without pre-heating. The trend in strength results can be confirmed from the previous microhardness measurements that show a wider and more affected HAZ in the 247°C samples.
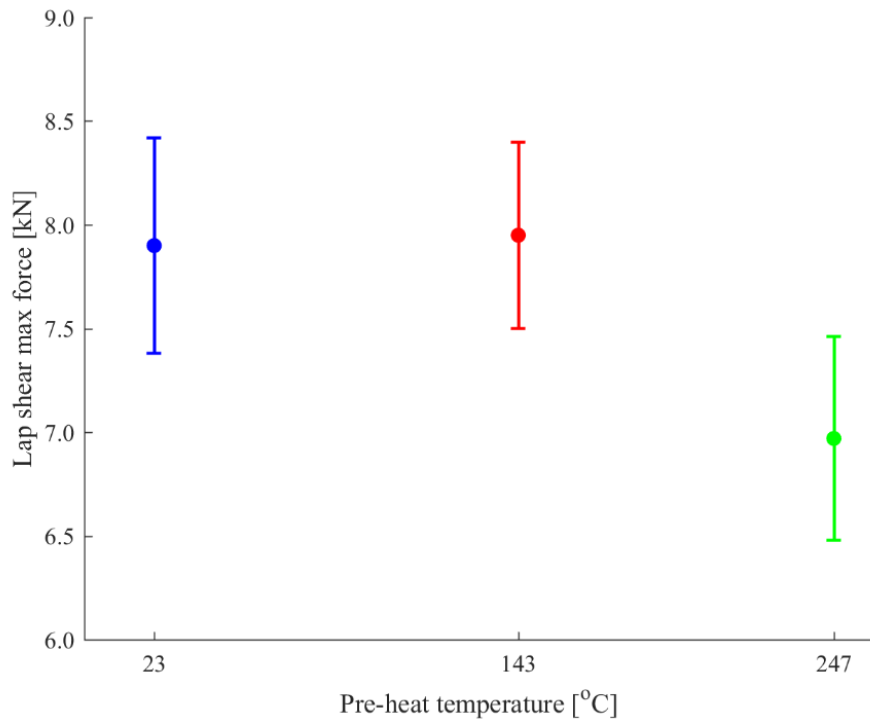
Figure 6–12: Effect of TA on lap shear strength
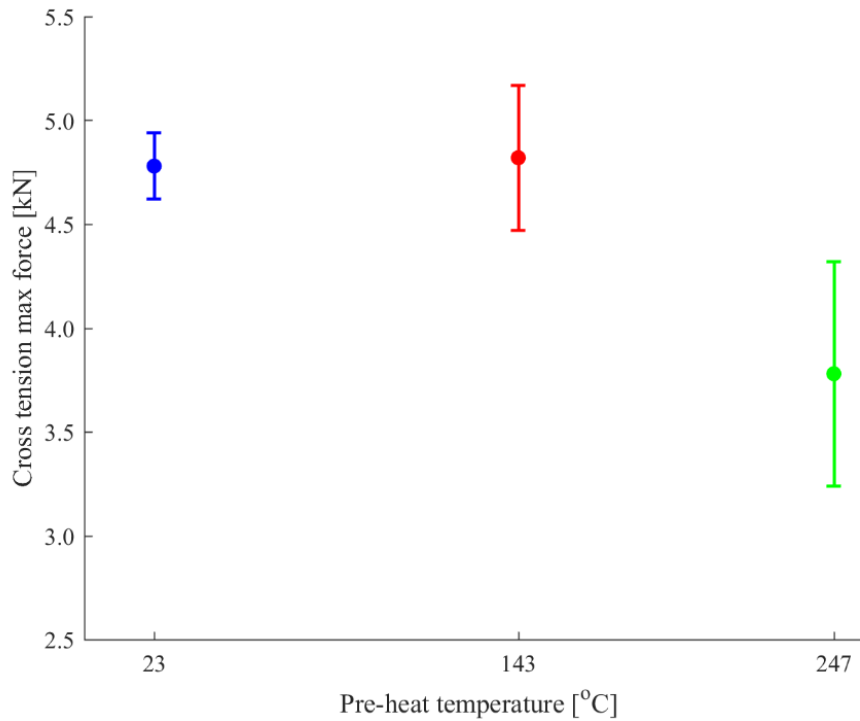
Figure 6–13: Effect of TA on cross tension strength

6.4. Conclusions

Thermally-assisted flow drill screwing showed that pre-heating the workpieces using a conduction ring:

- Reduces process time by 34% and 52% for those workpieces pre-heated to 143°C and 247°C, respectively

- Reduces installation torque by 10% and 21% for those workpieces pre-heated to 143°C and 247°C, respectively; widening the design space for thicker/stronger materials

- Caused a larger and more softened HAZ (compared to baseline) for those samples heated to 247°C but did not worsen those heated to 143°C

- Improved the joint secureness by increasing the breakloose torque

- Did not influence the joint lap shear or cross tension strength when heated to 143°C, but negatively affected it when heated to 247°C

These conclusions suggest that thermal assistance can provide benefit to the FDS process by reducing process time, reducing installation torque, and increasing joint secureness, while not negatively affecting the joint strength; providing the pre-heat temperature is around 143°C. Beyond this, the added temperature softens the material significantly and causes a drop in joint strength, thus providing no further advantage. Due to the success of thermally augmenting the FDS process with a conduction ring, investigation into implementing electricity to rapidly heat the workpiece is presented in the next chapter.

7. ELECTRICALLY-ASSISTED FLOW DRILL SCREWING

7.1. Electrically-Assisted Manufacturing

The frictional nature of FDS induces thermal softening of the material but requires time for the heat to build. The previous section's work with thermal assistance has shown that pre-heating the workpieces leads directly to reducing penetration time but may add to overall cycle time. A more efficient augmentation approach through Electrical Augmentation (EA) is investigated to reduce cycle time. An experimental investigation of the EA-FDS process is presented in this section, with the joint metrics quantified through installation torque, process time, and breakloose torque.

Electrically assisted manufacturing (EAM) has been demonstrated to lower a metal's yield point while simultaneously increasing the material's ductility [97]. This effect is known as the electroplastic effect and, while not fully understood, is most commonly believed to be caused by localized resistive heating at the atomic level. Temperature rise from joule heating is shown in Equation 34, where I is the current, R is the resistance, t is the time, and C_p is the specific heat. While the cause of the EAM behavior has not been fully established, the effects have been examined and proven to be repeatable and controllable. Thus, the lack of a definitive theoretical basis has not limited the adaption of the technology within industry.

$$\Delta T = \frac{I^2 R t}{C_p} \tag{34}$$

Electrically assisted forming (EAF) is one of the most energy efficient methods for deforming sheet metal when compared to thermally-assisted forming and traditional straight mechanical forming. The creation of the term "electroplastic effect" was coined by Troitskii in 1969, while researching the effect of electricity on dislocations with respect to creation and movement in

various metallic alloys [98]. Electrically assisted manufacturing has recently been applied to similar and dissimilar material joining technologies, though so far, the only technology augmented is friction stir welding (FSW).

In 2005, Long created an FEA model of an electrically enhanced friction stir welding process [99]. The FEA model accounted for resistive and frictional heating which resulted in material softening. The model predicted a reduction in plunge force and the possibility to conduct tests at 2 times the welding rate of a standard friction stir weld. Testing was not conducted to validate the model. This work was followed by Ferrando in 2008, this work applied electric current through the forming tool to busses underneath the workpiece [100]. This paper lists various materials that could be used for the friction stir tool, Ferrando tested with molybdenum (TZM) and Tantalum. It was determined that the plunge force was greatly reduced and that an increase in welding speed may be possible. Similar results to Ferrando were found by showing that welding and plunging force was reduced with the introduction of electricity to a friction stir welding process for 6061 aluminum [101,102]. In 2015, Lui conducted the first electrically assisted dissimilar friction stir welds joining 6061 aluminum to TRIP 780 steel [103]. Unlike the previous papers, electricity was passed through brushes on each side of the welding tool rather than through the tool itself. It was shown that the axial welding force was reduced with electricity and that the formation of intermetallic compounds was enhanced with electrical assistance.

7.2. Experimental Setup

In this study, two 1.3mm sheets of Al6063-T5 were selected to be the 2T (2-layer) stackup, Figure 7–1. The FFS machine had to be modified to insulate the electronics from any possible electricity being passed through the aluminum sheets. A special fixture also had to be manufactured to allow current to flow from one side of the sheet to the other which ensured electricity was passing

120

through the joining zone, the fixture is shown in Figure 7–2. The layers in the clamping fixture are for thermal and electrical isolation; the ceramic is for thermal isolation to protect the layers underneath of it. The electrical contacts are copper and are simple welding leads, the dimension of the electrical contact is negligible as the electricity flowing through the cross-sectional area is what matters. The leads are spaced far enough apart that the electricity should fully engulf the cross-sectional area. The only difference between the EA process and the traditional process is that electricity is flowing through the part, the actual process itself is no different from the FDS machine's or process control standpoint.

Figure 7–1: EA 2T joint stackup
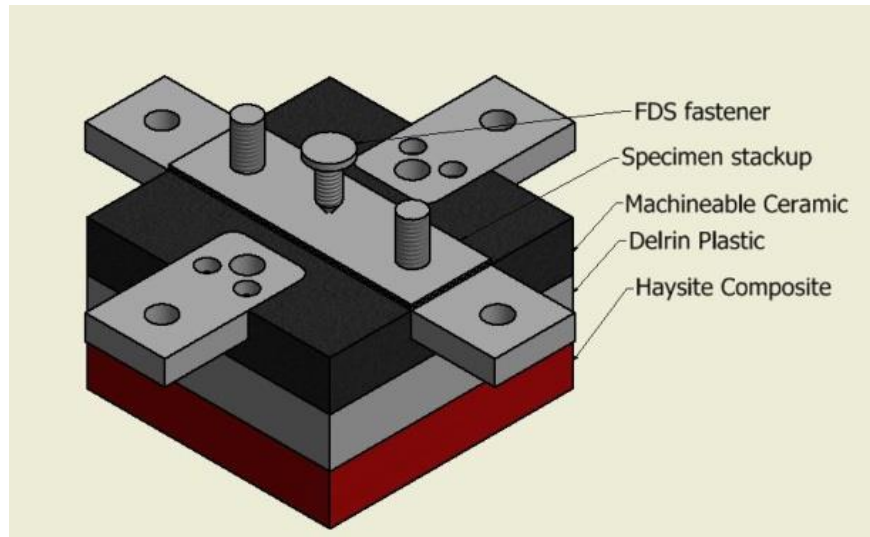
Figure 7–2: Electrically insulative clamping fixture

Three current densities, 0, 45, and 90A/mm^2, were chosen for this study to determine what effect electrical augmentation had on the joining of Al6063 during FDS, where current density is calculated to be the applied current divided by the workpiece cross-sectional area. 0A/mm^2 was chosen as a baseline to represent an un-augmented process, 90A/mm^2 was selected due to the 3000A limitation of the power supply, and 45 was chosen as a midpoint between the two.

The parameters for the FDS process were kept constant regardless of current density to allow for joint metric comparison, with the parameters listed in Table 7–1, and the resultant torque plots shown in Figure 7–3.

Table 7–1: Electrically assisted test matrix

Current Density [A/mm^2]	Pre-Heat Temperature [°C]	Drilling Speed [RPM]	Drilling Force [N]	Tightening Torque [N-m]
0	28			
45	51	6000	600	6
90	128			
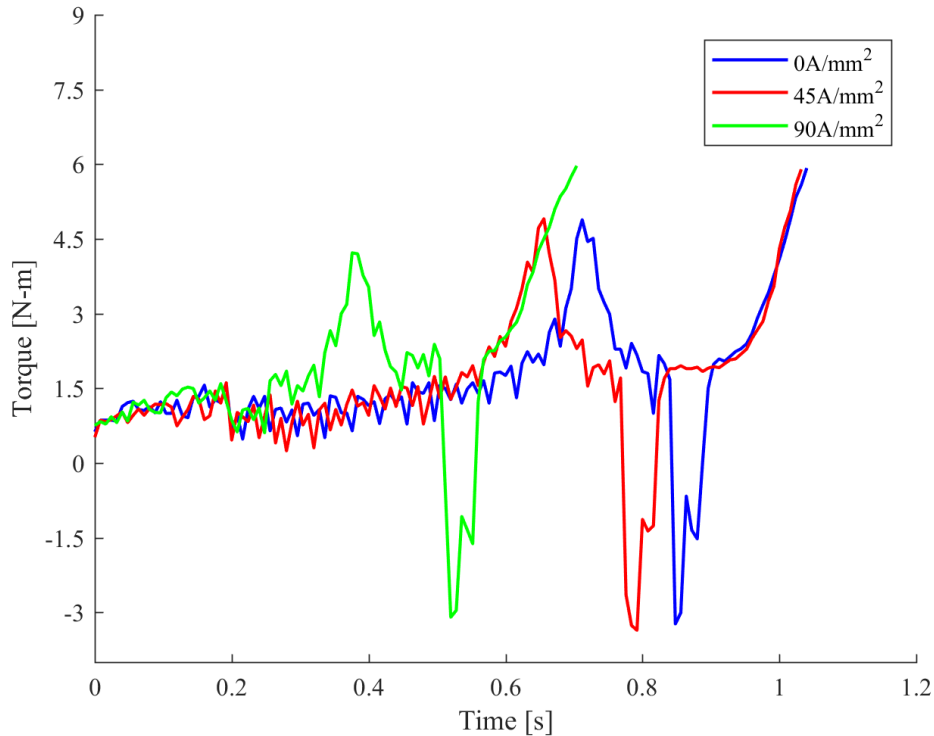
Figure 7–3: EA-FDS torque curves

7.3. Joint Evaluation

Process Temperature

Temperature measurements were taken using a FLIR A40 infrared camera to observe the rise in temperature from the electrical augmentation Figure 7–4. The samples were spray painted black to ensure accurate measurements from the thermal camera and a thermocouple used to verify the temperature values.

Three distinct slopes (prior to heat generation through screw friction) can be observed for the three different current densities. As expected, the 90A/mm^2 sample has the quickest temperature rise and reached a pre-process temperature of 128°C. Despite the three current densities being able to pre-heat the workpiece to the different starting temperatures of 28°C, 51°C, and 128°C, they all

123

reached approximately the same maximum temperature of 280°C. This occurs because although the electricity is adding heat the process, it is also thermally softening the material quicker and thus the screw can penetrate the stackup quicker and requires less frictional energy from the screw to increase the material temperature.
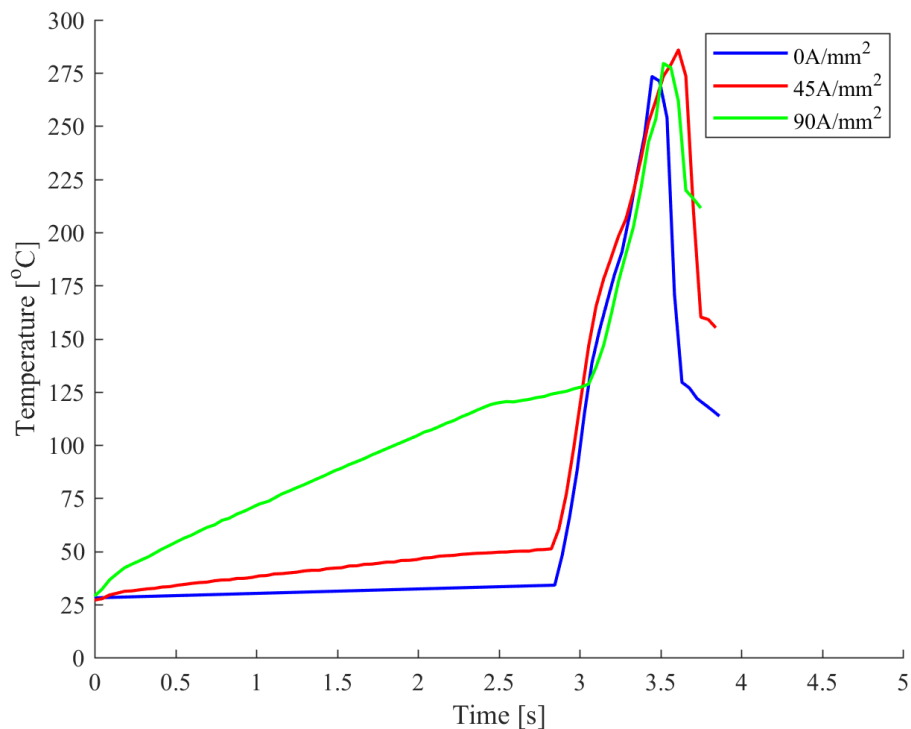
Figure 7–4: Effect of EA on process temperature

Process Time

Process time comparisons among the three current densities only considered the interaction between the screw and the workpiece; it did not include the ~3 second workpiece pre-heating time. The power supply used for this study was limited to 3000A and therefore restricted the rate at which the workpiece could be heated. Given a larger power supply, the workpiece temperature could be risen almost instantaneously. No reduction in process time was observed for the 45A/mm^2 current density as it was only able to pre-heat the workpiece to 51°C. However, as the 90A/mm^2 sample

could raise the workpiece temperature to 128°C in the same amount of time, a 20% reduction in process time was achieved. As the material is thermally-softened prior to the screw-workpiece frictional process, the screw can penetrate the stackup quicker and achieve a shorter process time.
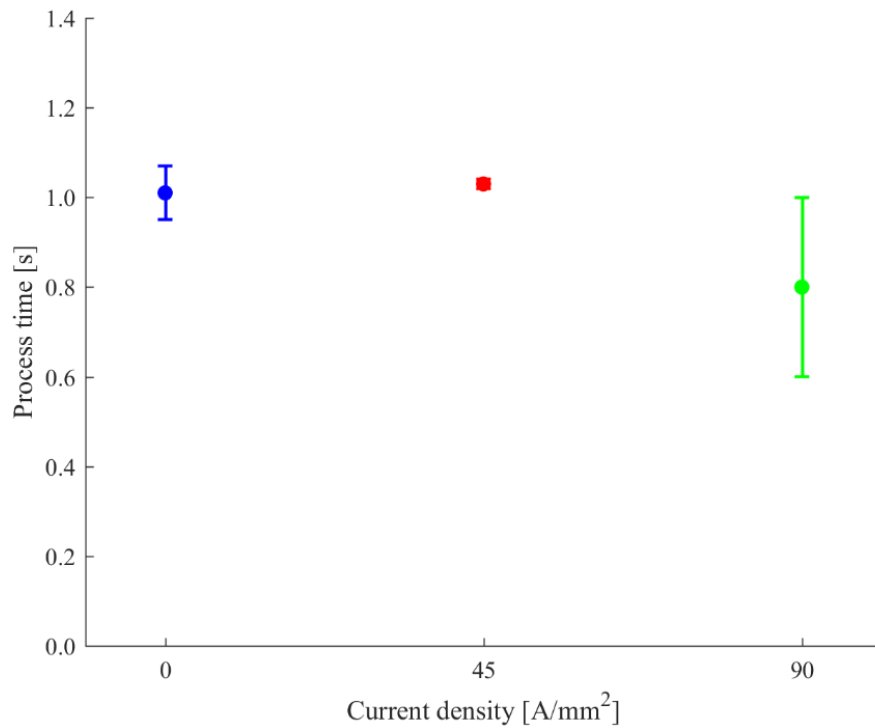
Figure 7–5: Effect of EA on process time

Installation Torque

Installation torque is the amount required to thread-form the stackup during the FDS process. It is the value that limits the stackup configuration based on a combination of the workpiece thickness and strength; with the torque limited to 8.3N-m. The ability to lower the installation torque not only pushes the boundary for what the current thickness limitation, approximately 6mm, but also increases the factor of safety towards potential screw failure during installation. Previous work by the same authors showed that pre-heating the material to 143°C with a conduction ring decreased installation torque by 10%. However, with electricity being the utilized as the supplementary heat source, a 13% decrease in installation torque was achieved with only a pre-

process temperature of 128°C, Figure 7–6. While the baseline installation torque value of 5.12N-m is far below the 8.3N-m limit, the results from this study show that the 6mm stackup thickness limitation can be overcome with the assistance of electrical augmentation.
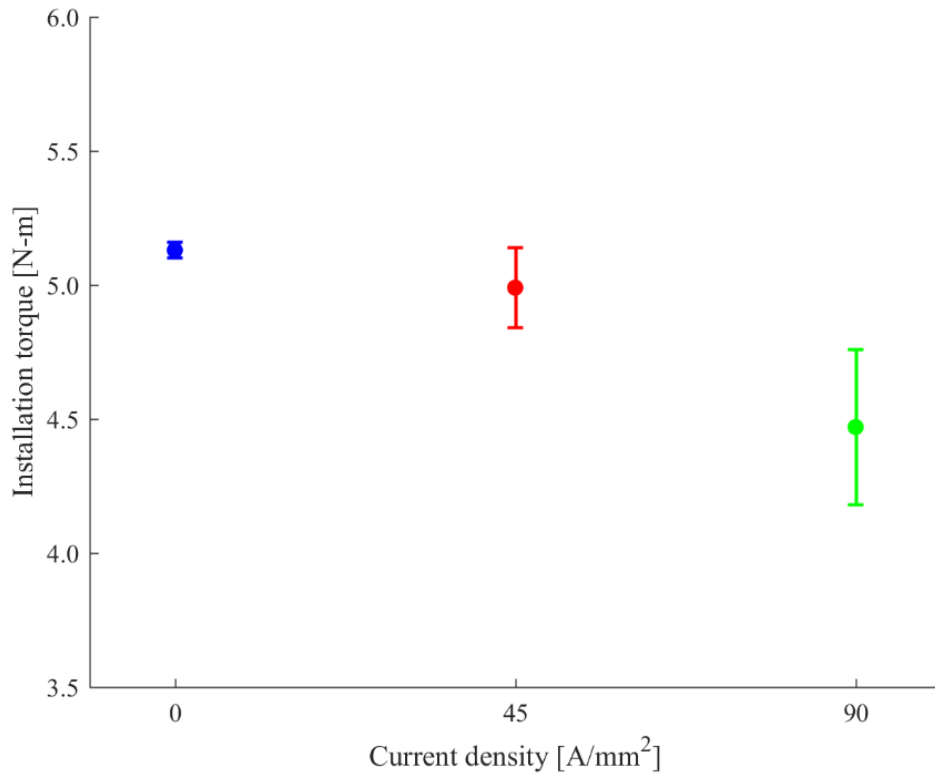
Figure 7–6: Effect of EA on installation torque

Breakloose Torque

One FDS joint strength metric used to quantify the quality of the joint is the breakloose torque. This torque value is the required torque to loosen the screw (in the counter-clockwise direction) after a complete installation has occurred. Manufacturers perform this study to ensure little to no clamp load is lost as the joint returns to ambient temperature. During this study, a final torque of 6N-m is imposed on all the joints and is used as a reference to the required torque to loosen the screw. Three replications for each current density were tested and an average breakloose torque for the 0A/mm^2, 45A/mm^2, and 90A/mm^2 samples were 5.58N-m, 5.60N-m, and 5.62N-m,

respectively. The authors conclude that the electrical augmentation has no detrimental effect on the joint metric of breakloose torque.

7.4. Extended Application of EA-FDS

Initial studies of electrically-assisted flow drill screwing produced positive results that saw a reduction in both process time and installation torque. Process time is a major driving factor towards the process's viability in a production setting, with OEMs always considerate of how a newly adopted joining process may affect their takt time. An installation torque of 8.3N-m has been discussed as the limiting factor to what material strengths and thicknesses can be joined under the technology's current form. While this 8.3N-m value cannot be increased, as it is dependent upon the fastener strength, the recent evidence suggested that the torque required to thread-form the workpiece (i.e. installation torque) can be reduced through thermal softening.

The current trend of lightweighting by material substitution is not solved exclusivity with aluminum alloys. Ultra High Strength Steels (UHSS) are increasing in usage as they provide amazing strength and stiffness for such a small gauge material thickness. The drawback to this material is evident when trying to join it to dissimilar materials; as the material's brittleness does not make it a viable candidate for SPR. UHSS cannot be joined using FDS either as the current technology's viability is restricted to a thickness of 1.5mm for a 600MPa material and 1mm for an 800MPa material. Presently OEMs are either resistance spot welding the UHSS to a milder steel (that can then be joined to aluminum using SPR or FDS) or pre-drilling a pilot hole for application as a top sheet in an FDS stackup. Neither of these are cost efficient as they hinder part consolidation or require an additional manufacturing step.

A preliminary trial was performed to demonstrate whether EA-FDS could be utilized for joining aluminum to UHSS (without any additional manufacturing steps such as pre-drilling). A

non-assisted FDS process was compared to an electrically-assisted FDS process to join together a 1.3mm sheet of 6063-T5 and a 1.5mm sheet of 1500MPa UHSS. Without electrical assistance, the screw was not able to penetrate the stackup, Figure 7–7(a), but applying a current density of $60A/mm^2$ across the part allowed successful penetration of the screw, Figure 7–7(b). The total process time was only 4 seconds and in that short amount of time, the electricity could soften the UHSS enough for the screw to penetrate the stackup without damage to itself.

The initial trial involving UHSS demonstrated the potential that electrical-assistance has to push the current boundaries of FDS. Penetration of an FDS screw through a 1500MPa UHSS was a unique feat and thus the inventors (Brandt J. Ruszkiewicz, Jamie D. Skovron, and Laine Mears) filed a patent application under the name "Electrically Assisted Flow Drill Screwdriving and Fixture Therefore". Figures regarding fixture designs can be found in the Appendix.
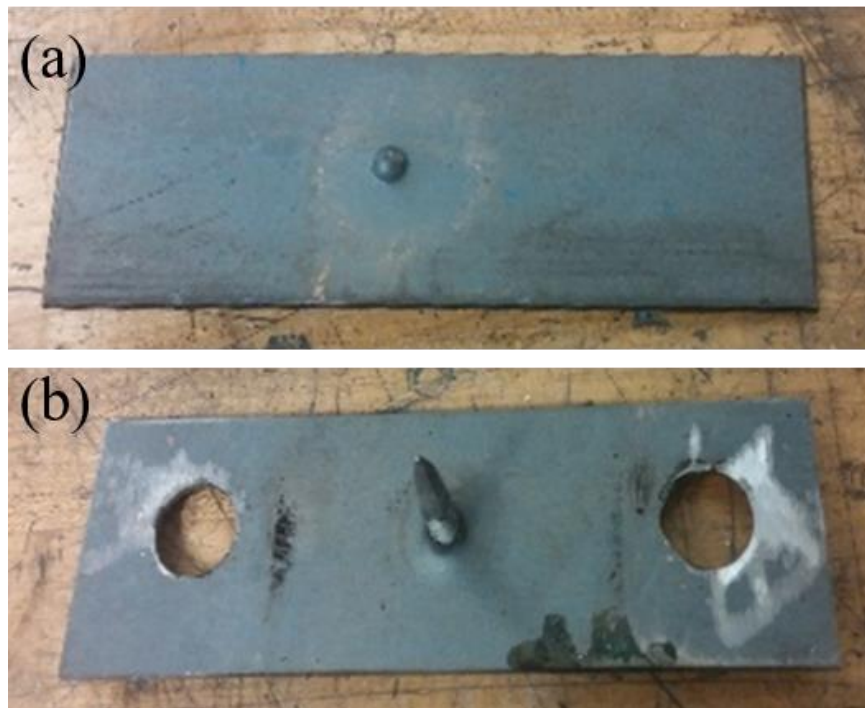
Figure 7–7: FDS of UHSS (a) without and (b) with electricity

7.5. Conclusions

Electrically-assisted flow drill screwing showed that pre-heating the workpieces through resistive heating:

- Raises the workpiece temperature far more efficiently than by using a conduction ring, making it a viable option for a mass-production environment

- Reduces process time by 20% and installation torque by 13%, for aluminum stackups pre-heated to 128°C

- Widens the process feasibility space to thicker/stronger materials through addition of an inexpensive supplementary power supply

8. SUMMARY AND CONCLUSIONS

8.1. Intellectual Merit

This research sought to predict both torque and temperature during the flow drill screw process through application of an existing friction phenomenon, the slip-stick contact condition. This mechanical contact condition dictates whether the heat is generated through frictional sliding (slip) or shear deformation (stick), and was used to describe the interaction between the rotating non-deformable steel screw and the stationary aluminum workpiece. This research created the first FDS coupled thermo-mechanical model that incorporated both a slipping and sticking contact condition, and goes beyond the current approach of combining material strength and friction coefficient terms as one sole source of heat generation. The terms were isolated into their respective slip and stick heat generation mechanisms through identification and modeling of the progressive plastic deformation that the aluminum workpiece underwent. This progressive plastic deformation was tracked by applying the stop-action technique, previously used to observe material flow in FSW, but expanded the method to incorporate angles and aspect ratios of the traced grains into the plasticity model. It was determined that a fully sticking condition overestimates both the process torque and temperature, while a fully slipping condition (though theoretically impossible for a plastic deformation process) underestimates these two values; owing to why current approaches rely on coupling the material strength and friction coefficient terms. As such it was shown that the process exhibits both a slipping and sticking contact condition, with the friction coefficient term showing direct dependence upon temperature due to its influence on the screw coating removal.

Variations in process parameters were shown to influence the heat generation mechanism and consequently the total heat generated; with both contributing to the volume of workpiece material affected by the thermal aspects of the process. The research presented can aid in the accuracy of

these existing crash simulation models that currently assume virgin workpiece material properties near the joining location. Not only did the newly contributed model in this research accurately predict torque and temperature under a given parameter set, but its accuracy extended to both varied process parameters and material thicknesses, demonstrating its robustness. This research goes beyond the current method that relies on an unverifiable friction coefficient and delivers a true understanding to the process mechanics.

8.2. Broader Impact

This research demonstrated the viability of predictive modeling and reducing the dependency upon purely experimental measures. The identification of failure mechanisms under joint loading aids designers in knowing what their potential weak-point is in the structure with established guidelines eliminating that knowledge gap. The secondary research goal confirmed that supplementary heating through both conduction and resistive heating sources reduces the amount of frictional work normally required of the screw. Not only did process efficiency increase, through a reduction in process time up to 52%, but reducing material strength through thermal softening lead to a reduction in the required process torque; leading to an increased design space for joining thicker/stronger materials. Augmentation showed the ability to join thicker/stronger materials beyond the current limitations without the need to replace capital equipment.

8.3. Future Work

The validated model presented in this research can help enhance existing finite element joint-strength prediction models that lack the required information about process-affected zones. These current models, used towards full-vehicle crash simulations, assume virgin material properties at the screw-workpiece interface; which, through this research, has shown not to be representative of the actual process. This research has confirmed that a heat-affected zone, with reduced strength

131

properties, exists and therefore needs to be implemented into the strength-prediction models based on chosen process parameters. The extent of the HAZ was also found to influence the joint failure mechanism, shown through the thermal augmentation of FDS.

The model should also be expanded to stripping torque predictions to aid in selecting a safe and therefore appropriate tightening torque. This could be done by combining existing bolt tightening models with the temperature model presented in this research. A longer cool-down time will allow the workpiece to regain some of its strength, but at the expense of an increased process time; knowledge towards a tradeoff is warranted. The model could also be enhanced through predictive modeling of a dissimilar material two sheet stackup. The challenge with a two sheet stackup is the potential for sheet separation to occur which leads to varying boundary conditions in the thermal model. Research regarding the tribology of the coating removal would certainly provide a further understanding of the process, ass corrosion is a current talking point among OEMs due to the imminent increase in applications of dissimilar material joining.

8.4. Journal Publications and Conference Proceedings

Skovron, J. D., and Mears, L., (2018), "Slip-Stick Contact Conditions for the Thermo-Mechanically   Coupled Flow Drill Screw Process," ASME 13th International Manufacturing Science and Engineering   Conference, College Station, TX.

Skovron, J. D., and Ruszkiewicz, B. J., (2017), "Investigation of the Cleaning and Welding Steps from the Friction Element Welding Process," ASME 12th International Manufacturing Science and   Engineering Conference, Los Angeles, CA.

Skovron, J. D., and Ruszkiewicz, B. J., (2016), "Effect of Electrical Augmentation on the Joining of   Al6063-T5 Using Flow Drill Screws," ASME 11th International Manufacturing Science and   Engineering Conference, Blacksburg, VA.

Milner, J.L., Gnäupel-Herold T., **Skovron, J.D.** (2016), "Residual Stresses in Flow Drill Screwdriving   of Aluminum Alloy Sheets," ASME 11th International Manufacturing Science and Engineering   Conference, Blacksburg, VA.

Skovron, J.D., Prasad, R., Ulutan, D., Mears, L., *et al.* (2015), "Effect of Thermal Assistance on the Joint Quality of Al6063-T5A During Flow Drill Screwdriving," ASME Journal of Manufacturing Science and Engineering, Forming and Joining Special Issue, Vol. 137, No. 5.

Skovron, J., Mears, L., Ulutan, D., Detwiler, D. *et al.* (2015), "Characterization of Flow Drill Screwdriving Process Parameters on Joint Quality," SAE International Journal of Materials and Manufacturing, Vol. 8, No. 1.

9. APPENDICES

9.1. Additional Figures

Figure 9–1: Etched material near the screw-workpiece interface – sample 1 middle

Figure 9–2: Image intensity region of interest - sample 1 middle

Figure 9–3: SZ image intensity plot - sample 1 middle

Figure 9–4: Etched material near the screw-workpiece interface – sample 2 top

Figure 9–5: Image intensity region of interest - sample 2 top

Figure 9–6: SZ image intensity plot - sample 2 top

137

Figure 9–7: Etched material near the screw-workpiece interface – sample 2 middle

Figure 9–8: Image intensity region of interest - sample 2 middle
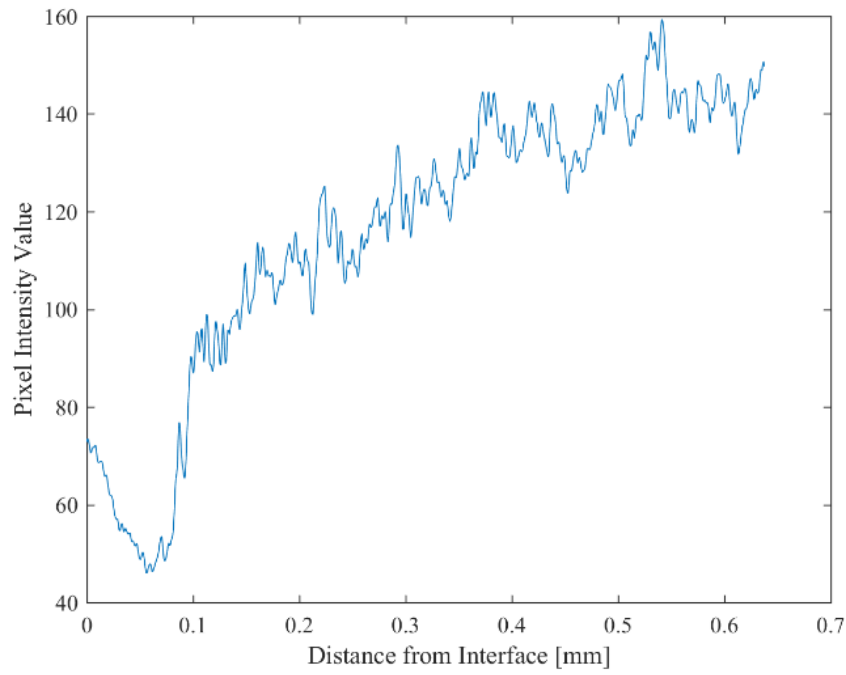
Figure 9–9: SZ image intensity plot - sample 2 middle
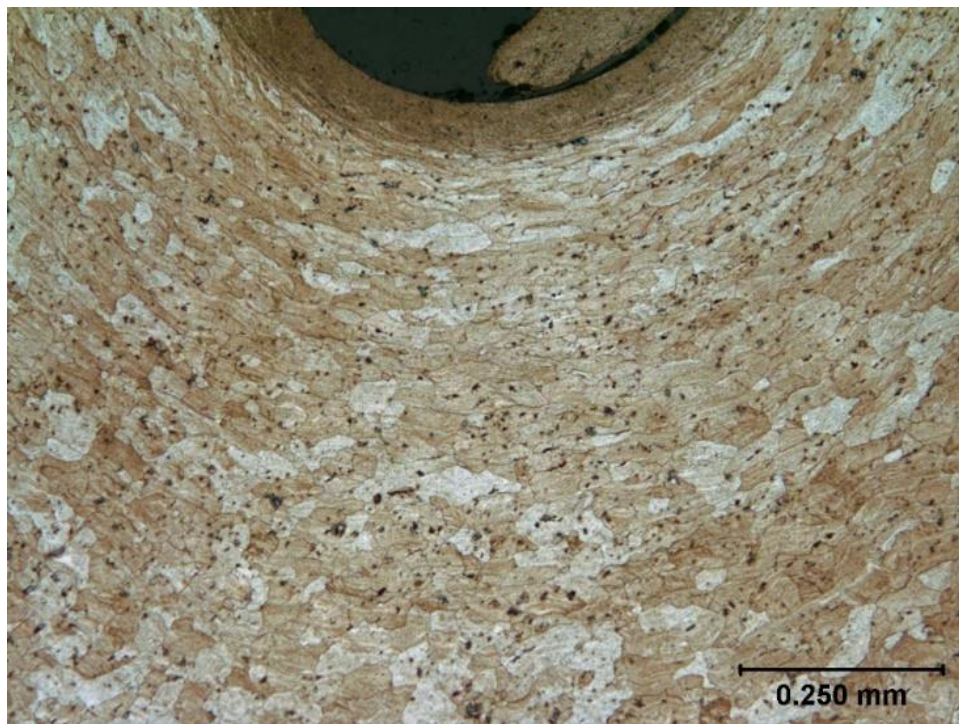
Figure 9–10: Etched material near the screw-workpiece interface – sample 2 bottom

139
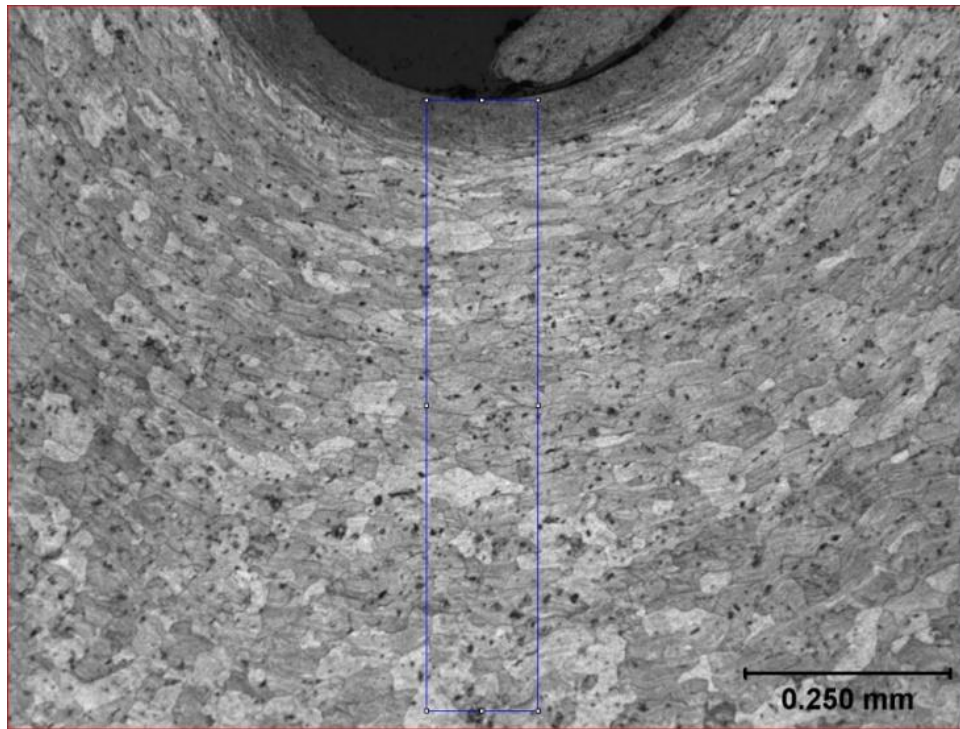
Figure 9–11: Image intensity region of interest - sample 2 bottom
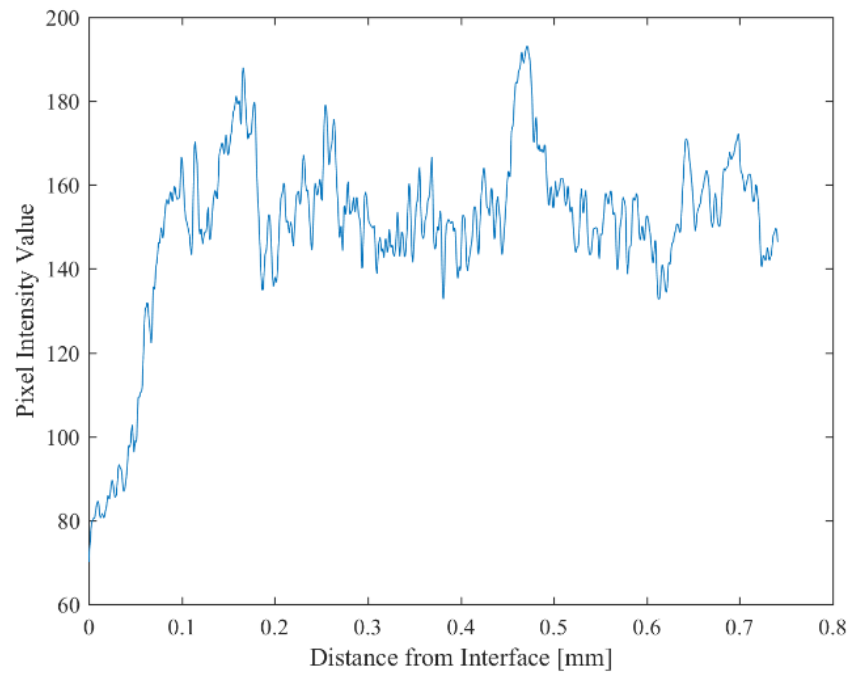
Figure 9–12: SZ image intensity plot - sample 2 bottom

140
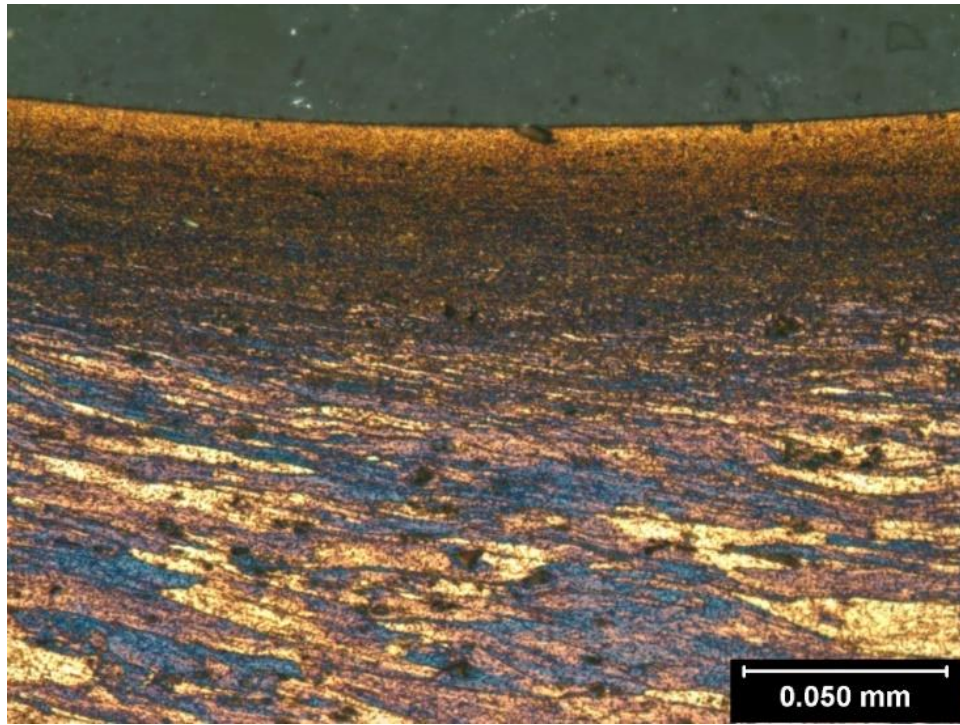
Figure 9–13: Etched material near the screw-workpiece interface – sample 3 top
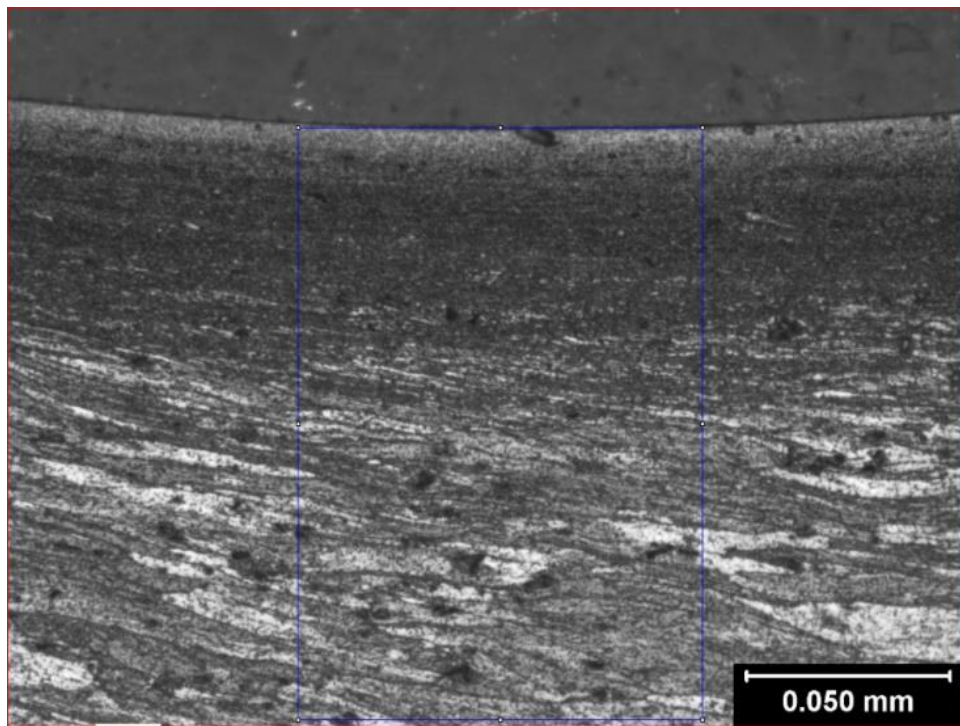
Figure 9–14: Image intensity region of interest - sample 3 top

141
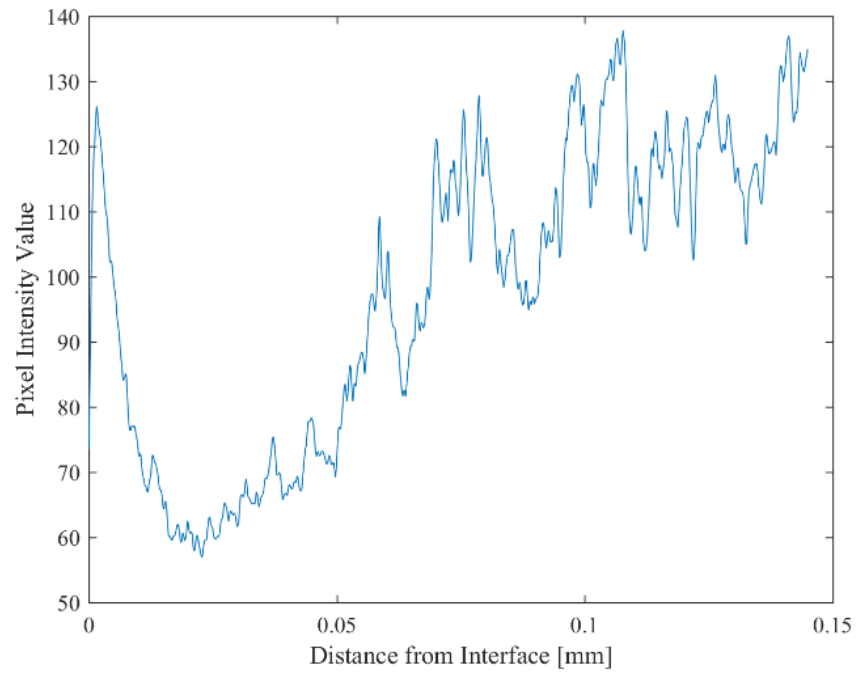
Figure 9–15: SZ image intensity plot - sample 3 top
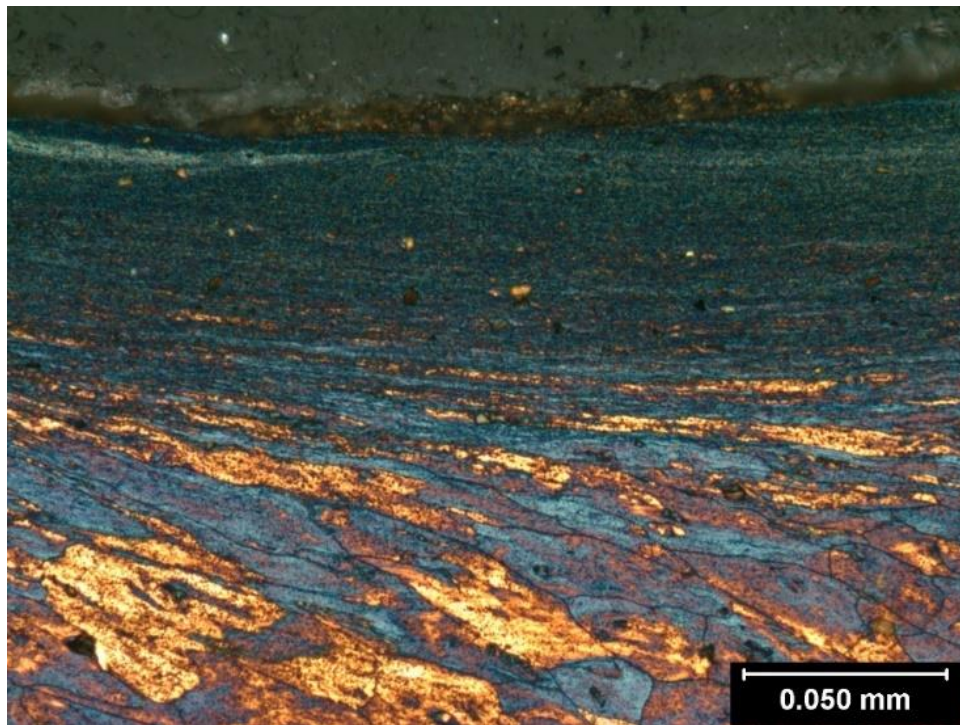
Figure 9–16: Etched material near the screw-workpiece interface – sample 3 middle

Figure 9–17: Image intensity region of interest - sample 3 middle
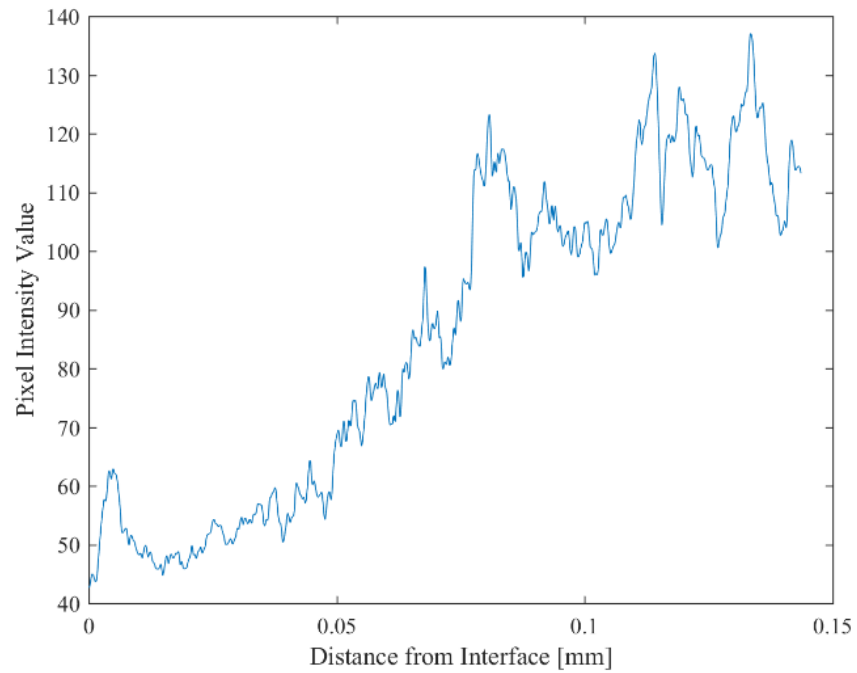
Figure 9–18: SZ image intensity plot - sample 3 middle

143
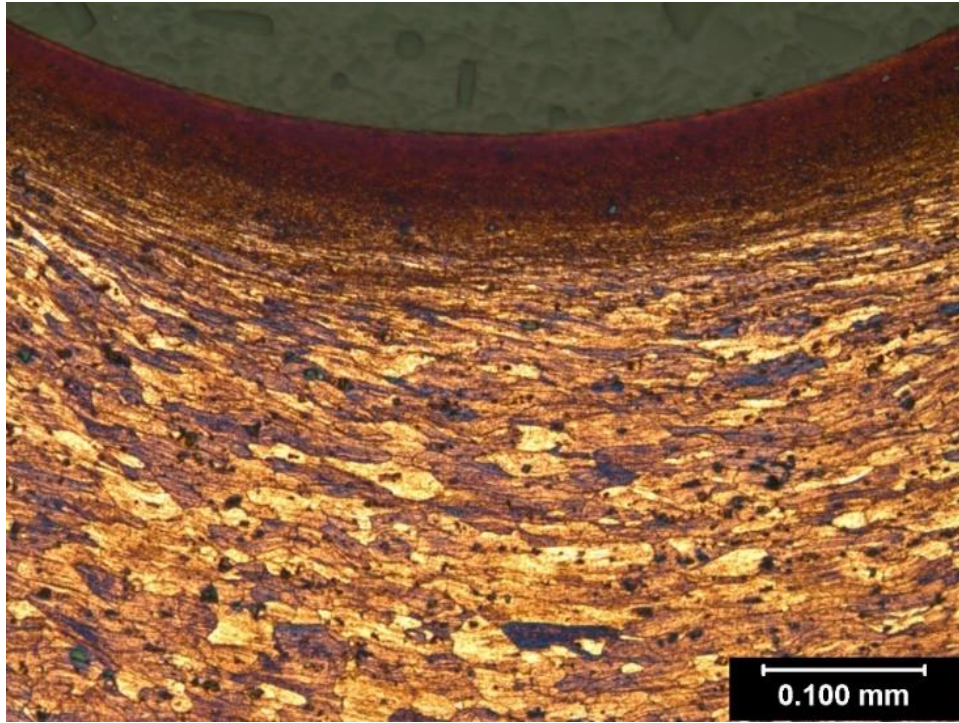
Figure 9–19: Etched material near the screw-workpiece interface – sample 3 bottom
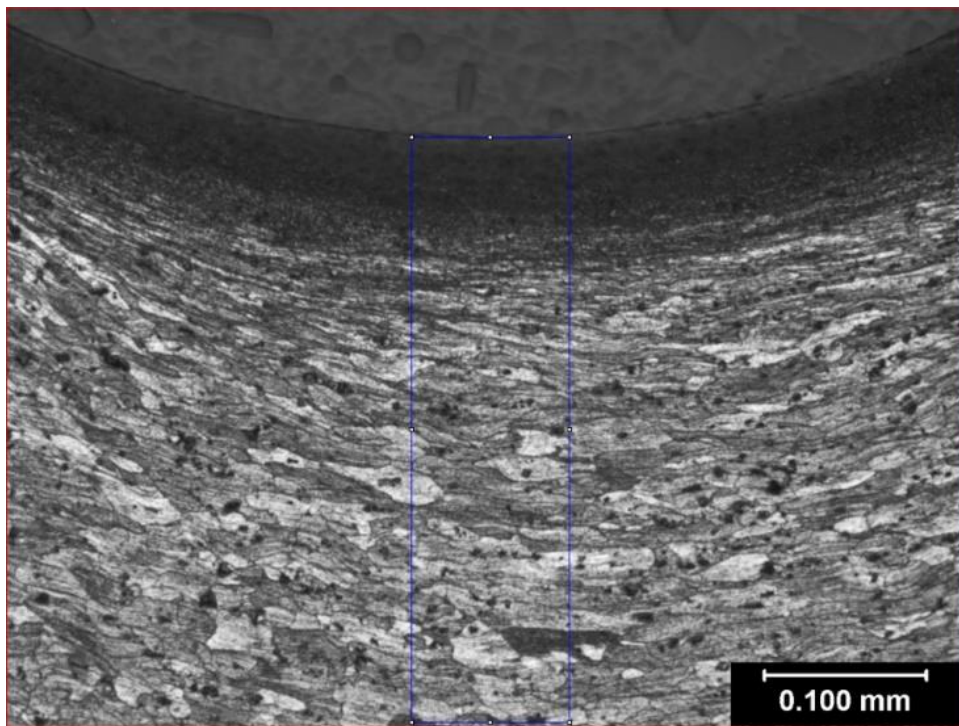
Figure 9–20: Image intensity region of interest - sample 3 bottom
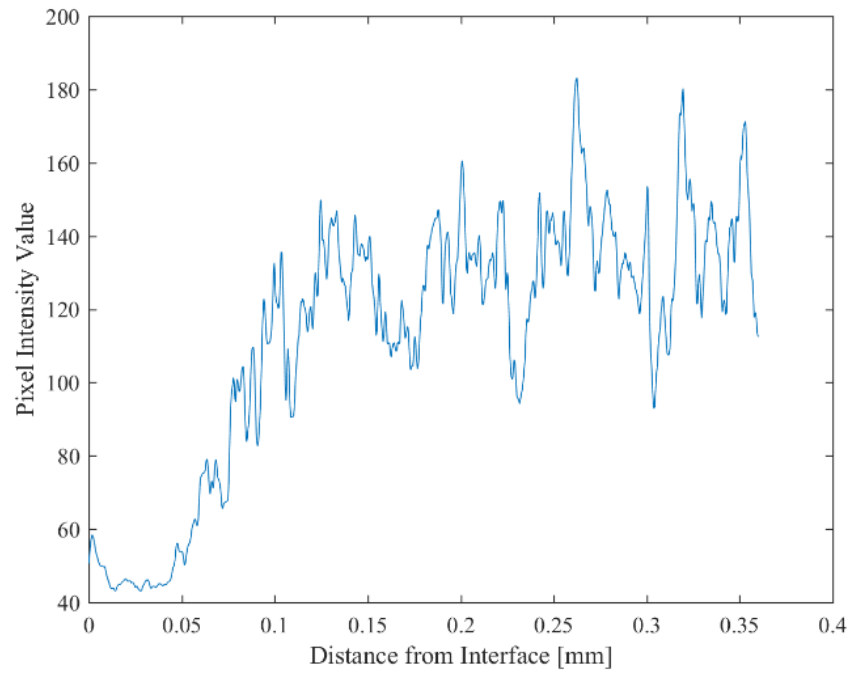
Figure 9–21: SZ image intensity plot - sample 3 bottom
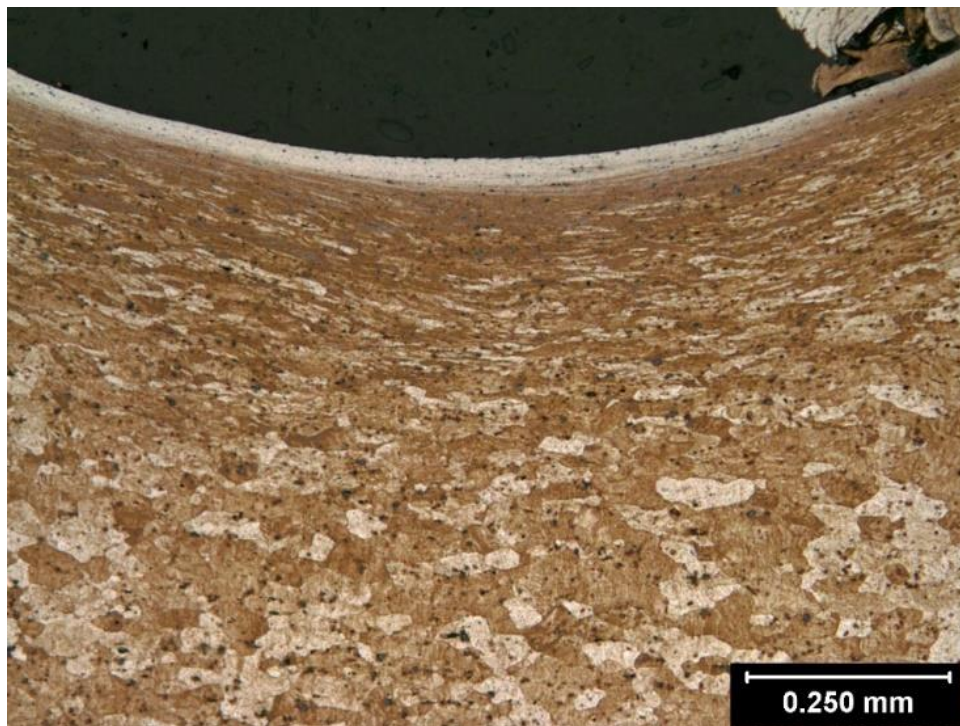
Figure 9–22: Etched material near the screw-workpiece interface – sample 4 top

145
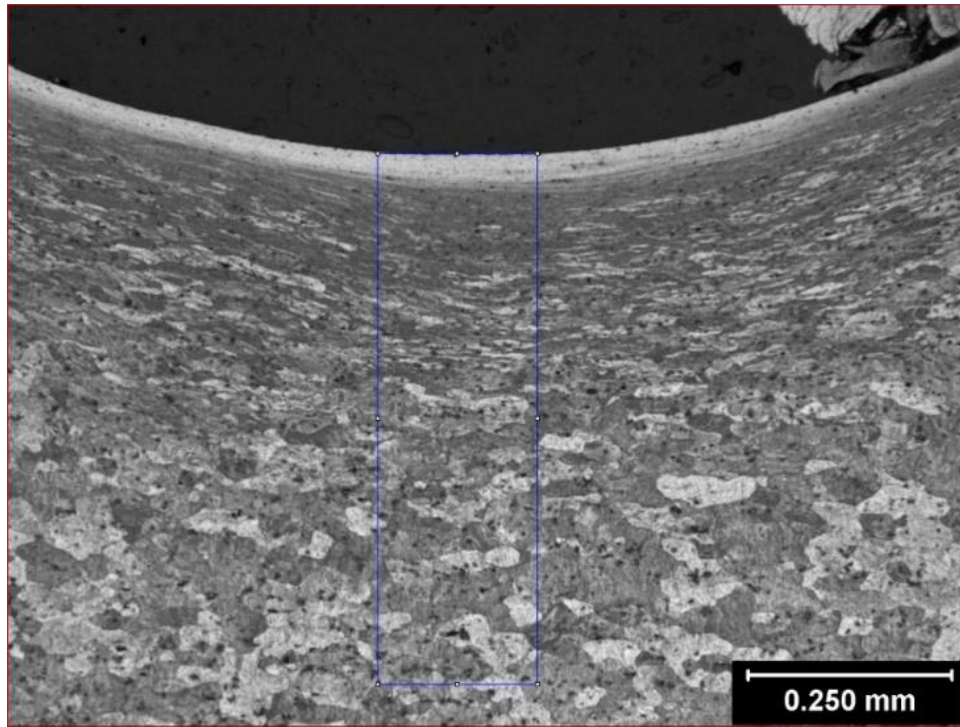
Figure 9–23: Image intensity region of interest - sample 4 top
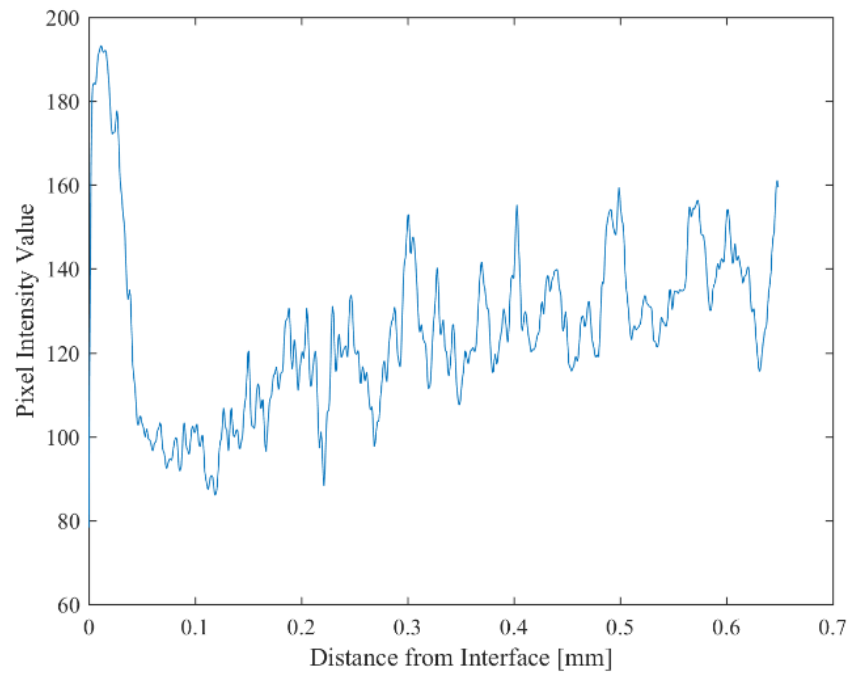
Figure 9–24: SZ image intensity plot - sample 4 top

146
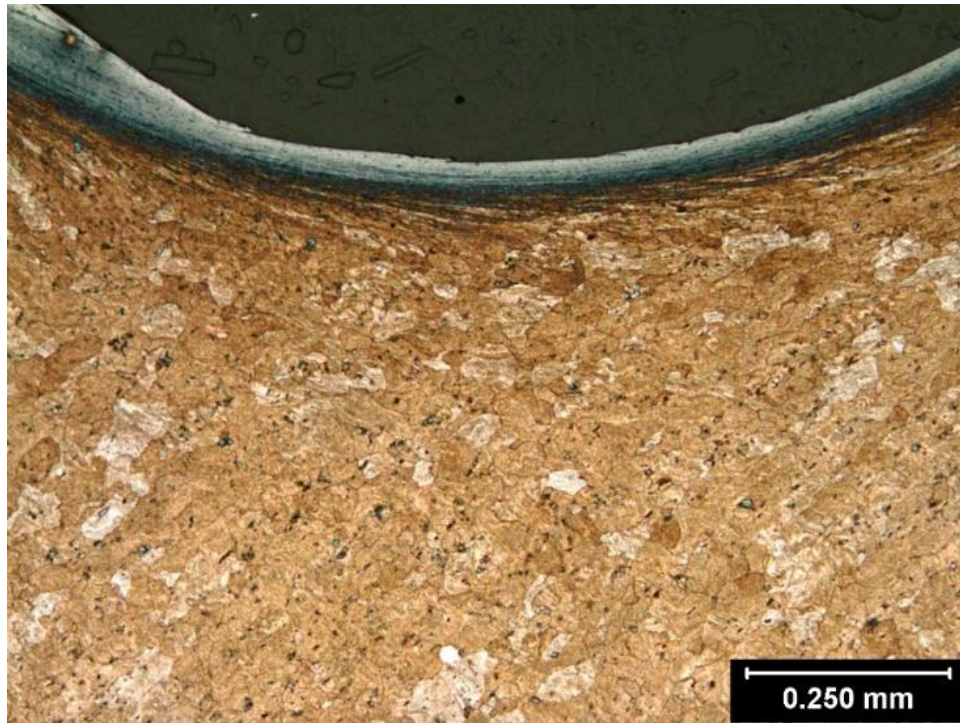
Figure 9–25: Etched material near the screw-workpiece interface – sample 4 middle
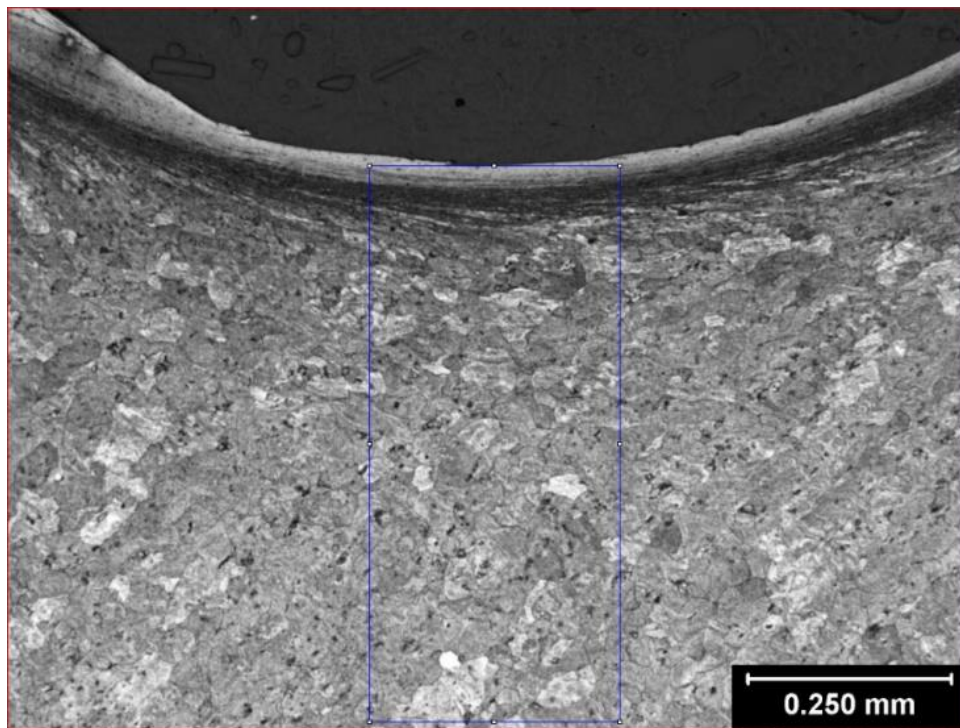
Figure 9–26: Image intensity region of interest - sample 4 middle
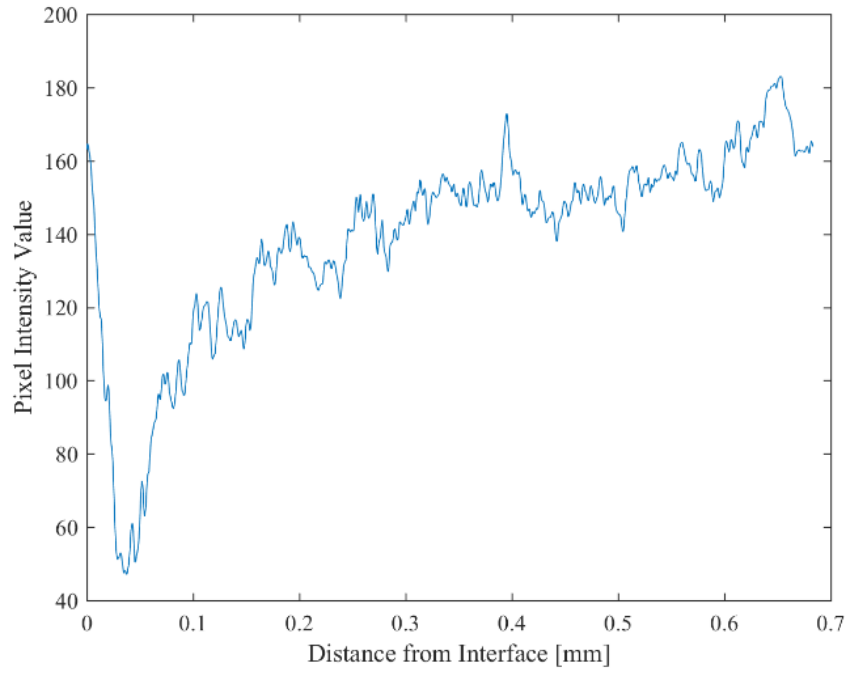
Figure 9–27: SZ image intensity plot - sample 4 middle
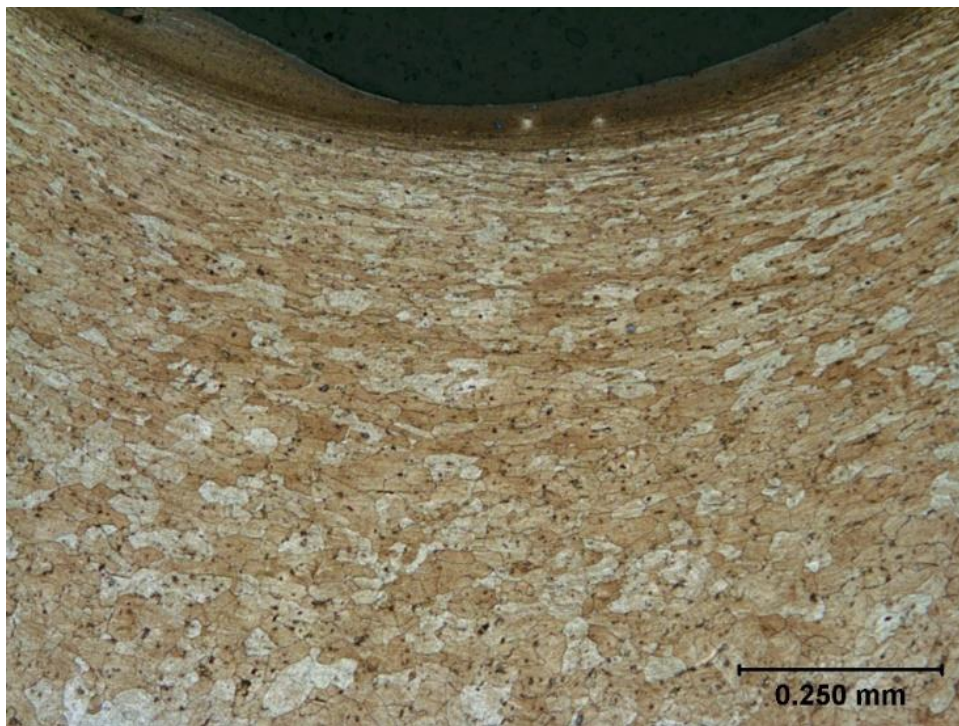
Figure 9–28: Etched material near the screw-workpiece interface – sample 4 bottom

148
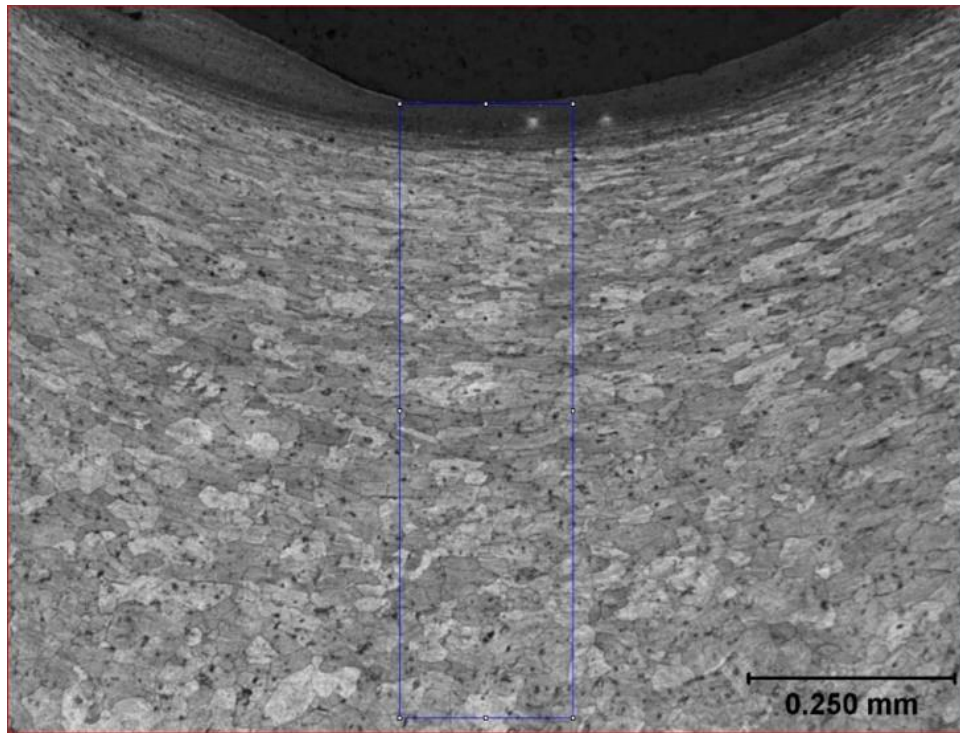
Figure 9–29: Image intensity region of interest - sample 4 bottom
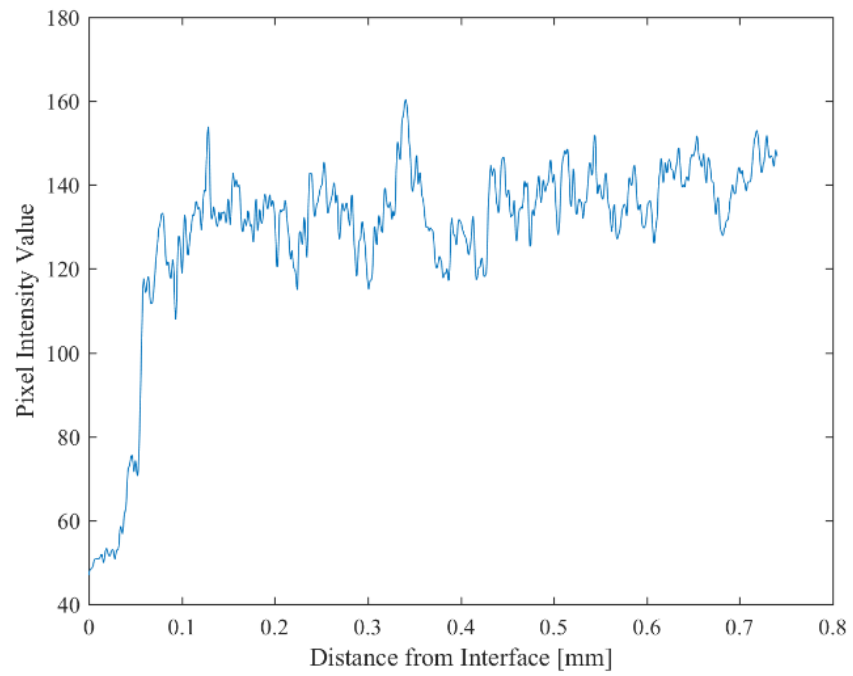
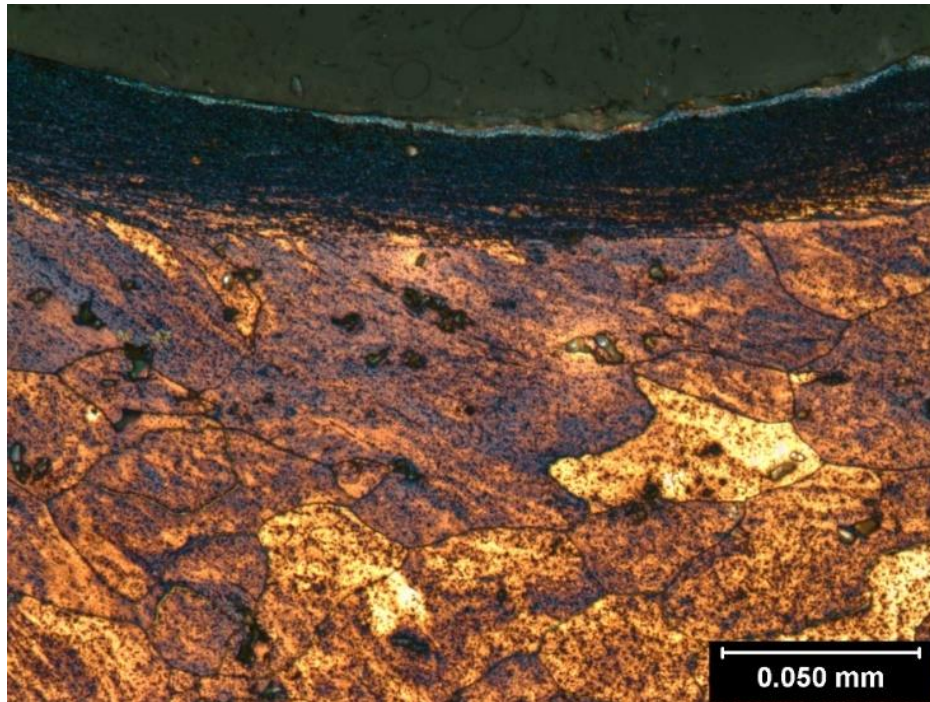*Figure 9–30: SZ image intensity plot - sample 4 bottom*

149
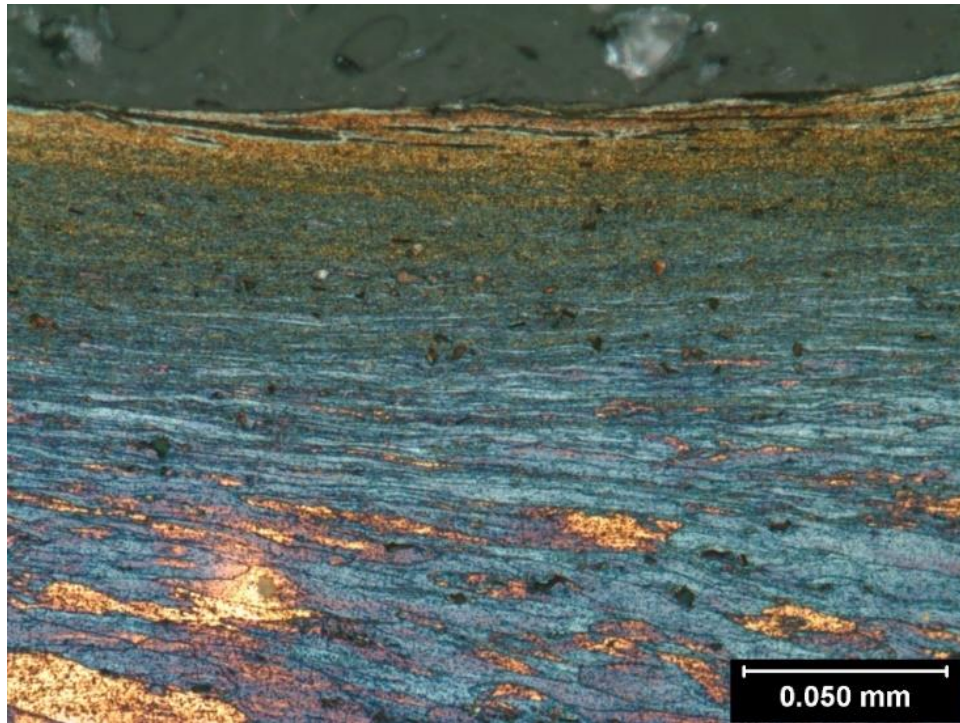
Figure 9–31: Etched material near the screw-workpiece interface – sample 5 top
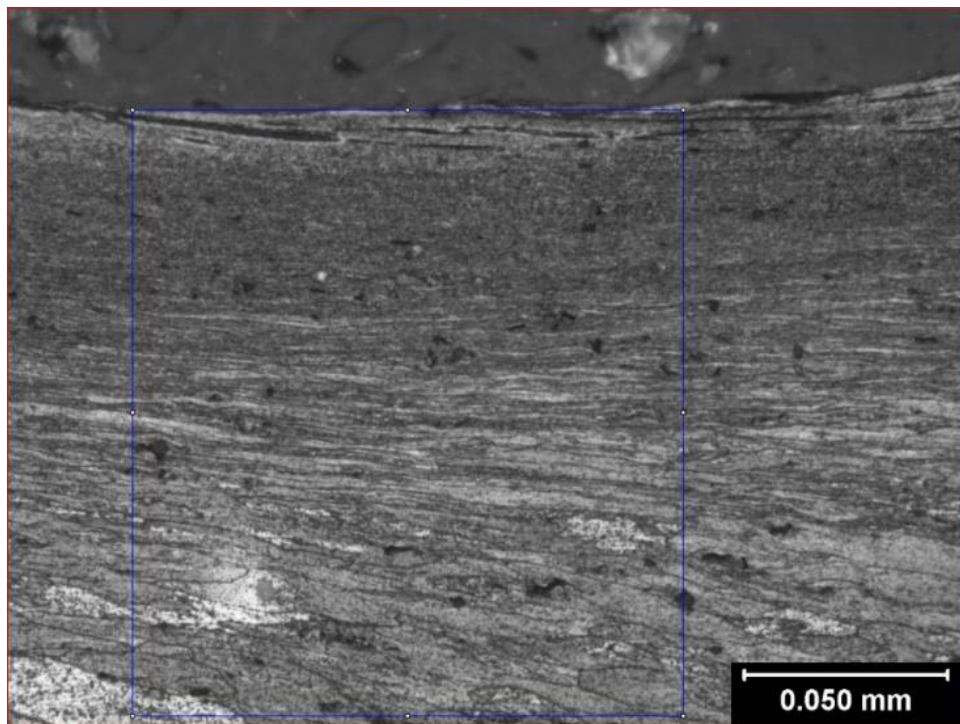
Figure 9–32: Image intensity region of interest - sample 5 top
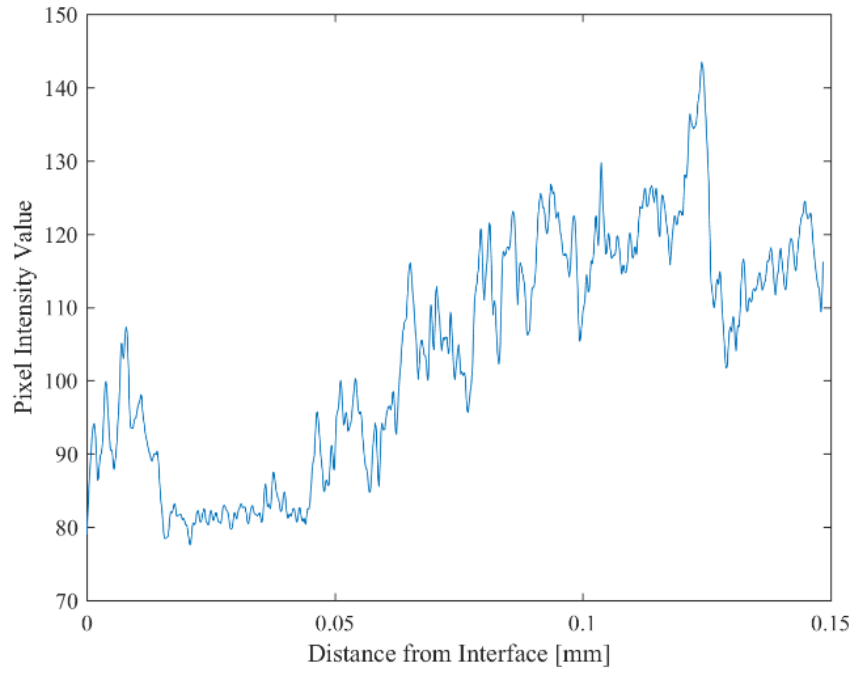
Figure 9–33: SZ image intensity plot - sample 5 top
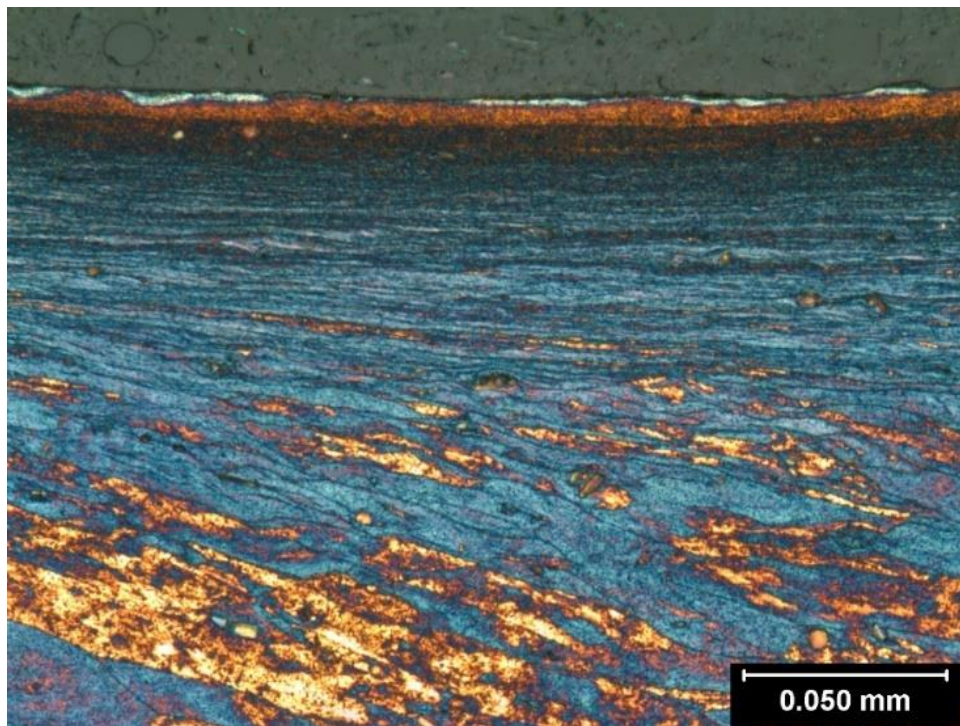
Figure 9–34: Etched material near the screw-workpiece interface – sample 5 middle
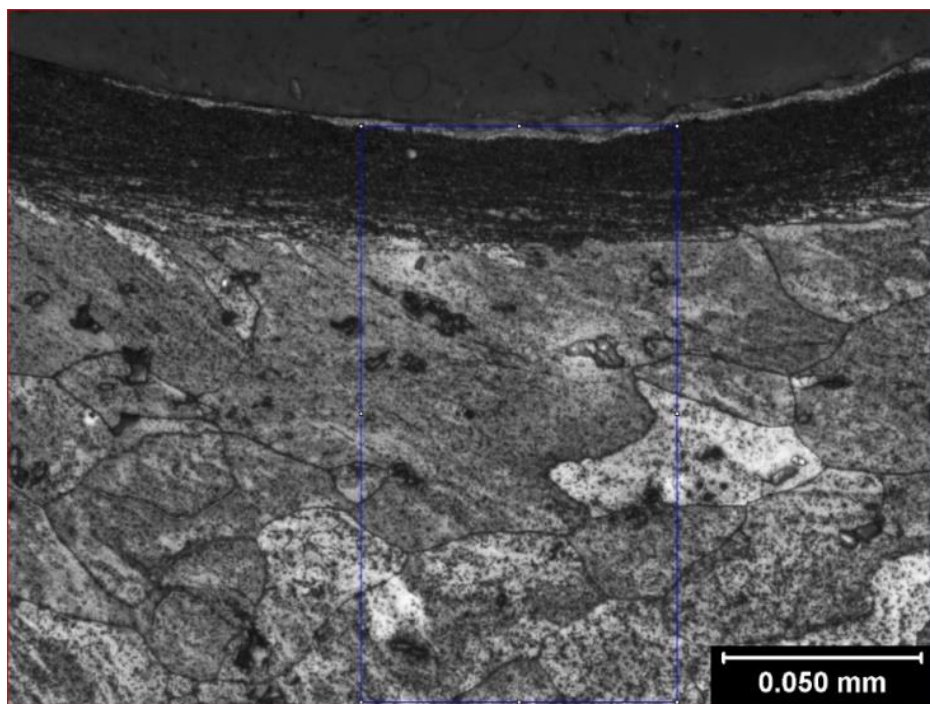
151
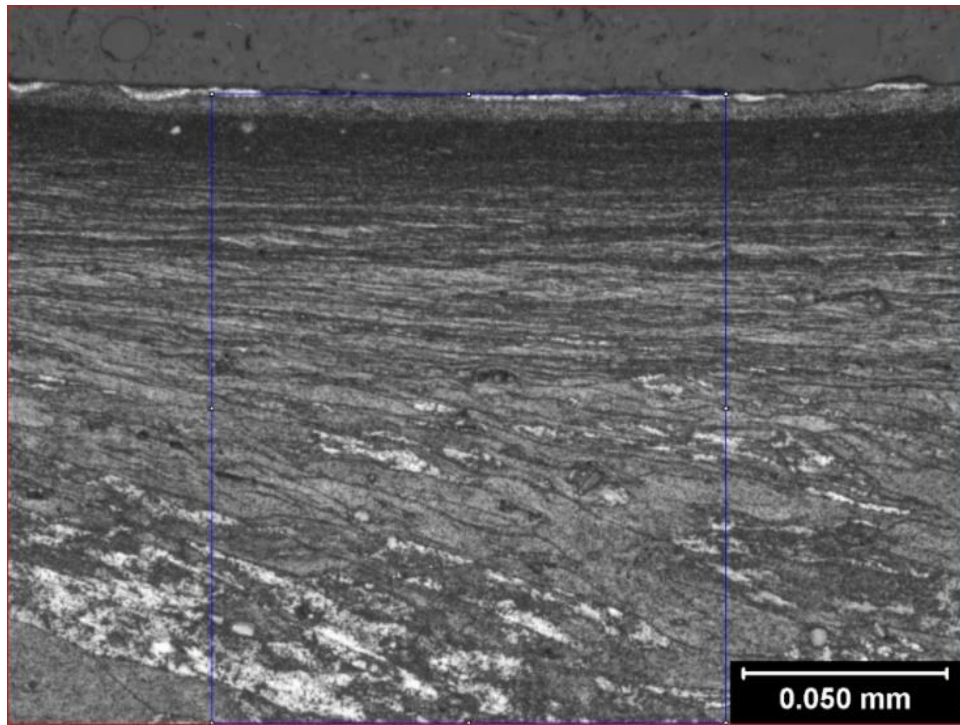
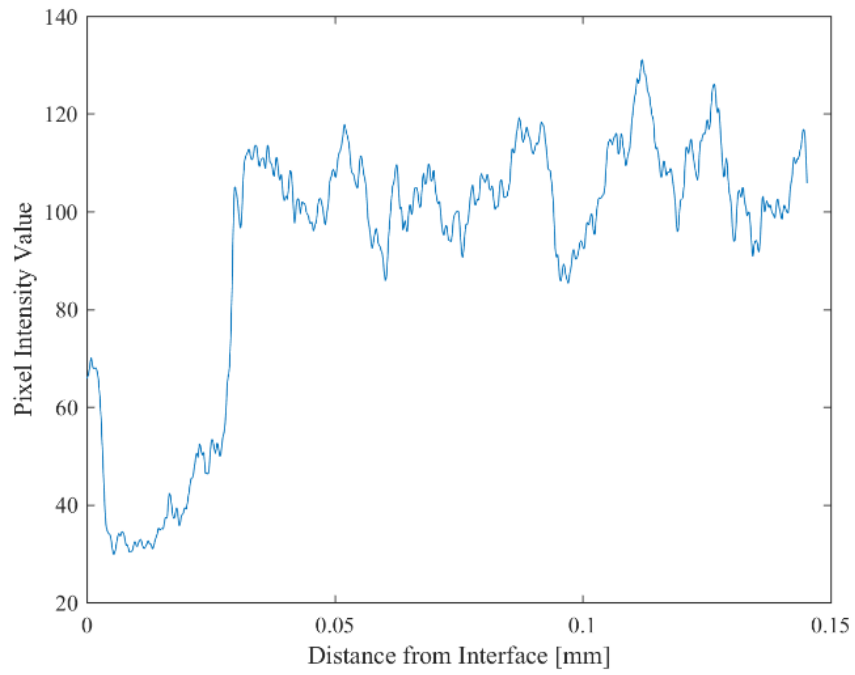*Figure 9–35: Image intensity region of interest - sample 5 middle*
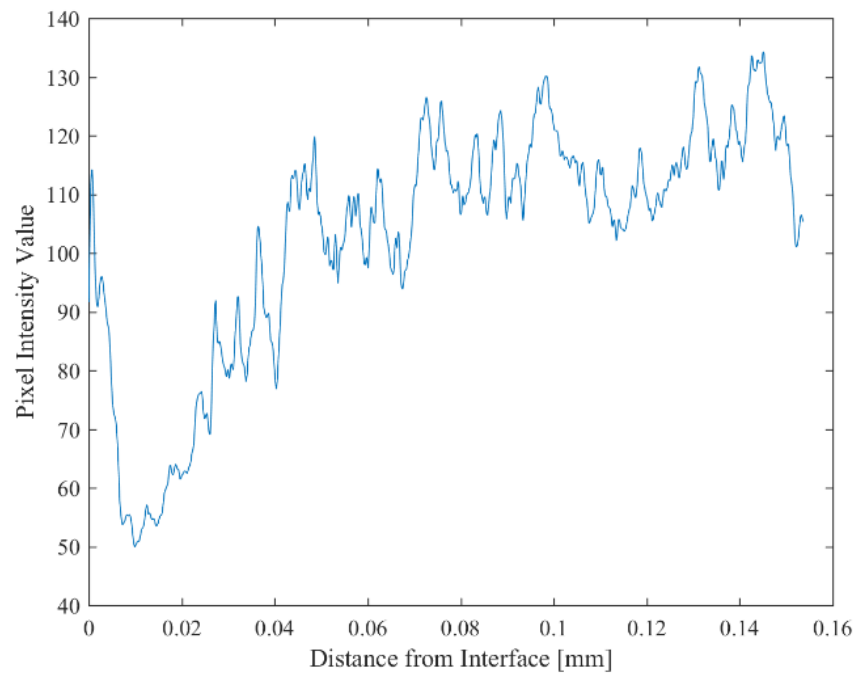
Figure 9–36: SZ image intensity plot - sample 5 middle

Figure 9–37: Etched material near the screw-workpiece interface – sample 5 bottom
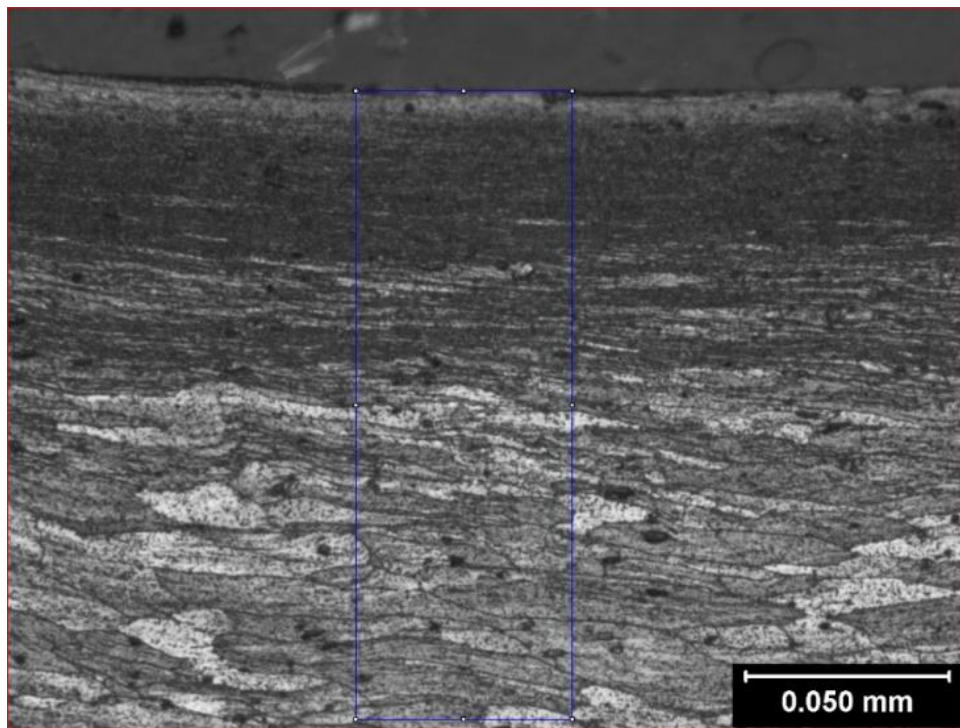
Figure 9–38: Image intensity region of interest - sample 5 bottom

153
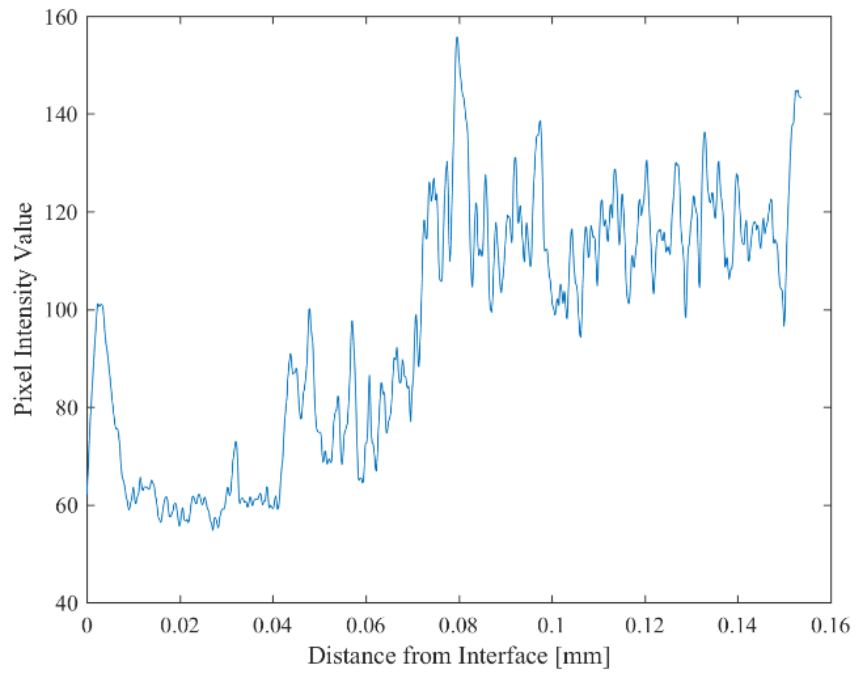
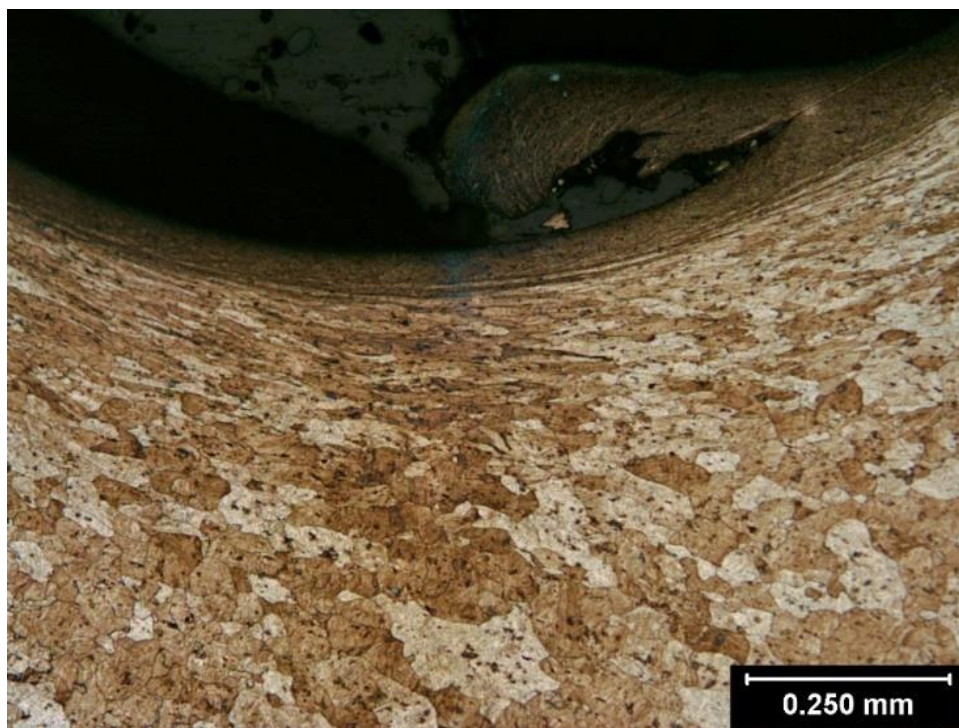*Figure 9–39: SZ image intensity plot - sample 5 bottom*

Figure 9–40: Etched material near the screw-workpiece interface – sample 6 top

154
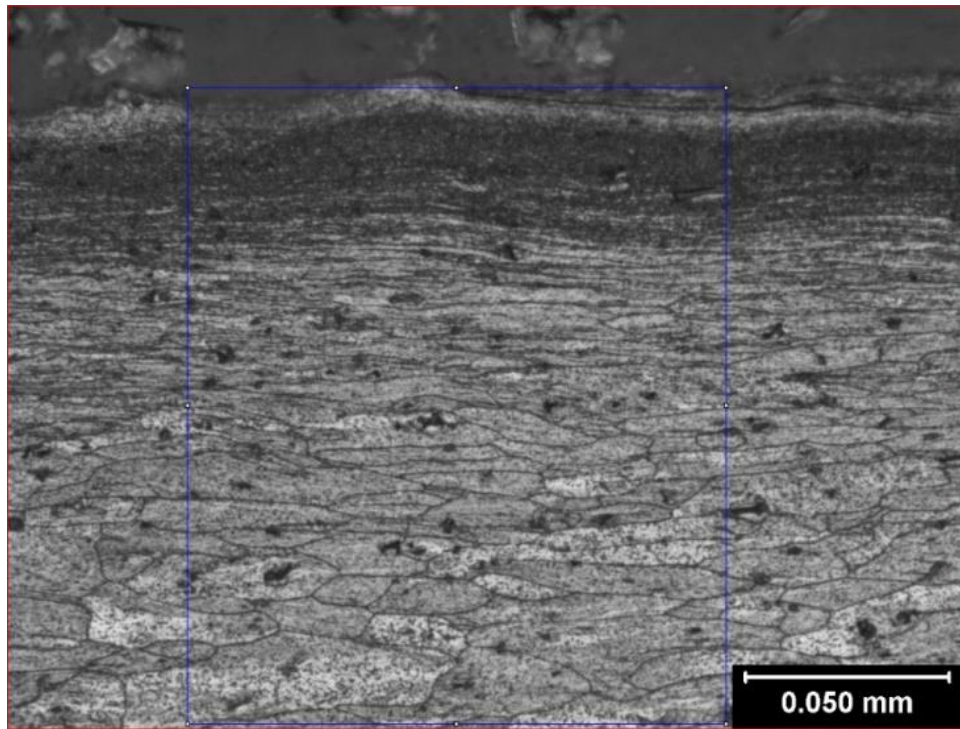
Figure 9–41: Image intensity region of interest - sample 6 top
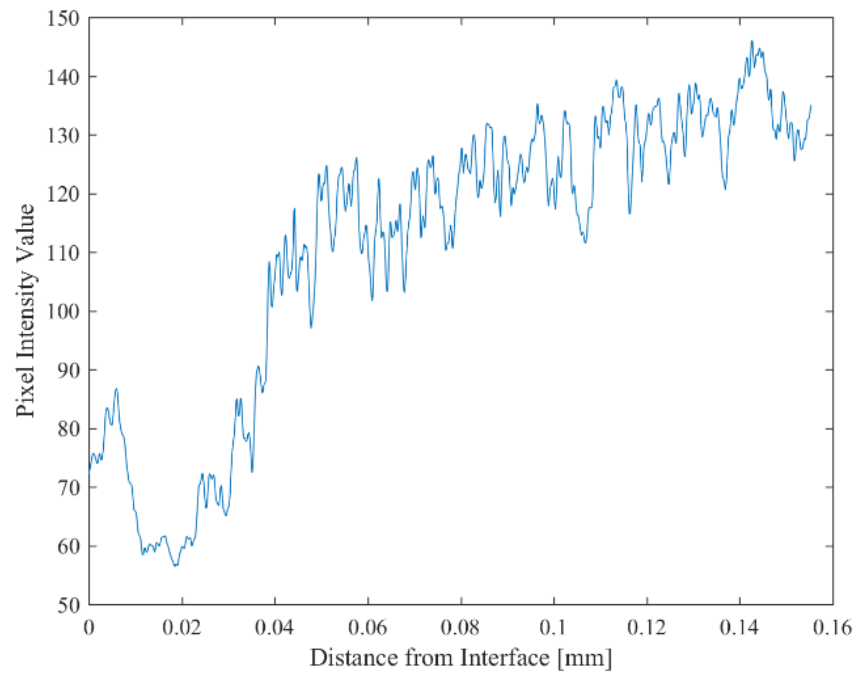
Figure 9–42: SZ image intensity plot - sample 6 top
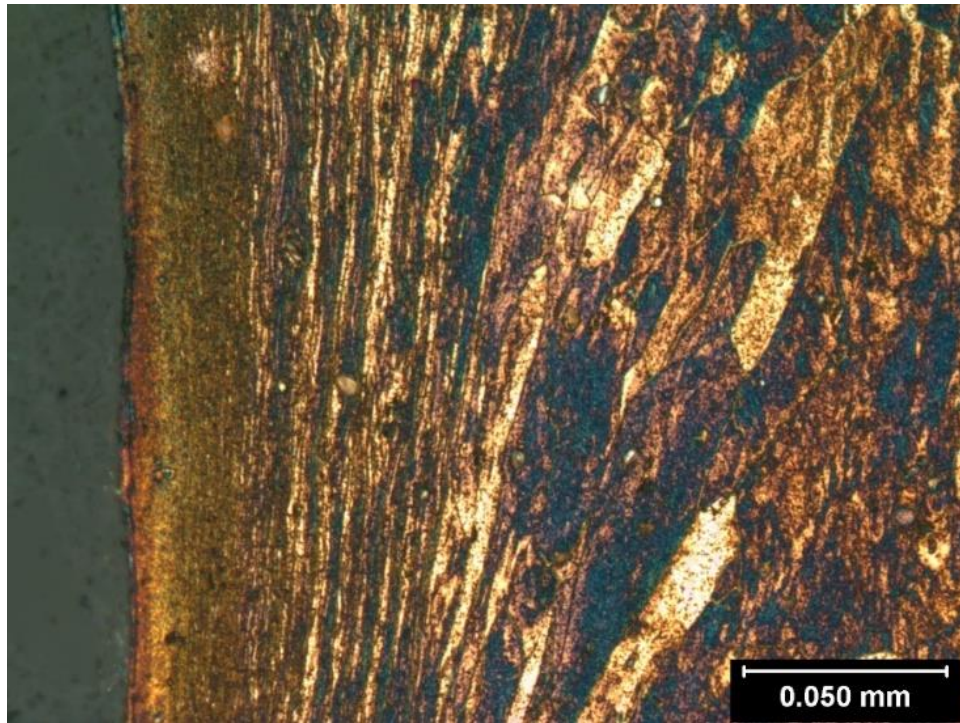
Figure 9–43: Etched material near the screw-workpiece interface – sample 6 middle
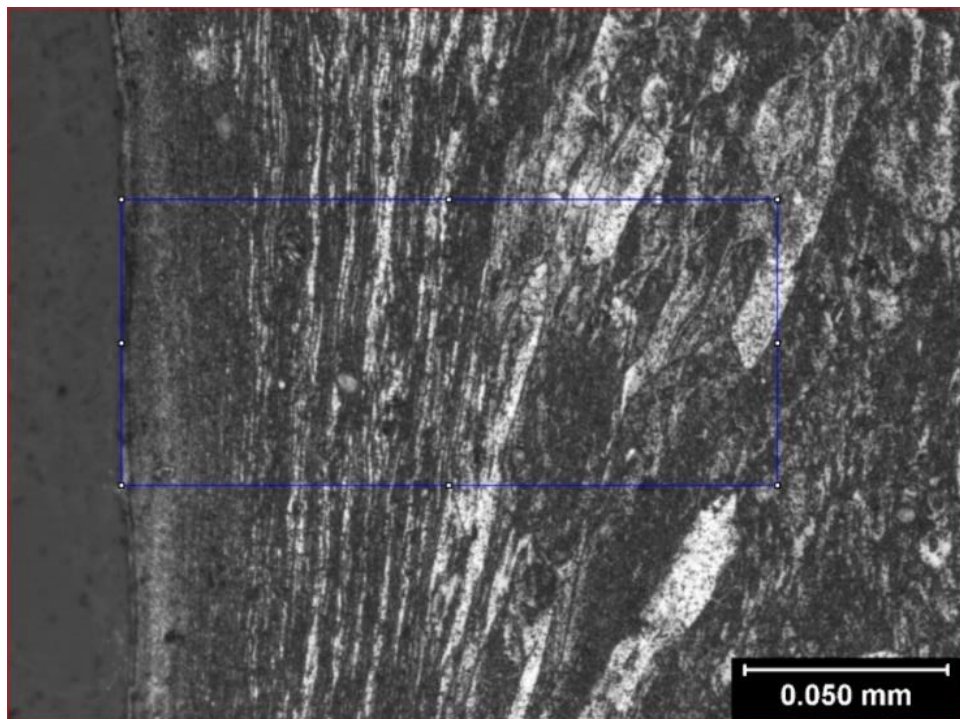
Figure 9–44: Image intensity region of interest - sample 6 middle
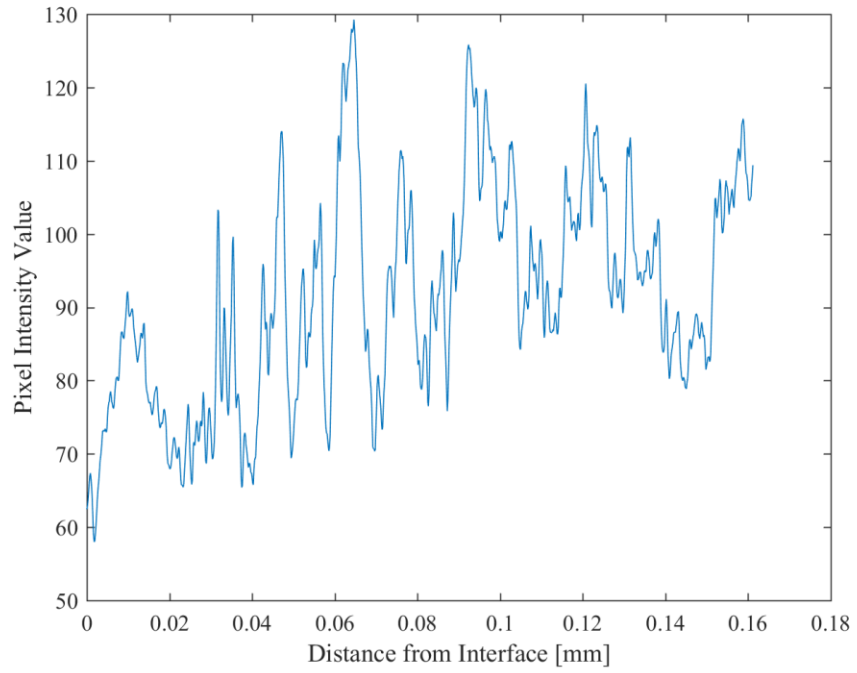
Figure 9–45: SZ image intensity plot - sample 6 middle

Figure 9–46: Etched material near the screw-workpiece interface – sample 6 bottom
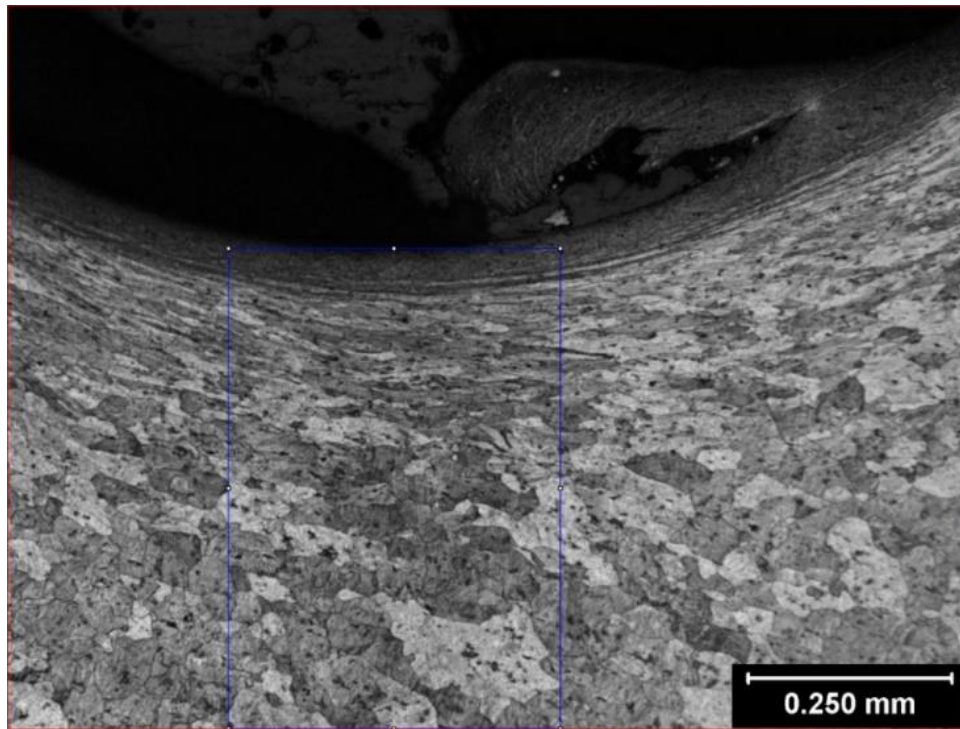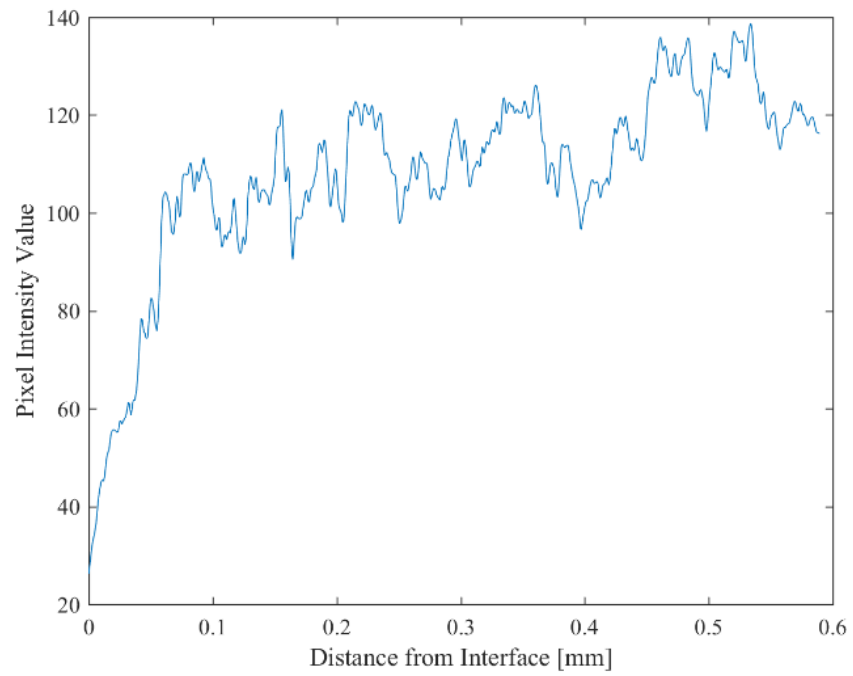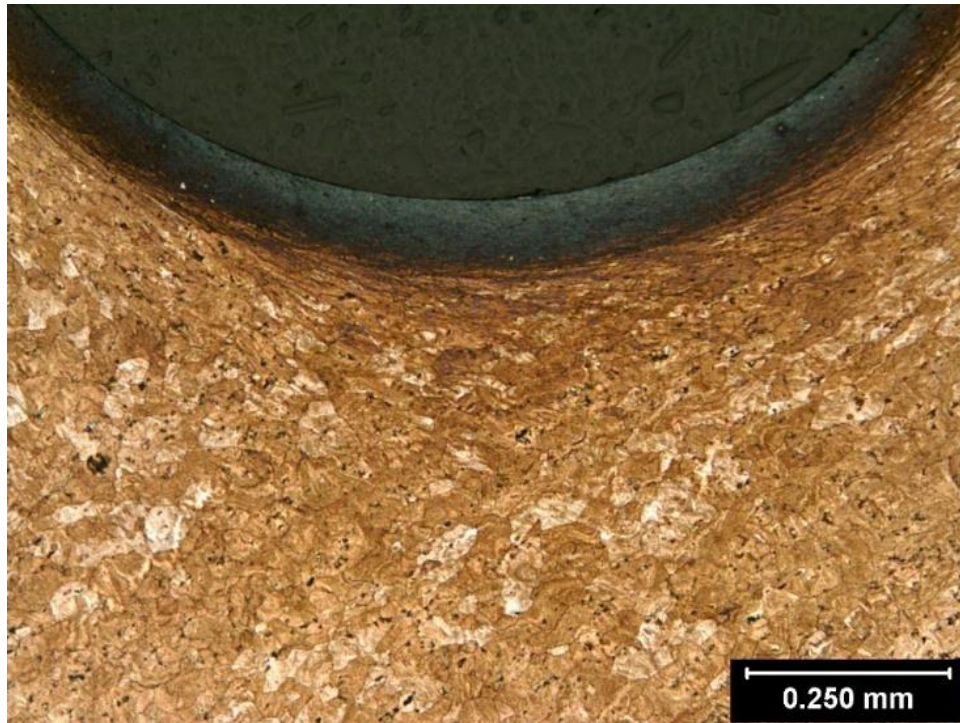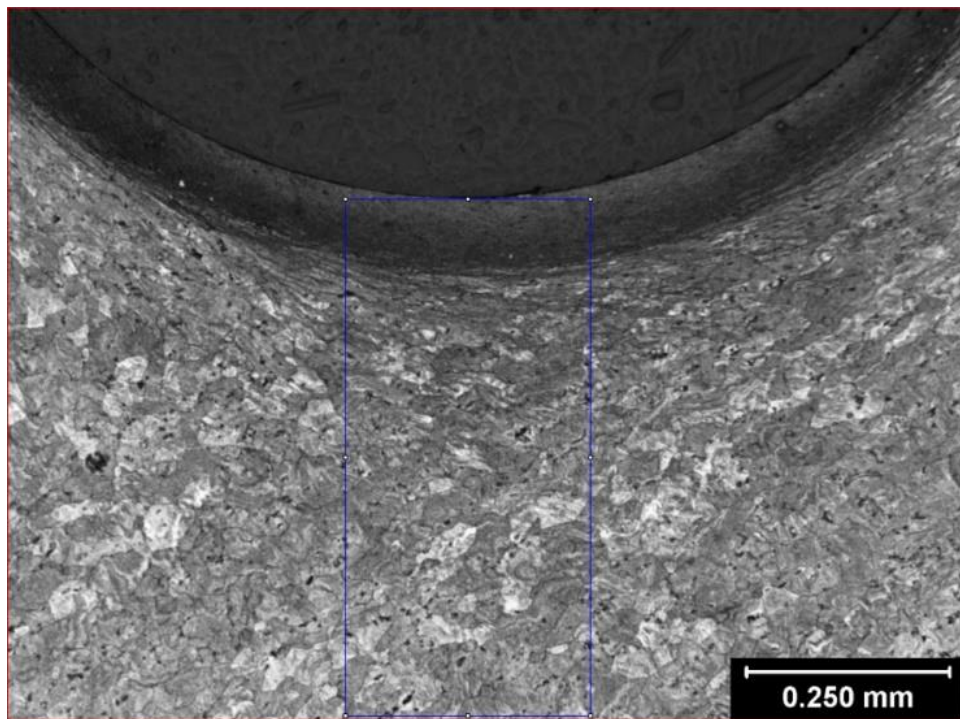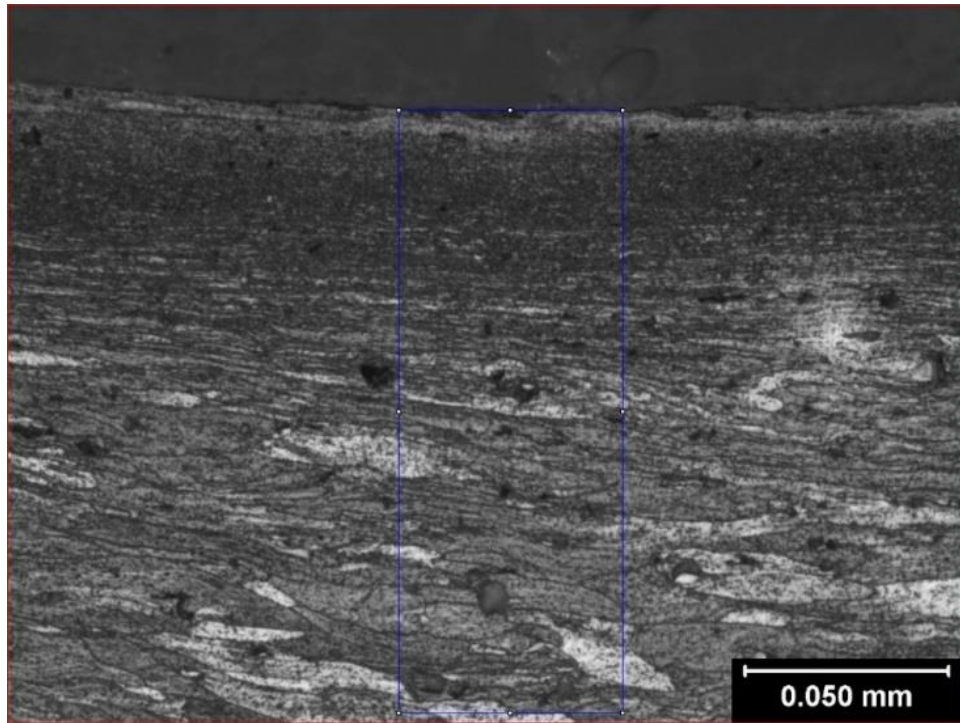
Figure 9–47: Image intensity region of interest - sample 6 bottom
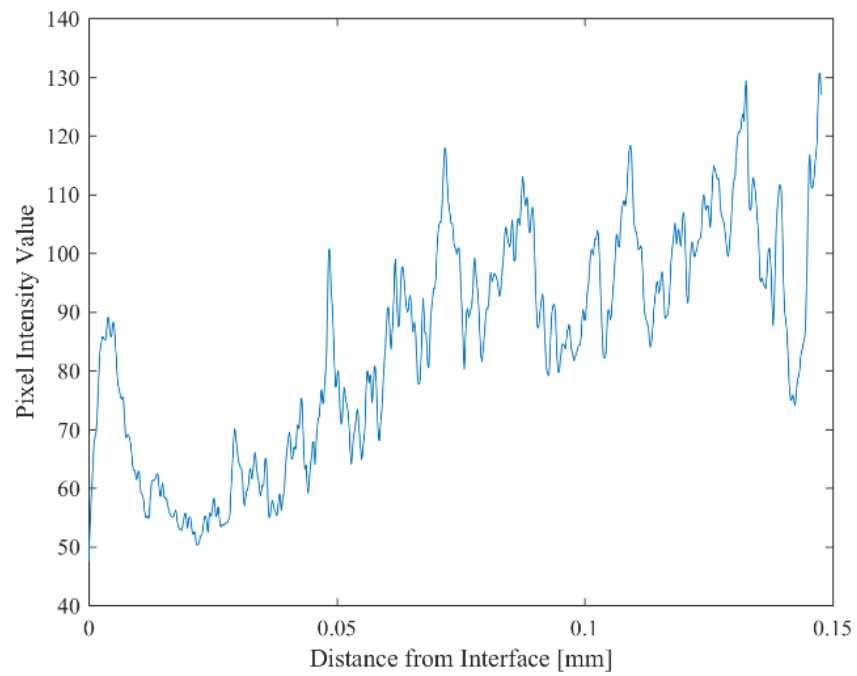
Figure 9–48: SZ image intensity plot - sample 6 bottom

158
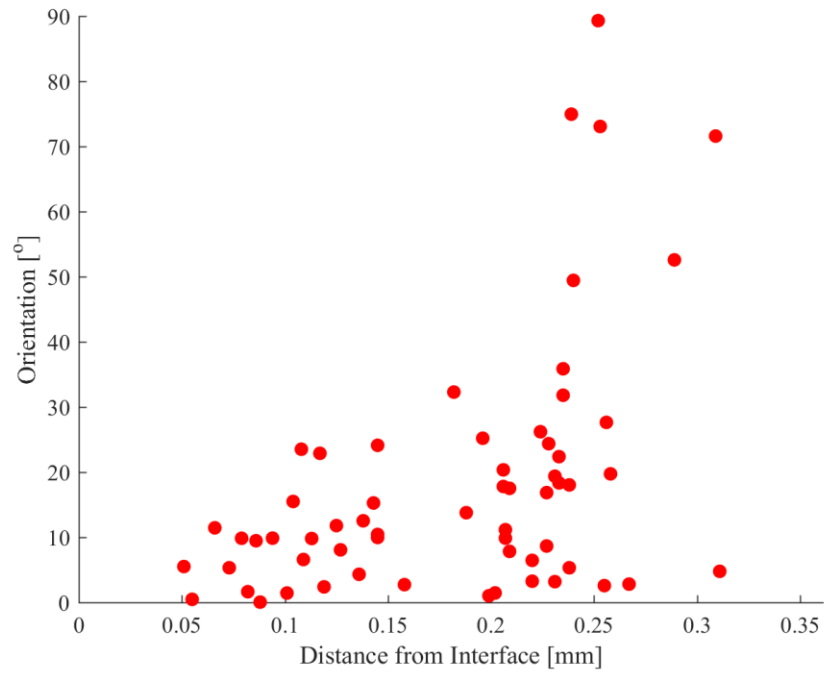
Figure 9–49: Grain orientations – sample 1 top
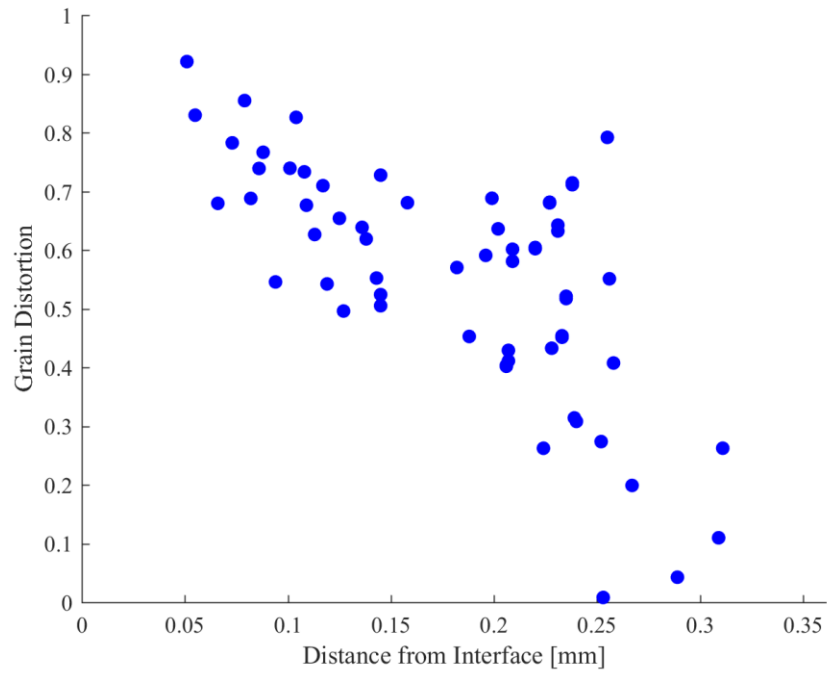
Figure 9–50: Grain distortions – sample 1 top
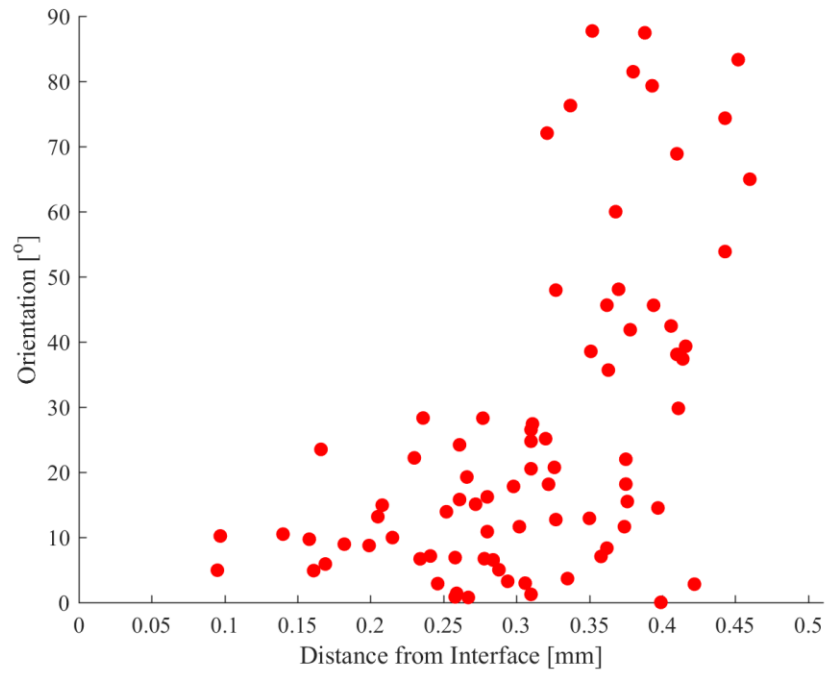
Figure 9–51: Grain orientations – sample 2 top
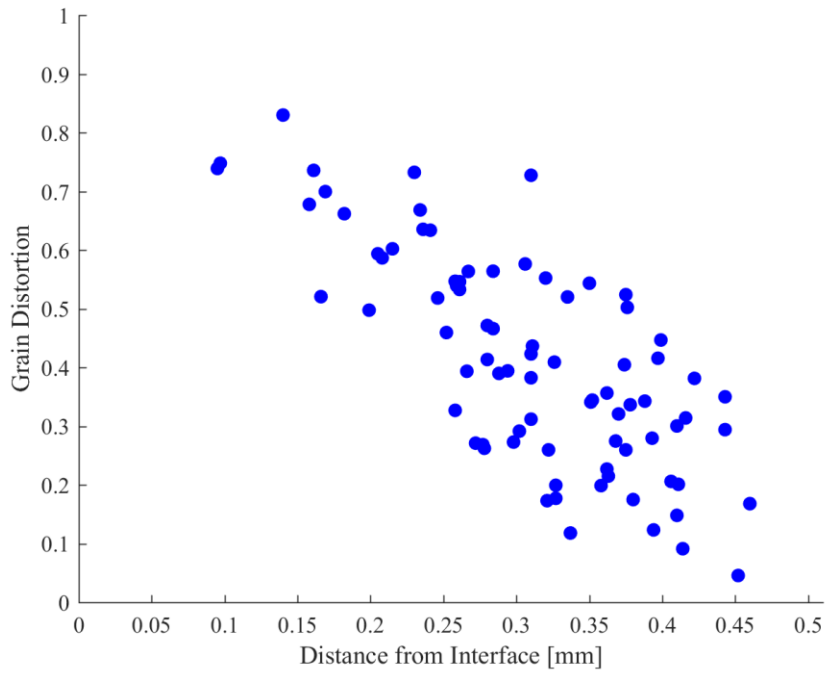
Figure 9–52: Grain distortions – sample 2 top

160
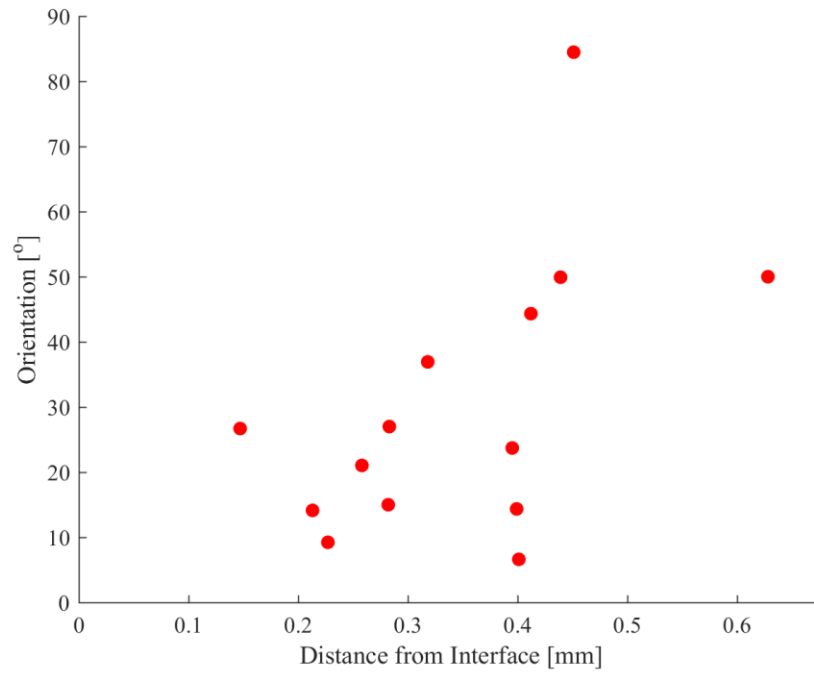
Figure 9–53: Grain orientations – sample 2 middle
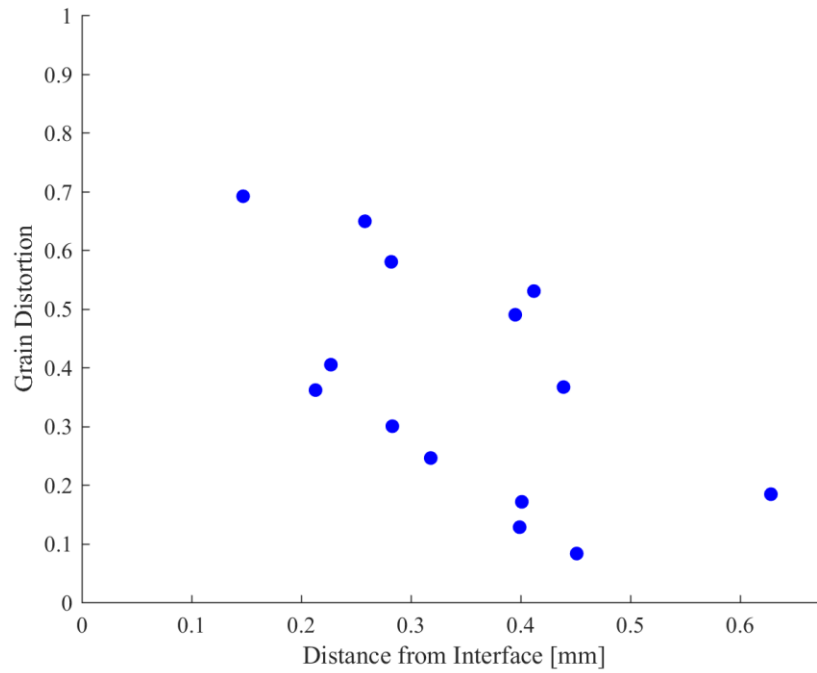
Figure 9–54: Grain distortions – sample 2 middle

161
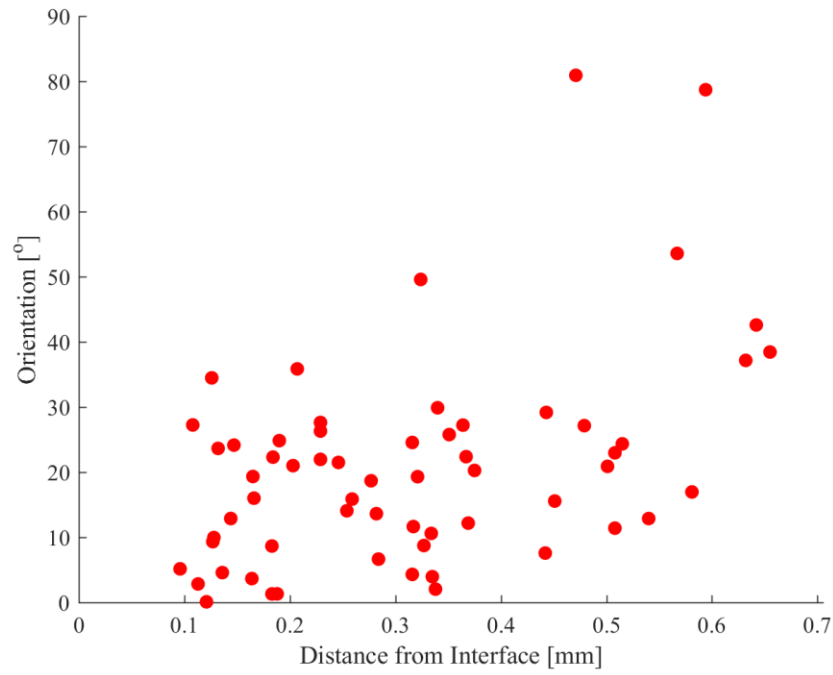
Figure 9–55: Grain orientations – sample 2 bottom
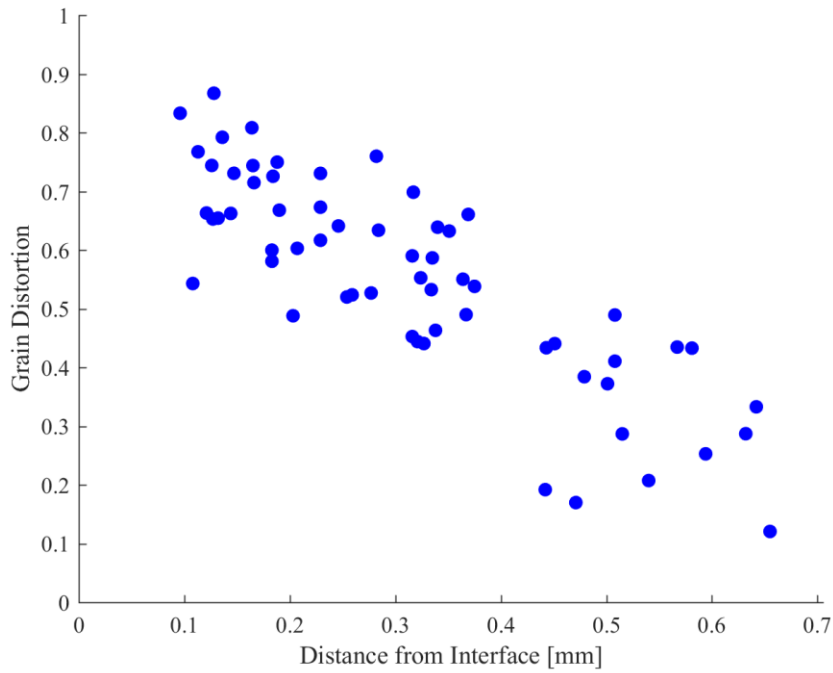
Figure 9–56: Grain distortions – sample 2 bottom

162
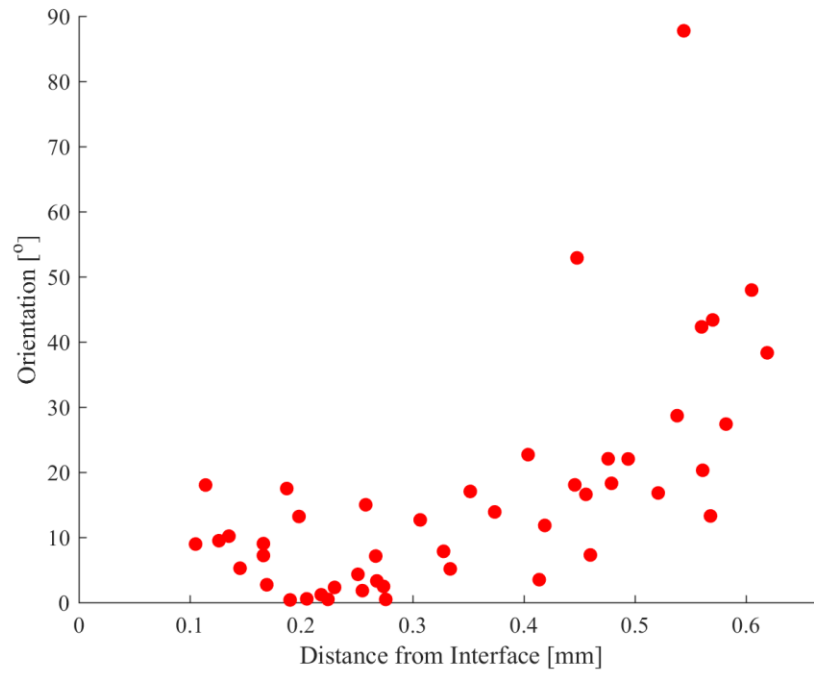
Figure 9–57: Grain orientations – sample 3 top
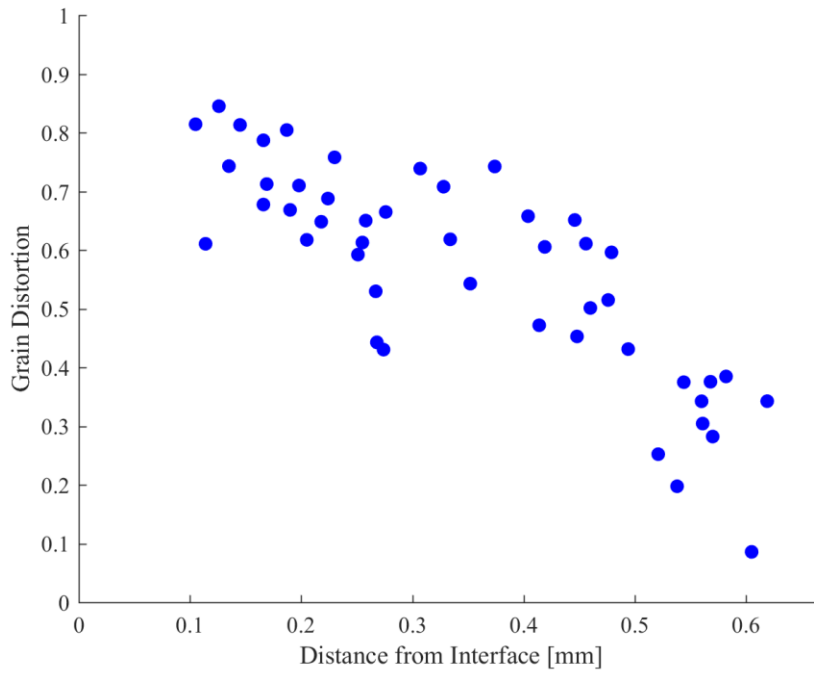
Figure 9–58: Grain distortions – sample 3 top

163
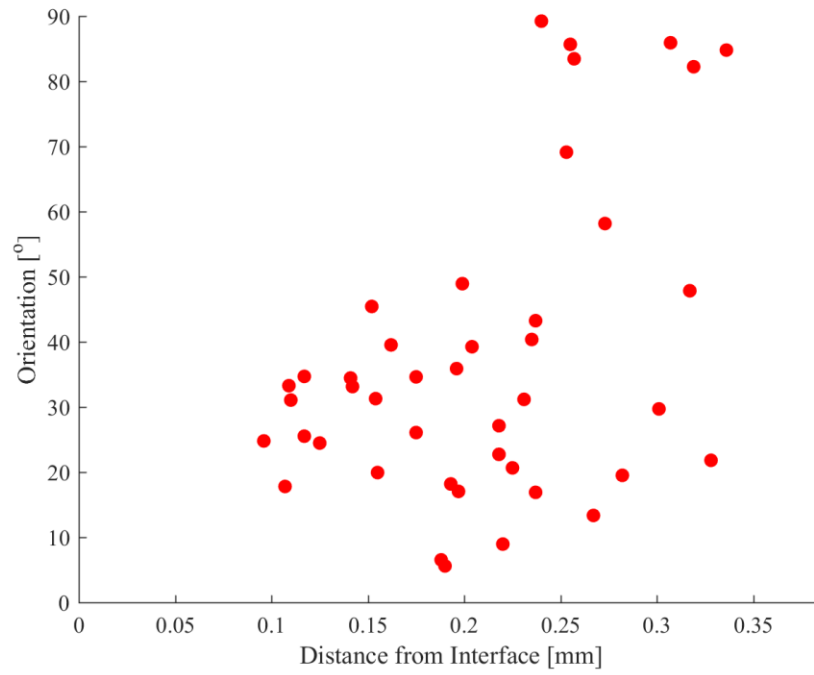
Figure 9–59: Grain orientations – sample 3 middle
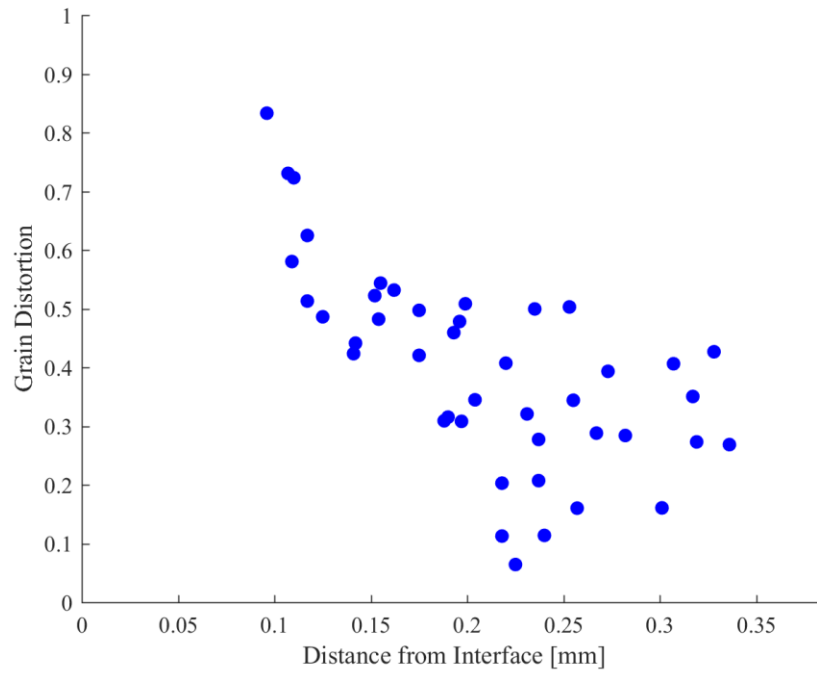
Figure 9–60: Grain distortions – sample 3 middle

164
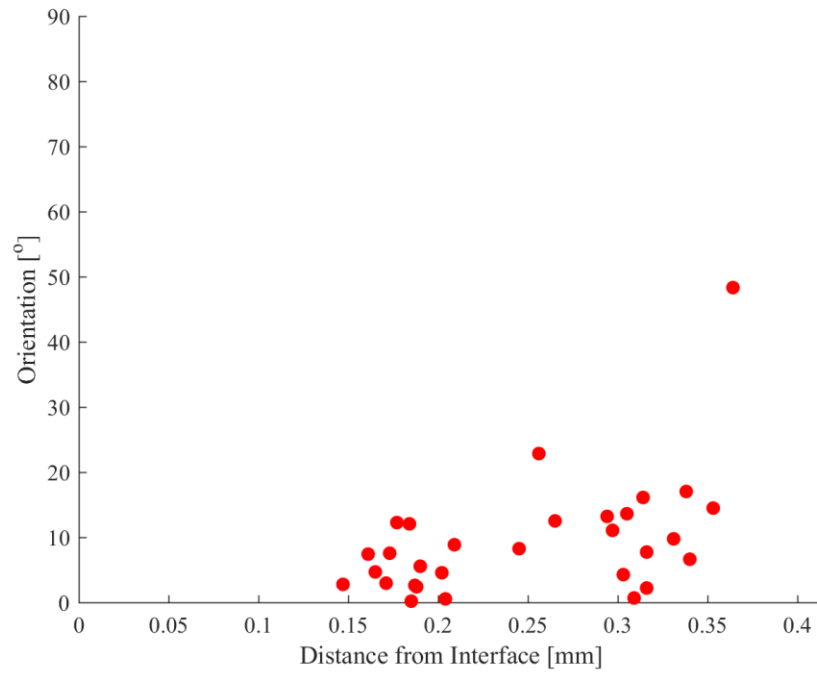
Figure 9–61: Grain orientations – sample 3 bottom
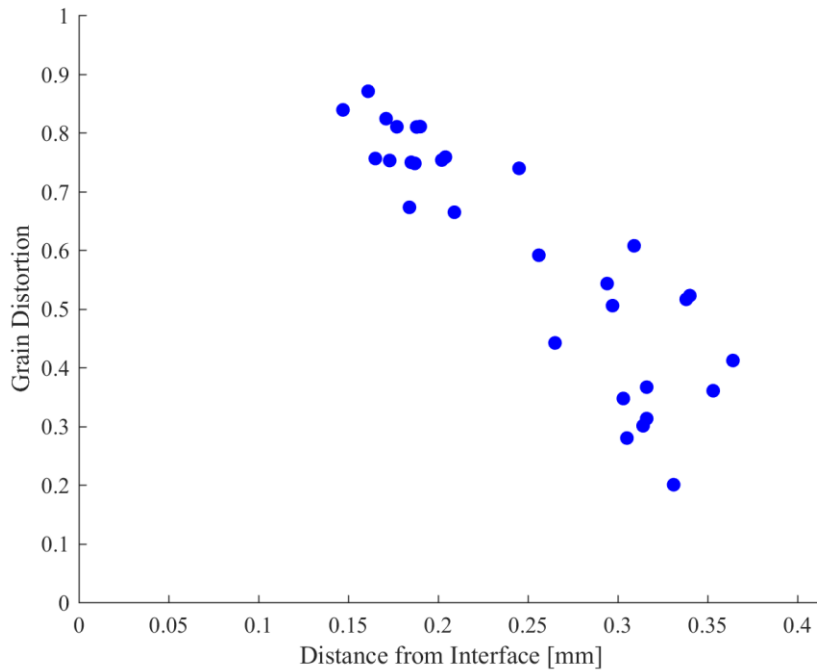
Figure 9–62: Grain distortions – sample 3 bottom

165
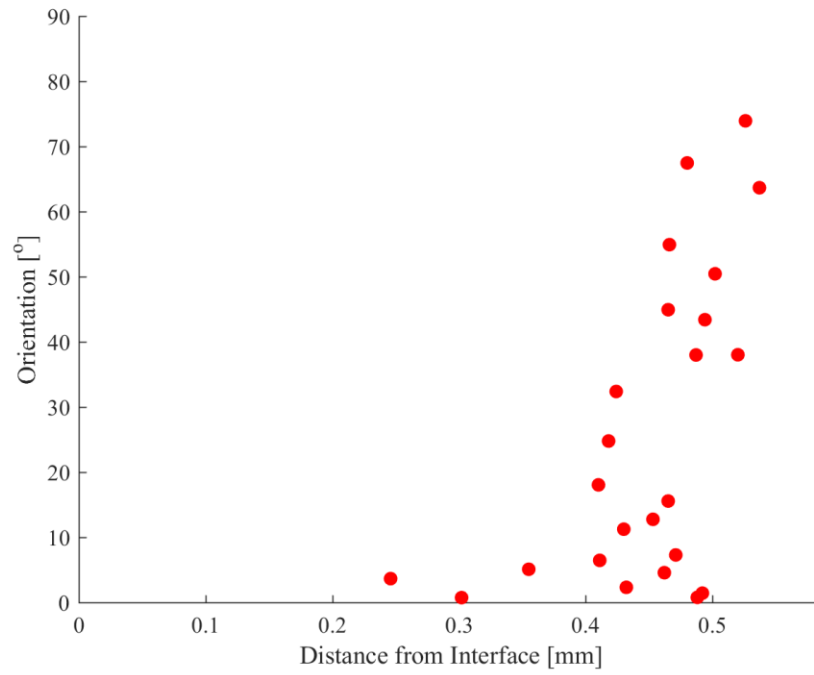
Figure 9–63: Grain orientations – sample 4 top
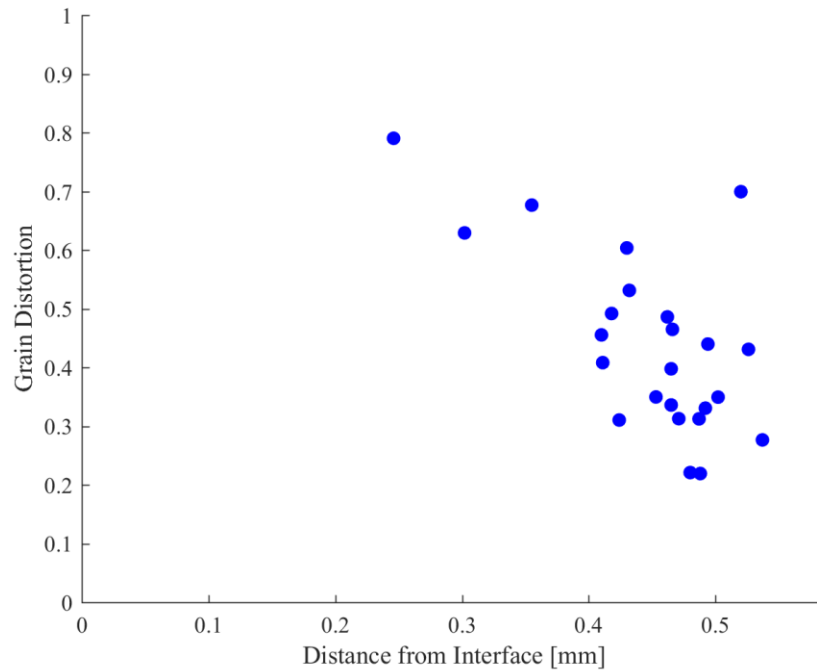
Figure 9–64: Grain distortions – sample 4 top
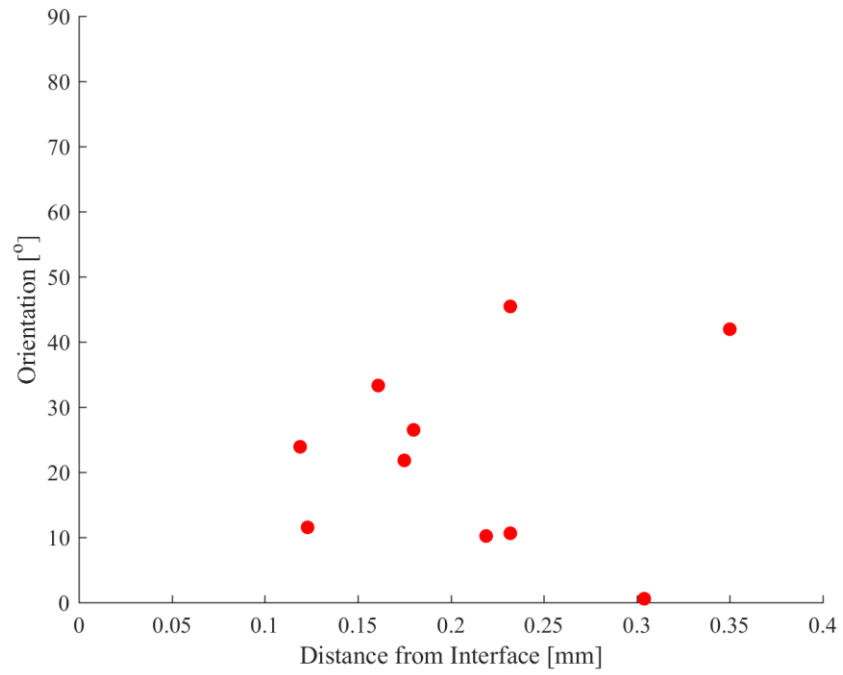
Figure 9–65: Grain orientations – sample 4 middle
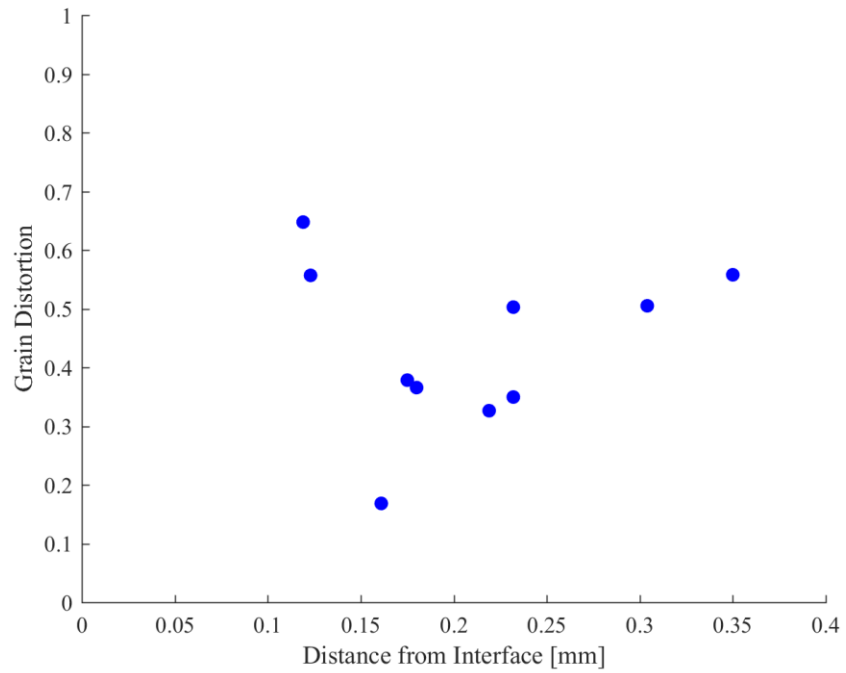
Figure 9–66: Grain distortions – sample 4 middle

167
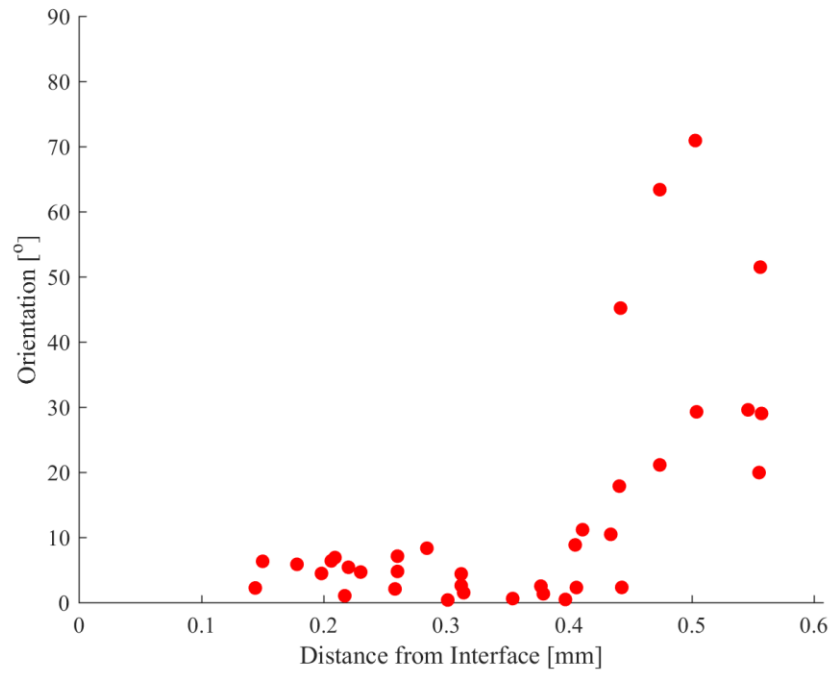
Figure 9–67: Grain orientations – sample 4 bottom
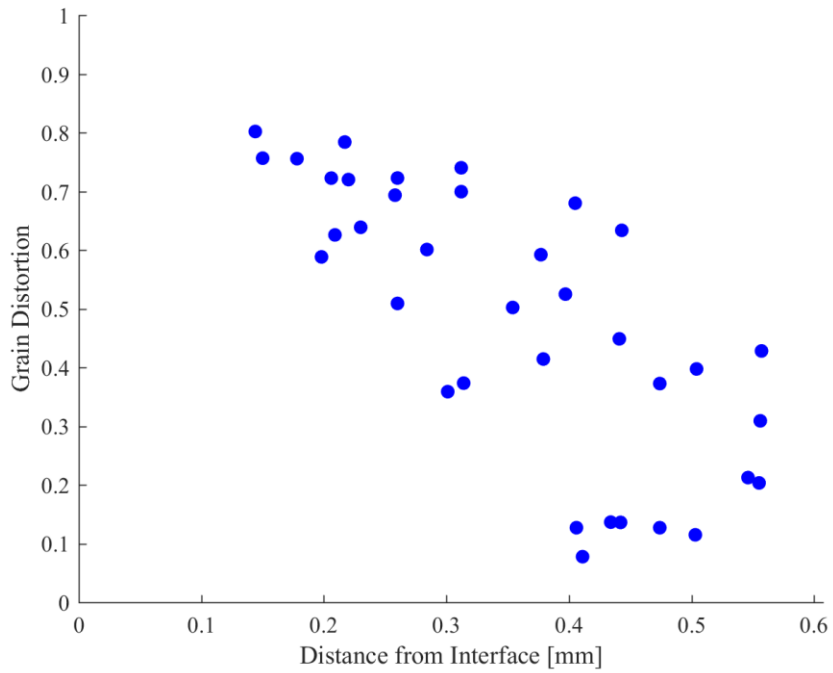
Figure 9–68: Grain distortions – sample 4 bottom

168
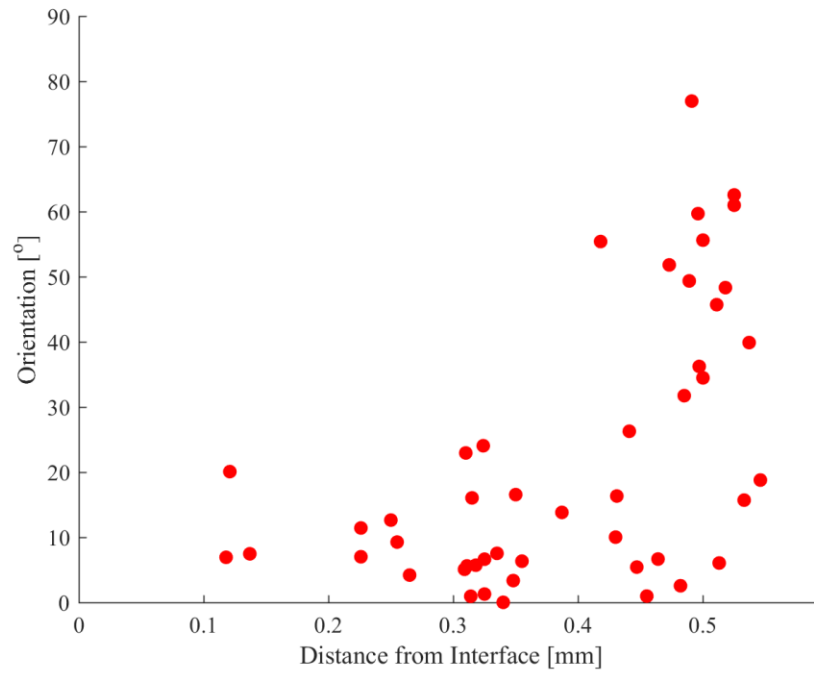
Figure 9–69: Grain orientations – sample 5 top
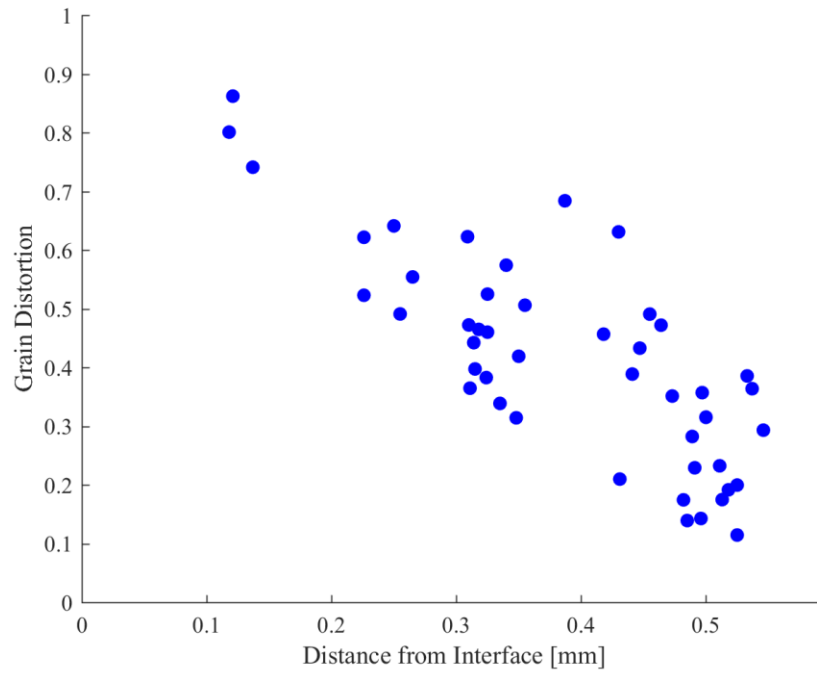
Figure 9–70: Grain distortions – sample 5 top

169
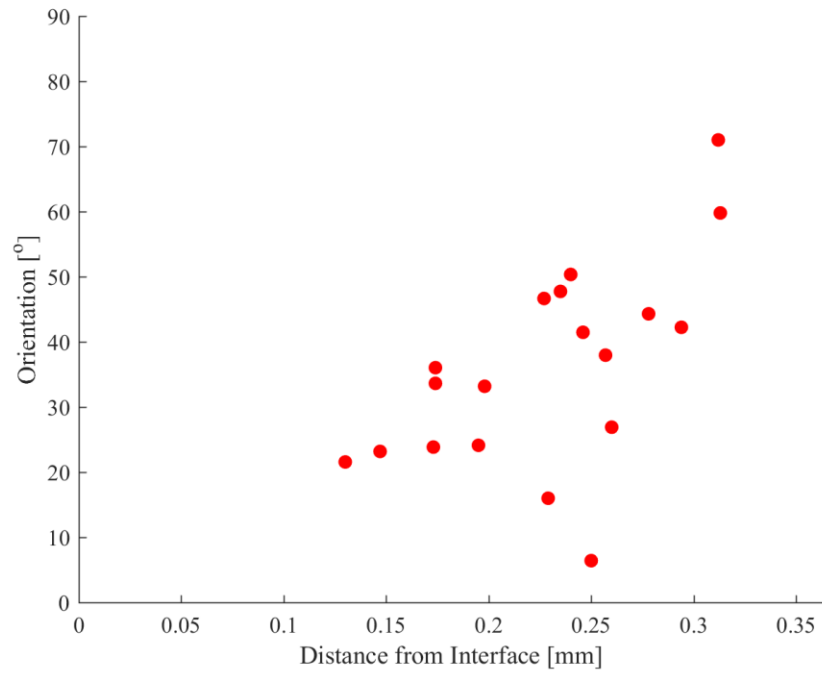
Figure 9–71: Grain orientations – sample 5 middle
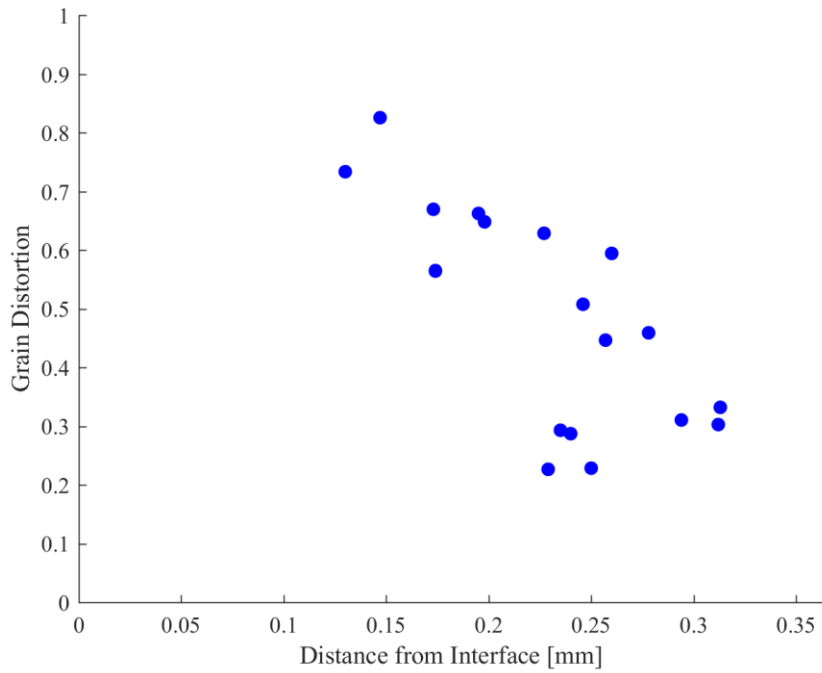
Figure 9–72: Grain distortions – sample 5 middle

170
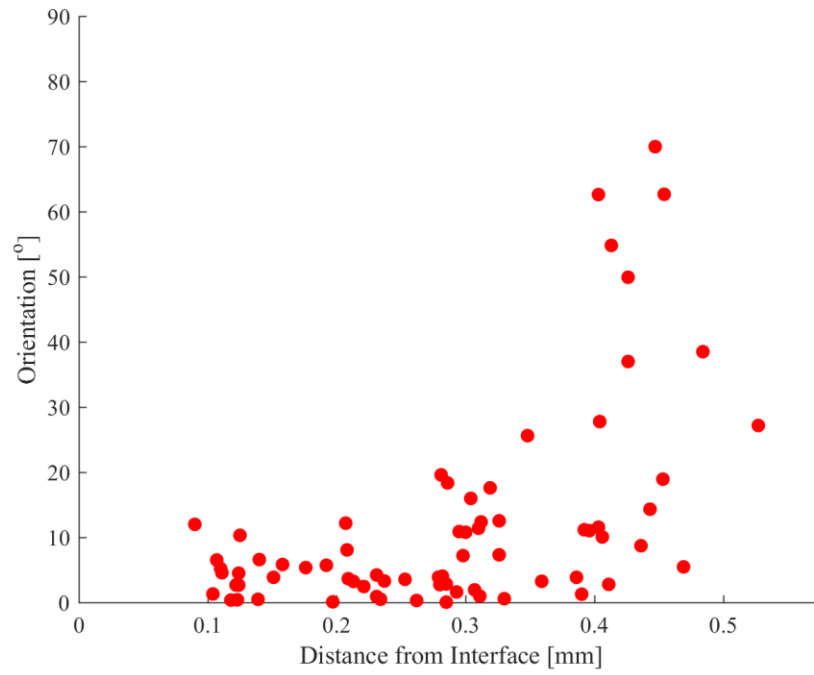
Figure 9–73: Grain orientations – sample 5 bottom
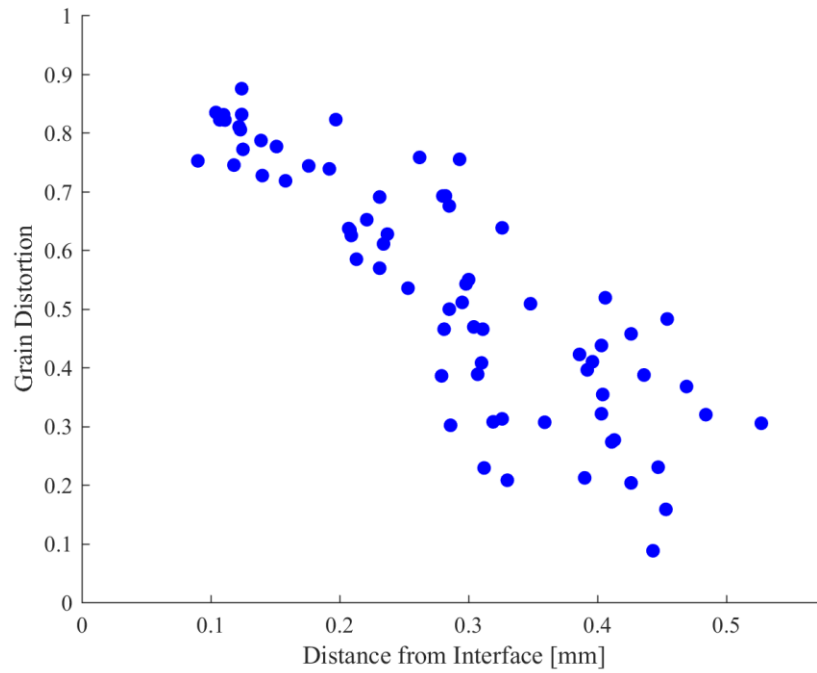
Figure 9–74: Grain distortions – sample 5 bottom

171
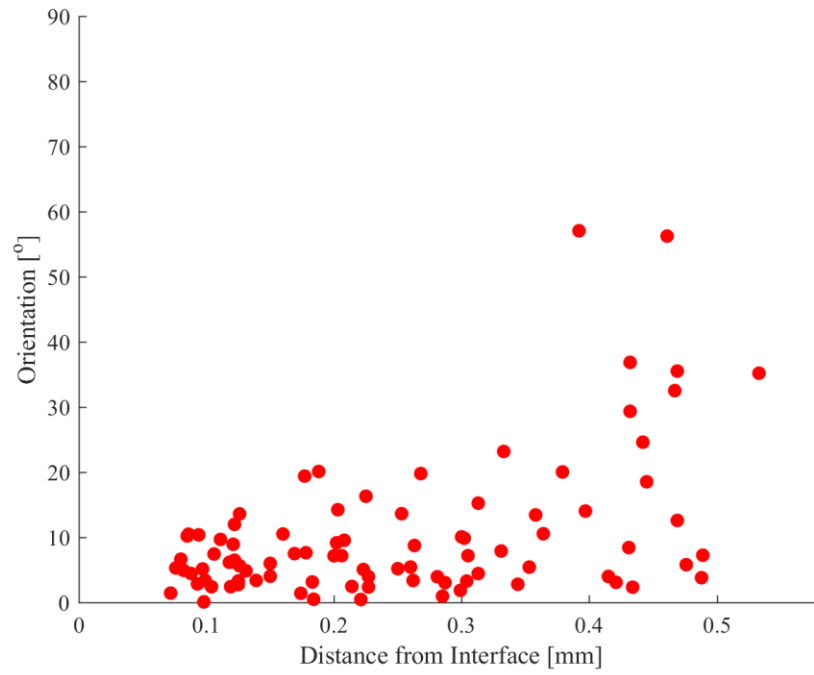
Figure 9–75: Grain orientations – sample 6 top
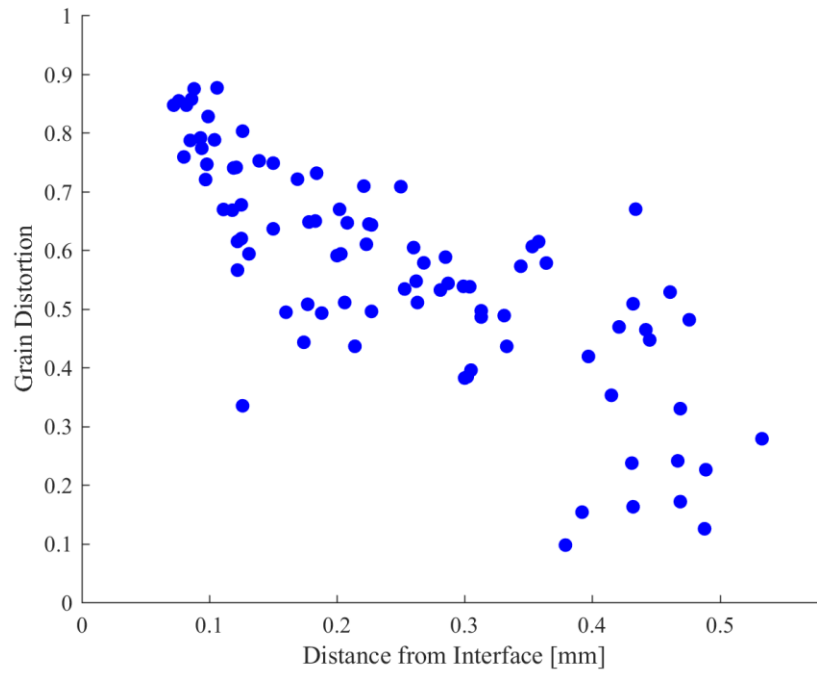
Figure 9–76: Grain distortions – sample 6 top

172
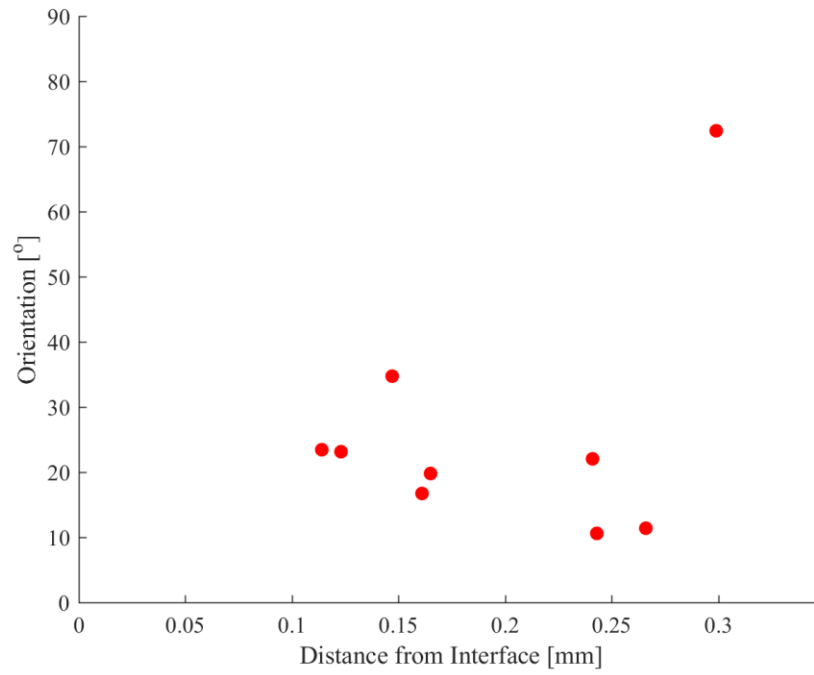
Figure 9–77: Grain orientations – sample 6 middle
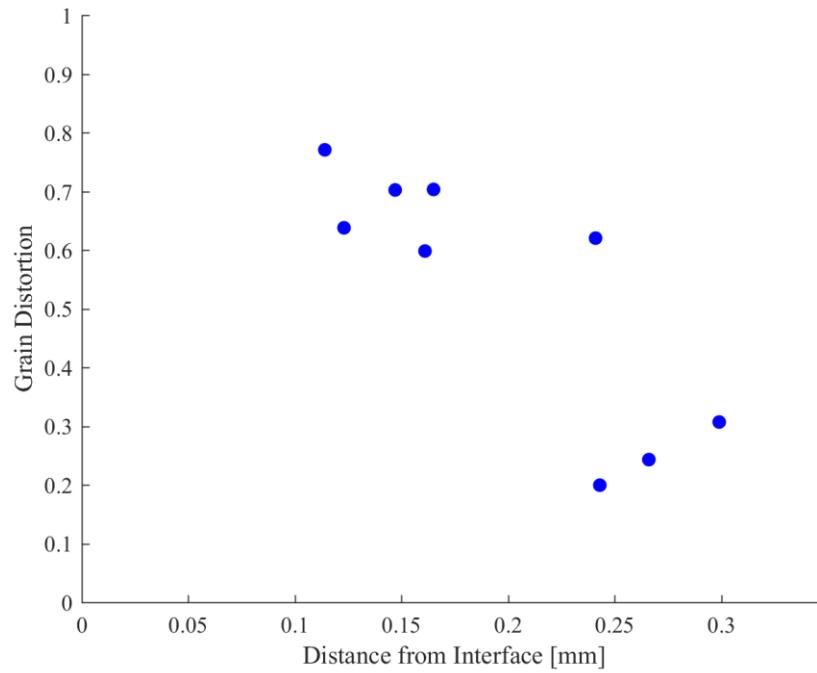
Figure 9–78: Grain distortions – sample 6 middle

173
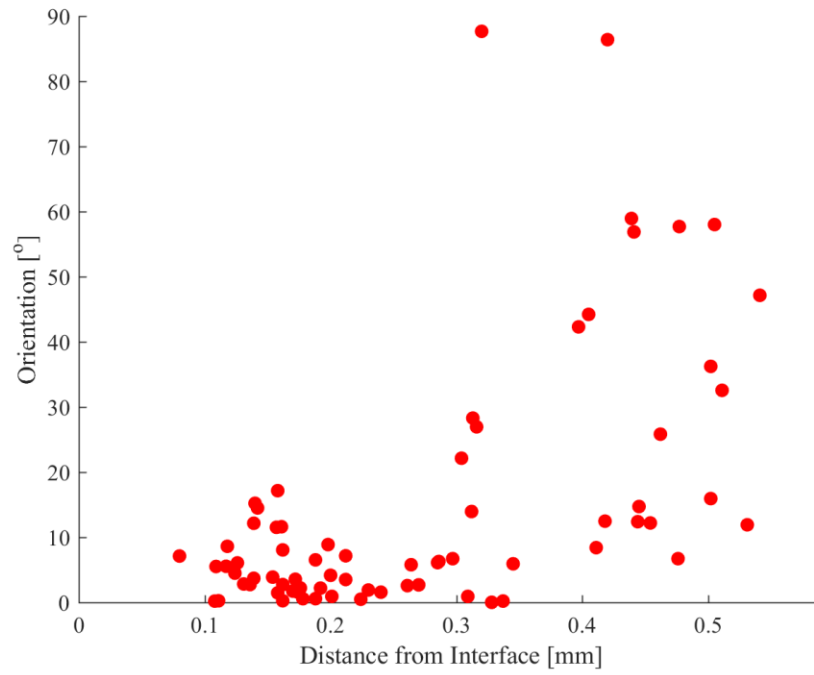
Figure 9–79: Grain orientations – sample 6 bottom
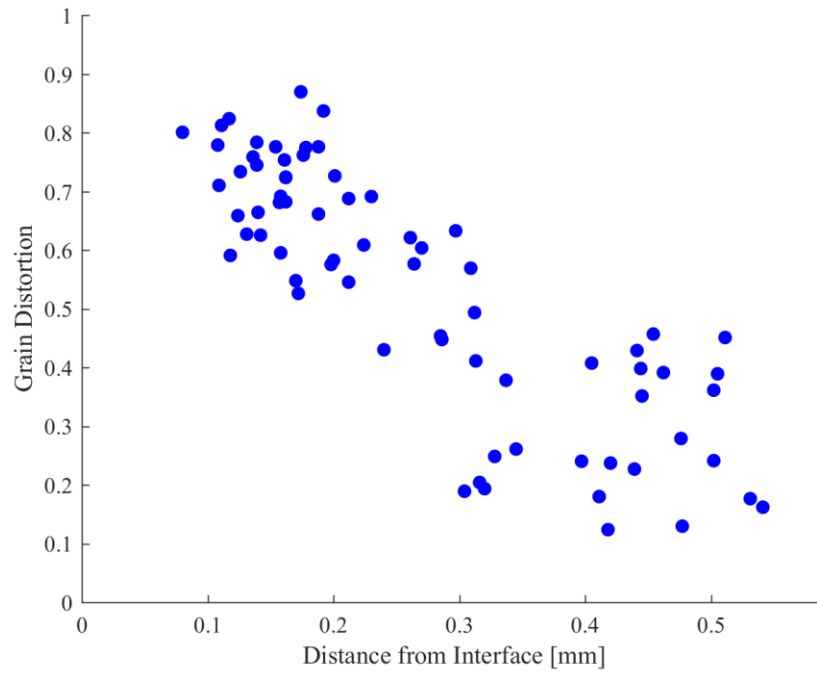
Figure 9–80: Grain distortions – sample 6 bottom

174

9.2. Grain Measurement MATLAB Code

```matlab
% Get the orginal image & show
[fileName, pathName] = uigetfile('*.tif;*.png','Select the Picture file');
I = fullfile(pathName, fileName);
I = imread(I);

% Background subtraction; Use Morphological Opening to Estimate the Background
background = imopen(I,strel('disk',7));
I2 = I - background;

% Get the Black and white Image
BW = im2bw(I2,0.15);

s = regionprops(pure, 'Orientation','MajorAxisLength',
'MinorAxisLength','Eccentricity', 'Centroid');

imshow(I)
hold on

phi = linspace(0,2*pi,50);
cosphi = cos(phi);
sinphi = sin(phi);

for k = 1:length(s)
    xbar = s(k).Centroid(1);
    ybar = s(k).Centroid(2);

    a = s(k).MajorAxisLength/2;
    b = s(k).MinorAxisLength/2;

    theta = pi*s(k).Orientation/180;
    R = [ cos(theta)   sin(theta)
        -sin(theta)   cos(theta)];

    xy = [a*cos(phi); b*sin(phi)];
    xy = R*xy;

    x = xy(1,:) + xbar;
    y = xy(2,:) + ybar;

    figure(1)
    plot(x,y,'r','LineWidth',.2);
    text(xbar,ybar,num2str(k),'Color','w','FontSize',8)

    AR(k)=b/a;

end
hold off

s=struct2cell(s);
Orientation=cell2mat(s(5,:));
MajorAxisLength=cell2mat(s(2,:));
MinorAxisLength=cell2mat(s(3,:));
Eccentricity=cell2mat(s(4,:));
Centroid=cell2mat(s(1,:));
CentroidX=Centroid(1:2:length(Centroid));
CentroidY=Centroid(2:2:length(Centroid));
```

9.3. Finite Volume MATLAB Code

```matlab
%clear all
clearvars -except WeberTimeRaw RPMDataRaw TorqueDataRaw DepthRaw EndloadRaw
DepthGradientRaw CamTimeRaw MaxTempRaw Cursor1Raw Cursor2Raw Cursor3Raw
Cursor4Raw Cursor5Raw
clc
fclose('all');
close all

tic

%%%Workpiece Data%%%
%Material: 6061-T6%
PartThick=1.6;                            %[mm] workpiece thickness
PartThick=PartThick/1000;                 %[m] workpiece thickness
PartDiam=40;  %60                              %[mm] workpiece width
PartDiam=PartDiam/1000;                   %[m] workpiece width
%%%Material Properties of Al Workpiece at 274[K] from MPDB%%%
Kwp=167; %154.9                                %[W/m-K]  intialize thermal
conductivity of workpiece
Cpwp=896; %1015                                %[J/kg-K] initialize specific
heat of workpiece
Densitywp=2700;                           %[kg/m^3] initialize density of
workpiece
thermaldiffwp=Kwp/(Cpwp*Densitywp);       %[m^2/s] thermal diffusivity of Al
workpiece


Beta=0.9;                                 %Inelastic Heat Fraction
Eff=0.95;                                 %Frictional Sliding Efficiency

%%%Screw Data%%%
%Material: 4340%
ScrewLength=20;   %18.4                      %[mm] screw length
ScrewLength=ScrewLength/1000;             %[m] screw length
rscrewmax=2.5;                              %[mm] max screw radius
rscrewmax=rscrewmax/1000;                      %[m] max screw radius
rscrewminor=2.0095;                        %[mm] screw minor radius
rscrewminor=rscrewminor/1000;                  %[m] screw minor radius
pitch=0.8;                                %[mm] screw pitch
pitch=pitch/1000;                         %[m] screw pitch
lead=pitch;                               %[m] screw lead = screw pitch
(single start thread)
crestangle=30;                            %[degrees] crest angle for iso
standard thread

%%%Material Properties of Steel Screw%%%
Kscrew=36.1;                                   %[W/m-K]  thermal
conductivity of screw
Densityscrew=7850;                             %[kg/m^3] density of screw
Cpscrew=475;                                   %[J/kg-K] specific heat of
screw
thermaldiffscrew=Kscrew/(Cpscrew*Densityscrew);    %thermal diffusivity of
Steel screw
```

176

```matlab
%%%%%%%%%%%%%%%%%%%%%%%%%%%%%%%%%%%%%%%%%%%%%%%%%%%%%%%%%%%%%%%%%%%%%%%%
%Load Experimental Data%
%%%%%%%%%%%%%%%%%%%%%%%%%%%%%%%%%%%%%%%%%%%%%%%%%%%%%%%%%%%%%%%%%%%%%%%%

filename='Sample27Comb_V2.xlsx';
WeberTimeRaw=xlsread(filename,'A:A');
RPMDataRaw=xlsread(filename,'B:B');
TorqueDataRaw=xlsread(filename,'C:C');
DepthRaw=xlsread(filename,'D:D');
EndloadRaw=xlsread(filename,'E:E');
CamTimeRaw=xlsread(filename,'G:G');
MaxTempRaw=xlsread(filename,'H:H');
Cursor1Raw=xlsread(filename,'I:I');
Cursor2Raw=xlsread(filename,'J:J');
Cursor3Raw=xlsread(filename,'K:K');
Cursor4Raw=xlsread(filename,'L:L');

FricTempData=load('FricTempData.mat');
FricData=load('FricData.mat');


%%%Save Imported Experimental Data%%%
FricTempData=FricTempData.FricTempData;
FricData=FricData.FricData;

%%Import Curl CA Percent Lookup Table
CurlCAPerc=load('CurlCAPerc_V2.mat');
CurlCAPerc=CurlCAPerc.Output;

%%%%%%%%%%%%%%%%%%%%%%%%%%%%%%%%%%%%%%%%%%%%%%%%%%%%%%%%%%%%%%%%%%%%%%%%
%Define number of nodes in workpiece, time step, ambient temperature,BC values,
and nodal setup
%%%%%%%%%%%%%%%%%%%%%%%%%%%%%%%%%%%%%%%%%%%%%%%%%%%%%%%%%%%%%%%%%%%%%%%%

nthick=4;                    %number of elements through workpiece thickness
nwidth=30;                     %Multiples of 8 due to rmax node being whole
number  %number of elements along workpiece width
nlength=1;                     %number of elements around theta direction

Tambient=26;        %23;                      %[C] ambient temperature
Tambient=Tambient+273.15;      %[K] ambient temperature
hcomb=22;                      %[W/m^2-K] combined convection radiation coeff

elementwidth=(PartDiam/2)/nwidth;      %[m] calculates element width
elementthick=PartThick/nthick;         %[m] calculates element thickness

dr=elementwidth;                       %define nodal space in r direction
dz=elementthick;                       %define nodal space in z direction
dtheta=2*pi/nlength;                   %define nodal space in theta direction

%%%Areas and Volumes for Workpiece%%%
for m=1:nwidth
    elementlength(m)=(m)*dr*dtheta;
    SA1wp(m)=(m-1)*dr*dtheta*dz;                    %[m^2] cross sectional area
radially outward
    SA2wp(m)=(m)*dr*dtheta*dz;                      %[m^2] cross sectional area
radially inward
    SA3wp(m)=((m*dr)-(dr/2))*dtheta*dr;             %[m^2] cross sectional area
through sheet thickness
```

177

```matlab
    SA4wp(m)=SA3wp(m);                              %[m^2] same area in z-
direction for a given 'm'
    Volwp(m)=SA3wp(m)*dz;                           %[m^3] CV volume for a given
radial 'm' node
end

%%%convergence criteria for 2D conduction used in dts%%%
tmp=[dr,dz,dh,elementlength];
small=min(tmp(:));
rt=.25;
dts=rt*(small^2)/thermaldiffwp;         %suggested time step

timestep=0.9*dts;                       %[s] timestep
endtime=max(WeberTimeRaw);              %[s] process end time (stop criteria)
iterations=floor(endtime/timestep);    %calculates number of iterations to
complete solution

%%%Interpolates Original Data Based on Desired Timestep%%%
[Trq,RPM,DistTip,Endload,MaxTempBox,TempCursor1,TempCursor2,TempCursor3,TempCur
sor4]=InterpolateDataV3(timestep,endtime,WeberTimeRaw,TorqueDataRaw,RPMDataRaw,
DepthRaw,EndloadRaw,CamTimeRaw,MaxTempRaw,Cursor1Raw,Cursor2Raw,Cursor3Raw,Curs
or4Raw);
%%%%%%%%%%%%%%%%%%%%%%%%%%%%%%%%%%%%%%%%%%%%%%%%%%%%%%%%%%%%%%%%%%%%%%%%%%%%%%%%
%intialize temperature and properties
%%%%%%%%%%%%%%%%%%%%%%%%%%%%%%%%%%%%%%%%%%%%%%%%%%%%%%%%%%%%%%%%%%%%%%%%%%%%%%%%

count1=0;           %arbitrary time step variable for assigning temperatures
count3=0;           % counting variable for current time step
count2=1;           %counting variable for new time step
time=0;             %initialize time to 0

%GenLocationsSC=0;

for t=0:timestep:(endtime-timestep)     %assign temperature as ambient to fill
entire wp matrix
    count1=count1+1;
    for m=1:nwidth
        for n=1:nthick
            %Twp(m,n,count1)=Tambient;
            Twp(:)=Tambient;
             MaterialClass(m,n,count1)="Al";
        end
    end
end

count1=0;
PrePunch=1.35;
PrePunch=PrePunch/1000;
DistTip(:)=DistTip(:)+PrePunch;

%%Main Loop%%
while time<(endtime-timestep)            %main loop solution loop stepped by
timestep time

    %step count values and increase time
    count3=count3+1;
    count2=count2+1;

    time=time+timestep;
```

```matlab
    %plottable time variables
    timesave(count3)=time;


if count3>1
    if DistTip(count3)<DistTip(count3-1)
        DistTip(count3)=DistTip(count3-1);
    else
        DistTip(count3)=DistTip(count3);
    end
end

RevTime(count3)=60/RPM(count3);

Omega(count3)=RPM(count3)*(2*pi/60);

%Updated Radius Function [WP DESIGNATION] (04.15.18)
for n=1:nthick
    if DistTip(count3)<n*dz
        rmajor(n,count3)=0;
        rmean(n,count3)=0;
    elseif DistTip(count3)-n*dz<=0.009294
        rmajor(n,count3)=3152.5*((DistTip(count3)-n*dz)^3)-
(78.173*((DistTip(count3)-n*dz)^2))+(0.6621*(DistTip(count3)-n*dz))+0.0001;
        rmean(n,count3)=rmajor(n,count3);
    elseif DistTip(count3)-n*dz<0.013267
        rmajor(n,count3)=3152.5*((DistTip(count3)-n*dz)^3)-
(78.173*((DistTip(count3)-n*dz)^2))+(0.6621*(DistTip(count3)-n*dz))+0.0001;
        rmean(n,count3)=(rmajor(n,count3)+rscrewminor)/2;
    else
        rmajor(n,count3)=0.0025;
        rmean(n,count3)=(rmajor(n,count3)+rscrewminor)/2;
    end
end

if count3>1
    for n=1:nthick
        radiuschange(n,count3)=(rmean(n,count3)-rmean(n,count3-1))/timestep;
    end
DistChange(count3)=(DistTip(count3)-DistTip(count3-1))/timestep;
end

rinstmax(count3)=max(rmajor(:,count3));

DistTipValue=DistTip(count3);

TotalNodalCA(count3)=0;
%Individual Nodal CA (NEW 04.16.18)
for n=1:nthick
    if DistTip(count3)<n*dz
        NodalCA(n,count3)=0;
    else
        NodalCA(n,count3)=2*pi*rmean(n,count3)*dz;
    end
    TotalNodalCA(count3)=NodalCA(n,count3)+TotalNodalCA(count3);
end

%%%%%%%%%%%%%%%%%%%%%%%%%%%%%%%%%%%%%%%%%%%%%%%%%%%%%%%%%%%%%%%%%%%%%%%%
%Temperature Dependent Material Properties
%%%%%%%%%%%%%%%%%%%%%%%%%%%%%%%%%%%%%%%%%%%%%%%%%%%%%%%%%%%%%%%%%%%%%%%%
```

```matlab
[Kwp,Cpwp,Densitywp]=TempDepPropWp(Twp(:,:,count3));              %Workpiece
Properties
%%%%%%%%%%%%%%%%%%%%%%%%%%%%%%%%%%%%%%%%%%%%%%%%%%%%%%%%%%%%%%%%%%%%%%%%%%%%

%Determines if wp nodes are consumed by steel and assigns a material class
  for m=1:nwidth
      for n=1:nthick
          if (m-1)*dr<rmean(n,count3)     %Criteria for being within screw
              MaterialClass(m,n,count3)="Steel";
          end
      end
  end


%Assigns wp nodes either steel or aluminum properties depending on material
class
for m=1:nwidth
      for n=1:nthick
          if MaterialClass(m,n,count3)=="Steel"
              K(m,n)=Kscrew(ceil((DistTip(count3)-n*dz)/dh));
              Cp(m,n)=Cpscrew(ceil((DistTip(count3)-n*dz)/dh));
              Density(m,n)=Densityscrew(ceil((DistTip(count3)-n*dz)/dh));
              Twp(m,n,count3)=Tscrew(ceil((DistTip(count3)-n*dz)/dh),count3);
              K(m,n)=Kscrew(ceil((DistTip(count3)-n*dz)/dh));
              Cp(m,n)=Cpscrew(ceil((DistTip(count3)-n*dz)/dh));
              Density(m,n)=Densityscrew(ceil((DistTip(count3)-n*dz)/dh));
              Twp(m,n,count3)=Tscrew(ceil((DistTip(count3)-n*dz)/dh),count3);
              MaterialClassNumeric(m,n,count3)=1;
          elseif MaterialClass(m,n,count3)=="Al"
              K(m,n)=Kwp(m,n);
              Cp(m,n)=Cpwp(m,n);
              Density(m,n)=Densitywp(m,n);
              MaterialClassNumeric(m,n,count3)=2;
          end
      end
end


for m=1:nwidth
    for n=1:nthick
        thermaleff(m,n,count3)=(K(m,n)*Cp(m,n)*Density(m,n))^0.5;
    end
end

%Re-Initializes QGenwp to zeros
 for m=1:nwidth
        for n=1:nthick
            QGenwp(m,n,count3)=0;
        end
 end

 GenLocationsWP(count3)=0;
 for m=1:nwidth-1
    for n=1:nthick
        if MaterialClass(m,n,count3)=="Steel" &&
MaterialClass(m+1,n,count3)=="Al"
           GenLocationsWP(count3)=GenLocationsWP(count3)+1;          %Counts
how many nodes on outer edge
       end
    end
```

```matlab
 end

if count3>1
for m=1:nwidth-1
    for n=1:nthick
        if MaterialClass(m,n,count3)=="Steel" &&
MaterialClass(m+1,n,count3)=="Al"  %Checks if node is on outer edge of screw
        QGenwp(m+1,n,count3)=(Beta*MStick(n,count3-1)+Eff*MSlip(n,count3-
1))*Omega(count3-1); %combined Slip-Stick
        end
    end
end
end


%%%%%%%%%%%%%%%%%%%%%%%%%%%%%%%%%%%%%%%%%%%%%%%%%%%%%%%%%%%%%%%%%%%%%%%%%%
    %%%%%%%%%%%%%%%%%%%%%%%%%%%%%%%%%%%%%%%%%%%%%%%%%%%%%%%%%%%%%%%%%%%%%%
    %Heat Transfer calculation for WP
    %%%%%%%%%%%%%%%%%%%%%%%%%%%%%%%%%%%%%%%%%%%%%%%%%%%%%%%%%%%%%%%%%%%%%%
    %loop through elements to solve for new temperatures%
    for m=1:nwidth %loop through columns
        for n=1:nthick %loop through rows

            if m==1     %Left Edge [Center of sheet] which is axis of symmetry;
Q1 becomes insulated B.C. [unless location of heat Gen]

                if n==1  %Top Left Node; Q3 becomes convection B.C.
                    %heat from left(radial inner)
                    Q1(m,n,count3)=0;
                    %heat from right (radial outer)
                    Q2(m,n,count3)=K(m,n)*SA2wp(m)/(dr/2)*(Twp(m+1,n,count3)-
Twp(m,n,count3));
                    %heat from top
                    Q3(m,n,count3)=hcomb*SA3wp(m)*(Tambient-Twp(m,n,count3));
                    %heat from bottom
                    Q4(m,n,count3)=K(m,n)*SA4wp(m)/dz*(Twp(m,n+1,count3)-
Twp(m,n,count3));
                    %total heat

Qtotal(m,n,count3)=Q1(m,n,count3)+Q2(m,n,count3)+Q3(m,n,count3)+Q4(m,n,count3)+
QGenwp(m,n,count3);
                    %temperature change

dT(m,n,count3)=timestep/(Density(m,n)*Cp(m,n)*Volwp(m))*(Qtotal(m,n,count3));
                    %determine new temperature and save to matrix
                    Twpnew(m,n,count2)=Twp(m,n,count3)+dT(m,n,count3);

                elseif n==nthick %Bottom Left Node; Q4 becomes insulated B.C.
                    %heat from left(radial inner)
                    Q1(m,n,count3)=0;
                    %heat from right (radial outer)
                    Q2(m,n,count3)=K(m,n)*SA2wp(m)/(dr/2)*(Twp(m+1,n,count3)-
Twp(m,n,count3));
                    %heat from top
                    if MaterialClassNumeric(m,n-1,count3)==1
                        SA3wp(m)=SA4screw(ceil((DistTip(count3)-n*dz)/dh)+1);
                        dz=dh;
                    end
                    Q3(m,n,count3)=K(m,n)*SA3wp(m)/dz*(Twp(m,n-1,count3)-
Twp(m,n,count3));
```

```
                    SA3wp(m)=((m*dr)-(dr/2))*dtheta*dr;
                    dz=elementthick;
                    %heat from bottom
                    Q4(m,n,count3)=0;
                    %total heat

Qtotal(m,n,count3)=Q1(m,n,count3)+Q2(m,n,count3)+Q3(m,n,count3)+Q4(m,n,count3)+
QGenwp(m,n,count3);
                    %temperature change

dT(m,n,count3)=timestep/(Density(m,n)*Cp(m,n)*Volwp(m))*(Qtotal(m,n,count3));
                    %determine new temperature and save to matrix
                    Twpnew(m,n,count2)=Twp(m,n,count3)+dT(m,n,count3);

                else %Remaining nodes along centerline edge
                    %heat from left(radial inner)
                    Q1(m,n,count3)=0;
                    %heat from right (radial outer)
                    Q2(m,n,count3)=K(m,n)*SA2wp(m)/(dr/2)*(Twp(m+1,n,count3)-
Twp(m,n,count3));
                    %heat from top
                    Q3(m,n,count3)=K(m,n)*SA3wp(m)/dz*(Twp(m,n-1,count3)-
Twp(m,n,count3));
                    %heat from bottom
                    Q4(m,n,count3)=K(m,n)*SA4wp(m)/dz*(Twp(m,n+1,count3)-
Twp(m,n,count3));
                    %total heat

Qtotal(m,n,count3)=Q1(m,n,count3)+Q2(m,n,count3)+Q3(m,n,count3)+Q4(m,n,count3)+
QGenwp(m,n,count3);
                    %temperature change

dT(m,n,count3)=timestep/(Density(m,n)*Cp(m,n)*Volwp(m))*(Qtotal(m,n,count3));
                    %determine new temperature and save to matrix
                    Twpnew(m,n,count2)=Twp(m,n,count3)+dT(m,n,count3);
                end

        elseif m==nwidth %Right Edge [edge of sheet]; Q2 becomes insulated
B.C.

                if n==1 %Top Right Node; Q3 becomes convection B.C.
                    %heat from left(radial inner)
                    Q1(m,n,count3)=K(m,n)*SA1wp(m)/dr*(Twp(m-1,n,count3)-
Twp(m,n,count3));
                    %heat from right (radial outer)
                    Q2(m,n,count3)=0;
                    %heat from top
                    Q3(m,n,count3)=hcomb*SA3wp(m)*(Tambient-Twp(m,n,count3));
                    %heat from bottom
                    Q4(m,n,count3)=K(m,n)*SA4wp(m)/dz*(Twp(m,n+1,count3)-
Twp(m,n,count3));
                    %total heat

Qtotal(m,n,count3)=Q1(m,n,count3)+Q2(m,n,count3)+Q3(m,n,count3)+Q4(m,n,count3)+
QGenwp(m,n,count3);
                    %temperature change

dT(m,n,count3)=timestep/(Density(m,n)*Cp(m,n)*Volwp(m))*(Qtotal(m,n,count3));
                    %determine new temperature and save to matrix
                    Twpnew(m,n,count2)=Twp(m,n,count3)+dT(m,n,count3);
```

```matlab
                    elseif n==nthick %Bottom Right Node; Q4 becomes insulated B.C.
                        %heat from left(radial inner)
                        Q1(m,n,count3)=K(m,n)*SA1wp(m)/dr*(Twp(m-1,n,count3)-
Twp(m,n,count3));
                        %heat from right (radial outer)
                        Q2(m,n,count3)=0;
                        %heat from top
                        Q3(m,n,count3)=K(m,n)*SA3wp(m)/dz*(Twp(m,n-1,count3)-
Twp(m,n,count3));
                        %heat from bottom
                        Q4(m,n,count3)=0;
                        %total heat

Qtotal(m,n,count3)=Q1(m,n,count3)+Q2(m,n,count3)+Q3(m,n,count3)+Q4(m,n,count3)+
QGenwp(m,n,count3);
                        %temperature change

dT(m,n,count3)=timestep/(Density(m,n)*Cp(m,n)*Volwp(m))*(Qtotal(m,n,count3));
                        %determine new temperature and save to matrix
                        Twpnew(m,n,count2)=Twp(m,n,count3)+dT(m,n,count3);

                    else %Remaining nodes along right edge of workpiece
                        %heat from left(radial inner)
                        Q1(m,n,count3)=K(m,n)*SA1wp(m)/dr*(Twp(m-1,n,count3)-
Twp(m,n,count3));
                        %heat from right (radial outer)
                        Q2(m,n,count3)=0;
                        %heat from top
                        Q3(m,n,count3)=K(m,n)*SA3wp(m)/dz*(Twp(m,n-1,count3)-
Twp(m,n,count3));
                        %heat from bottom
                        Q4(m,n,count3)=K(m,n)*SA4wp(m)/dz*(Twp(m,n+1,count3)-
Twp(m,n,count3));
                        %total heat

Qtotal(m,n,count3)=Q1(m,n,count3)+Q2(m,n,count3)+Q3(m,n,count3)+Q4(m,n,count3)+
QGenwp(m,n,count3);
                        %temperature change

dT(m,n,count3)=timestep/(Density(m,n)*Cp(m,n)*Volwp(m))*(Qtotal(m,n,count3));
                        %determine new temperature and save to matrix
                        Twpnew(m,n,count2)=Twp(m,n,count3)+dT(m,n,count3);
                    end

            elseif n==1 && (m>1 || m<nwidth) % Remaining Nodes on top surface; Q3
becomes convection B.C.
                        %heat from left(radial inner)
                        Q1(m,n,count3)=K(m,n)*SA1wp(m)/dr*(Twp(m-1,n,count3)-
Twp(m,n,count3));
                        %heat from right (radial outer)
                        Q2(m,n,count3)=K(m,n)*SA2wp(m)/dr*(Twp(m+1,n,count3)-
Twp(m,n,count3));
                        %heat from top
                        Q3(m,n,count3)=hcomb*SA3wp(m)*(Tambient-Twp(m,n,count3));
                        %heat from bottom
                        Q4(m,n,count3)=K(m,n)*SA4wp(m)/dz*(Twp(m,n+1,count3)-
Twp(m,n,count3));
                        %total heat
```

```matlab
Qtotal(m,n,count3)=Q1(m,n,count3)+Q2(m,n,count3)+Q3(m,n,count3)+Q4(m,n,count3)+
QGenwp(m,n,count3);
                        %temperature change

dT(m,n,count3)=timestep/(Density(m,n)*Cp(m,n)*Volwp(m))*(Qtotal(m,n,count3));
                        %determine new temperature and save to matrix
                        Twpnew(m,n,count2)=Twp(m,n,count3)+dT(m,n,count3);

            elseif n==nthick && (m>1 || m<nwidth) % Remaining Nodes on bottom
surface; Q4 becomes insulated B.C.
                        %heat from left(radial inner)
                        Q1(m,n,count3)=K(m,n)*SA1wp(m)/dr*(Twp(m-1,n,count3)-
Twp(m,n,count3));
                        %heat from right (radial outer)
                        Q2(m,n,count3)=K(m,n)*SA2wp(m)/dr*(Twp(m+1,n,count3)-
Twp(m,n,count3));
                        %heat from top
                        Q3(m,n,count3)=K(m,n)*SA3wp(m)/dz*(Twp(m,n-1,count3)-
Twp(m,n,count3));
                        %heat from bottom
                        Q4(m,n,count3)=0;
                        %total heat

Qtotal(m,n,count3)=Q1(m,n,count3)+Q2(m,n,count3)+Q3(m,n,count3)+Q4(m,n,count3)+
QGenwp(m,n,count3);
                        %temperature change

dT(m,n,count3)=timestep/(Density(m,n)*Cp(m,n)*Volwp(m))*(Qtotal(m,n,count3));
                        %determine new temperature and save to matrix
                        Twpnew(m,n,count2)=Twp(m,n,count3)+dT(m,n,count3);

            else %Remaining Central Nodes with all Conduction conditions
                        %heat from left(radial inner)
                        Q1(m,n,count3)=K(m,n)*SA1wp(m)/dr*(Twp(m-1,n,count3)-
Twp(m,n,count3));
                        %heat from right (radial outer)
                        Q2(m,n,count3)=K(m,n)*SA2wp(m)/dr*(Twp(m+1,n,count3)-
Twp(m,n,count3));
                        %heat from top
                        Q3(m,n,count3)=K(m,n)*SA3wp(m)/dz*(Twp(m,n-1,count3)-
Twp(m,n,count3));
                        %heat from bottom
                        Q4(m,n,count3)=K(m,n)*SA4wp(m)/dz*(Twp(m,n+1,count3)-
Twp(m,n,count3));
                        %total heat

Qtotal(m,n,count3)=Q1(m,n,count3)+Q2(m,n,count3)+Q3(m,n,count3)+Q4(m,n,count3)+
QGenwp(m,n,count3);
                        %temperature change

dT(m,n,count3)=timestep/(Density(m,n)*Cp(m,n)*Volwp(m))*(Qtotal(m,n,count3));
                        %determine new temperature and save to matrix
                        Twpnew(m,n,count2)=Twp(m,n,count3)+dT(m,n,count3);
            end
        end
    end

Twp(:,:,count2)=Twpnew(:,:,count2); %assign new temperature to main temperature
matrix and progress to next time step
```

```matlab
%%%%%%%%%%%%%%%%%%%%%%%%%%%%%%%%%%%%%%%%%%%%%%%%%%%%%%%%%%%%%%%%%%%%%%%
%%%Torque Mechanics%%%
%%%%%%%%%%%%%%%%%%%%%%%%%%%%%%%%%%%%%%%%%%%%%%%%%%%%%%%%%%%%%%%%%%%%%%%

%Surface Velocity Calculation
for n=1:nthick
    SurfVel(n,count3)=RPM(count3)*2*(rmean(n,count3))*pi/60; %[m/s]
end

for n=1:nthick
    if DistTip(count3)-n*dz>0.009294
    ThreadElementWidth(n,count3)=(rmajor(n,count3)-
rscrewminor)*(1+(tand(0.5*crestangle))^2)^0.5;

ThreadElementLength(n,count3)=(((rmean(n,count3))^2+(pitch/(2*pi))^2)^0.5)*2*pi
*(dz/lead);

ThreadElementArea(n,count3)=ThreadElementWidth(n,count3)*ThreadElementLength(n,
count3);
    end
end

for n=1:nthick
    if DistTip(count3)<n*dz
      NormalPress(n,count3)=0;
    else

NormalPress(n,count3)=(Endload(count3)*cosd(slopeangle(n,count3)))/(0.5*NodalCA
(n,count3));
    end
end

for n=1:nthick
      AreaProj(n,count3)=pi*(((rmajor(n,count3))^2)-(rscrewminor)^2);
end

for n=1:nthick
    if DistTip(count3)-n*dz>=0.009294

ThreadPress(n,count3)=(Endload(count3)/(cosd(15)))/(AreaProj(n,count3));
    end
end

ThreadDepth=0.614*pitch;

%Thread Cross-Sectional Area
for n=1:nthick
    if DistTip(count3)-n*dz>=0.0128
        ThreadShearNodalCA(n,count3)=0.5*pitch*ThreadDepth*2*pi;
    else

ThreadShearNodalCA(n,count3)=(0.5*pitch*ThreadDepth*2*pi)*((DistTip(count3)-
n*dz)/(0.0128));
    end
end


MaxStrain=3.5;
for n=1:nthick
```

```matlab
    if MaxTempBox(count3)>=170 && MaxTempBox(count3)<=235 &&
SurfVel(n,count3)>=0.6 && SurfVel(n,count3)<=0.9
        Strain(n,count3)=MaxStrain*(1.64/1.64);
    elseif  MaxTempBox(count3)<220 && SurfVel(n,count3)<.45
        Strain(n,count3)=MaxStrain*(1.0/1.64);
    elseif MaxTempBox(count3)>235 && SurfVel(n,count3)>.75
        Strain(n,count3)=MaxStrain*(1.12/1.64);
    else
        Strain(n,count3)=MaxStrain*(1.3/1.64);
    end
end


MaxTempBoxKelv(count3)=MaxTempBox(count3)+273.15;
Tstar(count3)=((MaxTempBoxKelv(count3)-Tambient)/(Tmelt-Tambient));

for n=1:nthick

JCmodel(n,count3)=(Aparameter+Bparameter*(Strain(n,count3).^nparameter))*(1-
(Tstar(count3).^mparameter));
    ShearStrength(n,count3)=(JCmodel(n,count3)/(3^0.5));
end

ShearStrengthAVG(count3)=mean(ShearStrength(:,count3));


NonContactThickTotal(count3)=0;
for n=1:nthick
    if DistTip(count3)<n*dz
        NonContactThick(n,count3)=1;

NonContactThickTotal(count3)=NonContactThick(n,count3)+NonContactThickTotal(cou
nt3);
    end
end

%Shearing and Sliding Contact Area Percentages%%
for n=1:nthick
    if DistTip(count3)<n*dz
        ShearingAreaPerc(n,count3)=0;
        SlidingAreaPerc(n,count3)=0;
    elseif DistTip(count3)-n*dz>0.006559 && DistTip(count3)-n*dz<0.009294
        ShearingAreaPerc(n,count3)=0;
        SlidingAreaPerc(n,count3)=1;
    else
        ShearingAreaPerc(n,count3)=0.1542*((DistTip(count3)-n*dz)^(-0.1));
        SlidingAreaPerc(n,count3)=0.0586*log((DistTip(count3)-n*dz))+0.7894;
    end
end

ShearingArcLength=2*pi*rinstmax(count3)*0.1542*(DistTip(count3)^(-0.1));

ShearingAreaTriangle(count3)=0.5*ShearingArcLength*PartThick;

PercShearingAreaTriangle(count3)=ShearingAreaTriangle(count3)/TotalNodalCA(coun
t3);

for n=1:nthick
```

```
ShearingNodalArcLength(n,count3)=2*pi*rmean(n,count3)*ShearingAreaPerc(n,count3
);
    ShearingNodalAreaBox(n,count3)=ShearingNodalArcLength(n,count3)*dz;
end

for n=1:nthick
    if DistTip(count3)<n*dz || DistTip(count3)-n*dz>DistCyl
        PressSlip(n,count3)=0;
    else
        PressSlip(n,count3)=Endload(count3)/TotalNodalCA(count3);
    end
end

for n=1:nthick
    if DistTip(count3)<n*dz
        PressStick(n,count3)=0;
    else

PressStick(n,count3)=(Endload(count3)*cosd(slopeangle(n,count3)))/((CurlPerc(n,
count3))*NodalCA(n,count3));
    end
end

CurlDepth=PartThick;
CurlArea=CurlLength*CurlDepth;
CurlAreaAVG=CurlArea/nthick;

MStickTotal(count3)=0;
for n=1:nthick
    if DistTip(count3)-n*dz<=DistTFThreads

MStick(n,count3)=ShearStrength(n,count3)*rmean(n,count3)*ShearingNodalAreaBox(n
,count3);
    elseif DistTip(count3)-n*dz<DistThreads

MStick(n,count3)=ShearStrength(n,count3)*ThreadElementArea(n,count3)*rmean(n,co
unt3);
    else
        MStick(n,count3)=0;
    end
MStickTotal(count3)=MStickTotal(count3)+MStick(n,count3);
end

%%%Assuming Full Sticking Condition%%%
MFullStickTotal(count3)=0;
for n=1:nthick
    if DistTip(count3)-n*dz<=0.009294

MFullStick(n,count3)=ShearStrength(n,count3)*rmean(n,count3)*NodalCA(n,count3);
    else

MFullStick(n,count3)=ShearStrength(n,count3)*ThreadElementArea(n,count3)*rmean(
n,count3);
    end
MFullStickTotal(count3)=MFullStickTotal(count3)+MFullStick(n,count3);
end

MSlipTotal(count3)=0;
for n=1:nthick
```

187

```matlab
    if DistTip(count3)-n*dz<DistCyl

MSlip(n,count3)=PressSlip(n,count3)*FricCoeff(n,count3)*SlidingAreaPerc(n,count
3)*NodalCA(n,count3)*rmean(n,count3);
    elseif DistTip(count3)-n*dz<DistThreads
        MSlip(n,count3)=0;
    else

MSlip(n,count3)=ThreadPress(n,count3)*FricCoeff(n,count3)*ThreadElementArea(n,c
ount3)*rmean(n,count3);
    end
MSlipTotal(count3)=MSlipTotal(count3)+MSlip(n,count3);
end

MSlipPlusStickTotal(count3)=MSlipTotal(count3)+MStickTotal(count3);


%%%Assuming Full Slipping Condition%%%
MFullSlipTotal(count3)=0;
for n=1:nthick
    if DistTip(count3)-n*dz<0.0065

MFullSlip(n,count3)=PressSlip(n,count3)*FricCoeff(n,count3)*NodalCA(n,count3)*r
mean(n,count3);
    else

MFullSlip(n,count3)=ThreadPress(n,count3)*FricCoeff(n,count3)*ThreadElementArea
(n,count3)*rmean(n,count3);
    end
MFullSlipTotal(count3)=MFullSlipTotal(count3)+MFullSlip(n,count3);
end


end %end main loop
```

9.4. 'Electrically Assisted Flow Drill Screwing Process (FDS) and Fixturing' Patent Figures
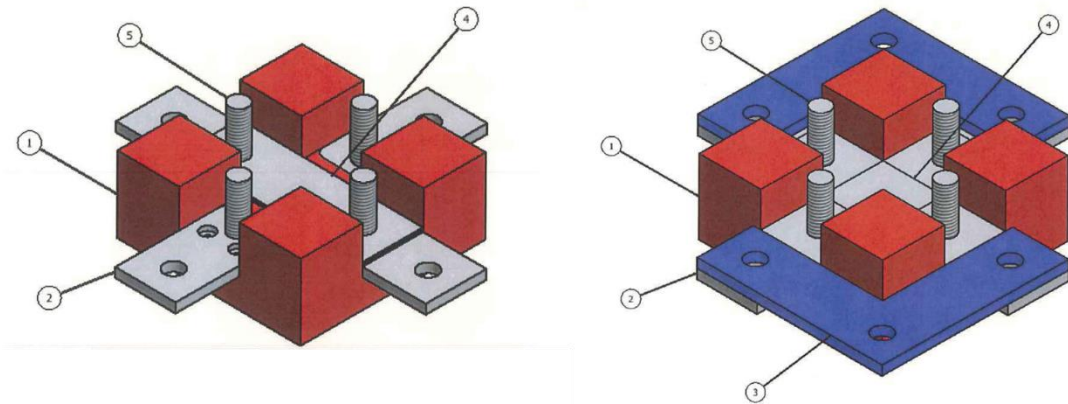
Figure 9–81: Electrical application fixture (current design)

Item	Part	Description
1	Base	Electrically insulative material
2	Electrical lead	Aluminum lead
3	Cross tension bridge	For applying current through both pieces
4	Workpiece specimen	FDS stackup
5	Threaded rod	Used to secure specimen and electrical leads
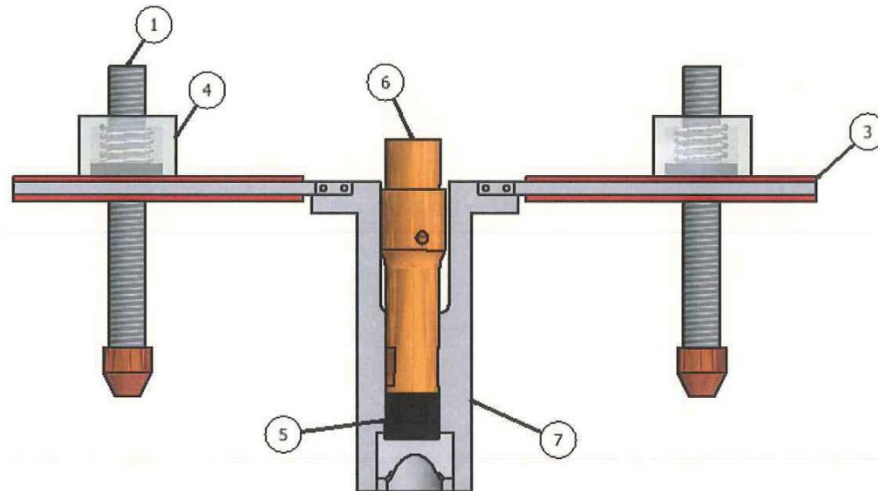
Figure 9–82: Electrical application without need for clamping fixture (concept)

Item	Part	Description
1	Contact tip	Contacts workpiece
2	Spring	Ensures contact between workpiece and contacts
3	Support	Supports and holds electrical lead fixture

4	Top box	Holds springs
5	Bit	Contacts FDS screw
6	Bit holder	Insulates machine from electricity
7	Solid downholder	Holds workpiece in place

10.REFERENCES

[1]   2013, Vehicle Fuel Efficiency (CAFE) Requirements by Year, U.S. Environmental
        Protection Agency.

[2]   Achorn, G., 2010, "4T:Reviews & Road Tests," Fourtitude.

[3]   Weissler, P., 2014, "2015 F-150 aluminum body creates challenge for auto body shops,"
        SAE.

[4]   "The Technical Challenge" [Online]. Available: http://www.spottrack.eu/why-
        spottrack/technical-challenge.jsp.

[5]   Böllhoff, "RIVSET Self-Pierce Riveting" [Online]. Available:
        https://www.boellhoff.com/de-en/products-and-services/assembly-technology/self-pierce-
        riveting-rivset.php.

[6]   Skovron, J. D., and Ruszkiewicz, B. J., 2017, "Investigation of the Cleaning and Welding
        Steps from the Friction Element Welding Process," ASME 2017 12th International
        Manufacturing Science and Engineering Conference, Los Angeles, CA.

[7]   Claus, L., and Weitzel, S., 2014, "Self-Tapping Fasteners for Lightweight Designs," SAE
        Tech. Pap., **1**.

[8]   EJOT, 2004, "Flow Drill Screws for High Strength Sheet Metal" [Online]. Available:
        http://www.ejot.com/Industrial-Fasteners-
        Division/Products/c/PRODUCTS_INDUSTRIAL_FASTENERS.

[9]   Miller, S. F., Tao, J., and Shih, A. J., 2006, "Friction drilling of cast metals," Int. J. Mach.
        Tools Manuf., **46**(12–13), pp. 1526–1535.

[10]   Szlosarek, R., Karall, T., Enzinger, N., Hahne, C., and Meyer, N., 2013, "Mechanical testing of flow drill screw joints between fibre-reinforced plastics and metals," Mater. Test., **55**(10), pp. 737–742.

[11]   Miller, S. F., Blau, P. J., and Shih, A. J., 2005, "Microstructural Alterations Associated With Friction Drilling of Steel, Aluminum, and Titanium," J. Mater. Eng. Perform., **14**(5), pp. 647–653.

[12]   Lee, S. M., Chow, H. M., and Yan, B. H., 2007, "Friction Drilling of IN-713LC Cast Superalloy," Mater. Manuf. Process., **6914**(July), pp. 893–897.

[13]   Chow, H. M., Lee, S. M., and Yang, L. D., 2008, "Machining characteristic study of friction drilling on AISI 304 stainless steel," J. Mater. Process. Technol., **207**(1–3), pp. 180–186.

[14]   Boopathi, M., Shankar, S., and Kanish, T. C., 2017, "Investigation of Surface Texture Generated by Friction Drilling on Al2024-T6 52," (April), pp. 302–306.

[15]   Demir, Z., 2015, "Investigate the Temperature and Bushing Shape in Pre-Drilling Friction Drilling of Al7075-T651," 2nd International Iron and Steel Symposium, Karabuk, Turkey, pp. 381–389.

[16]   Fernández, A., Lopez De Lacalle, L. N., and Lamikiz, A., 2010, "Friction drilling of stainless steels pipes," Int. Conf. Adv. Mater. Process. Technol., pp. 1187–1192.

[17]   Ozler, L., and Dogru, N., 2013, "An Experimental Investigation of Hole Geometry in Friction Drilling," Mater. Manuf. Process., **28**(4), pp. 470–475.

[18]   Kaya, M. T., Aktas, A., Beylergil, B., and Akyildiz, H. K., 2014, "An experimental study on friction drilling of ST12 steel," Trans. Can. Soc. Mech. Eng., **38**(3), pp. 319–329.

[19]   Lee, S. M., Chow, H. M., Huang, F. Y., and Yan, B. H., 2009, "Friction drilling of austenitic stainless steel by uncoated and PVD AlCrN- and TiAlN-coated tungsten carbide tools," Int. J. Mach. Tools Manuf., **49**(1), pp. 81–88.

[20]   Ozek, C., and Demir, Z., 2013, "Investigate the effect of tool conical angle on the bushing height , wall thickness and forming in friction drilling of A7075-T651 aluminum alloy," Usak Univ. J. Mater. Sci., **1**, pp. 61–74.

[21]   Boopathi, M., Shankar, S., Manikandakumar, S., and Ramesh, R., 2013, "Experimental investigation of friction drilling on brass, aluminium and stainless steel," Procedia Eng., **64**, pp. 1219–1226.

[22]   Demir, Z., and Ozek, C., 2014, "Investigate the effect of pre-drilling in friction drilling of A7075-T651," Mater. Manuf. Process., **29**(5), pp. 593–599.

[23]   Ozek, C., and Demir, Z., 2013, "Investigate the Friction Drilling of Aluminium Alloys According to the Thermal Conductivity," Technol. Educ. Manag. Informatics, **2**(1), pp. 93–101.

[24]   El-Bahloul, S. A., El-Shourbagy, H. E., and El-Midany, T. T., 2015, "Optimization of Thermal Friction Drilling Process Based on Taguchi Method and Fuzzy Logic Technique," Int. J. Sci. Eng. Appl., **4**(2), pp. 55–59.

[25]   Patil, S. S., and Bembrekar, V., 2016, "Optimization and thermal analysis of Friction Drilling on Aluminium and Mild Steel by using Tungsten Carbide Tool," Int. Res. J. Eng. Technol., **3**(12), pp. 1468–1474.

[26]   Krishna, P. V. G., Kishore, K., and Satyanarayana, V. V, 2010, "Some Investigations in Friction Drilling Aa6351 Using High Speed Steel Tools," J. Eng. Appl. Sci., **5**(3), pp. 11–

15.

[27]   Ku, W. L., Hung, C. L., Lee, S. M., and Chow, H. M., 2011, "Optimization in thermal friction drilling for SUS 304 stainless steel," Int. J. Adv. Manuf. Technol., **53**(9–12), pp. 935–944.

[28]   Grujicic, M., Snipes, J., and Ramaswami, S., 2015, "Process modeling, joint virtual testing and construction of joint connectors for mechanical fastening by flow-drilling screws," Multidiscip. Model. Mater. Struct., **10**(4), pp. 631–658.

[29]   Pan, J., Chen, W.-N., Sung, S.-J., Su, X., and Friedman, P., 2018, "Failure Mode and Fatigue Behavior of Flow Drill Screw Joints in Lap-Shear Specimens of Aluminum 6082-T6 Sheets Made with Different Processing Conditions," SAE, p. 13.

[30]   Sønstabø, J. K., Holmstrom, P. H., Morin, D., and Langseth, M., 2015, "Macroscopic strength and failure properties of flow-drill screw connections," J. Mater. Process. Technol., **222**, pp. 1–12.

[31]   Sønstabø, J. K., Morin, D., and Langseth, M., 2016, "Macroscopic modelling of flow-drill screw connections in thin-walled aluminium structures," Thin-Walled Struct., **105**, pp. 185–206.

[32]   Scholz, C. S., Kopp, G., and Friedrich, H. E., 2016, "Influence of Corrosive Conditions on the Mechanical Performance of Flow Drill Screw Joints between Light Metals," Mater. Sci. Forum, **879**, pp. 1725–1730.

[33]   Engbert, T., Heymann, T., Biermann, D., and Zabel, A., 2010, "Flow drilling and thread forming of continuously reinforced aluminium extrusionsg," J. Eng. Manuf., **225**(B), pp. 398–407.

[34]   Miller, S. F., Li, R., Wang, H., and Shih, A. J., 2006, "Experimental and Numerical Analysis of the Friction Drilling Process," J. Manuf. Sci. Eng., **128**(3), pp. 802–810.

[35]   Miller, S. F., and Shih, A. J., 2007, "Thermo-Mechanical Finite Element Modeling of the Friction Drilling Process," J. Manuf. Sci. Eng., **129**(3), p. 531.

[36]   Qu, J., and Blau, P. J., 2008, "A New Model to Calculate Friction Coefficients and Shear Stresses in Thermal Drilling," J. Manuf. Sci. Eng., **130**(1), p. 014502.

[37]   Johnson, R. L., and Bisson, E. E., 1955, BEARINGS AND LUBRICANTS FOR AIRCRAFT TURBINE ENGINES.

[38]   Awang, M., 2007, "Simulation of Friction Stir Spot Welding (FSSW) Process: Study of Friction Phenomena," West Virginia University.

[39]   Song, M., and Kovacevic, R., 2003, "Thermal modeling of friction stir welding in a moving coordinate system and its validation," Int. J. Mach. Tools Manuf., **43**(6), pp. 605–615.

[40]   Schmidt, H., Hattel, J., and Wert, J., 2004, "An analytical model for the heat generation in friction stir welding," Model. Simul. Mater. Sci. Eng., **12**, pp. 143–157.

[41]   Frigaard, Ø., Grong, Ø., and Midling, O. T., 2001, "A Process Model for Friction Stir Welding of Age Hardening Aluminum Alloys," Metall. Mater. Trans. A, **32**(5), pp. 1189–1200.

[42]   Miller, S. F., 2006, "Experimental Analysis and Numerical Modeling of the Friction Drilling Process," The University of Michigan.

[43]   Krasauskas, P., Kilikevicius, S., Cesnavicius, R., and Pacenga, D., 2014, "Experimental

analysis and numerical simulation of the stainless AISI 304 steel friction drilling process," Mechanika, **20**(6), pp. 590–595.

[44]   Krasauskas, P., 2011, "Experimental and statistical investigation of thermo-mechanical friction drilling process," Mechanika, **17**(6), pp. 681–686.

[45]   Gemme, F., Verreman, Y., Dubourg, L., and Jahazi, M., 2010, "Numerical analysis of the dwell phase in friction stir welding and comparison with experimental data," Mater. Sci. Eng. A, **527**(16–17), pp. 4152–4160.

[46]   Schmidt, H. N. B., Dickerson, T. L., and Hattel, J. H., 2006, "Material flow in butt friction stir welds in AA2024-T3," Acta Mater., **54**(4), pp. 1199–1209.

[47]   Chen, Z. W., Pasang, T., and Qi, Y., 2008, "Shear flow and formation of Nugget zone during friction stir welding of aluminium alloy 5083-O," Mater. Sci. Eng. A, **474**(1–2), pp. 312–316.

[48]   Hamilton, C., Dymek, S., and Sommers, A., 2008, "A thermal model of friction stir welding in aluminum alloys," Int. J. Mach. Tools Manuf., **48**(10), pp. 1120–1130.

[49]   Qian, J., Ou, Y., Li, J., Xiao, Y., Wu, L., and Xu, Y., 2016, "An analytical model to calculate the peak temperature for friction stir welding," Sci. Technol. Weld. Join., pp. 1–6.

[50]   Quintana Cuellar, K. J., and Silveira, J. L. L., 2017, "Analysis of Torque in Friction Stir Welding of Aluminum Alloy 5052 by Inverse Problem Method," J. Manuf. Sci. Eng., **139**(4), p. 041017.

[51]   Khandkar, M. Z. H., Khan, J. a., and Reynolds, a. P., 2003, "Prediction of temperature distribution and thermal history during friction stir welding: input torque based model,"

Sci. Technol. Weld. Join., **8**(3), pp. 165–174.

[52]   Su, H., Wu, C. S., Pittner, A., and Rethmeier, M., 2014, "Thermal energy generation and

distribution in friction stir welding of aluminum alloys," Energy, **77**(July 2015), pp. 720–

731.

[53]   Liechty, B. C., and Webb, B. W., 2008, "Modeling the frictional boundary condition in

friction stir welding," Int. J. Mach. Tools Manuf., **48**(12–13), pp. 1474–1485.

[54]   Deng, Z., Lovell, M. R., and Tagavi, K. A., 2001, "Influence of Material Properties and

Forming Velocity on the Interfacial Slip Characteristics of Cross Wedge Rolling," J.

Manuf. Sci. Eng., **123**(4), p. 647.

[55]   Nandan, R., Roy, G. G., Lienert, T. J., and Debroy, T., 2007, "Three-dimensional heat and

material flow during friction stir welding of mild steel," Acta Mater., **55**(3), pp. 883–895.

[56]   Nandan, R., DebRoy, T., and Bhadeshia, H. K. D. H., 2008, "Recent advances in friction-

stir welding - Process, weldment structure and properties," Prog. Mater. Sci., **53**(6), pp.

980–1023.

[57]   Arora, A., Nandan, R., Reynolds, A. P., and DebRoy, T., 2009, "Torque, power

requirement and stir zone geometry in friction stir welding through modeling and

experiments," Scr. Mater., **60**(1), pp. 13–16.

[58]   Mehta, M., Arora, A., De, A., and Debroy, T., 2011, "Tool geometry for friction stir

welding - Optimum shoulder diameter," Metall. Mater. Trans. A Phys. Metall. Mater. Sci.,

42(9), pp. 2716–2722.

[59]   Arora, A., De, A., and Debroy, T., 2011, "Toward optimum friction stir welding tool

shoulder diameter," Scr. Mater., **64**(1), pp. 9–12.

[60]   Shi, L., and Wu, C. S., 2017, "Transient model of heat transfer and material flow at different stages of friction stir welding process," J. Manuf. Process., **25**, pp. 323–339.

[61]   Bastier, A., Maitournam, M. H., Dang Van, K., and Roger, F., 2006, "Steady state thermomechanical modelling of friction stir welding," Sci. Technol. Weld. Join., **11**(3), pp. 278–288.

[62]   Liu, X., Chen, G., Ni, J., and Feng, Z., 2017, "Computational Fluid Dynamics Modeling on Steady-State Friction Stir Welding of Aluminum Alloy 6061 to TRIP Steel," J. Manuf. Sci. Eng. Trans. ASME, **139**(5).

[63]   Cho, H.-H., Hong, S.-T., Roh, J.-H., Choi, H.-S., Kang, S. H., Steel, R. J., and Han, H. N., 2013, "Three-dimensional numerical and experimental investigation on friction stir welding processes of ferritic stainless steel," Acta Mater., **61**(7), pp. 2649–2661.

[64]   Chao, Y. J., Liu, S., and Chien, C. H., 2008, "Friction stir welding of al 6061-T6 thick plates: Part I - experimental analyses of thermal and mechanical phenomena," J. Chinese Inst. Eng., **31**(5), pp. 757–767.

[65]   Chao, Y. J., Qi, X., and Tang, W., 2003, "Heat Transfer in Friction Stir Welding— Experimental and Numerical Studies," J. Manuf. Sci. Eng., **125**(1), p. 8.

[66]   Qian, J. W., Li, J. L., Xiong, J. T., Zhang, F. S., Li, W. Y., and Lin, X., 2012, "Periodic variation of torque and its relations to interfacial sticking and slipping during friction stir welding," Sci. Technol. Weld. Join., **17**(4), pp. 338–341.

[67]   International Organization for Standardization, 2009, "Mechanical properties of fasteners made of carbon steel and alloy steel-Part 1," ISO 898-1.

[68]   Aslan, F., Langlois, L., Mangin, P., and Balan, T., 2018, "Identification of drilling

parameters during the flow drill screw driving process," Key Eng. Mater., **767 KEM**, pp. 465–471.

[69]   Alkelani, A., and Housari, B., 2011, "Development of Tightening Torque for Self Tapping and Thread Rolling Fasteners," ASME Pressure Vessels & Piping Division Conference.

[70]   Yang, X., and Nassar, S., 2010, "Vibration-Induced Loosening Performance of Preloaded Threaded Fasteners," ASME 2010 Pressure Vessels & Piping Division, Bellevue, WA.

[71]   Holmstrøm, P. H., and Sønstabø, J. K., 2013, "Behaviour and Modelling of Self-Piercing Screw and Self-Piercing Rivet Connections," Norwegian University of Science and Technology.

[72]   Chen, Z. W., and Cui, S., 2009, "Strain and strain rate during friction stir welding/processing of Al-7Si-0.3Mg alloy," IOP Conf. Ser. Mater. Sci. Eng., **4**, p. 012026.

[73]   Suhuddin, U., Fischer, V., Geesthacht, H., Mechanics, M., and Processes, S. J., 2013, "Microstructure in Dissimilar Friction Spot Weld of Al to Mg Alloys Observed by Stop-Action Technique," The Minerals, Metals & Materials Society, pp. 263–270.

[74]   Gerlich, A., Yamamoto, M., and North, T. H., 2008, "Local melting and tool slippage during friction stir spot welding of Al-alloys," J. Mater. Sci., **43**(1), pp. 2–11.

[75]   Schneider, C. A., Rasband, W. S., and Eliceiri, K. W., 2012, "NIH Image to ImageJ: 25 years of image analysis," Nat. Methods, **9**(7), pp. 671–675.

[76]   Gonzalez, Woods, and Eddins, 2009, Digital Image Processing Using MATLAB, Gatesmark Publishing.

[77] Etter, A. L., Baudin, T., Fredj, N., and Penelle, R., 2007, "Recrystallization mechanisms in 5251 H14 and 5251 O aluminum friction stir welds," Mater. Sci. Eng. A, **445–446**, pp. 94–99.

[78] Sato, Y. S., Urata, M., and Kokawa, H., 2002, "Parameters controlling microstructure and hardness during friction-stir welding of precipitation-hardenable aluminum alloy 6063," Metall. Mater. Trans. A, **33**(3), pp. 625–635.

[79] Su, J.-Q., Nelson, T. ., Mishra, R., and Mahoney, M., 2003, "Microstructural investigation of friction stir welded 7050-T651 aluminium," Acta Mater., **51**(3), pp. 713–729.

[80] Li, W., Zhang, Z., Li, J., and Chao, Y. J., 2012, "Numerical analysis of joint temperature evolution during friction stir welding based on sticking contact," J. Mater. Eng. Perform., **21**(9), pp. 1849–1856.

[81] Schmidt, H., and Hattel, J., 2005, "A local model for the thermomechanical conditions in friction stir welding," Model. Simul. Mater. Sci. Eng., **13**(1), pp. 77–93.

[82] Gao, Z. ., Wang, P. ., Cheng, D. ., Niu, J. . B., and Sommitsch, C. ., 2015, "Numerical simulation of material flow in AA6082 during friction stir spot welding," Eng. Rev., **35**(3), pp. 283–289.

[83] Xu, S., Deng, X., Reynolds, A. P., and Seidel, T. U., 2001, "Finite element simulation of material flow in friction stir welding," Sci. Technol. Weld. Join., **6**(3), pp. 191–193.

[84] Sønstabø, J. K., Morin, D., and Langseth, M., 2018, "Testing and modelling of flow-drill screw connections under quasi-static loadings," J. Mater. Process. Technol., **255**(7491), pp. 724–738.

[85] Hong, L., Girsang, I. P., and Dhupia, J. S., 2016, "Identification and control of stick–slip

vibrations using Kalman estimator in oil-well drill strings," J. Pet. Sci. Eng., **140**, pp. 119–127.

[86] Aarsnes, U. J. F., and Shor, R. J., 2018, "Torsional vibrations with bit off bottom: Modeling, characterization and field data validation," J. Pet. Sci. Eng., **163**(October 2017), pp. 712–721.

[87] Berman, A. D., Ducker, W. A., and Israelachvili, J. N., 1996, "Origin and Characterization of Different Stick - Slip Friction Mechanisms," Langmuir, **12**(1), pp. 4559–4563.

[88] Seneviratne, L. D., Ngemoh, F. A., Earles, S. W. E., and Althoefer, K. A., 2001, "Theoretical modelling of the self-tapping screw fastening process," Proc. Inst. Mech. Eng. Part C J. Mech. Eng. Sci., **215**(2), pp. 135–154.

[89] Knight, W., and Boothroyd, G., 2005, Fundamentals of Metal Machining and Machine Tools, CRC Press.

[90] Nassar, S. A., and Zaki, A. M., 2009, "Effect of Coating Thickness on the Friction Coefficients and Torque-Tension Relationship in Threaded Fasteners," J. Tribol., **131**(2), p. 021301.

[91] Toros, S., Ozturk, F., and Kacar, I., 2008, "Review of warm forming of aluminum-magnesium alloys," J. Mater. Process. Technol., **207**(1–3), pp. 1–12.

[92] Liu, H. J., Lang, L. H., and Li, T., 2009, "Investigation of formability of aluminum alloy sheet at elevated temperature," Int. J. Plast., **16**(3), pp. 145–148.

[93] Bolt, P. J., Lanboo, N. A. P. M., and Rozier, P. J. C. ., 2001, "Feasibility of Warm Drawing of Aluminum Products," J. Mater. Process. Technol., **115**, pp. 118–121.

[94]   Wang, H., Luo, Y. B., Friedman, P., Chen, M. H., and Gao, L., 2012, "Warm forming behavior of high strength aluminum alloy AA7075," Trans. Nonferrous Met. Soc. China, **22**, pp. 1–7.

[95]   Li, D., and Ghosh, A. K., 2003, "Tensile deformation behavior of aluminum alloys at warm forming temperatures," Mater. Sci. Eng. A, **352**(1–2), pp. 279–286.

[96]   Li, D., and Ghosh, A. K., 2004, "Biaxial warm forming behavior of aluminum sheet alloys," J. Mater. Process. Technol., **145**(3), pp. 281–293.

[97]   Salandro, W. A., Jones, J. J., Bunget, C., Mears, L., and Roth, J. T., 2015, Introduction to Electrically Assisted Forming, Springer International Publishing.

[98]   Troitskii, O. A., 1969, "Electromechanical Effect in Metals," Zh. Eksp. Teor. Fiz., **10**, pp. 18–22.

[99]   Long, X., and Khanna, S. K. S. K., 2005, "Modelling of Electrically Enhanced Friction Stir Welding Process Using Finite Element Method," Sci. Technol. Weld. Join., **10**(4), pp. 482–487.

[100]   Ferrando, W. A., 2008, "The Concept of Electrically Assisted Friction Stir Welding (EAFSW) and Application to the Processing of Various Metals."

[101]   Pitschman, M., Dolecki, J. W., Johns, G. W., Zhou, J., and Roth, J. T., 2010, "Application of Electric Current in Friction Stir Welding," ASME 2010 International Manufacturing Science and Engineering Conference, pp. 185–189.

[102]   Potluri, H., Jones, J. J., and Mears, L., 2013, "Comparison of Electrically-Assisted and Conventional Friction Stir Welding Processes by Feed Force and Torque," ASME 2013 International Manufacturing Science and Engineering Conference.

[103]   Liu, X., Lan, S., and Ni, J., 2015, "Electrically Assisted Friction Stir Welding for Joining Al 6061 to TRIP 780 steel," J. Mater. Process. Technol., **219**, pp. 112–123.